NANOMAGNETIC AND NANOSTRUCTURAL STUDIES OF THIN FILM MAGNETIC SYSTEMS

John Rose

Submitted for the degree of Doctor of Philosophy at the Department of Physics and Astronomy, The University of Glasgow.

December, 1997

ProQuest LLC.
789 East Eisenhower Parkway
P.O. Box 1346
Ann Arbor, MI 48106 – 1346

How's things?

Contents

Acknowledgements

First of all I would like to thank my supervisors Professor John Chapman and Dr Stephen McVitie for all their help and guidance, as well as their patience. A further mention must go to Professor Chapman for the provision of the facilities within the solid state group.

Thanks also to Q Meng and J C Lodder at the University of Twente, S Casey, E W Hill and J J Miles at the University of Manchester, H Holloway and D J Kubinski at Ford Research Labs in Michigan and D Raasch at Philips in Aachen for the provision of samples. Thanks to K O'Grady and G Phillips at the University College of North Wales at Bangor and Q Meng and J C Lodder for not only allowing me to use, but teaching me to use their AGFM and VSM respectively.

A special hug must be given to everyone in the solid state physics group for their frequent help and support and without whom I would have lost my sanity a long time ago. In particular I would like to thank Dr L Heyderman for persuading me to take notes, Drs M Mackenzie, P Thompson, P Aitchison, S McVitie, K Kirk and soon to be Drs P McHendry, L Christie, A Gallagher, R Lindsay and J King for proof reading and bouncing questions off and Dr P Nicholson for providing hot water and milk at coffee time. For technical support I would like to thank A Howie, C How, S Conner, D MacDonald and J Simms. Another mention must go to John at this stage for extreme patience and being prepared to read some fairly awful first drafts.

Thanks also to various family and friends for putting up with my being a student for so long. A special mention must go to my parents for understanding that I didn't want to be a merchant banker, and my sister for providing me with a holiday home.

Finally I would like to thank EPSRC and CAMST for funding.

Declaration

This thesis is a record of work carried out by me in the department of Physics and Astronomy at the University of Glasgow. The work described herein is my own apart from the deposition of the samples and computer modelling. Some of the work contained in this thesis has been published in the following papers:

S Casey, E Hill, J Miles, P Sivasamy, K Birtwistle, B. Middleton, J Chapman and J Rose, "A study of PtCo films used for longitudinal recording.", J. Magnetism and Magnetic Materials, **155,** No.1-3, 348-351, 1996.

S Casey, E Hill, J Miles, P Sivasamy, K Birtwistle, B. Middleton, J Chapman and J Rose, "A microstructural study of PtCo thin-films.", IEEE Transactions on Magnetics, **32,** 5 Pt1, 3831-3833, 1996.

J.Rose, J N Chapman, J C Lodder and Q Meng, "TEM studies of CoNi/Pt multilayers", Journal of the Magnetics Society of Japan, 20, 263 - 266, 1996.

J.Rose, J.N.Chapman, S.Casey, E.W.Hill and J.J.Miles, "TEM studies of the magnetisation processes in CoPt Alloys", accepted for publication in IEEE transactions on Magnetics 1997.

J.Rose, J.N.Chapman, G.N.Phillips, H.Laidler and K.O'Grady, "Time dependent effects in materials with two-stage reversal processes", accepted for publication 1997.

J.N.Chapman, J.Rose, I.S.Weir, I.S.Molchanov and D.M.Titterington, "The direct observation of magnetisation reversal in films of interest for high density information storage", accepted for publication Journal of the Magnetics society of Japan 1997.

J.N.Chapman, J.Rose, P.Aitchison, H.Holloway and D.Kubinski, "Direct observation of magnetisation processes in AF-coupled Co/Cu multilayers with different Co and Cu layer thicknesses", accepted for publication 1997.

This thesis has not been previously submitted for a higher degree.

Summary

The work described in this thesis involves the study of advanced thin film magnetic systems. All the systems investigated have proposed commercial applications and are examined to determine both their physical properties on the nanometre scale and their magnetic properties to a resolution of ≈20nm. Most of the work was carried out on the highly modified Philips CM20 transmission electron microscope (TEM) at the University of Glasgow. Use was also made of the JEOL 2000FX TEM at the University of Glasgow, an alternating gradient field magnetometer (AGFM) at the University College of North Wales at Bangor and a vibrating sample magnetometer (VSM) at the University of Twente in Enschede, the Netherlands.

In chapter 1 the basic concepts of thin film magnetism along with the thin film systems which are to be investigated are introduced. In chapter 2 TEMs and magnetometers are described with particular reference to the instruments used. This is followed by a description of the processes of image formation and collection and the other techniques used in the study.

The experimental techniques developed to apply magnetic fields to the samples are described in chapter 3. They allow a microscopist to apply a changing field of up to several thousand Oersteds to a thin film sample while it is being imaged magnetically. This allows details of the micromagnetic structure to be determined that would otherwise be very

difficult to deduce. These types of experiment form a large part of the work contained in this thesis, and the results are discussed in chapter 4 to 6.

In chapter 4, Co/Cu and CoCu/Cu multilayers with giant magnetoresistance (GMR) properties are described. These thin films have proposed applications as position sensors. The magnetisation reversal processes of these films are described and are compared with a model. The latter suggests that there is an anisotropy present in the films where the thickness of the Cu spacer layer is at the 1st antiferromagnetic maximum (AFM). The model further indicates that the uniaxial anisotropy constant for the film with alternating magnetic layer thicknesses $|K| \approx 1.25|J/t|$ where J is the ferromagnetic coupling constant and t is the thickness of the thinner magnetic layer and the uniaxial anisotropy constant for the film with magnetic layers of equal thickness, $|K| \approx |J/t|$. This anisotropy is not detected in all the samples examined, and since it was not introduced deliberately, its presence is surprising.

Chapters 5 and 6 both involved the study of magnetic information storage media. In chapter 5 CoNi/Pt multilayers and NdTbFeCo amorphous alloys with attractive properties for use as magneto optic (MO) media at low laser wavelengths are described. Two characteristic hysteresis loop shapes for perpendicularly magnetised media are considered and their micromagnetic reversals are contrasted. To aid the understanding of the reversal mechanisms, they are compared with results from computer model predictions for samples with the same physical parameters. From these comparisons the following estimates are

made: a wall energy (σ_w) of 1.8×10^{-3} Jm^{-2} and an activation volume (V_{act}) of 0.015 of the crystallite volume. The validity of these figures is then discussed.

Proposed in-plane longitudinal recording media are described in chapter 6. The samples are CoPt alloys deposited under varying conditions, to different compositions and thicknesses and onto two different types of substrate. The crystallite structure of the samples are shown to be independent of the thickness of the sample but are found to vary as the deposition conditions vary. The micromagnetic properties are shown to be dependent on the thickness of the samples and the crystallite structure of the samples. Two different reversal mechanisms are identified and described in detail. They involve domain walls moving through the sample in one case and the nucleation of many independent reverse domains in the other. Bits, which have been written on the sample deemed most suitable, are then examined and related to the reversal mechanism. This showed that the domain size during reversal and the transition width are comparable.

Chapter 7 contains conclusions drawn from the discussions in chapters 4 to 6 and proposals for future work.

Chapter 1

Ferromagnetism, magnetic recording and sensing

1.0 Introduction

Ferromagnetic materials are materials which possess a spontaneous magnetic dipole moment at temperatures below a well defined temperature called their Curie temperature (T_c). Above this temperature, the spins of the individual atoms are randomly orientated so that there is no overall magnetic moment. Even at temperatures below the Curie temperature, the individual atomic dipoles are not all aligned parallel with each other; instead the orientations of the dipoles are governed by energy considerations. The dipoles align themselves in a way to minimise the energy of the system. For ferromagnetic systems, the energies which must be considered are: Exchange energy (E_A), Anisotropy energy (E_k), Magnetostatic energy (E_m), Zeeman energy (E_H) and Magnetostriction energy (E_s). Magnetostriction is the change in length of a ferromagnetic material caused by the magnetisation of the sample and will not be discussed further in this thesis.

1.1.1 Exchange energy

The exchange energy within a magnetic system arises from the relative orientations of neighbouring dipoles. It is a consequence of the Pauli exclusion principle, which forbids electrons with the same spins from having the same spatial wavefunction [1]. This results in different mean separations for electrons with spin parallel and spin anti-

parallel, so the electrostatic energy of the system becomes dependant on the spins of the electrons. The energy associated with this exchange interaction for a pair of spins is:

$$E_A = -2J_{ij}\underline{S}_i \cdot \underline{S}_j \qquad [1.1]$$

where J_{ij} is a constant called the exchange integral and $\underline{S}_i$ and $\underline{S}_j$ are the spins on the electrons. The exchange integral for ferromagnetic materials is positive. The negative sign in the expression then implies that a minimum exchange energy results from spins aligned parallel. For antiferromagnetic coupling this exchange integral is negative, giving the result that antiparallel alignment is preferred. The total exchange energy is calculated by summing the exchange interactions of each pair of electrons, although as the interaction is generally short range this only involves the nearest neighbours:

$$E_A = \frac{nJs^2}{a}\int_V \left[(\nabla\alpha)^2 + (\nabla\beta)^2 + (\nabla\gamma)^2\right] dV \qquad [1.2]$$

with α, β and γ representing the directional cosines of the magnetisation vector, $\underline{M}_i = M_s\underline{m}_i(\alpha(\underline{r}), \beta(\underline{r}), \gamma(\underline{r}))$ and a is the lattice constant of the material, n is a constant depending on the crystalline structure (1 for simple cubic, 2 for body centre cubic and hexagonal close packed, 4 for face centre cubic) [2], J is the exchange constant and S is the magnitude of the spin magnetic moment.

1.1.2 Anisotropy energy

There are several sources of anisotropy energy: magnetocrystalline, interface, shape and induced anisotropy. The magnetocrystalline anisotropy energy allows for a preferred direction within the crystal lattice. Within each crystal type there will be one or more axes along which the magnetisation will prefer to lie. This will be the minimum energy state, and the energy will increase as the magnetisation direction rotates away from this axis. The simplest case is for hexagonal cobalt [3], where the easy axis is along the "c" axis and the energy density varies with the form:

$$E_k = K_1 \sin^2\Phi + K_2 \sin^4\Phi \qquad [1.3]$$

where K_1 and K_2 are the first and second order magnetocrystalline anisotropy constants and Φ is the angle of rotation away from the easy axis. For cubic materials such as iron, nickel and cubic cobalt the expression becomes:

$$E_k = K_1(\alpha^2\beta^2 + \alpha^2\chi^2 + \beta^2\chi^2) + K_2\alpha^2\beta^2\chi^2 \qquad [1.4]$$

where K_1 and K_2 are as before and α, β and χ are the direction cosines of the magnetisation relative to the cube axes.

The other sources of anisotropy energy can be just as important as the magnetocrystalline anisotropy. Interface anisotropy arises at the interface of some multilayer thin films and is responsible for the perpendicular magnetic anisotropy which

results in some films being suitable for magneto optic recording [4]. In polycrystalline materials the magnetocrystalline anisotropy will change as the orientations of the crystallites changes; however it is possible to induce an anisotropy. The induced anisotropy can be created in polycrystalline samples which are deposited in a magnetic field and is caused by a preferential ordering of atom pairs in the otherwise random alloy [3]. During deposition an interaction between the local magnetisation and the atom pairs tends to align the "pair axis" and the magnetisation vector. This results in a "pair axis" throughout the sample and, after deposition, the induced anisotropy remains. Shape anisotropy arises from magnetostatic considerations which are discussed in the next section. Each of these anisotropies result in an energy term which to the first order is similar to that for the hexagonal crystal lattice [equation 1.3].

1.1.3 Magnetostatic energy

If there is a net magnetisation perpendicular to the surface of a magnetic body, magnetic surface charge is formed. Similarly volume charge can be formed where two domains meet which are magnetised with components perpendicular to the domain wall and in opposite directions. The magnetic charges result in an magnetic field, called the stray field, emanating beyond the surface of the material, and an internal field called the demagnetising field (H_d) [3]. The internal field, as its name suggests, opposes the magnetisation within the domain, and is given by the expression:

$$H_d(\underline{r}) = \frac{1}{4\pi}\int_v -\frac{\nabla \cdot \underline{\underline{M}}}{r^2} dV + \frac{1}{4\pi}\int_s \frac{\underline{\underline{M}} \cdot \underline{n}}{r^2} dS \qquad [1.5]$$

where $\underline{r}$ is the position vector for the field plots, $\underline{n}$ is the unit vector normal to the surface, $\nabla \cdot \underline{M}$ denotes the volume charge density and $\underline{M} \cdot \underline{n}$ denotes the surface charge density. The magnetostatic energy is then given by:

$$E_m = -\frac{1}{2}\mu_0 \int_V \underline{M} \cdot \underline{H_d} dV \qquad [1.6]$$

Calculation of the demagnetising field is difficult, and is dealt with in section 3.2. The magnetostatic energy is highly dependent on the sample geometry, and is at a minimum when the magnetisation forms a closed loop, resulting in no surface charge.

1.1.4 Zeeman energy

The Zeeman energy arises from the interactions of the magnetic dipoles with external magnetic fields and is given by:

$$E_H = -\mu_0 \int_V \underline{M} \cdot \underline{H} dV \qquad [1.7]$$

where H is the external field. For a minimum energy state the magnetisation should align with the field.

1.1.5 Domains and domain wall energies

Domains are volumes of a magnetic sample where the magnetisation is aligned; alignment directions are different in adjacent regions [5][6].

In the absence of an external field, exchange and anisotropy energies would be minimised if all the magnetisation within a single crystal sample was aligned in the same direction, along an easy axis. This could however result in large magnetostatic energies if the sample shape was such that there was a large amount of surface charge. However in order to eliminate this charge, domains would have to be formed where the magnetisation was parallel to the surface of the sample. The formation of domains, however involves the formation of domain walls with their associated energy costs. Domain walls are regions of the sample where the magnetisation orientation changes gradually between the magnetisation orientations in the two neighbouring domains. Domain wall widths are often in the range 10nm to 100nm [2] and they arise due to the prohibitively expensive exchange energy costs that would occur if the magnetisation orientation changed abruptly. The structure of a domain wall depends on the sample. There are two extreme forms of domain wall: the Bloch wall [7] and the Néel wall [8]. Bloch walls (figure 1.1a) occur in bulk and thicker thin film samples. The magnetisation rotates out of the plane of the film. This would result in high magnetostatic energy costs at the surface of a thinner film, and in such situations Néel walls occur (figure 1.1b). In this type of wall the magnetisation rotates in the plane of the film. Other domain wall configurations exist which are hybrids of these two wall types such as cross-tie walls and walls in multilayers [9]. In some multilayer systems it has been proposed that the domain walls are of the form of the wall illustrated in figure

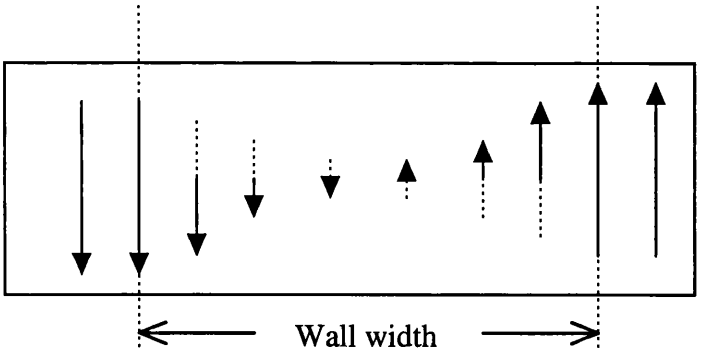

Figure 1.1a: Looking down on a Bloch Wall.

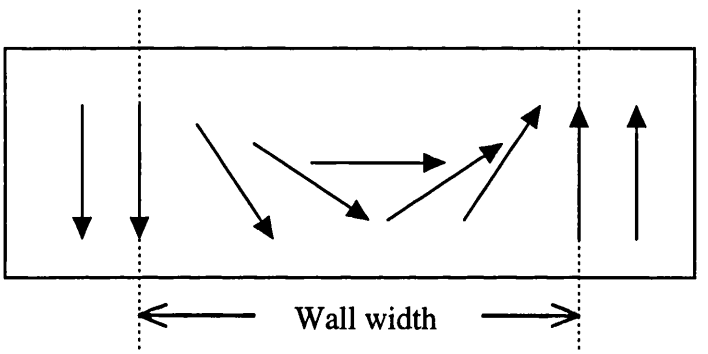

Figure 1.1b: Looking down on a Neel wall

1.2. This wall geometry would account for the low wall energies observed in such systems.

The final domain configuration in a sample will be a balance of the energy considerations discussed earlier and will depend on the geometry of the sample and any external fields applied. This is a particular problem in magnetic recording since the regular domain shapes which are desirable tend to be expensive in magnetostatic energy. The lower energy configuration which is often adopted results in an irregular edge to the domain that reduces the area where magnetisation vectors meet head on.

The lowest energy domain configuration will change if an external field is applied; the area of the sample magnetised in the direction of the field will want to increase. This can be done by (i) moving the domain walls so that preferentially orientated domains are enlarged, (ii) creating new domains aligned in the direction of the field or (iii) changing the orientation of the magnetisation vector in domains which are not aligned with the field. Each of these methods has energy implications. The domain walls may be fixed in position, caused by pinning sites which are often crystal defects or boundaries over which the domain wall finds it difficult to move. The formation of new domains requires the formation of new domain walls (or the destruction of stable wall structures) along with the associated energy costs. Changing the orientation of the magnetisation vector will inevitably involve changes with respect to the easy axis. This will have an associated anisotropy energy cost.

These energy costs will mean that the change in magnetisation of a sample will often be less than would be expected for the application of a particular external field. In extreme

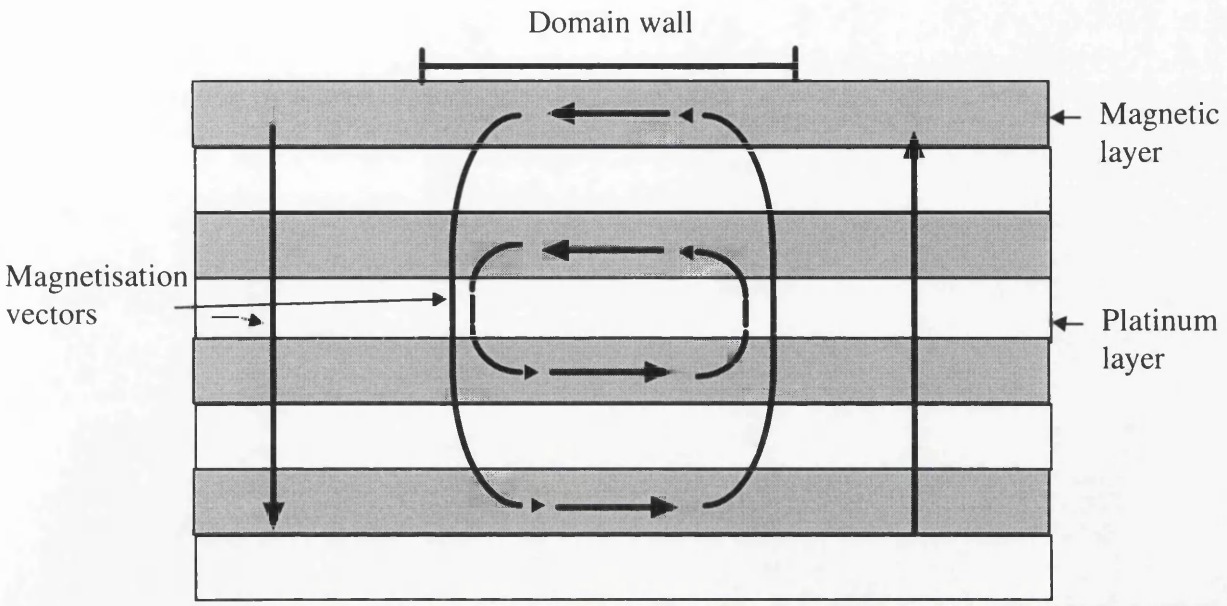

Figure 1.2: The domain wall structure previously predicted for Co/Pt multilayers (shown for a film with four magnetic layers). The dark arrows represent the magnetisation directions.

cases this may mean that large fields (≥10000Oe) may be required even to change the magnetisation slightly. This is called magnetic hysteresis. The hysteresis of a sample gives rise to a characteristic plot of the magnetisation of the sample against the field applied, called the M-H curve, or hysteresis curve. A hysteresis curve is shown for a cobalt-nickel/platinum multilayer (figure 1.3). From these curves, characteristice values can be measured: saturation magnetisation (M_s) which is the maximum magnetic moment for the sample; remanence (M_r) which is the magnetisation which remains after the sample has been saturated and the external field is then reduced to zero; coercivity (H_c) which is the field which is required to reduce the magnetisation to zero after it has been saturated.

1.2 Magnetic recording

The application of magnetic materials to store information has been recognised for decades. The concept of magnetic hysteresis is fundamental to the magnetic recording process; when a field is applied to a randomly magnetised ferromegnetic medium, the magnetisation of the media will align itself to a degree with the field and will continue to have a component aligned with the applied field direction after the field has been removed. This is the basis of all magnetic recording regimes. Magnetic recording can be split into three main categories: in-plane recording, perpendicular recording and magneto optic (MO) recording. As its name suggests, in-plane recording involves arranging the in-plane magnetisation of a thin film sample in such a way that the stray fields produced by the domain configurations can be detected by the a read head, and the stored information thereby retrieved. There are two types of in plane recording: longitudinal and transverse [10]. Longitudinal recording is at present dominant and

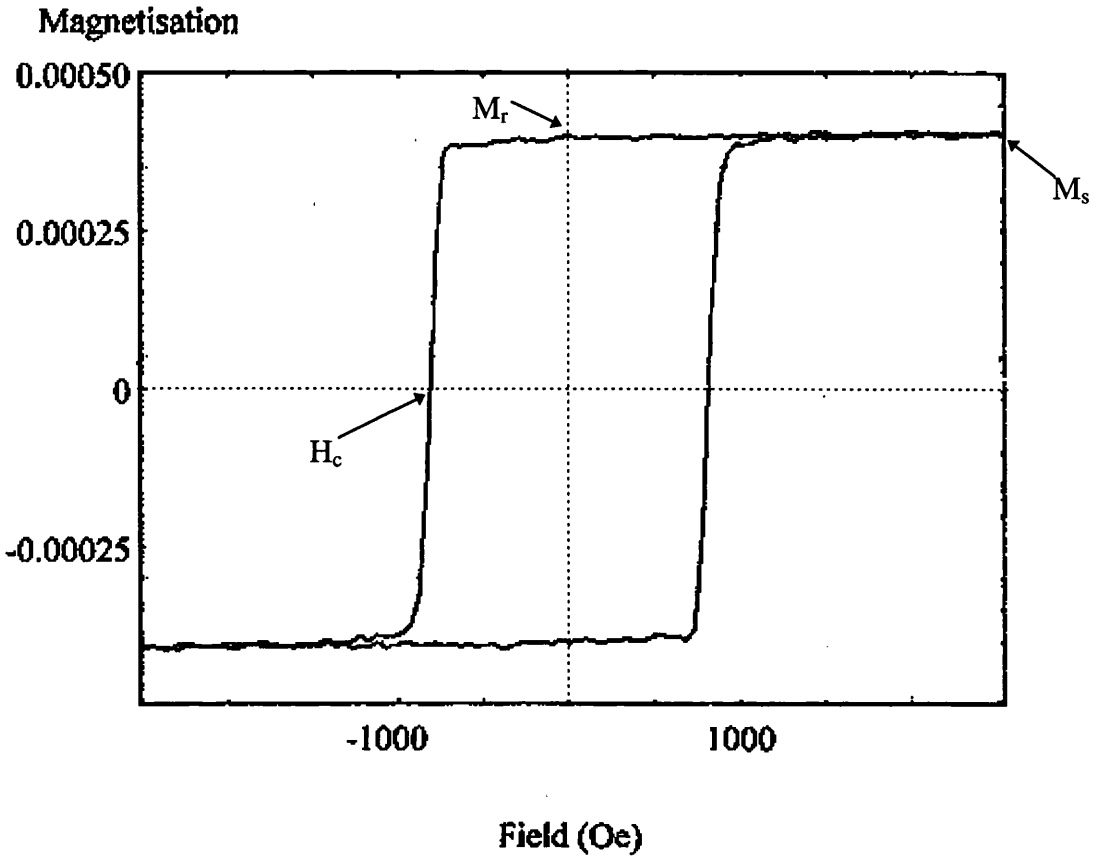

Figure 1.3: A hysteresis loop for a CoNi/Pt multilayer, showing the position of the saturation magnetisation (M_s), remanent magnetisation (M_r) and coercive field (H_c).

involves writing bits with the magnetisation aligned in the direction of the recording track. Transverse recording involves writing bits with the magnetisation at right angles to the track direction. Perpendicular recording involves writing bits where the magnetisation is aligned perpendicular to the surface of the media. These bits are detected by the read head in a similar manner to the in-plane recording regimes. MO recording, on the other hand, involves the writing of the component of the magnetisation perpendicular to the surface of the media. Information stored in this way can be retrieved optically by making use of the magneto optic Kerr effect (MOKE). In this thesis I will only consider longitudinal and MO recording.

1.2.1 In-plane recording

This type of recording can be either analogue or digital; in this thesis I will concentrate on digital recording. Bits are recorded by passing a write head over the surface of the medium, while varying the current to the head in the binary pattern required. The varying current through the recording head produces a varying magnetic field between the poles of the recording head which has a large enough in plane component to write permanent magnetic domains to the media (figure 1.4).

The recorded domains produce large stray fields where oppositely magnetised domains meet head on (figure1.5). These stray fields produce a signal response in a read head when it is passed over the media. This response can be electronically processed to give the original bit pattern signal which was passed through the write head. The read head can be either inductive or magnetoresistive; write heads are inductive. Current media have recording densities up to 5gigabits/inch^2 [11] and are based on cobalt chromium

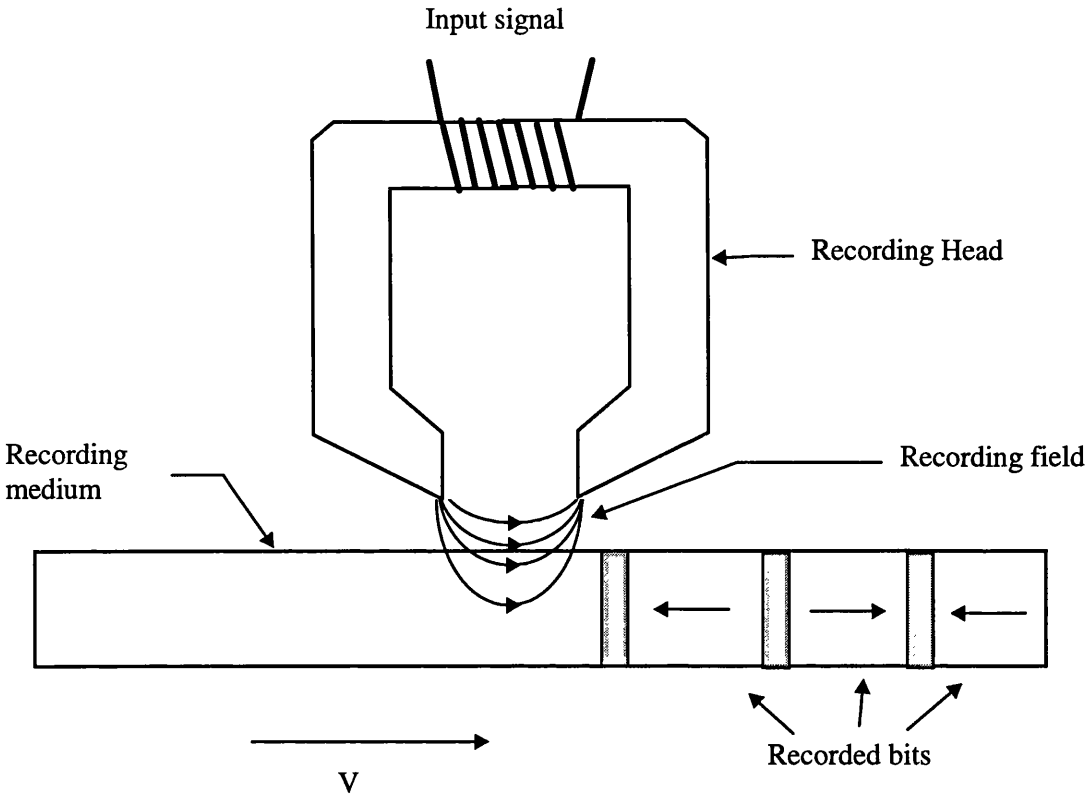

Figure 1.4: Schematic of an in-plane recording head and the in-plane recording process.

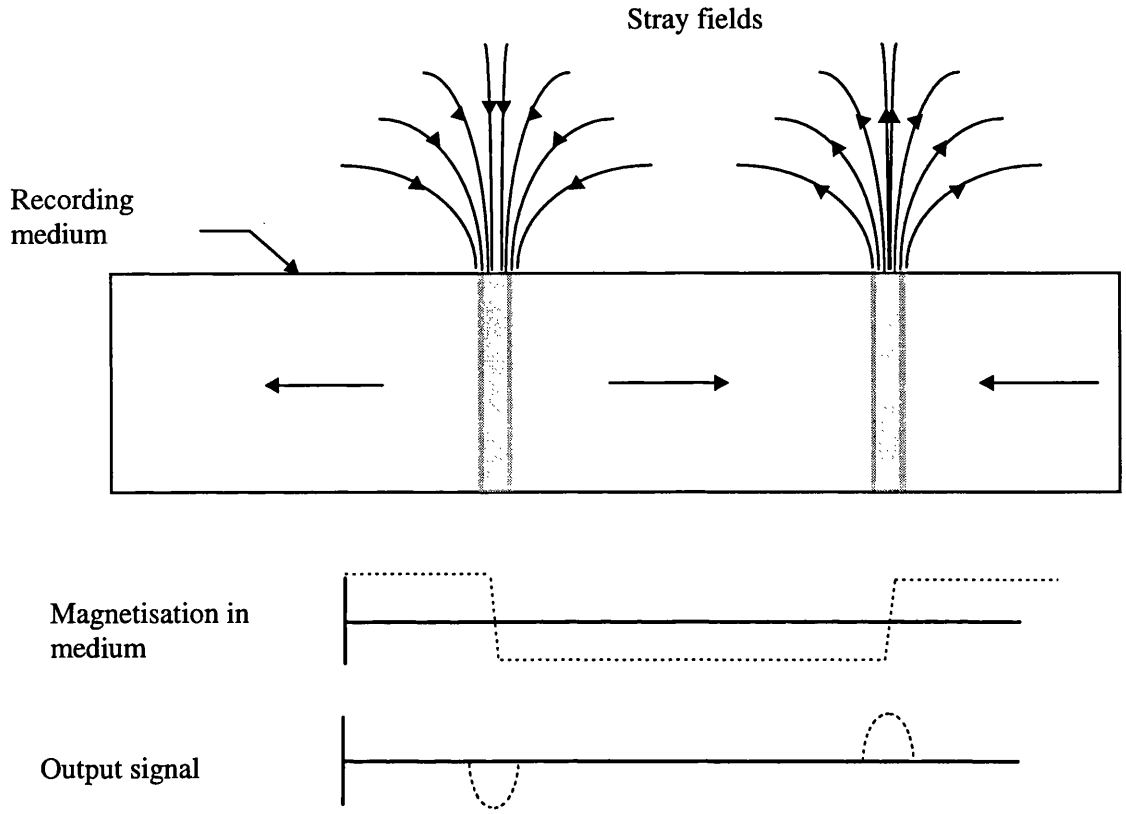

Figure 1.5: The stray fields produced by recorded in-plane bits, and signal readout.

(CoCr) alloys. Hard disk recording systems based on in plane recording have the highest data transfer rates (≈30megabits/s), however they are susceptible to dust contamination.

1.2.2 Magneto-optic recording

An alternative to recording bits magnetised in the plane of the media and reading the stray field that results, is to record marks where the magnetisation is perpendicular to the surface of the media and to read the effect these marks have on polarised light. This is called magneto optic (MO) recording.

The first MO recording system was released onto the market in 1988. At that time MO recording had the advantage of being a high capacity removable storage media. The recording medium could be easily transferred between different locations, or stored in an archive, due to the recording systems lack of sensitivity to dirt and other contaminents which arises from the non contact recording system (figure1.6). Current magneto optic storage media are made of rare earth-transition metal (RETM) amorphous alloys. Recent developements also mean that: data transfer rates are approaching those of magnetic recording systems, even higher volumes of data can be recorded on a single disk (5gigabytes on a 5¾ inch disk) [12] and the system has a proven record of over a million read/erase cycles.

Recording MO marks in the simplest case involves heating up an local area of the media to a temperature above its Curie temperature. The area then cools down in an applied field and the magnetisation of the local area is fixed in the direction of the applied field. Recording mark sequences can be done by either laser power modulation (LPM) or

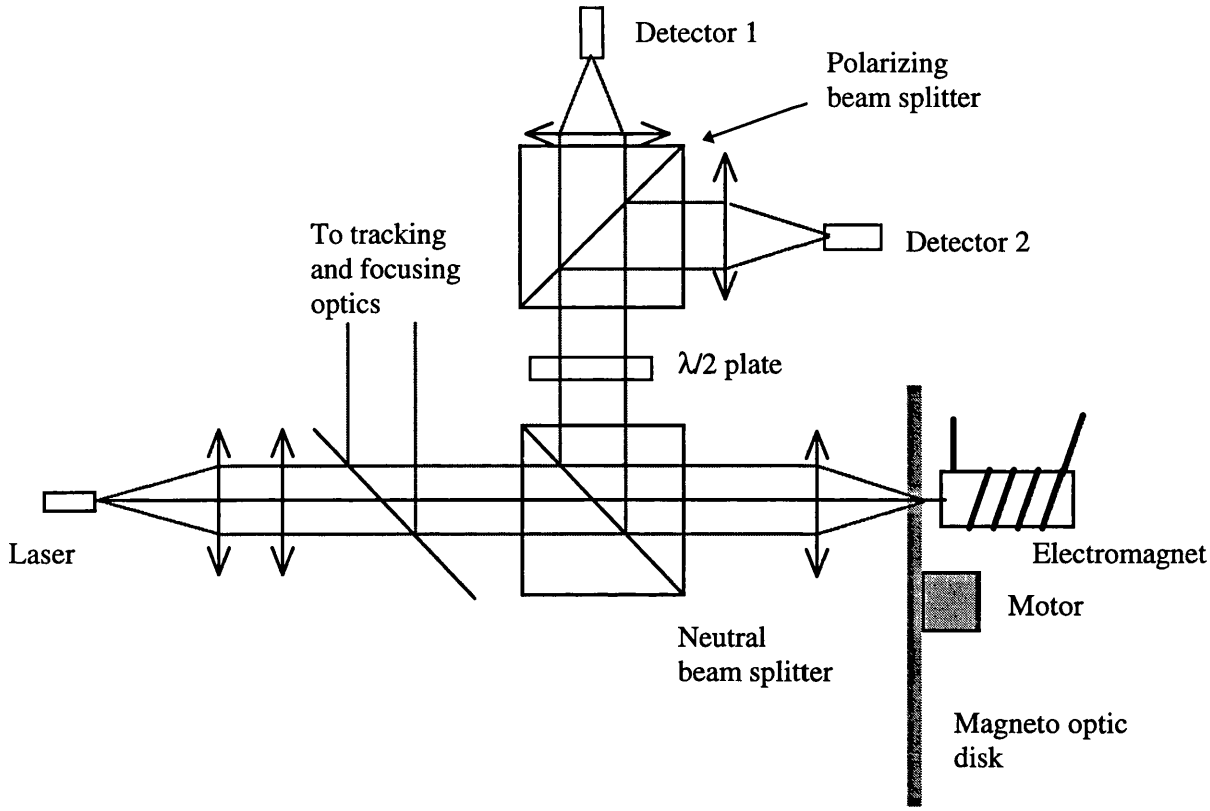

Figure 1.6: Schematic of a magneto optic read/write system.

magnetic field modulation (MFM). Laser power modulation involves recording bits by turning the laser on and off in a constant magnetic field when bits are required to be recorded. This recording system requires that any previously recorded data is deleted beforehand. Magnetic field modulation involves keeping the laser beam switched on and altering the magnetic field in the pattern required. This regime can write directly over old data. In both cases the recorded area is defined principally by the laser spot.

Read out is done using the magneto optic Kerr effect (MOKE). This is where polarised light is shone onto the sample, the polarisation of the light is rotated as it is reflected off the magnetised media. The sense of the rotation depends on the direction of the magnetisation (figure1.7). The reflected light can then be analysed to determine the recorded pattern. A typical MO medium will rotate the polarisation by around 0.5°.

1.2.3 Giant magneto resistance

Magnetoresistance (MR) is the change in electrical resistance of a material in the presence of an external magnetic field. Giant magnetoresistance (GMR) was first reported in 1988 for Fe/Cr multilayers [13]. The multilayers were grown by molecular beam epitaxy and at T=4.2K the resistivity was lowered by a factor of 2 in a field of 2T. Baibich, et al., who grew the samples and discovered the phenomena, attributed the change in resistance to the spin dependent scattering of the electrons at the interfaces of the layers. To date several other multilayers and granular systems have displayed GMR effects, including a Co/Cu multilayer system which displayed a 115% GMR effect with the current in the plane of the film [14].

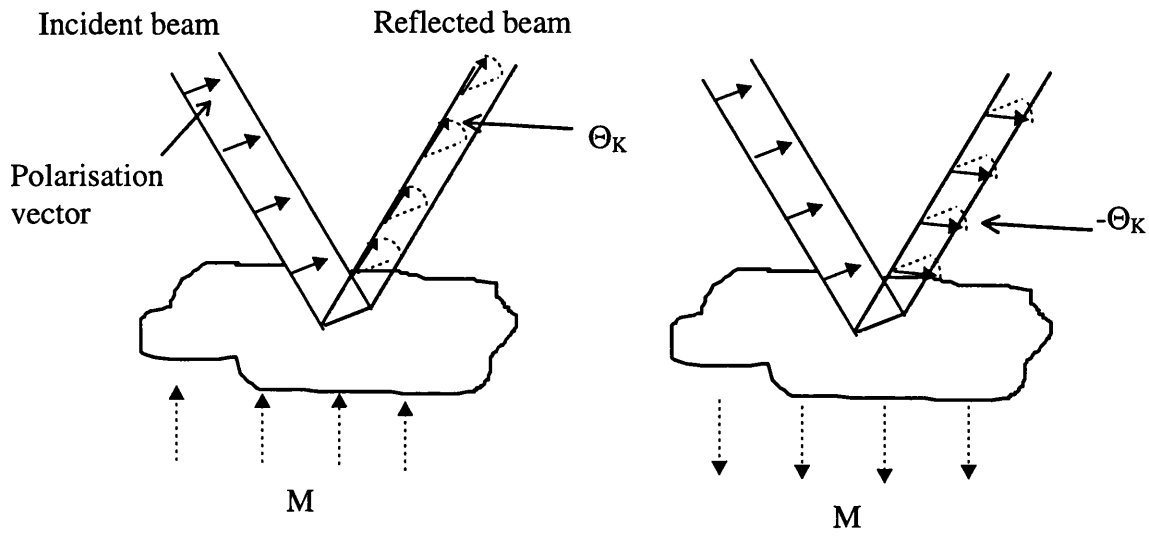

Figure 1.7: A schematic showing the Kerr rotation of polarised light by the magnetisation in a magneto optic medium.

The size of the GMR effect is related to the coupling between the layers, and the spin dependent scattering of the system. While the spin dependent scattering is an inherent property of the interfaces between the layers, the coupling can be controlled by the non-magnetic spacer layer thickness (figure 1.8). For Co/Cu multilayers, the ideal copper thicknesses are 0.9 and 2.0 nm, corresponding to the first and second maxima in antiferromagnetic coupling.

GMR materials have uses in magnetic field sensing devices, and magnetic random access memory. The field sensing devices can be used as either position sensors, or read heads in magnetic storage devices. As read heads, GMR devices are potentially much more sensitive than current anisotropic magnetoresistive (AMR) or inductive heads. As absolute position sensors, the output signal of the sensor must be independent of the magnetic history of the sensor in order to give an unambiguous response. This would require little or no hysteresis in the magnetic response of the sensor. In this thesis I will only consider materials suitable for this application.

1.3 Scope of this thesis

In this chapter I have discussed some of the magnetic processes present in thin films. I have also indicated where they are of commercial use, and the direction in which they are heading.

In chapter two I discuss the imaging modes of the transmission electron microscope (TEM) which can be used to reveal both structural and magnetic information on a thin

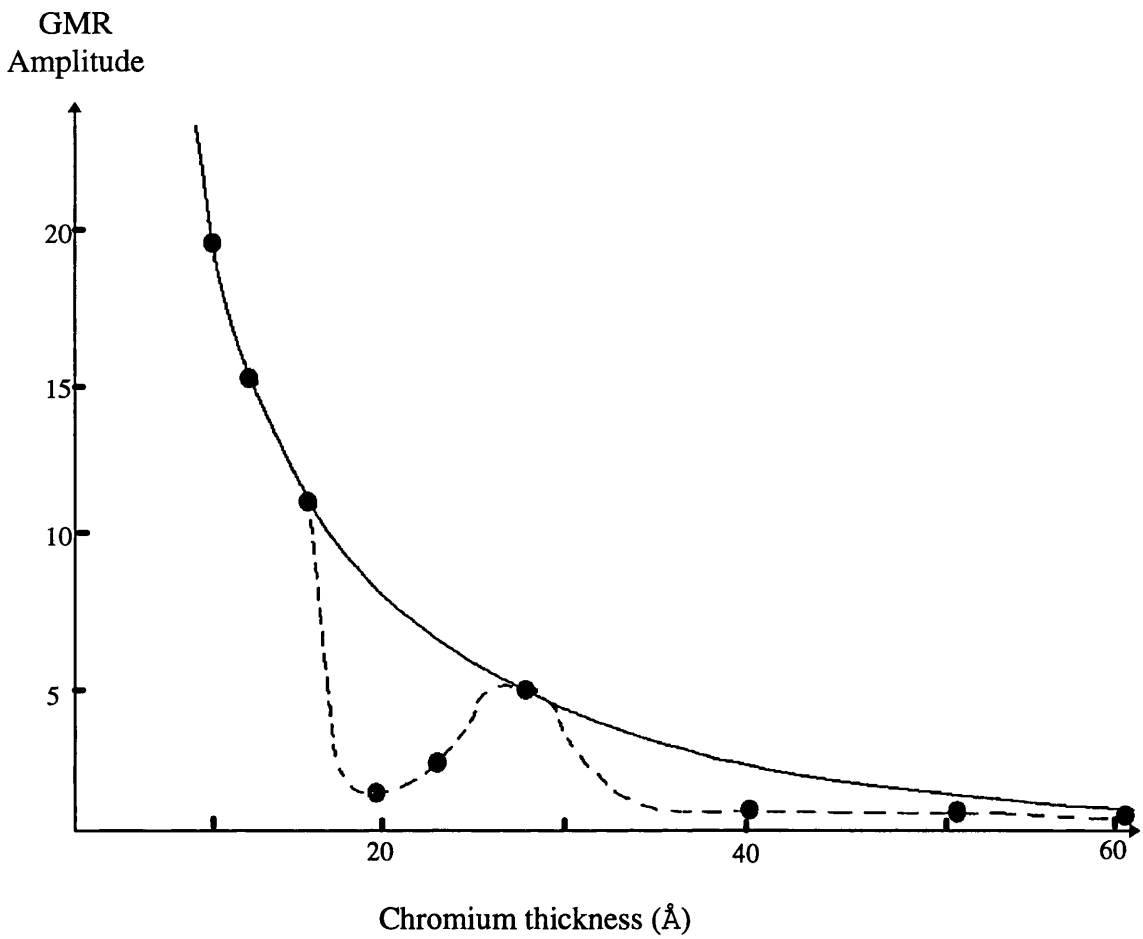

Figure 1.8: GMR amplitude of Fe/Cr multilayers plotted against Cr layer thickness. Experimental and calculated data from [15]. The dotted line was fitted to the experimental data while the solid line represents a theoretical curve.

film sample down to the nanometer scale. I also discuss two types of bulk magnetometers, which can be used to give additional information when used in conjunction with TEM experiments.

In chapter three I discuss novel methods for applying magnetic fields of up to several thousand Oersted to samples while they are being magnetically imaged in the TEM. These techniques provide a great deal of information about the micromagnetic properties of a thin film sample. Such information will be invaluable in the understanding of the bulk properties of these media, and will determine whether they are suitable for future applications.

In chapters four, five and six, I apply the techniques as outlined in chapters two and three to GMR sensing media, magneto optic recording media and magnetic recording media respectively. These media display a wide range of magnetic properties and by accurately describing their micromagnetic properties, I am able to prove the usefulness of the techniques described in chapter three.

References

[1] W.Heisenberg, Z. Phys. **49** (1928) 619.

[2] D.Jiles, "Magnetism and magnetic materials", Chapman and Hall, (1991).

[3] S.Chikazumi, "Physics of magnetism", John Wiley and sons, (1964).

[4] P.J.H.Bloemen, W.J.M. de Jonge, F.J.A. den Broeder and W.Hoving, J. Magn. Magn. Mater. **93** (1991) 105.

[5] R.Becker, Z. Phys. **62** (1930) 253.

[6] F.Bitter, Phys. Rev. **38** (1931) 1903.

[7] F.Bloch, Z. Phys. **74** (1932) 295.

[8] A.Hubert, Phys. Solidi. **38** (1970) 699.

[9] R.Ploessl, J.N.Chapman, M.R.Scheinfein, J.L.Blue, M.Mansuripur and H.Hoffmann, J.Appl. Phys. **74** (1993) 7431.

[10] H.N.Bertram, IEEE Trans. Mag. **74** (1986) 1512.

[11] C.Tsang, T.Lin, S. MacDonald, N.Robertson, H.Santini, M.Doerner, T.Reith, L.Vo, T.Diola and P.Arnett, accepted for publication IEEE Trans. Mag. (1997).

[12] P.Asthana, IEEE spectrum (October 1994) 60.

[13] M.N.Baibich, J.M.Broto, A.Fert, F.Nguyen Van Dau, F.Petroff, P.Etienne, G.Creuzet, A.Freiderich and J.Chazelas, phys. Lett. **61** (1988) 2472.

[14] S.S.P.Parkin, N.More and K.P.Roche, Phys. Rev. Lett. **64** (1990) 2304.

[15] M.A.M. Gijs and M.Okada, Phys. Rev. B **46** (1992) 2908.

Chapter 2

Transmission electron microscopy instrumentation and techniques

2.0 Introduction.

In this chapter the application of a fixed beam and a scanning transmission electron microscope (TEM) as tools for the investigation of the physical and magnetic microstructures is discussed. The Philips CM20 CTEM/STEM and the JEOL 2000FX CTEM at the University of Glasgow are introduced in section 2.1. Here I discuss the imaging column along with the modifications made to both instruments and how they facilitate the micromagnetic and microstructural investigation of thin film samples.

In section 2.2 I discuss the interactions between the incident electron beam and the sample. In sections 2.3 and 2.4 I discuss image formation in the TEM and both the structural and Lorentz imaging modes which are used to reveal physical and magnetic microstructure. Finally in section 2.5 I discuss the use of bulk magnetometers to supplement the information obtained using the transmission electron microscope.

2.1 TEM instrumentation.

The majority of the experiments reported in this thesis have been performed on the Philips CM20 and the JEOL 2000FX electron microscopes at the University of

Glasgow. There is therefore in the following discussion an emphasis on aspects which are of a particular relevance to these microscopes.

2.1.1 The microscope column.

The microscope column is a series of lenses, deflection coils and apertures which can be set up in several modes to highlight some of the interactions between an electron beam and a specimen. Figure 2.1 shows the layout of these lenses for the Philips CM20 microscope. As can be seen the lenses are split into 3 groups: the condenser lenses, the objective lens system and the post specimen lenses. Each group has an aperture associated with it. The condenser lenses and condenser aperture control the illumination on to the specimen. The objective lens system is the imaging lens. As in visible light systems the aberrations in this lens control the final resolution that is attainable. The objective aperture can be used to create diffraction contrast by blocking Bragg diffracted electrons, or can be used for Foucault imaging (section 2.3.4). The post specimen lenses project the contrast produced by the objective lens system and aperture onto the viewing screen. This can be done by either focusing on the back focal plane of the objective lens system to produce an image of the sample, or by focusing on the diffraction plane of the sample to produce an image of the electrons diffracted by the sample. The selected area aperture allows diffraction patterns to be obtained from a well defined area of the sample.

Both the Philips CM20 and the JEOL 2000FX microscopes which have been used in this work were modified to improve their field free imaging resolution. In unmodified microscopes there is only a single objective lens and the specimen is placed in the field

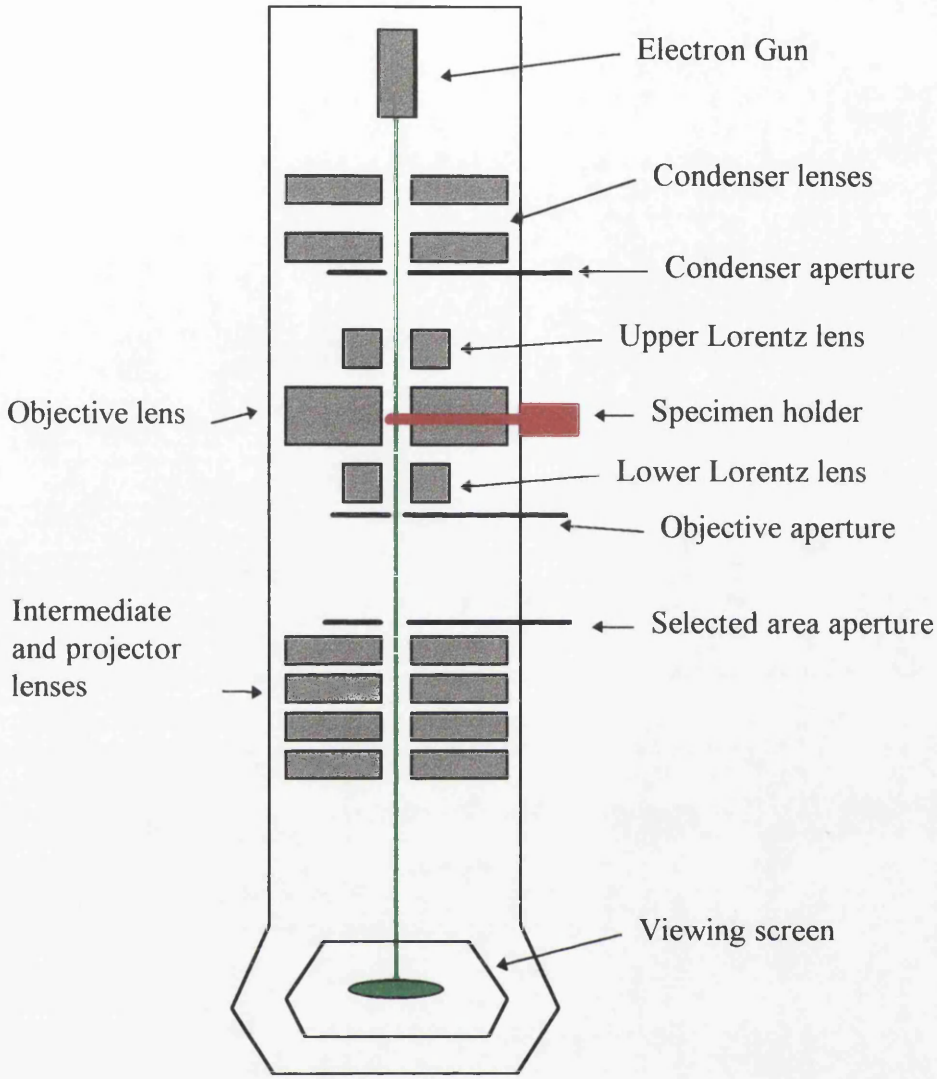

Figure 2.1:The lens layout for the Philips CM20 TEM

of this lens for viewing. This field can reach values of over 5000Oe. A magnetic field of this size would perturb the magnetic microstructure of the sample so this lens would have to be turned off to view magnetic features. This would decrease the magnifying power of the microscope available to the user, causing a great reduction in the resolution available. To overcome this problem the JEOL 2000FX has a "field free" objective lens incorporating a non-immersion pole piece which restricts the field at the specimen to less than 10 Oe even when the objective lens is fully excited. The Philips CM20 has two additional lenses, above and below the objective lens, called the upper and lower Lorentz lenses (Figure 2.1), which can be used to produce field free imaging when the objective lens is turned off. These modifications allow a magnetic resolution of <2nm compared to a typical resolution of 40-80nm in an unmodified system [1].

2.1.2 Magnetic lenses and their aberrations.

Magnetic lenses are preferred to electrostatic lenses because of their smaller aberrations and their freedom from trouble associated with high voltages. Magnetic lenses (figure 2.2) consist of a soft iron pole piece which produces an axially symmetric field for focusing the electrons. The pole pieces are magnetically coupled to the magnetic yoke which contains the windings. The magnetic field at the pole pieces is varied by changing the d.c. current which flows through the windings, and this leads to a change in the focal length of the lens. It should be noted that hysteresis effects within the lens mean that field produced by the lens with a particular current through the windings may vary, although it is steady to one part in a million.

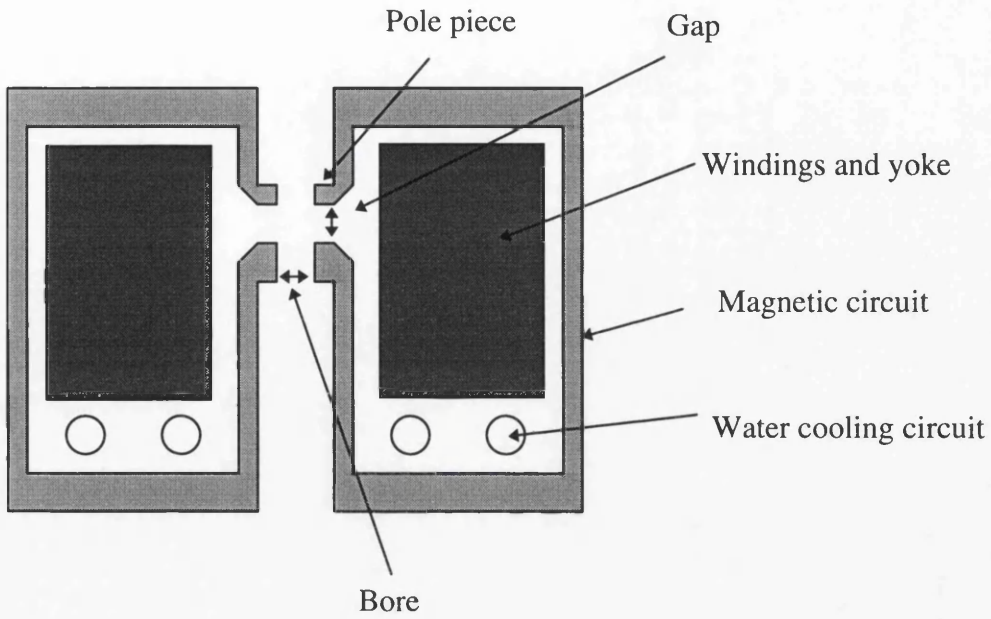

Figure 2.2: Schematic of a magnetic lens.

As with all lenses the resolution of magnetic lenses is limited by various types of aberration. This is especially important in the objective lens, since the aberrations in this lens determine the resolution of the whole system [2] . Hall (1953) lists a total of eight third order aberrations but here we will only discuss the three most relevant. These are spherical aberration, astigmatism and chromatic aberration. Technological advances have allowed microscopes to be produced where the other third order defects are reduced to insignificant values for most applications.

Spherical aberration is the dominant defect in magnetic lenses since at present there is no convenient way of correcting it. Spherical aberration occurs since the further from the centre of the lens that an electron passes the more strongly it is focused. (figure 2.3). This aberration is expressed in terms of the radius of confusion, which is related to the cube of the angle (α) at which the electron leaves the object (equation 2.1).

$$\Delta r_s = C_s \alpha^3 \qquad [2.1]$$

C_s is the spherical aberration coefficient of the lens. The C_s value for the Jeol 2000FX field free objective lens and the (large gap) objective lens of the Philips CM20 microscope is 6.5mm.The C_s value for the Lorentz lenses on the Philips CM20 microscope is 18mm. A typical value for a high resolution objective lens is 2-3mm. It should be noted that the spherical aberration is always positive so the off axis electron is always focused closer to the lens than the near axial electron.

Astigmatism results from asymmetry in the objective lens field usually caused by irregularities in the soft iron pole piece. The lens effectively has different focal lengths

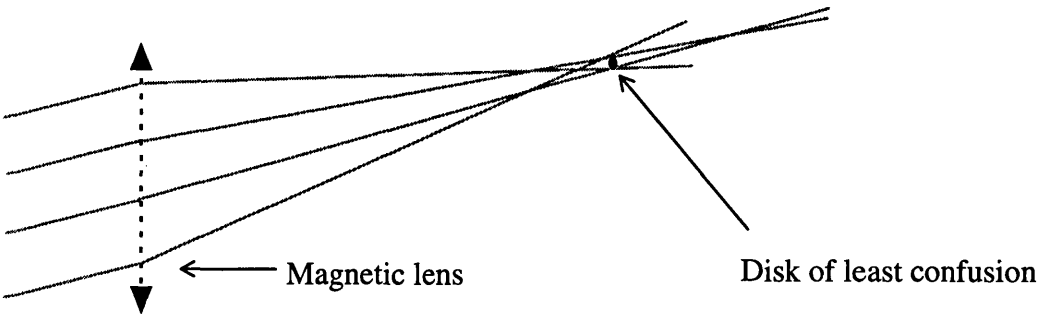

Figure 2.3: Schematic of spherical aberration showing the disc of least confusion

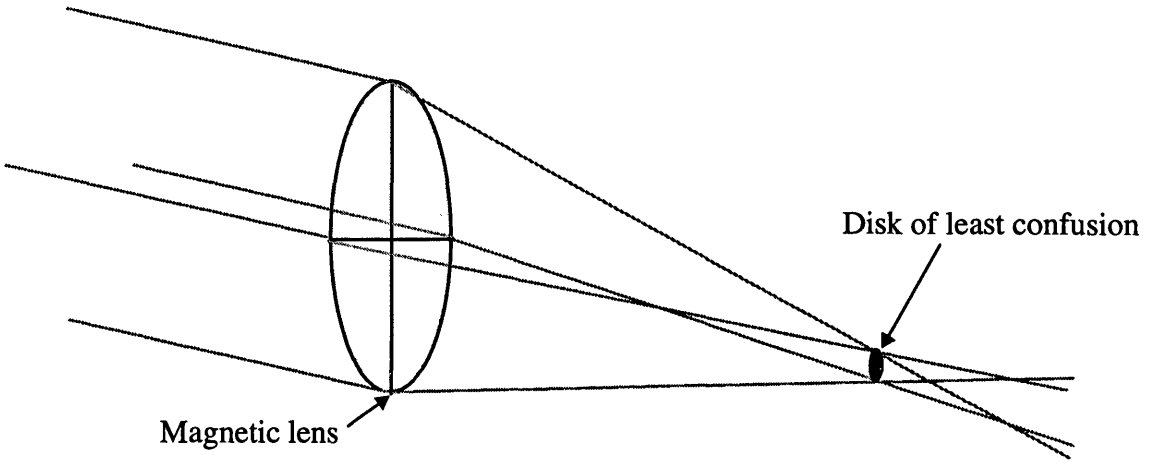

Figure 2.4: Schematic showing astigmatism showing the different focal lengths on the two principal axes.

for paraxial electrons on two different planes of symmetry (figure 2.4). Astigmatism can be corrected by introducing an equal and opposite astigmatism using octopole stigmators. Each lens system has an associated set of stigmators.

Chromatic aberration arises if there is an energy spread in the imaging electrons. The energy spread may be caused by instabilities in the accelerating voltage, instabilities in the lenses further up the column or may be introduced by the specimen itself. This results in a disc of confusion which is expressed in terms of the energy spread of the electrons (ΔE), and the angle of incidence of the electrons to the lens axis(α), the mean energy of the electrons (E) and the chromatic aberration coefficient (C_c) (equation 2.2).

$$\Delta r_c = C_c \alpha \frac{\Delta E}{E} \qquad [2.2]$$

The C_c values for the Jeol 2000FX field free objective lens and the large gap objective lens on the Philips CM20 are 5.0mm. The corresponding value for the Lorentz lenses on the Philips CM20 microscope is 40mm. Typical values for C_c are of the same order but slightly less than *f*, the focal length of the lens.

2.1.3 The electron gun system.

The electron gun consists of an electron source, an electrostatic lens and accelerating plates (figure 2.5) [3]. The electrons leave the source and are accelerated and partly focused by the electrostatic lens typically to an energy of 40keV. The electrons are then further accelerated by the accelerating plates. Both the microscopes I use accelerate the electrons to an energy of up to 200keV. For electrons with an energy of 200keV the corresponding electron wavelength is 0.0251Å.

For high resolution imaging and magnetic imaging the resolution is limited by the quality of the lenses and the coherence of the source, and for ease of image collection the source should be as bright as possible. Brightness is determined by the current density per steradian. There are three main types of electron source which are used in electron guns: the tungsten filament, the lanthanum hexaboride (LaB_6) filament and the field emission gun (FEG) [4]. The tungsten filament provides an inexpensive, but low brightness electron source. A tungsten source will produce a current of up to 0.5μA The LaB_6 filament provides a ten fold increase in brightness by reducing the electron work function on the surface of the source. The FEG can produce a very small source with a brightness up to one thousand times brighter than the tungsten source. Field emission occurs when a material with a suitable work function is placed in a strong extraction electric field. There are two types of field emission gun: cold FEG and thermally assisted FEG. Cold FEGs use a pointed tungsten cathode and are very bright sources, producing currents of up to 500μA, however they are prone to short term instabilities and require the tip to be flashed with a heating current to increase the filament lifetime to beyond a few minutes. Thermally assisted FEGs uses a tungsten tip

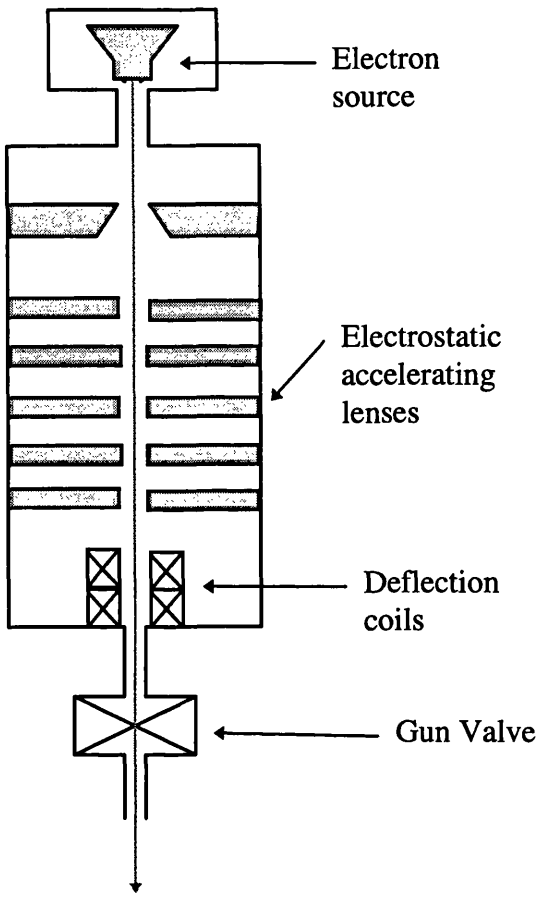

Figure 2.5: Schematic of the electron gun system.

which is zirconiated to reduce the work function, and provides a greater stability than cold FEGs but with a slight reduction in the brightness.

The JEOL 2000FX uses a tungsten filament source and the Philips CM20 uses a thermally assisted FEG source. The electron source on the Philips CM20 will produce a current of up to 400μA

2.1.4 Image collection and recording

Electron microscopy images can be recorded on either a photographic plate, a TV camera or on a slow scan CCD camera. Photographic plates were used for many experiments, indeed it was the only recording method available on the JEOL 2000FX. The type of film used was CEA Reflex-15 due to its relatively short exposure times compared to other film types, a typical exposure time for bright field images being 1 second compared to 6 seconds, for diffraction patterns 0.2 seconds compared to 1 second, and for magnetic images 5 seconds compared to over 80 seconds. Film however required time consuming developing and processing and was incapable of effectively capturing the time dependent phenomena which were involved in some experiments. A TV pick-up and video system is incorporated on the Philips CM20 underneath the camera chamber. This comprises a low light camera with a RCA silicon intensifier target tube (SIT) viewing a single crystal YAG screen. Images are acquired using an Agar camera control unit T1570 followed by an Arlunya image

processor TF6000. These allow the image to be integrated over several frames to increase the signal to noise ratio. Individual frames can be grabbed using a PC with a suitable video card, however the signal to noise ratio of these images is not sufficient to enable detailed analysis. The slow scan CCD camera provides a means for recording high resolution sequences of images with a high signal to noise ratio. The typical acquisition time of 0.25 seconds compared to several seconds that is often required for photographic film allows images of an evolving system to be more reliably obtained. The CCD camera is controlled by an Apple Macintosh Quadra computer which allows immediate on-line data analysis. Since the data is in digital form, the format of the data may be changed to allow the images to be read into a spreadsheet, or some other computer program, for direct analysis. The digital images are then written onto a CD ROM disk or a Magnetic ZIP disk for long term storage and recovery. This provides more reliable storage than photographic negatives, or video tape.

2.1.5 The vacuum system

The JEOL 2000FX operates at a vacuum of $\geq 10^{-4}$Pa, a typical value for most TEMs. The CM20, however, has three separate vacuum areas which are connected by differential pumping apertures. There are two ion-getter pumps around the gun region which maintain a vacuum of 5×10^{-7}Pa. The gun area can also be isolated from the rest of the column with the gun isolation valve, this ensures that the gun source is not damaged by gases which have been ionised by the electron current. The specimen region is maintained at a pressure of 2.7×10^{-5}Pa using another ion-getter pump and an

anti-contamination large surface gold plated cold finger. For clean specimen changes the specimen rod is pumped by a turbo pump and back filled with dry nitrogen in an automatic cycle. The viewing chamber has a vacuum maintained at $\approx 10^{-6}$Pa using an oil diffusion pump with a buffer tank and an intermittently pumping rotary pump.

2.2 Electron-specimen interactions

2.2.1 Structural interactions

The electron beam is scattered by the potential produced by the positive nucleus and the outer electrons. The frequency of scattering events increases with the square of the atomic number of the material the electrons are being scattered from. This means that for transmission experiments the sample must be thin enough (≤100nm) to allow transmission of enough electrons for a useable signal to be obtained. Contrast in structural experiments arises from the phase relationship between two or more scattered electrons, the origins of which can be described as follows. In 1912 Bragg gave an expression for the angle through which x-rays would have to be scattered from a regular crystal to produce positive interference:

$$2d_{hkl}\sin\Theta = \lambda \qquad [2.3]$$

where d_{hkl} is the interplanar distance for the lattice planes with the indices (h,k,l) and λ is the wavelength of the x-ray. In 1924 De Broglie predicted the dual wave-particle character of a stream of particles. This was demonstrated for electrons in 1927 by Davisson and Germer. The wavelength of an electron is expressed as:

$$\lambda = \frac{h}{m\ v} \qquad [2.4]$$

where v is the velocity, and m is the mass of the electron. h is Planck's constant. When calculating the velocity from the energy given to the electron by an accelerating voltage, corrections for relativistic effects give the equation for the wavelength of the electron as:

$$\lambda = \frac{h}{(2meV_r)^{\frac{1}{2}}} \qquad [2.5]$$

where:

$$V_r = V_0\left(\frac{1+eV_0}{2m_0c^2}\right) \qquad [2.6]$$

and V_0 is the accelerating voltage, e is the charge on an electron, m_0 is the rest mass of the electron, and c is the speed of light. For electrons accelerated in a voltage of 200kV this gives a wavelength of 2.51pm.

Furthermore the distances between the planes of atoms in a regular crystal can be expressed using a plane spacing equation. This equation is different for each type of crystal lattice, and for cubic crystals it is:

$$d_{hkl}^2 = \frac{a^2}{h^2+k^2+l^2} \qquad [2.7]$$

where h, k and l are Millar indices and a is the lattice constant. Combining this with the Bragg law and using the De Broglie formula to get the wavelength of the electron, allows us to express the angle of diffraction in terms of these crystal constants:

$$\sin^2\Theta = \frac{\lambda^2}{4a^2}(h^2+k^2+l^2) \qquad [2.8]$$

As the plane spacing equation varies for each crystal type, so will equation (2.8). This equation allows us to determine the crystal type, and lattice constant for a sample by measuring the Bragg diffraction angles.

2.2.2 Electron-ferromagnetic specimen interaction

The electron beam interaction with a ferromagnetic specimen can be explained classically in terms of the Lorentz force [5]. Figure 2.6 shows a ferromagnetic sample containing two domains where the magnetisation is oriented in opposite directions separated by a domain wall. The magnetisation directions are perpendicular to the page.

Electrons passing through the specimen are deflected in a direction perpendicular to both the electron path and the induction in the specimen. The angle of deflection is given by:

$$\beta_x(x,y) = \frac{e\lambda}{h}\int_{-\infty}^{\infty} B_y(x,y)dz \qquad [2.9]$$

where $B_y(x,y)$ is the component of magnetic induction in the y-direction at the point (x,y), e is the electronic charge, λ is the electron wavelength and h is Planck's constant. For a region of constant magnetisation (M_s) and a constant thickness (t) the deflection angle is given by:

$$\beta = \frac{eB_0\lambda t}{h} \qquad [2.10]$$

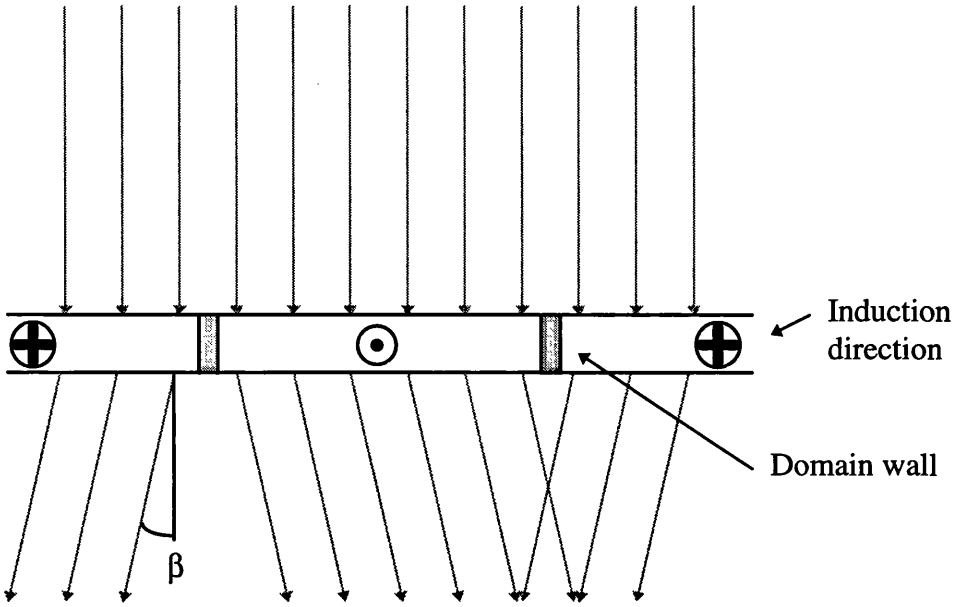

Figure 2.6: The deflection of electrons caused by the Lorentz force as they pass through domains magnetised perpendicular to the page.

where the magnetic induction is given by $B_0=\mu_0 M_s$.

The Lorentz deflection for 200keV electrons passing through a 50nm sample with a saturation induction of 1T gives $\beta=3x10^{-5}$radians. This angle is much smaller than the typical Bragg deflection of $\approx 10^{-2}$radians.

This result (equation 2.10) assumes there are no stray fields around the specimen. The presence of stray fields is described in chapter 1. Since stray fields will generally have a directionality opposed to the magnetisation in the specimen at that point, they will act to reduce the overall Lorentz deflection of the electron.

2.3 CTEM image formation

2.3.1 Diffraction patterns

Diffraction patterns are used to reveal the crystallite structure of the sample. The diffraction pattern is obtained by using the pre specimen lenses to focus the electrons on the back focal plane of the objective lens. The post specimen lenses are used to control the camera length, and project the diffraction pattern onto the viewing screen (figure 2.7a). Recording diffraction patterns of the specimen tilted to two or more

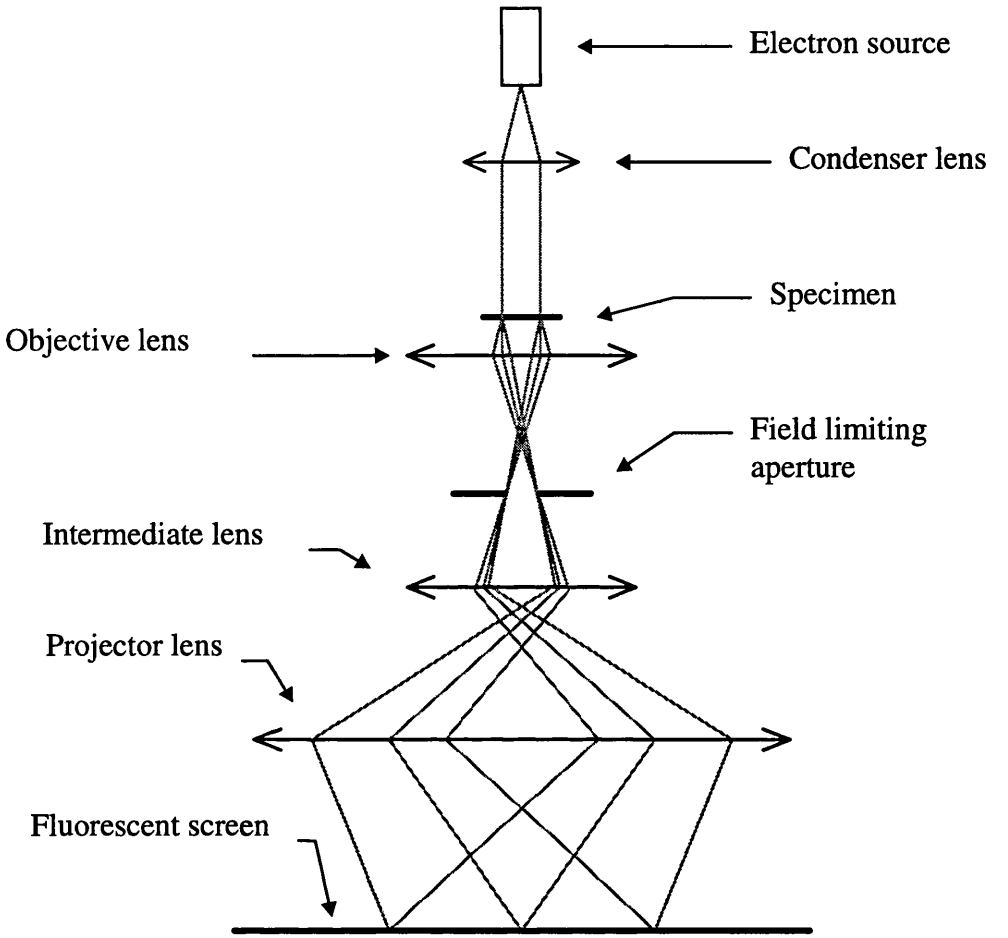

Figure 2.7a: Ray diagram showing the TEM in diffraction mode

angles to the electron beam can be used to determine if there is any crystallite texturing. Crystallite texturing occurs when there is a preferred crystalline orientation in the sample. The orientation of particular crystallites can be observed by focusing the beam down to a point on the specimen, although this does not give a point diffraction pattern. Alternatively a selected area aperture may be inserted (20-65μm across) to look at the orientations within an area. This technique can also give information on the degree to which neighbouring crystallites are oriented in the same direction since the diffraction pattern will change from being smooth rings to being a spot diffraction pattern if there are few enough crystalline orientations within the area of the selected area diffraction patterns.

2.3.2 Bright field and dark field imaging

To reveal specimen features there must be contrast in the image. This is achieved in bright field imaging by inserting an aperture in the back focal plane of the objective lens (figure 2.7b). This excludes any electrons that have been Bragg reflected from the resulting image. The resulting contrast is called "diffraction contrast". The electron beam may also be tilted or the aperture may be moved to allow only a selected Bragg-deflected beam to form the image, this is called dark field imaging.

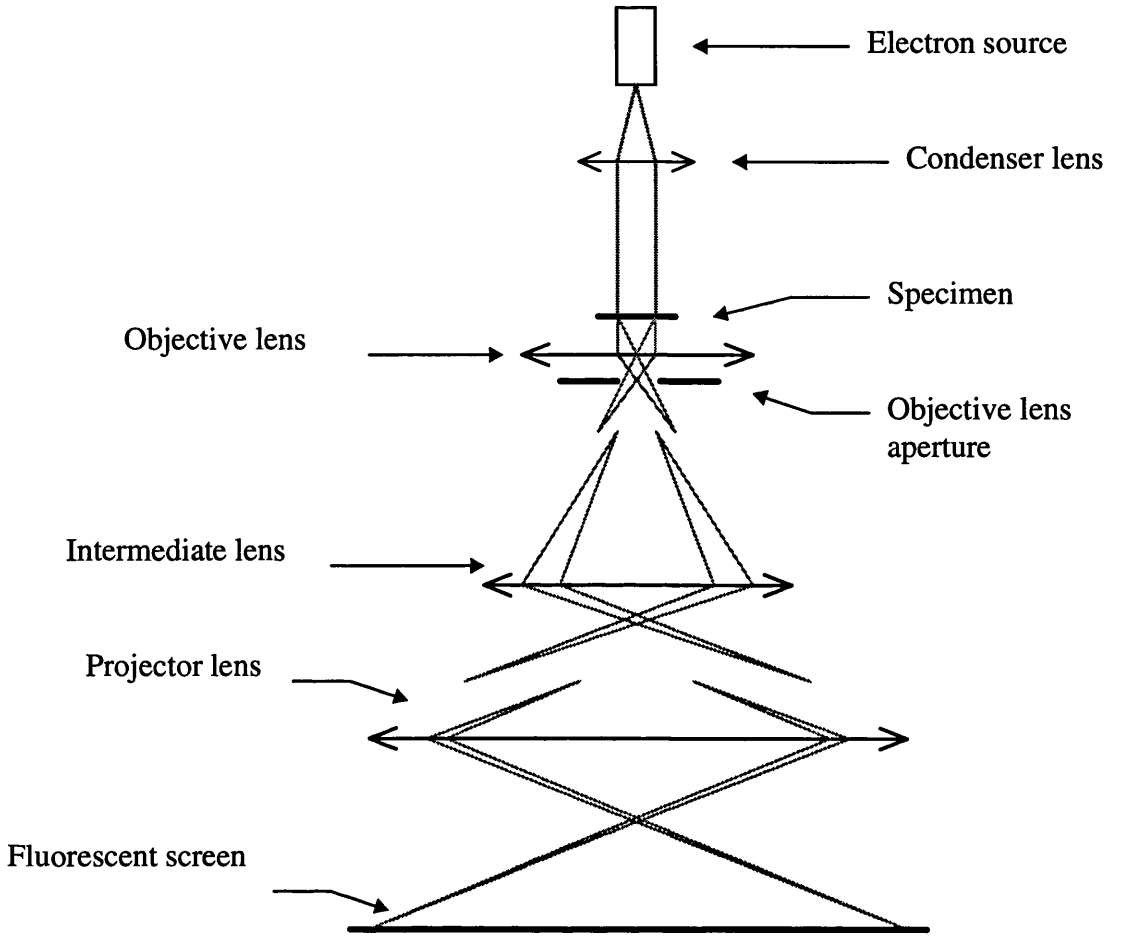

Figure 2.7b: Ray diagram showing the TEM in standard imaging mode

2.3.3 Fresnel imaging

Fresnel imaging is a mode of Lorentz electron microscopy [6]. The contrast in Lorentz modes arises from the interactions of the electron and the induction of the sample as discussed in section 2.2. The contrast in the Fresnel mode is achieved by defocusing the bright field image to observe a plane above or below the sample (figure 2.8). The interference effects shown when the Lorentz deflected electrons converge only occur when a highly coherent electron source is used, instead the domain walls usually appear as dark or light lines. The appearance of the contrast in the image is dependent on whether under focus or over focus is used, as domain walls which appear as light lines in under-focus appear as dark lines in over-focus.

The main advantages of Fresnel imaging are its ease of implementation, the high contrast of the domain walls and its relative lack of sensitivity to the defocus used. These advantages allow experiments to be performed which involve changing the lens settings while the sample is being imaged. This is virtually impossible in other Lorentz imaging modes.

The main disadvantages are the lack of directional information and the requirement for the image to be defocused. The defocus results in poor resolution and makes it difficult to obtain quantitative information from the images produced.

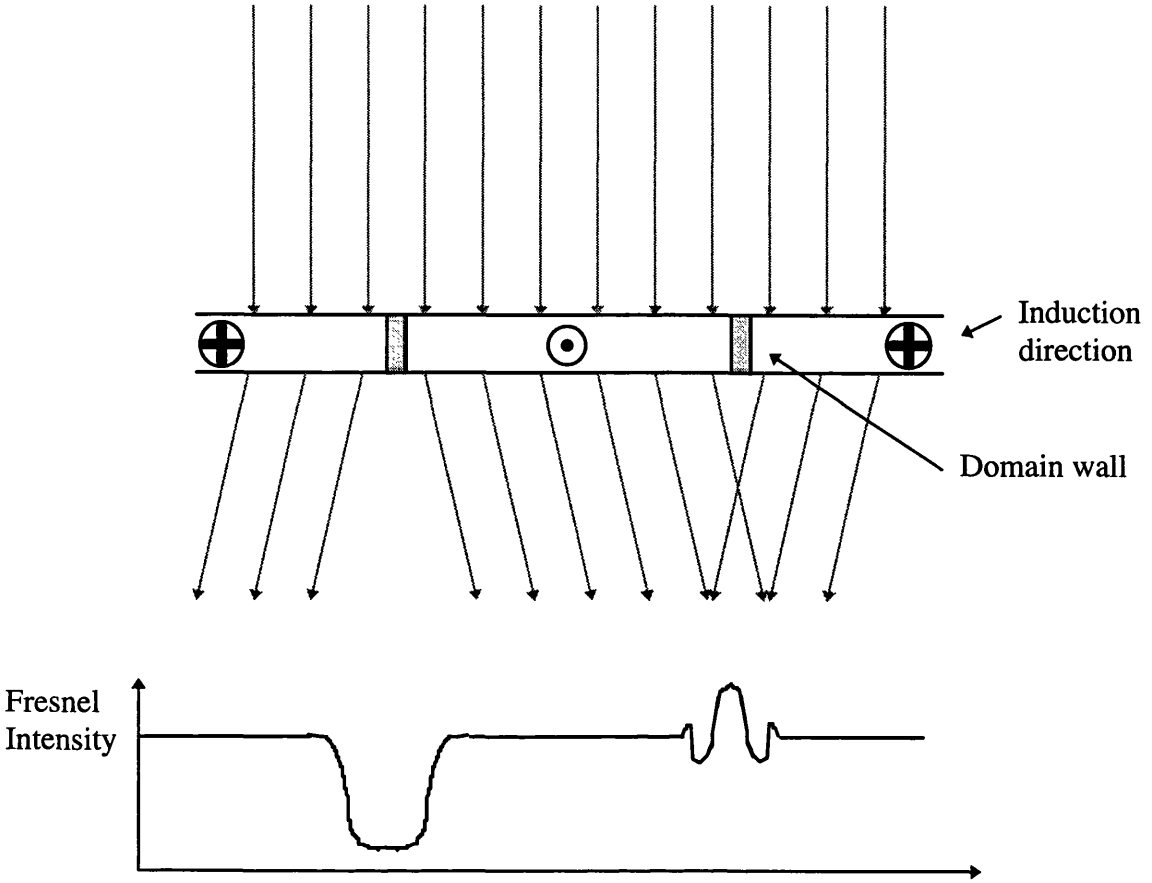

Figure 2.8: Schematic showing image formation in the Fresnel imaging mode.

2.3.4 Foucault imaging

In Foucault imaging an opaque aperture is positioned in the back focal plane to remove electrons, deflected through the Lorentz angle, from a limited range of magnetisation orientations (figure 2.9) [6]. This in-focus technique produces magnetic contrast relating to the direction of the magnetic induction in different domains, although for full information a pair of Foucault images must be taken with the aperture position placed in orthogonal directions. Foucault imaging provides information on the domain geometry and the approximate direction of the magnetic induction within each domain. There is great difficulty in obtaining quantitative information since the contrast is highly non-linear and is greatly dependent on the aperture positioning. The aperture is assumed to be perfectly opaque, but in reality the edge is non-uniform, partly electron transparent and susceptible to charging effects. The Foucault mode complements the Fresnel mode in allowing for a rapid investigation of the magnetic properties of thin films.

2.3.5 Low angle diffraction (LAD)

The deflections in the beam caused by the Lorentz force may also be viewed directly. This is done by setting the microscope up in diffraction mode and using very long camera lengths (>100m). The central spot is then imaged at a high enough

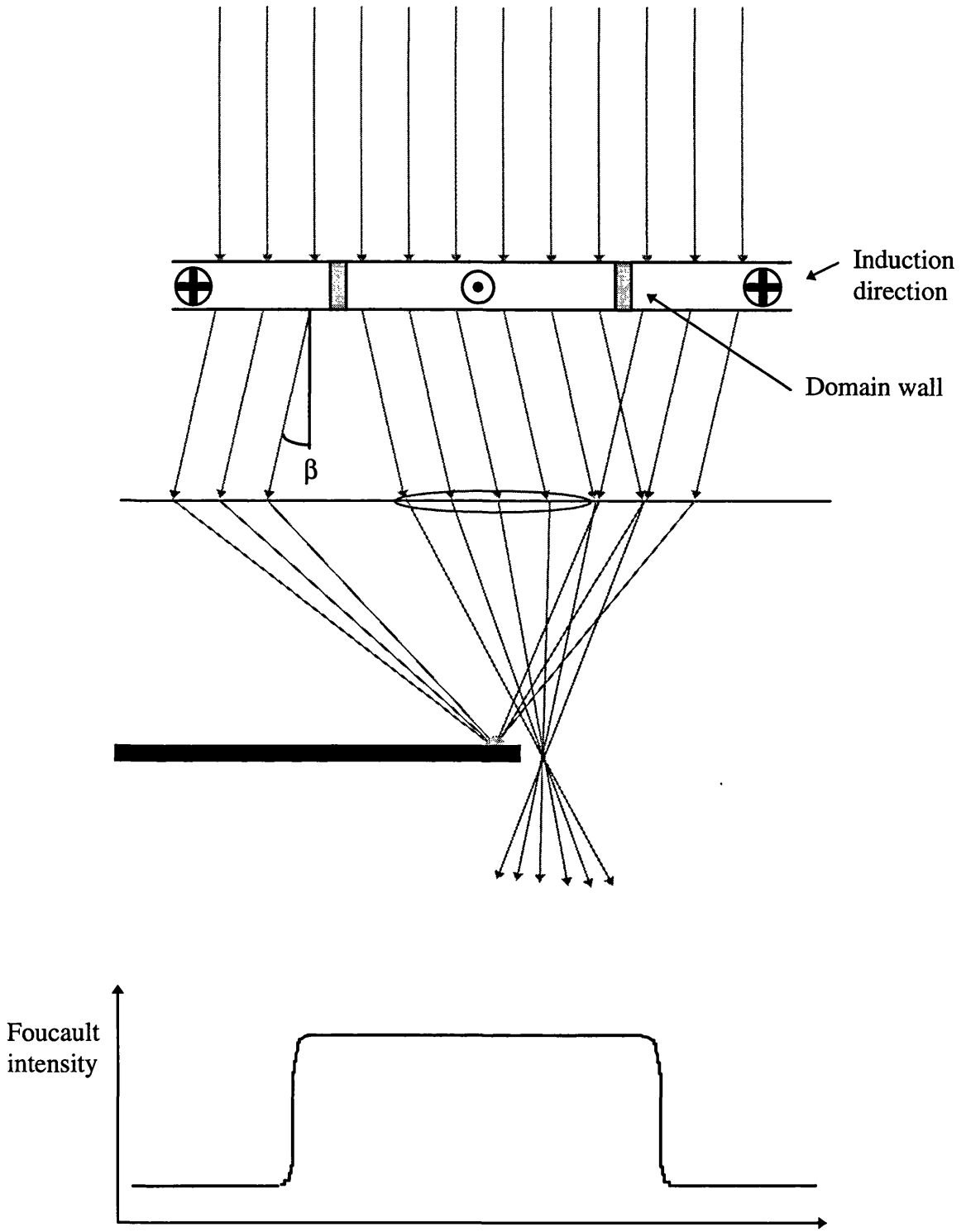

Figure 2.9: Schematic showing image formation in the Foucault imaging mode.

magnification that the Lorentz deflection results in a displacement of parts of the central spot of a few mm in the final image. For a sample with two magnetic domains in plane with magnetic induction in opposite directions and a Lorentz deflection angle of $3x10^{-5}$rad viewed in low angle diffraction mode with a camera length of 100m, the undiffracted beam would be viewed in the microscope chamber as two separate spots with a separation of 6mm.

2.4 STEM image formation

In CTEM the whole image is acquired over a period of time, while in STEM each pixel of the image is acquired sequentially over a much shorter period of time as the illumination is scanned across the specimen in a raster. Reciprocity states that any imaging mode performed in CTEM may also be performed in STEM provided that the detector response and source functions of the STEM and CTEM respectively are equivalent and there is no inelastic scattering in the sample. This has been shown to be true for magnetic imaging. Under STEM, however, there is the ability to modify the detector response function which allows for the novel imaging modes such as differential phase contrast (DPC) and modified differential phase contrast (MDPC) described in this section.

2.4.1 Differential phase contrast (DPC) imaging

In DPC imaging an electron probe is scanned across the sample, with the resultant cone of electrons being centred on a quadrant detector below the sample [7]. The scanning motion of the probe is removed from the cone of electrons by the descan coils below the sample (figure 2.10). Any magnetic induction in the sample causes the cone to be deflected by the angle β, this causes the proportion of the signal that falls on each detector to change in a manner which is related to the deflection. If a difference signal is taken from opposite sections of the quadrant detector, for example A-C, the resultant signal is directly related to the magnetic induction in the perpendicular direction. A bright field image can be obtained at the same time by summing the signals of the four detectors. In this way two images mapping magnetic induction in orthogonal directions and a bright field image may be obtained at the same time.

The main advantage of DPC imaging is the ability to obtain a set of images at the same time and the same area which represent the magnetic induction in two orthogonal directions and the crystallite contrast. This allows reliable computer manipulation of the images to produce a vector map of the induction vectors and makes interpretation of the images easier. The time taken to record a set of DPC images means that any magnetic states to be reliably investigated using this technique must not change during the period of acquisition. For a more in depth explanation of DPC imaging see [8].

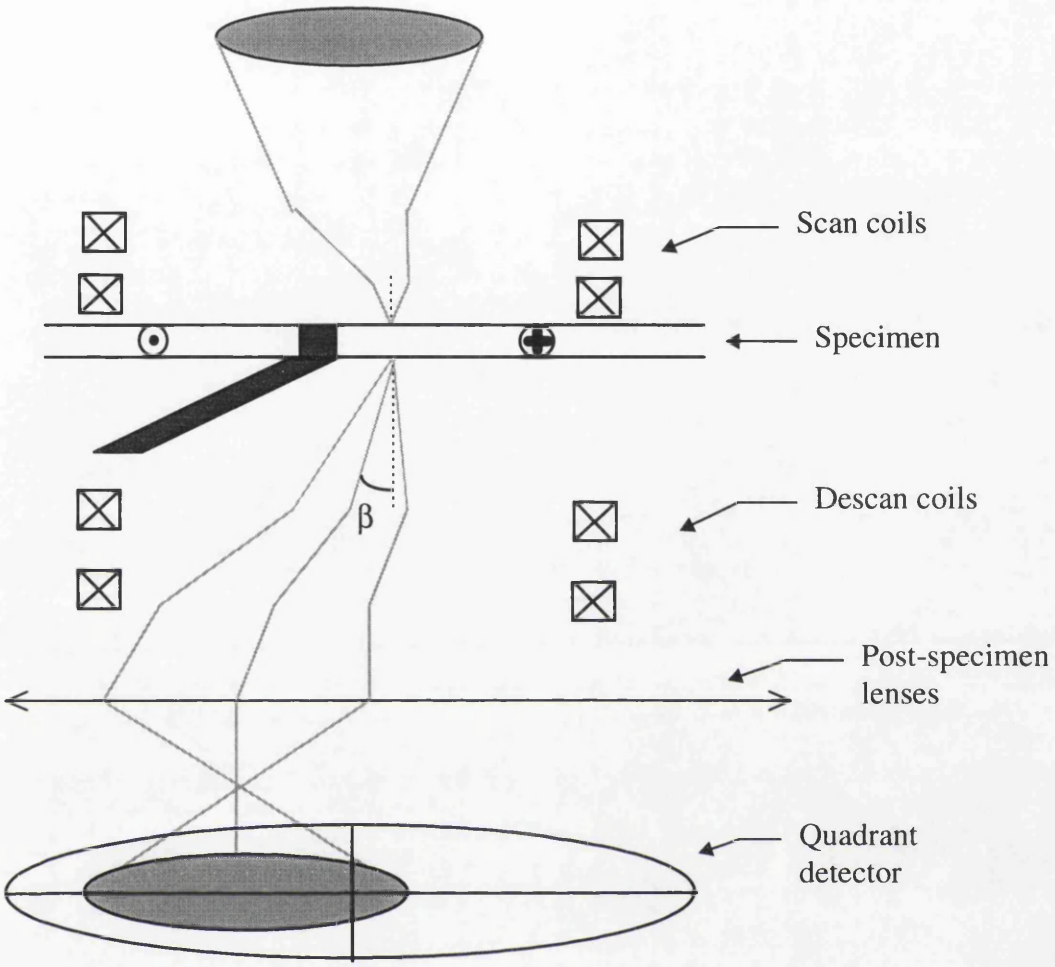

Figure 2.10: Contrast formation in DPC mode

2.4.2 Modified differential phase contrast (MDPC) imaging

In modified differential phase contrast (MDPC) imaging the quadrant detector used in DPC imaging is replaced by two quadrant detectors, one is situated in the position of a standard DPC detector, the other is situated in an annulus around the standard detector (figure 2.11). If a difference signal is taken using the outer detector and a suitable camera length (a suitable camera length for the Philips CM20 MDPC detector is between 17 and 20m) the detector response function acts as a filter, filtering out small scale structures in the image. Since the magnetic microstructure is normally at a substantially larger scale than the physical microstructure, the magnetic information in the final image is enhanced relative to the physical information. If the magnetic and physical microstructures are on the same, or similar scale as each other the effect of the modified detector response function is much reduced, and standard DPC imaging is often more effective.

2.5 Magnetometry.

In addition to the transmission electron microscope I used two different magnetometers to characterise some of my samples: A vibrating sample magnetometer (VSM) at the University of Twente, in the Netherlands, and an alternating gradient force magnetometer (AGFM) at the University College of North Wales at Bangor.

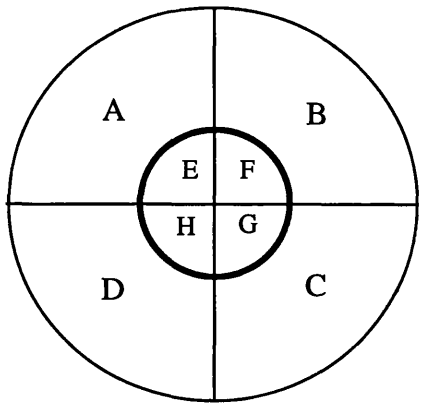

Figure 2.11: Position of the detectors for use in MDPC mode

The measurement of a M vs. H loop on a VSM is based on the principle that a moving magnetic system will induce a current in coils placed around it. This current is proportional to the component of the magnetisation perpendicular to the coils. Experimentally the sample is held in a fixed position, between the poles of an electromagnet, so that either in plane or perpendicular to the plane components can be measured. The sample is then vibrated at a chosen frequency, and the field at the sample is varied using the electromagnet.

An AGFM is a type of magnetometer with a sensitivity of up to 10^{-11}emu, although the machine I used had a sensitivity of $2x10^{-8}$emu. This is still ≈1000 times more sensitive than a typical VSM. To measure a M vs. H loop on an AGFM, the sample is held still between the poles of an electromagnet, supported on a cantilever which incorporates a piezoelectric element. As well as the field from the electromagnet, the sample is exposed to a small alternating field gradient (I used a field gradient of 1Oe/mm). This gradient leads to an alternating force on the sample which is proportional to the field gradient and the magnetic moment of the sample. The forces on the sample are detected by the electric output of the piezoelectric element. The frequency of the alternating gradient is also tuned to the resonant frequency of the sample support. This greatly increases the sensitivity of the magnetometer by providing an initial stage of amplification. Once the experiment has been completed, the output has to be corrected for the diamagnetic contribution of the cantilever itself. As well as being very precise this type of magnetometer is quite quick, with an entire M vs.H loop taking only ≈100seconds, where it would take ≈20 times longer on a VSM.

As well as recording M vs. H loops, other experiments can be carried out on these magnetometers. A typical experiment on a VSM would involve the application of a field large enough to saturate the sample, decreasing this field to a value between the nucleation and negative saturation fields, then increasing the field back to the field which would saturate the sample. The magnetisation of the sample would be recorded throughout, and the shape of the resulting loop should indicate whether reversible process are involved in the reversal mechansim of the sample at the negative field applied. (figure 2.12)

Two additional types of experiments could be carried out on the AGFM: remanence curves and time delay sequences. There are two types of remanence curves: isothermal remanence curves (IRM) and DC demagnetisation curves (DCD). These curves provide direct information on only the irreversible changes which are occuring [9]. To obtain these curves, the DC fields which are applied to the sample to change the magnetic state are removed before the remanent magnetisation is determined. The starting point for an IRM curve is a state of AC demagnetisation and measurements are made at increasing fields until saturation is attained (figure 2.13). Saturation is then the starting point for a DCD curve, which measures the remanent magnetisation for the sample as increasing negative fields are applied (figure 2.13). This continues until negative saturation is achieved.

Differentiating the remanence curves yields the irreversible susceptibility. This is defined as:

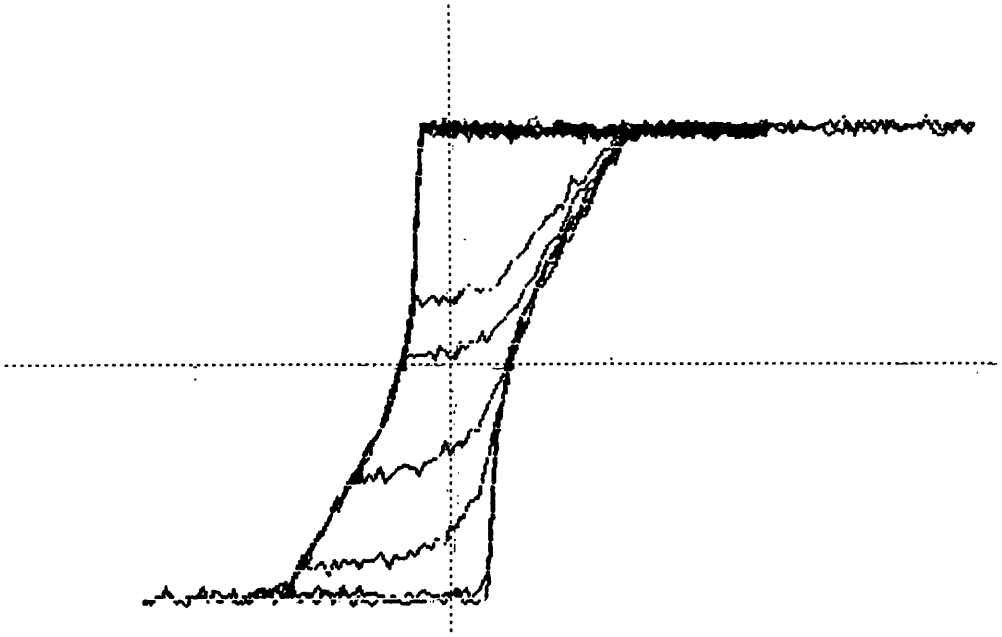

Figure 2.12: A print out of a VSM experiment on CoNi/Pt multilayers, showing the shape of the return path as the field is decreased from a value which does not saturate the sample.

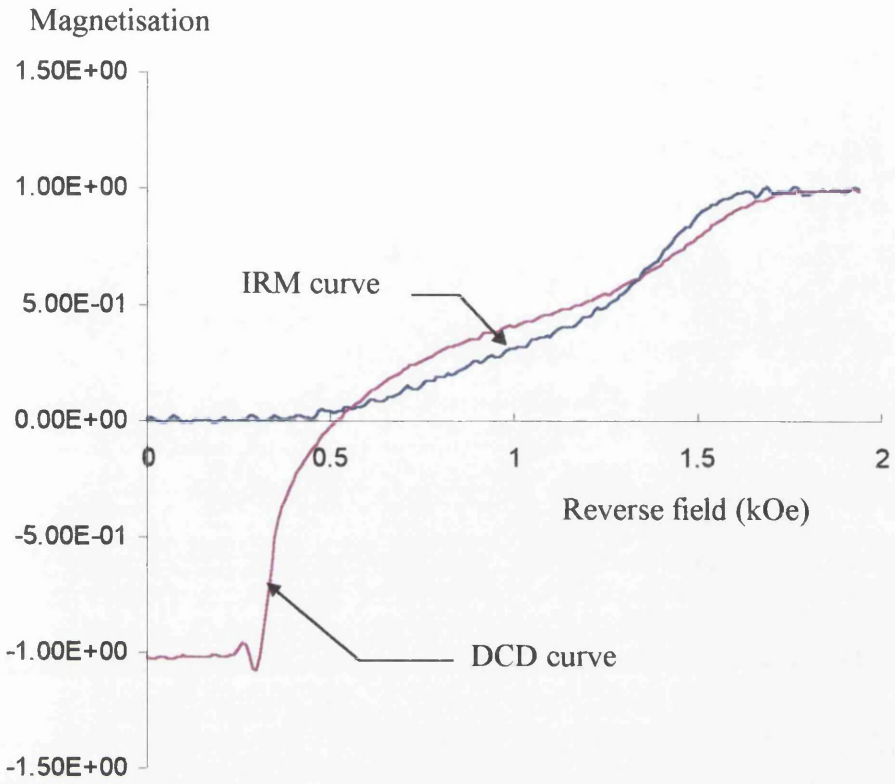

Figure 2.13: Undifferentiated remanence curves for CoNi/Pt multilayers in the annealed state. The field is reduced to zero before any magnetisation measurement is taken, so the reverse field represents the maximum field which the sample has been exposed to at that point of the curve.

$$\chi_{irr} = \left| \frac{d\left(\frac{M_r}{M_s}\right)}{dH} \right| \qquad [2.11]$$

for both the IRM and DCD measurements. The χ_{irr} curves obtained from the two remanence curves are different due to the variation in the initial configuration of the magnetisation. For the IRM case, existing domains are altered by domain wall processes. Hence the $\chi_{irr}(H)$ curve measures the distribution of energy barriers to these domain wall processes. For the DCD case, where the process starts with the material already saturated, the differentiated remanence curve measures the energy barrier for domain nucleation and then the mechanism by which reversal proceeds [9].

The second type of experiment that can be done on the AGFM is the measurement of time dependent effects. All magnetic materials which exhibit hysteresis effects also exhibit time dependent effects. This time dependence arises from thermally activated transitions over energy barriers, one measure of which is given by χ_{irr}. The time dependent behaviour is measured by saturating the sample, then applying a succession of negative fields. After each negative field is applied, the magnetisation is measured for a period of time as the field is held constant (I used 900 seconds), then the film is saturated again and a new negative field is applied. The shape of the magnetisation against log(time) plots is intrinsically related to the energy barrier distribution [10]. Narrow energy barrier distributions tend to produce non-linear plots, whilst broad energy distributions produce linear plots against log(time). These experiments would be impractical on the VSM due to the long acquisition times.

References

[1] J.N.Chapman, A.B.Johnston, L.J.Heyderman, S.McVitie, W.A.P.Nicholson and B Bormans, IEEE Trans. Mag. **30** (1994).

[2] Hirsch, Howie, Nicholson, Pashley and Whelan "Electron microscopy of thin crystals" Butterworth (1965)

[3] P.M.Mul, B.J.M.Bormans and L.Schaap, ICEM, **12** (1990) 100.

[4] Philips TEM CM20 FEG, Technical note.

[5] J.N.Chapman, J. Phys.D., **17** (1984) 623.

[6] J.P.Jakabovics, Microscopy in materials science, **4** (1975) 1303.

[7] J.N.Chapman, E.M.Waddell, P.E.Batson and R.P.Ferrier, Ultramicroscopy **4** (1979) 283.

[8] J.N.Chapman, I.R.McFadyen and S.McVitie, IEEE Trans. Mag. (1990) 1506.

[9] D.M.Donnet, V.G.Lewis, J.N.Chapman, K.O'Grady and H.W. van Kesteren, J. Phys. D **26** (1993) 1741.

[10] R.Street, P.G.McCormick and L.Folks, J.Magn. Magn. Mater., 104-107 (1992) 368.

Chapter 3

TEM setup and considerations

3.0 Introduction

Studies of modern high performance magnetic media in the TEM start with the imaging of the basic magnetic and physical microstructure. This is done using the standard methods described in chapter two. To gain further information on these samples as future high performance magnetic media, they are imaged in the presence of magnetic fields up to 3500Oe. These magnetic fields can be controlled to study either the in-plane or perpendicular magnetisation processes.

3.1 Initial studies

Initial studies were carried out on all samples to reveal their microstructural properties and to obtain basic information on the kind of micromagnetic structure they supported. These studies were carried out on the JEOL 2000FX CTEM. To establish the physical microstructure, bright field images, dark field images and diffraction patterns, with the plane of the sample perpendicular to the electron beam and tilted to 20° from perpendicular to the electron beam, were taken. The basic micromagnetic structure of each sample was established by employing Fresnel and Foucault imaging modes to take images of the samples in the as-supplied and AC demagnetised state.

3.1.1 Diffraction patterns

Diffraction patterns were taken with a camera length of 108cm. This camera length was calibrated using a standard sample and allowed most of the diffraction rings to be recorded but on a large enough scale so that ring diameters could be measured accurately to allow analysis of the pattern. Since diffraction patterns were taken with the sample lying both perpendicular and 20° from perpendicular to the electron beam the diffraction patterns could be used not only to establish the crystallite structure in the standard way but also to establish any preferred crystalline orientations (texturing). The diffraction patterns for a sample with texturing show extra rings, or rings breaking up, away from the tilt axis on the tilted diffraction pattern (figure 3.1). These are due to crystal planes which could not satisfy diffraction conditions with the electron beam perpendicular to the specimen but satisfy the conditions for diffraction as the sample is tilted or vice versa.

3.1.2 Bright and dark field images

Bright and dark field images were taken with a magnification of 125,000x. The magnification was again calibrated using a standard sample. These images were used to calculate the average crystallite grain size and to observe directly whether any crystallite clustering is present. Crystallite clustering occurs when neighbouring crystallites tend to have similar crystalline orientations and show up on the images as groups of crystallites with the same diffraction contrast in both bright and dark field images (figure 3.2). Crystallite clustering has been seen to have an effect on the magnetic properties of alloys such as CoPt [1]. A combination of both bright and dark

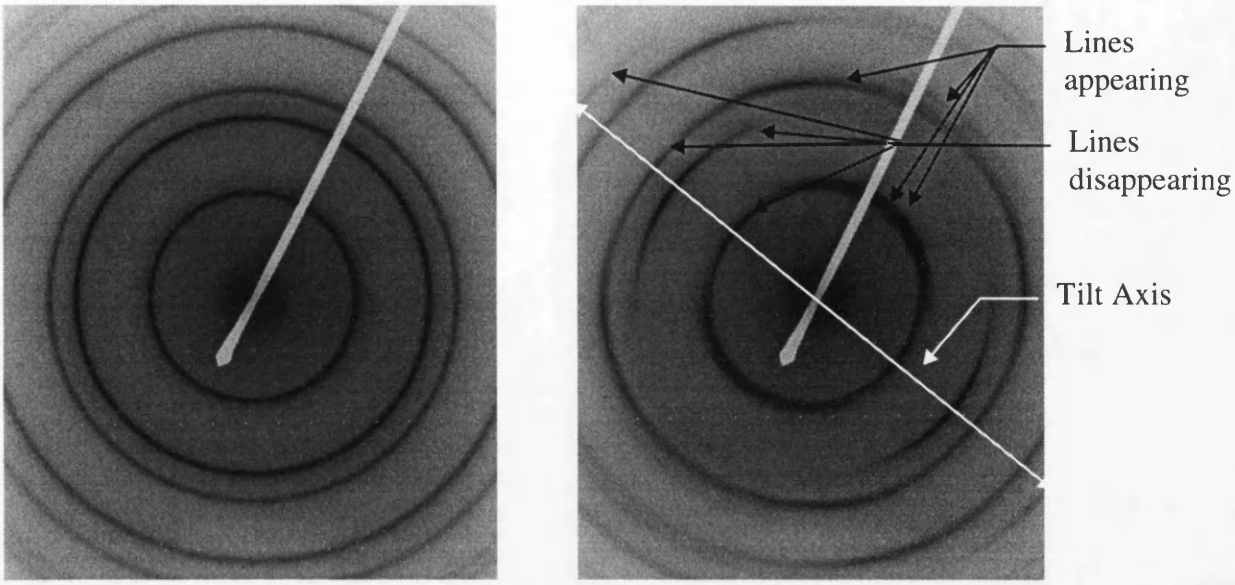

Figure 3.1: Diffraction patterns of the same sample both with sample lying flat, and tilted to an angle of 20°, showing the appearance of extra lines and disappearance of lines off the tilt axis as the sample is tilted

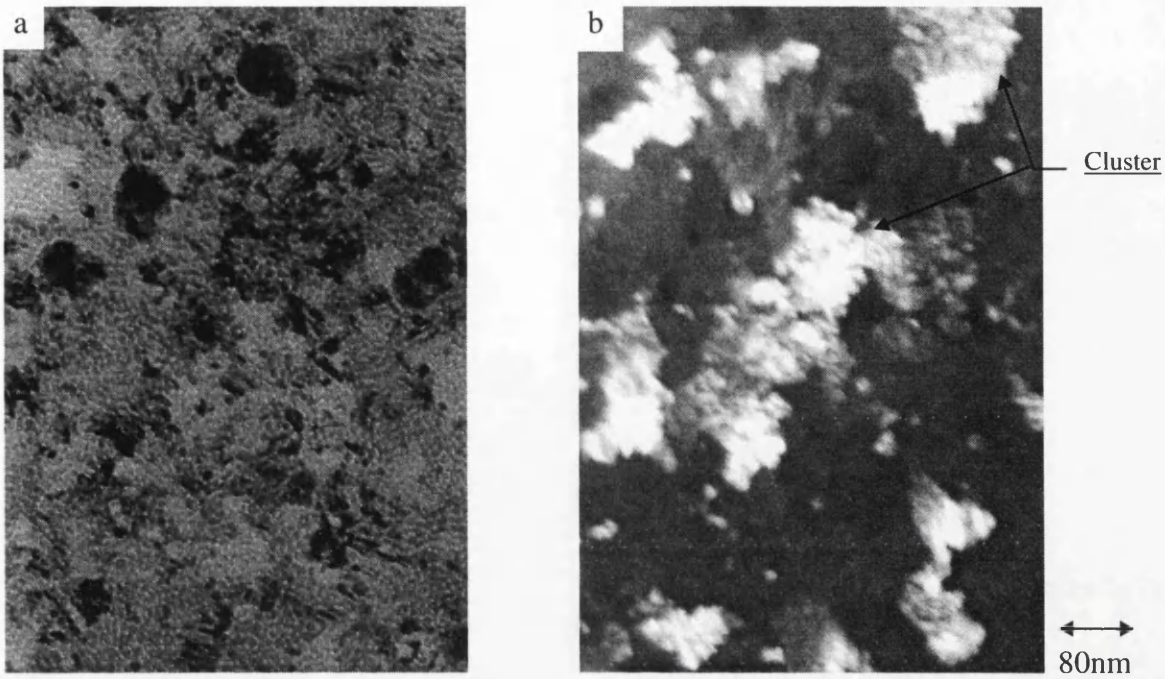

Figure 3.2: bright field (a) and dark field (b) images of the same area of a CoPt sample showing clustering.

field imaging was used since small features such as individual crystallites are more easily discernable on dark field images whereas larger features such as clusterring show up better on the bright field images.

3.1.3 Initial magnetic imaging

Magnetic images of the sample as it was received (without exposure to any external magnetic fields) were taken as a reference.

To image the magnetic microstructure of samples there must be a component of induction perpendicular to the electron beam. For samples with perpendicular magnetisation this required that the samples be tilted; a tilt angle of 20° was usually used in this work.

The AC-demagnetised state of all of the samples was achieved by spinning the sample rapidly about an axis perpendicular to the plane of the sample in a field of 10000Oe and then reducing this field over a period of several seconds. This produces a qualitatively reproducible magnetic state which can be used to get an indication of the characteristic micromagnetic feature size of each sample. The feature size was measured from images recorded using the Foucault imaging mode, measuring perpendicular to the mapping direction. Fresnel images of samples in the demagnetised state were used to indicate any in plane anisotropy within the sample. This would be evident as the domain walls would tend to point in a particular direction, indicating the anisotropy.

3.2 Applying a field to the sample

The AC demagnetised state is a qualitatively reproducible state which gives information on the steady state micromagnetic structure; however many applications of modern magnetic materials require the material to be exposed to a changing external field. Magnetic fields are generated in the electron lenses of electron microscopes, and in most microscopes the objective lens field would be too large in the region of the specimen, destroying the magnetic state of the sample. The Philips CM20 at the University of Glasgow has been modified in such a way that the field to which the sample is exposed can be controlled by the user while still maintaining the imaging conditions.

Two additional (Lorentz) lenses above and below the main objective lens, as described in chapter 2, can take over the function of the objective lens to provide near field free imaging (field $\leq$ 10Oe). Alternatively the two Lorentz lenses may be used in conjunction with the objective lens to image the sample in a controlled vertical field provided by the objective lens.

This vertical field may be applied directly to a sample with perpendicular magnetisation. The strength of the field can be changed over a small range by tilting the sample, but for most experiments the strength of the field must be changed by altering the excitation of the objective lens. This requirement to change the objective lens setting, and hence the defocus value, means that only the Fresnel mode of Lorentz microscopy is practical for imaging experiments on samples magnetised out of plane.

For samples with in-plane magnetisation a component of the vertical field is introduced into the plane of the sample by tilting it away from the initial horizontal position (figure 3.3). Since the sample can be tilted in both a positive and negative sense, this method can be used to expose the film to large (up to ≈2500Oe) positive and negative in-plane components without changing the settings of the lenses. These constant lens conditions allow the Lorentz imaging modes: Fresnel, Foucault, low angle diffraction, differential phase contrast and modified differential phase contrast to be performed while the sample is being exposed to a changing external field.

The effect of the out of plane component of the magnetic field on the sample must be considered [2]. Any effect of this component of the field will be opposed by the out of plane demagnetising field. The demagnetising field is the field produced by the surface charge distribution on the surface of a magnetised body. This demagnetising field is given by the equation:

$$H_d = N\frac{I_s}{\mu_0} \qquad [3.1]$$

where H_d is the demagnetising field, N is the demagnetising factor and I_s is the intensity of magnetisation. The demagnetising factor is a property of the shape of the object and changes for different directions within an object. For simple shapes however the demagnetising factors for the three main spatial axes add up to unity, ie.:

$$N_x + N_y + N_z = 1 \qquad [3.2]$$

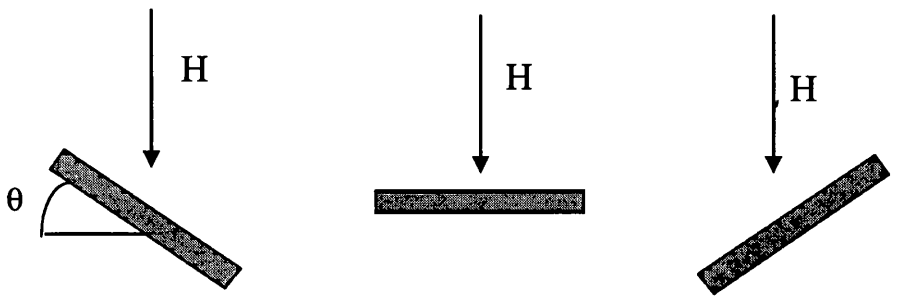

In plane field = Hsinθ In plane field = zero In plane field = -Hsinθ

The electron beam is parallel to H

Figure 3.3: Schematic showing how the in-plane field component is changed by tilting the sample.

In general the demagnetising factor is not simple to calculate since even uniform distributions of magnetisation will result in non-uniform demagnetising fields, which will in turn result in non-uniform distributions of magnetisation. Only in the case of an ellipsoid is it possible to calculate the demagnetising factor.

By assuming that a thin film can be approximated by an oblate spheroid with the short axis equal to the thickness of the film (≈30nm) and the two long axes approximating the in plane dimensions of the film (≈2mm) the demagnetising factor along the two in-plane axes are given by:

$$N_x = \frac{\pi}{4} \cdot \frac{l_z}{l_y} \quad , \qquad N_y = \frac{\pi}{4} \cdot \frac{l_z}{l_x} \qquad [3.3]$$

where l_x, l_y and l_z are the dimensions of the film with l_z being the thickness of the film. For a typical film described above these equations give a demagnetising factor of 0.000012 in the in-plane directions, and 0.99998 in the out-of-plane direction. By putting this value into equation 3.1, this gives an out of plane demagnetising field for example for the cobalt platinum alloys studied in chapter six of ≈10000Oe. Since the largest out of plane component of the field will be 3500Oe this can be ignored since any effect will be cancelled out by the demagnetising field, assuming there is no perpendicular or oblique anisotropy.

3.3 Experimental procedure

3.3.1 Magnetisation experiments on in-plane media

In a typical experiment for this type of media the objective lens would be excited to a value of 3500Oe and the sample would be tilted between angles of ±40°. This is equivalent to exposing the sample to an in-plane field cycle of ±2250Oe. This field is sufficient to saturate all the samples reported here. For samples with lower coercivities the vertical field would be reduced to reduce the sensitivity of the magnetic state to the tilt angle.

As no single imaging technique can provide a full picture of what is happening in the complex media of interest for magnetic recording, it is advantageous if a number of modes are used. Here Fresnel and Foucault modes of Lorentz imaging as well as low angle diffraction (LAD) have been successfully implemented to extract information on the magnetic characteristics of the materials being studied.

Since Fresnel imaging is the simplest mode to implement, it was used first to establish the ideal objective lens excitation (applied vertical field). This mode was also useful in the identification of large angle domain walls since Fresnel contrast results wherever there are changes in the magnetic induction vector. The Fresnel mode was implemented by setting up the microscope in standard field free magnetic imaging then turning on the objective lens to the excitation required. Although the objective lens is already providing some defocus, this is optimised by adjusting the lower Lorentz lens excitation.

Once the objective lens conditions had been established, Foucault mode was used to obtain images of the micromagnetic structure. By mapping the Foucault contrast in the same direction as the field, the areas which had reversed and those which were unchanged were highlighted. During a typical experiment the contrast would change from all light to all dark, or vice versa, as the magnetisation moved from being aligned with the original field to being aligned against it. The Foucault mode was implemented by aligning the microscope in the magnetic imaging mode but with the upper Lorentz lens switched off. The objective lens would then be switched on to the desired value and any further focusing would then be done using the lower Lorentz lens. The objective aperture would then be positioned in the diffraction plane so as to cut off part of the central electron beam as in normal Foucault imaging mode. It must be noted that since the focusing centre of the objective lens system has been changed by switching off the upper Lorentz lens and exciting the main objective lens that any magnification values given by normal settings of the microscope would have to be ignored, and any scale information would be calculated by imaging a standard sample under the same conditions. Results for these experiments are shown in chapters four and six.

For the Fresnel experiments I used spot size 3, and gun lens 3 with the second smallest condenser aperture (50μm across) to provide the illumination. However for the Foucault imaging gun lens 5 was used, as the use of a larger spot size, gun lens or condensor aperture tended to deteriorate the spot to an extent that Foucault imaging was impossible, especially when the objective lens was excited above around 1000mA. The nominal magnification selected on the microscope would depend on the field of view required, but for most of the results shown it was 660x.

3.3.2 Perpendicular media magnetisation experiments

Since the magnetic field from the objective lens already has a component in the direction that we want to apply it, the strength of the apparent field at the sample can be altered by simply changing the strength of the objective lens. Changing the strength of the objective lens has the additional effect of changing the defocus setting of the microscope. This means that only the Fresnel imaging mode, which is least sensitive to the defocus of the microscope, is practical for implementation on these specimens. In a typical magnetisation experiment on these samples the microscope would be aligned with the objective lens switched on to a moderate excitation within the range of the field values expected to be applied. The sample would then be tilted to an angle to the electron beam to introduce a component of the magnetisation perpendicular to the electron beam. The objective lens field would then be used to take the sample through its magnetisation cycle, but since all the perpendicular samples reported in this thesis have 100% remanence, the applied field would only have to be increased from zero once the sample had been magnetised in the opposite direction by reversing the sense of the objective lens and turning it up to full excitation. As the field is increased, another effect of increasing the objective lens strength is to change the magnification of the image, this was minimised by adjusting the condensor lens strength. Results for these types of experiments are shown in chapter five.

For these types of experiments the second largest condenser aperture was used (100μm across) along with spot size 2 and gun lens 3. This provided enough lens current to see through the relatively thick CoNi/Pt specimens without deteriorating the spot. The

lower Lorentz lens was set at a current of around 1000mA to provide the defocus and a nominal magnification of 500x was sufficient for most samples.

3.3.3 Time dependent experiments on perpendicular media

Time dependent experiments on perpendicular media are just a slight modification of the magnetisation experiments. The microscope and sample would be set up and the sample saturated as before. The tilt of the sample would then be increased to 40° to reduce the component of the field in the perpendicular direction and the reverse field would be increased to the desired value. The recording apparatus, and stopwatch would then be activated, and the tilt angle would be reduced to the experimental value (≈20°). This would have the effect of rapidly, and reliably increasing the field to the desired value for the experiment. Images of the micromagnetic structure would then be recorded over a period of time (see section 3.4).

3.3.4 Recording the results

The experimental results were recorded on each of the low light level TV camera and the slow scan CCD camera described in chapter 2. The results recorded on the TV camera allowed the dynamics of the magnetisation, or time dependent processes to be recorded, however the individual frames were too noisy to allow accurate analysis. This method of recording was invaluable in the study of the time dependent processes, especially where large changes occurred over a short period of time. Care would have to be taken when interpreting the Foucault images since the automatic light level

adjuster on the TV camera would tend to reduce the contrast change as the sample changed from saturation in the original direction to being fully reversed.

The images recorded on the slow scan CCD camera were recorded over a period of 0.25s; this was generally short enough to capture a single micromagnetic state with a sufficient signal to noise ratio for analysis. Images of stages throughout the magnetisation process were recorded with the field held steady during the recording process; however images of time dependent phenomena were normally recorded at fixed time intervals which were computer controlled. Unfortunately if the time intervals required between each image were less than five seconds, the computer controlled recording software could not record and save the images fast enough. In this case the images would be recorded manually by "freezing" the micromagnetic state while the image was being recorded. The micromagnetic state was frozen by increasing the tilt of the specimen to $\approx 40°$ to reduce the component of the field perpendicular to the sample. The elapsed time for the experiment would be taken as the time the sample was exposed to the higher field value. This method of freezing the micromagnetic state appeared to work as during the experiment no changes in the micromagnetic structure were observed once the tilt was at its higher value. Results for this type of experiment are shown in chapter five.

3.4 Discussion

As the requirement for high performance magnetic materials is increased, especially in the high-technology industries, there will be a greater need to fully understand the magnetic properties of the materials. Magnetometers such as vibrating sample

magnetometers (VSMs) and alternating gradient force magnetometers (AGFMs) can provide useful information on the bulk properties of the materials in the presence of changing conditions such as magnetic field, temperature and pressure. However these instruments are limited to bulk measurements, and any micromagnetic conclusions from these machines are inferred from the results rather than being observed directly. Optical microscopes and imaging techniques have the ability to image the sample in the presence of a field, however these methods are limited in their resolution due to the wavelength of light and are unable to observe the magnetic features present in the modern high density recording media. Magnetic force microscopy (MFM) also has problems with the resolution achievable, although the resolution is improving, and has recently been reported as 50nm with modern tips. MFM also has the demonstrated ability to image the sample in the presence of magnetic fields, however this type of imaging has the problem that the magnetic tip on the cantilever of the MFM can interact with the magnetic domains on the sample, and in some cases this may cause changes in the micromagnetic structure.

Only the methods outlined in this chapter have the demonstrated ability to image the micromagnetic structure with sufficient resolution for modern magnetic materials, in the presence of substantial magnetic fields (3500Oe perpendicular to the sample and 2500Oe in the plane of the sample). Such studies will be vital for future materials if their properties are to be fully understood and hence tailored for specific requirements. This will avoid the need for the "educated try and see" type method of finding future high performance magnetic materials that appears to be prevalent today.

References

[1] J.J.Miles, M.Wdomin, J.Oakley and B.K.Middleton, IEEE Trans. Mag. **31** (1995) 1007.

[2] S.Chikazumi, "Physics of magnetism". John Wiley and Sons, (1964).

Chapter 4

TEM investigations of giant magnetoresistive sensing media

4.0 Introduction

Giant magnetoresistance (GMR) and the uses for GMR media have been described in chapter one. In this chapter I present the results of TEM experiments carried out on GMR media with reduced hysteresis and improved sensitivity. All the systems I have been studying are based on Co/Cu multilayers and are intended for use as absolute position sensors. This work was carried out in conjunction with H.Holloway and D.J.Kubinski at the Ford Research Labaratory in Michigan, USA. The samples were deposited by D.J.Kubinski.

4.1 Giant magnetoresistance in Co/Cu multilayers

The giant magnetoresistance effect in Co/Cu multilayers arises from the spin dependent scattering of electrons at the boundaries between the cobalt and copper layers [1]. GMR materials can be used as magnetic field sensors and in particular read heads on magnetic storage devices and position sensors [2]. The materials investigated in this chapter are intended for use as position sensors. The main requirement for absolute position sensors is that the output signal they produce is unambiguous. For this to be the case, this signal has to be indepedent of the sensor's magnetic history. This requires that there is

negligable hysteresis in the magnetoresistive response. In addition the percentage change in resistance per unit of applied field should remain as high as possible as this is a measure of the sensitivity.

It is well established that the MR signal oscillates as a function of the copper thickness in Co/Cu multilayers, with the optimum values being 0.9 and 2.0nm. These thicknesses correspond to the first and second maxima in antiferromagnetic (AFM) coupling respectively [3][4]. For applications such as absolute position sensors, Co/Cu multilayers with a copper thickness corresponding to the first AFM maximum (0.9nm) can be used as there is little hysteresis, however the sensitivity of the response is reduced. Alternatively Co/Cu multilayers with a copper thickness corresponding to the second AFM maximum (2.0nm) can be used as the sensitivity is greater. These media however suffer from a prohibitively large amount of hysteresis in the magnetoresistive response. Two approaches which have been developed to improve the performance of these media are: (i) improve the sensitivity of Co/Cu multilayers at the first AFM maximum, (ii) reduce the magnetoresistive hysteresis of multilayers at the second AFM maximum.

(i) Increasing the sensitivity of multilayers at the first AFM maximum

Several compositions have been attempted to achieve this, in this chapter the use of multilayers with some cobalt layers having a cobalt thicknesses of 3.0nm rather than the more usual 1.5nm are considered. This approach arises from the assumption that the magnetic torque on the cobalt layers (and thus the width of the response) is proportional to the cobalt thickness [5]. Accompanying this it would also be expected that there would

be a decrease in the magnetoresistive response since the boundaries of the layers (where the spin dependent scatering originates) will make up a smaller percentage of the multilayer. For this reason a compromise thickness will have to be found which has the greatest sensitivity. Previous studies have shown this thickness to be 3.0nm [5]. In this chapter samples with alternating 1.0 and 3.0nm cobalt layer thicknesses are compared with ones with 2.0nm thick cobalt layers.

(ii) Reducing the hysteresis at the second AFM maximum

Several approaches have been tried out to achieve this. Amongst them are the use of very thin cobalt layers ($t_{Co} \leq 0.5$nm) [6][7], and the use of cobalt copper alloys in the magnetic layer [8]. Previous studies have shown that multilayers with cobalt layers in the range 0.3 to 0.5nm show greatly reduced hysteresis, but coupled with this is a loss in sensitivity [6]. The samples examined in this chapter have alternating thick and thin layers in an attempt to increase the sensitivity while the hysteresis is kept low. I will compare two samples with slightly different thicknesses of thin layers alternated with thick layers. The layer thickness over which the multilayers exhibit this reduced hysteresis however is very narrow, which would make the manufacturing process costly, so a second approach was developed. This second approach arises from an NMR study [9] which showed that the cobalt copper interface between layers in samples at the second AFM maximum with very thin cobalt layers which showed low hysteresis extended over a range of about 0.5nm and consisted of an alloy with the composition $Co_{0.6}Cu_{0.4}$. The assumption was that co-deposition of cobalt and copper in the magnetic layer would favour the formation of this

layer and hence reduce the hysteresis. In this chapter a sample with 0.9nm thick cobalt copper alloy layers is considered.

4.2 Structural studies of GMR media based on Co/Cu multilayers

The samples studied in this chapter are listed in table 4.1, along with a note of which AFM maximum the multilayer corresponds to.

Sample	Composition	
A332	$[0.32Co/2.0Cu/1.5Co/2.0Cu]_{10}$	2nd AFM
A333	$[0.42Co/2.0Cu/1.5Co/2.0Cu]_{10}$	2nd AFM
A337	$[0.9CoCu/2.0Cu]_{20}$	2nd AFM
A358	$[3.0Co/0.9Cu/1.0Co/0.9Cu]_{10}$	1st AFM
A359	$[2.0Co/0.9Cu]_{20}$	1st AFM
A338	$[3.0Co/0.9Cu]_{16}$	1st AFM

Table 4.1: The samples studied in this chapter.

Each of the samples were deposited onto a 7.5nm thick Ruthenium buffer layer. The GMR loops for these samples were recorded by H.Holloway and D.Kubinski, and are shown in figure 4.1.

Bright and dark field imaging together with electron diffraction were used to determine the structure of the samples. The bright and dark field images (figure 4.2) show that all

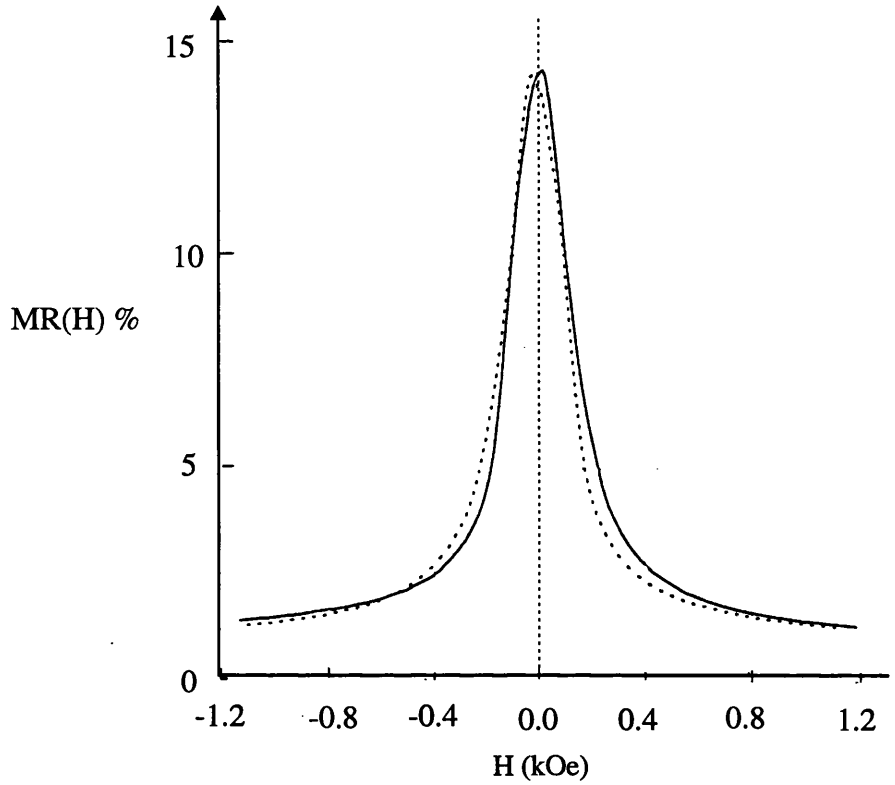

Figure 4.1a: GMR loop for sample A332. The solid line represents the forward scan and the dotted line represents the return scan.

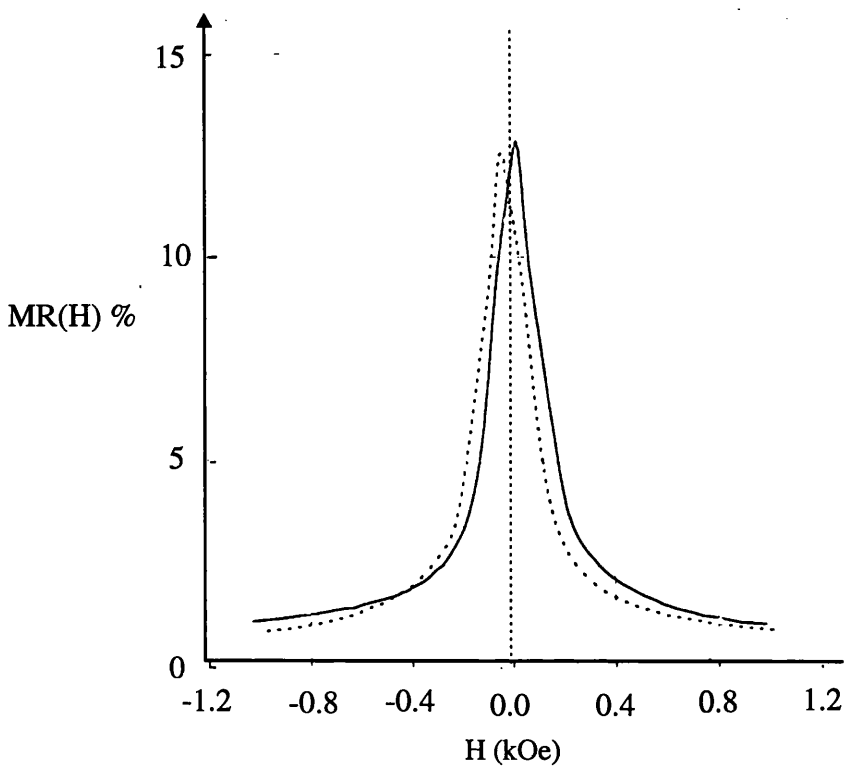

Figure 4.1b: GMR loop for sample A333

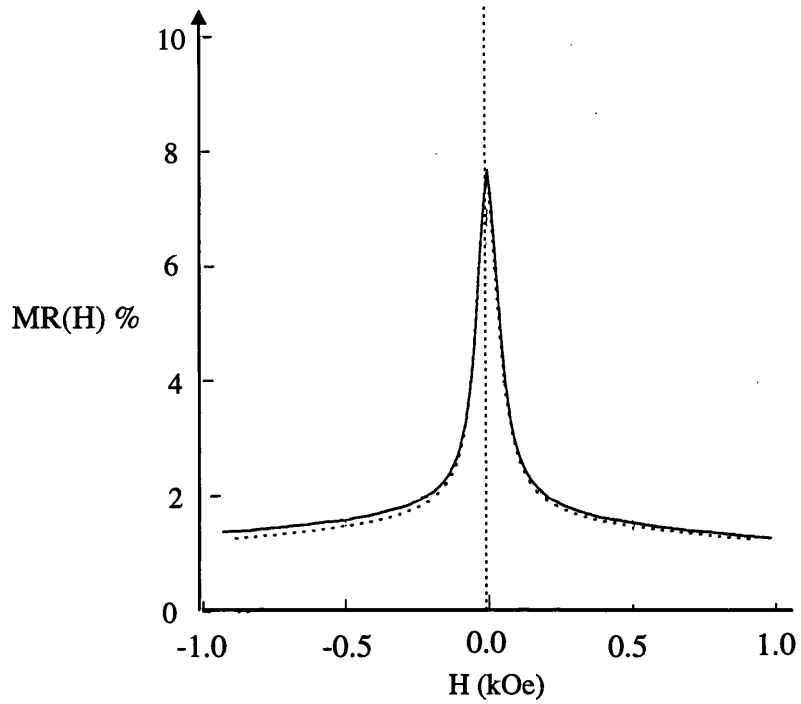

Figure 4.1c: GMR loop for sample A337

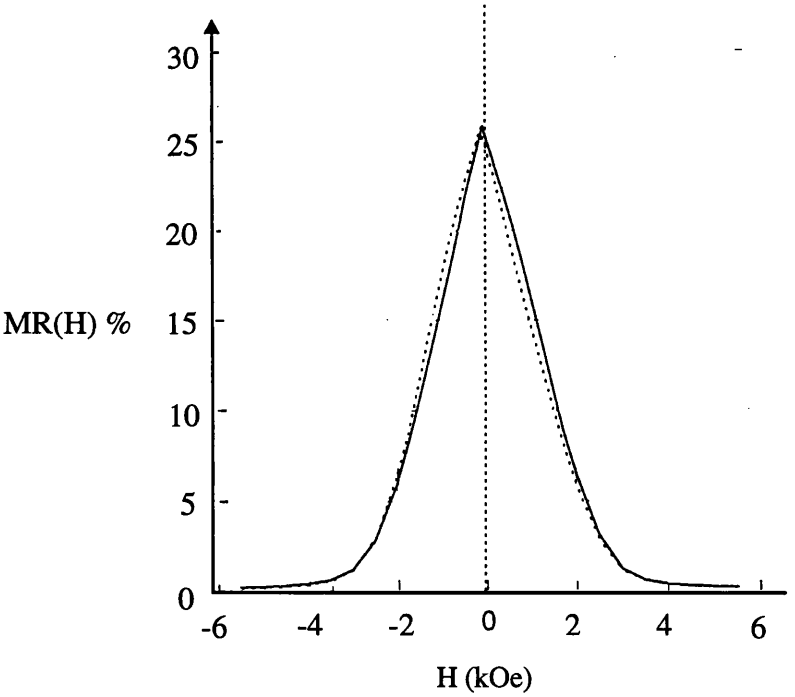

Figure 4.1d: GMR loop for sample A358

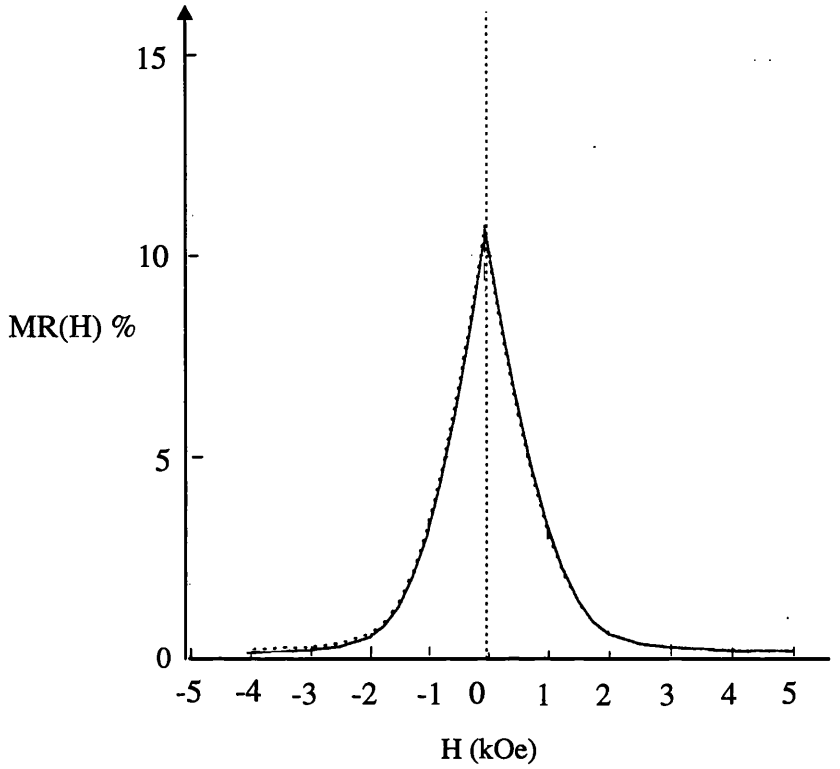

Figure 4.1e: GMR loop for sample A359

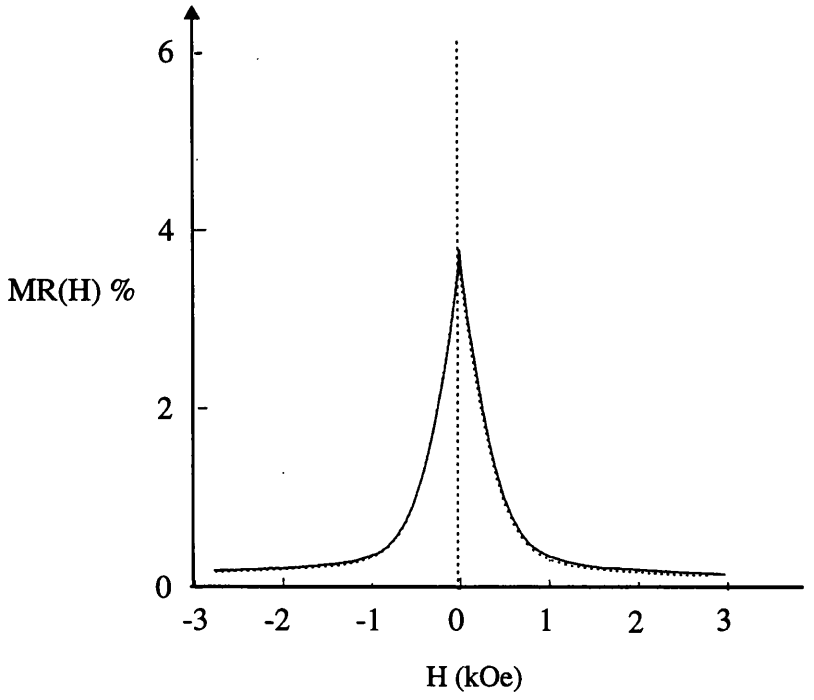

Figure 4.1f: GMR loop for sample A338.

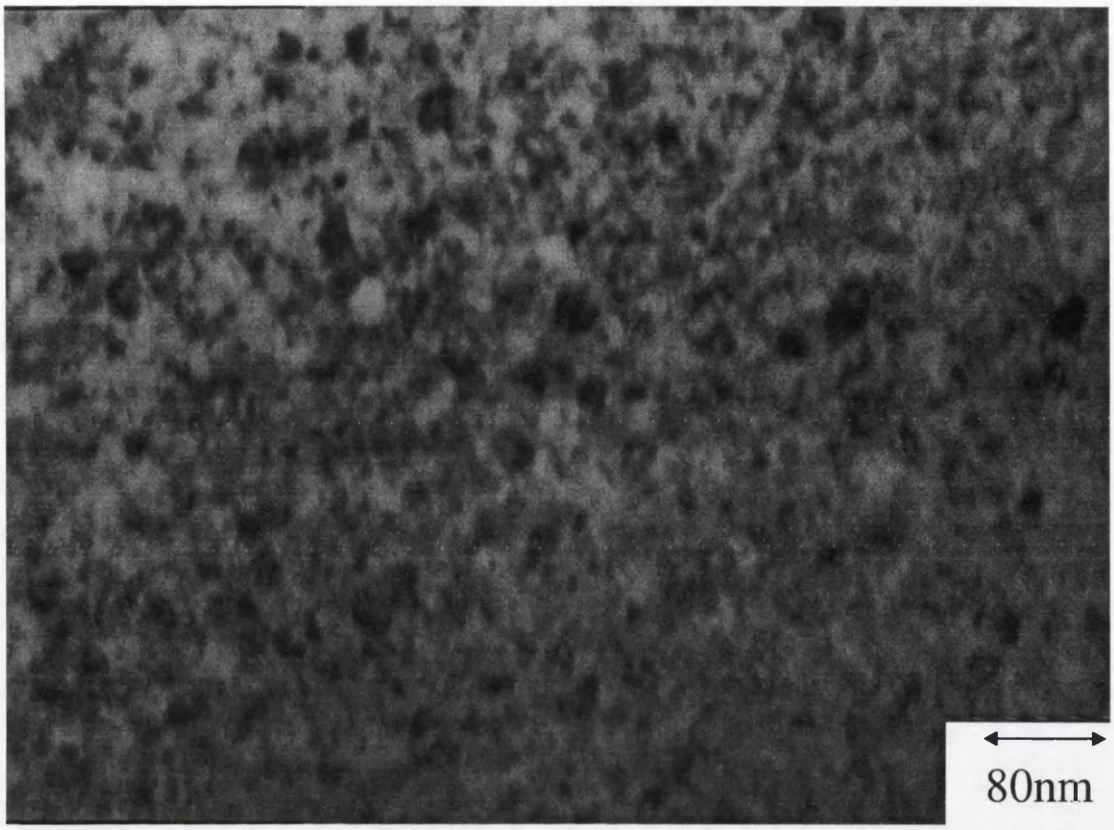

Figure 4.2a: Bright field image of sample A332

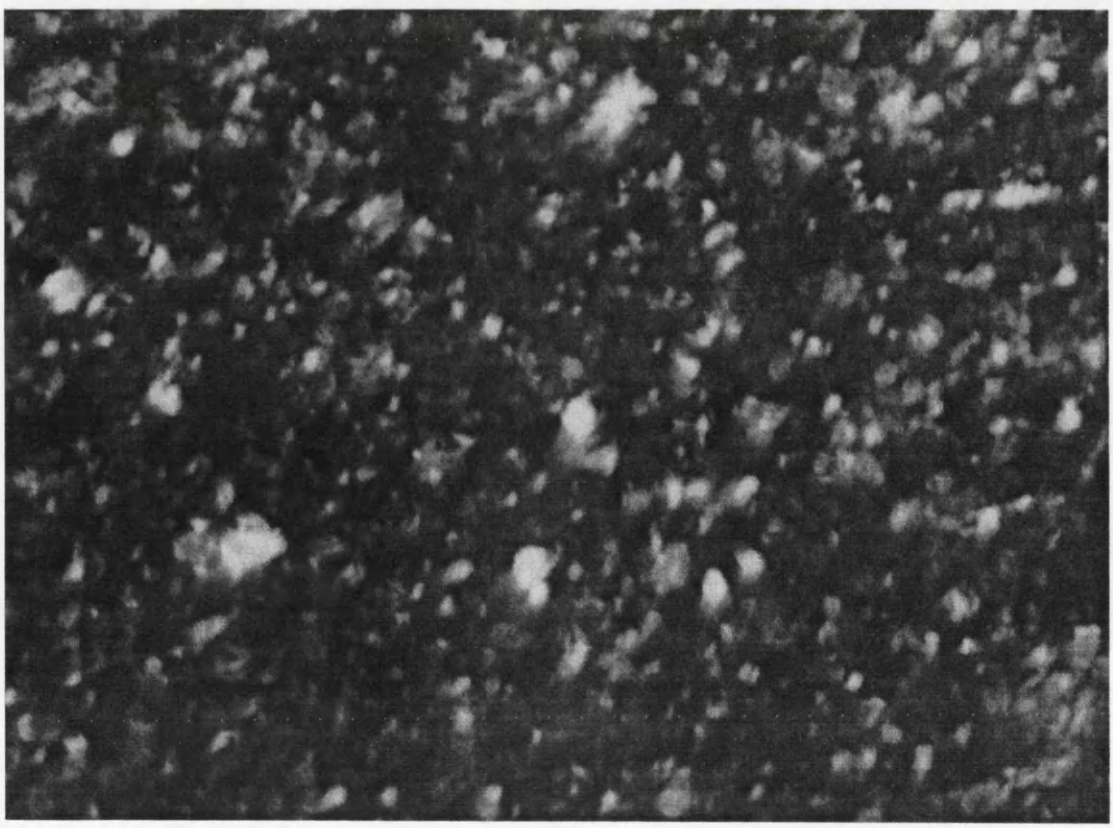
Figure 4.2b: Dark field image of sample A332

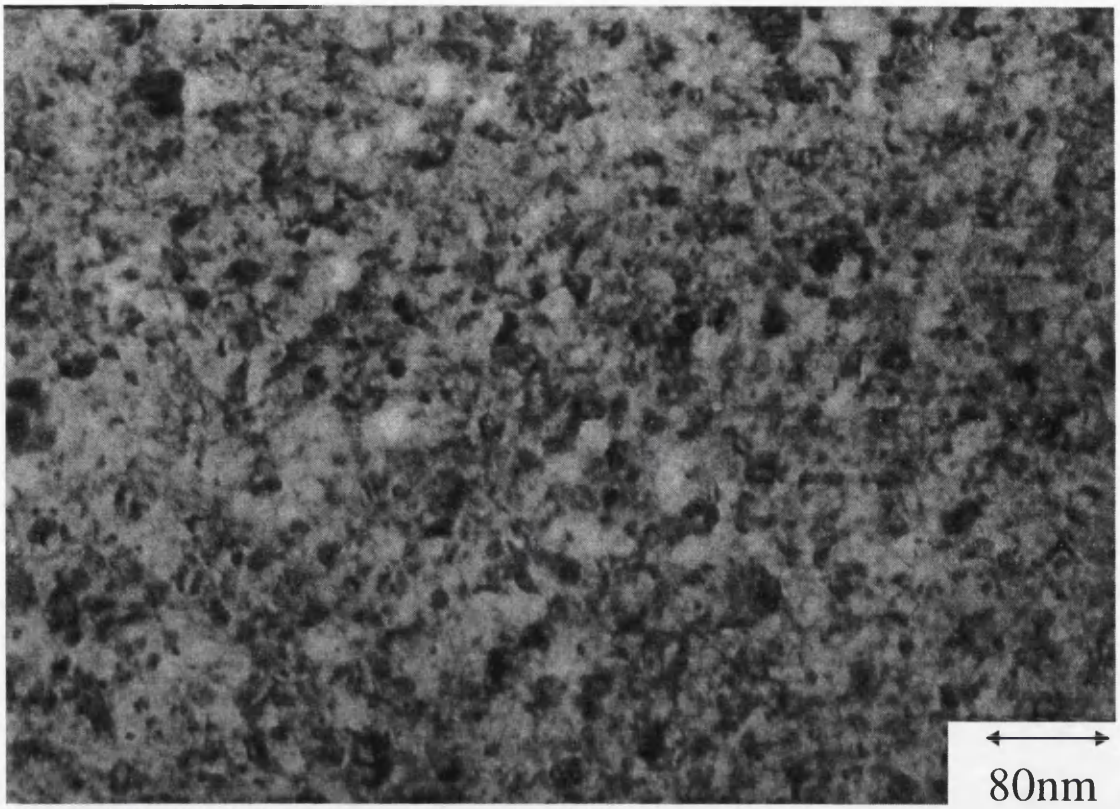

Figure 4.2c: Bright field image of sample A333

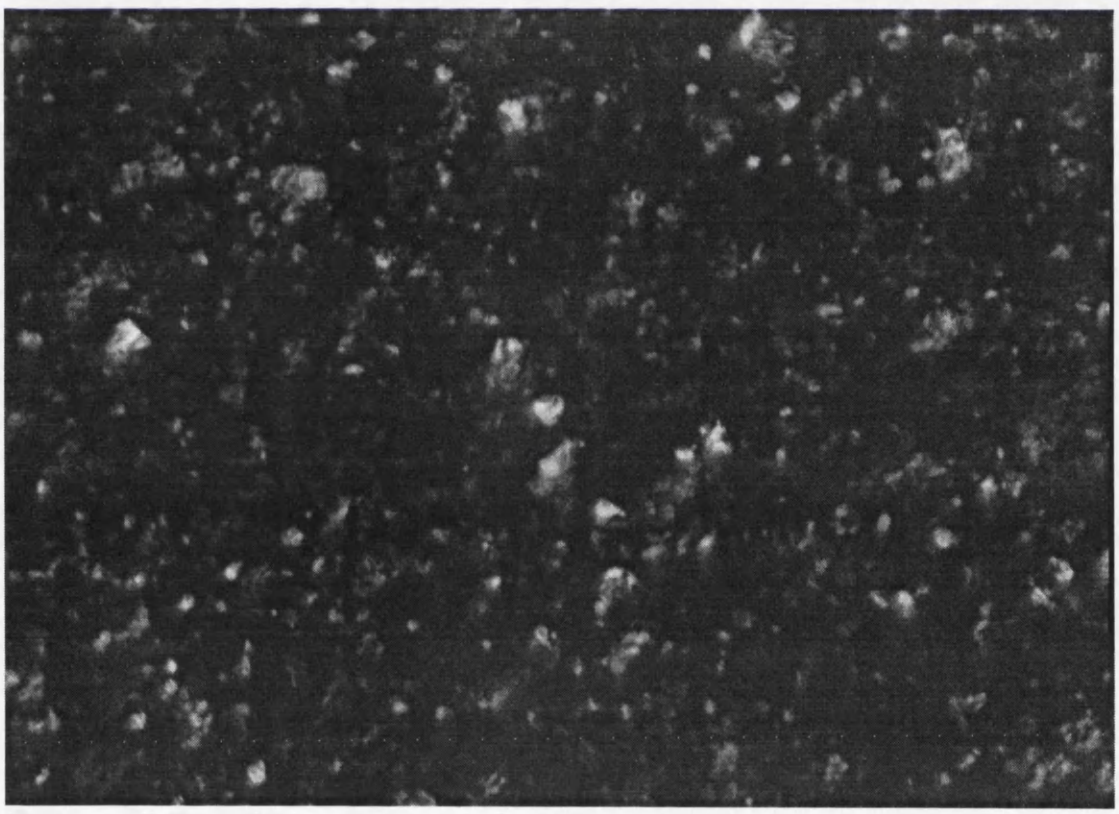
Figure 4.2d: Dark field image of sample A333

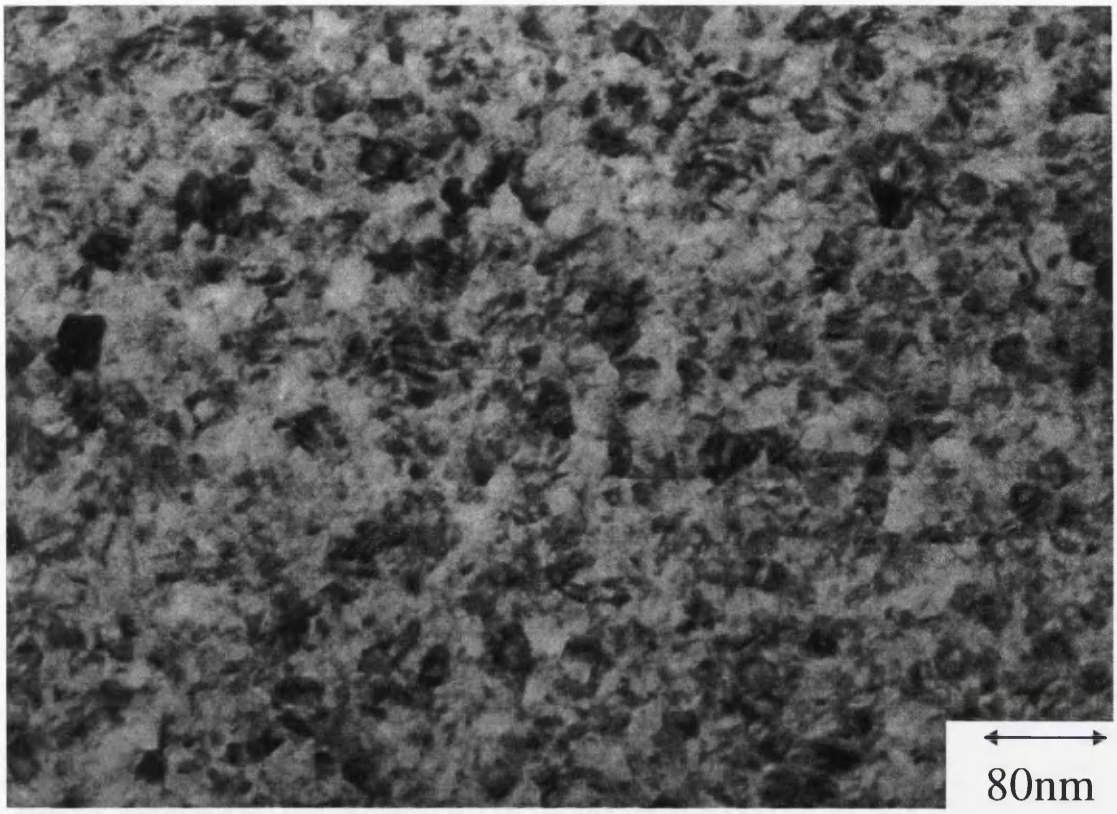

figure 4.2e: Bright field image of sample A337

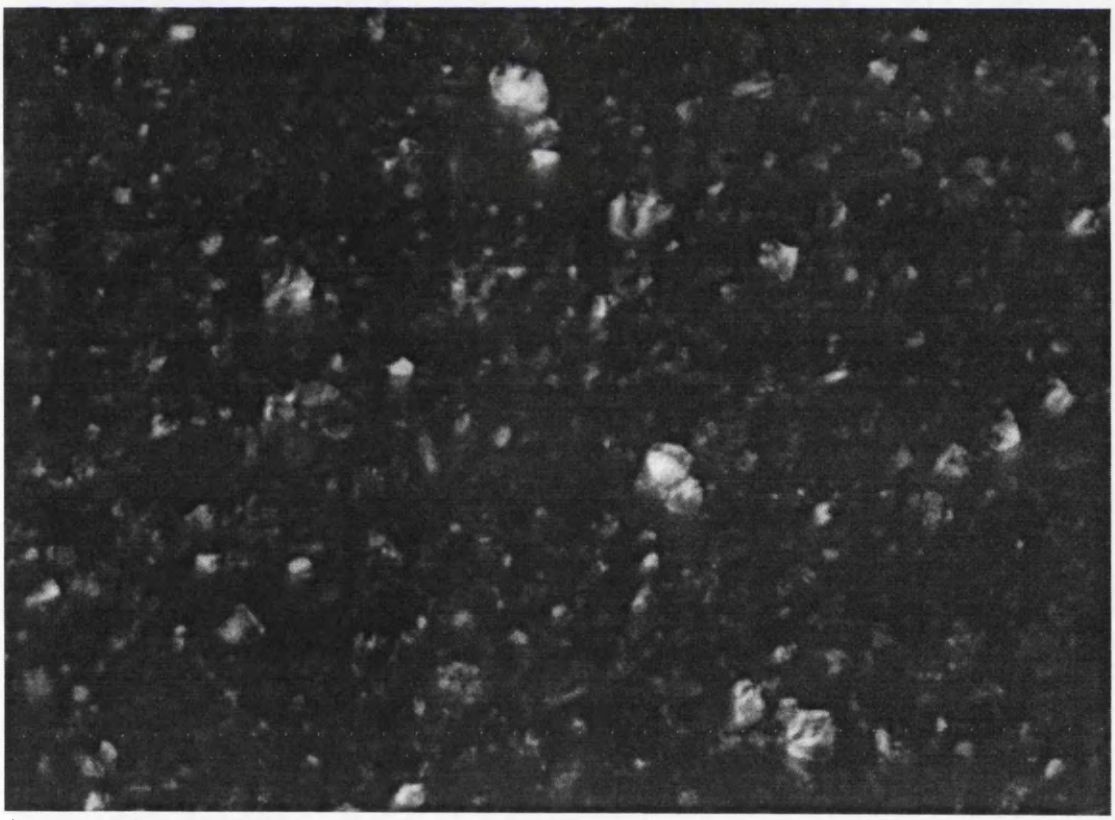
figure 4.2f: Dark field image of sample A337

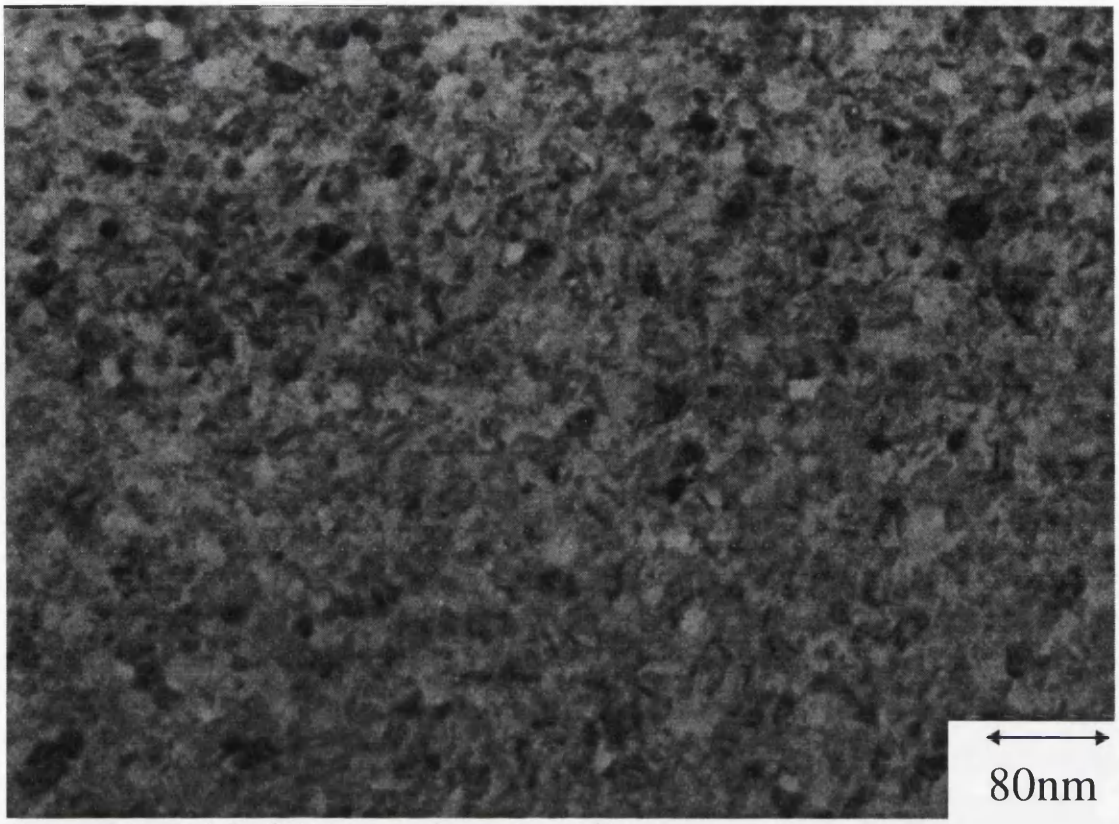

Figure 4.2g: Bright field image of sample A358

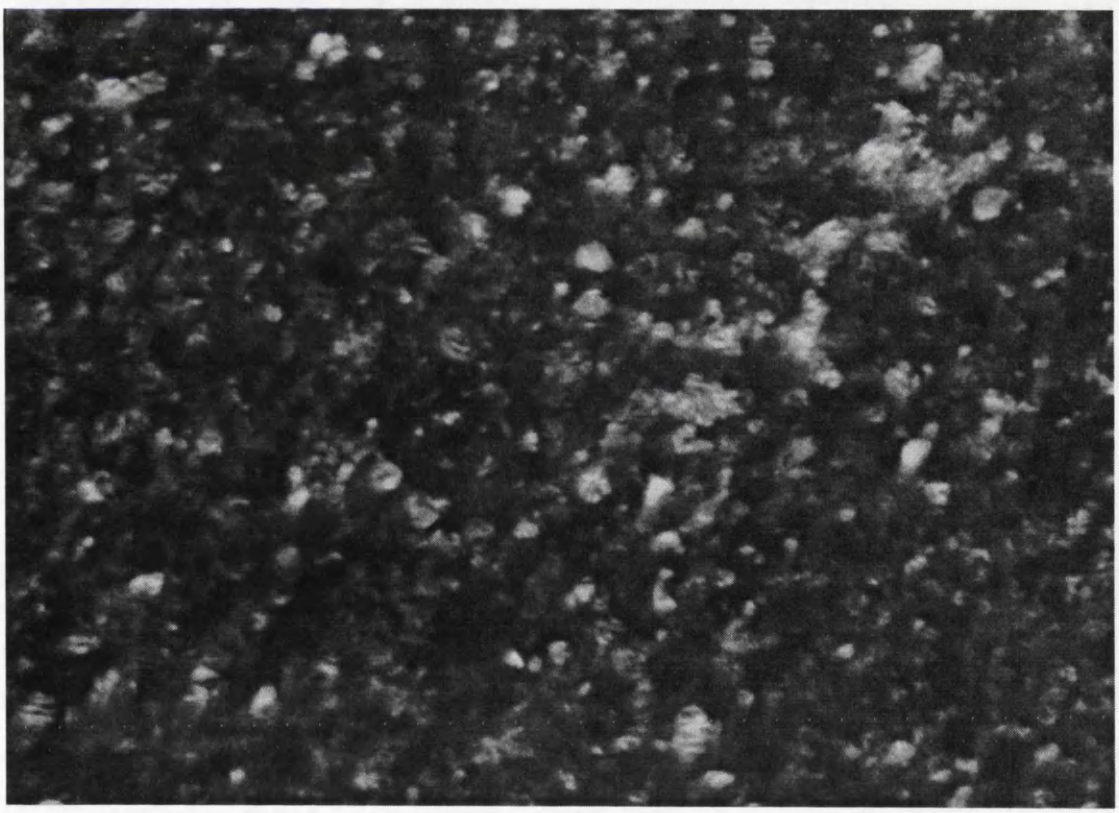
Figure 4.2h: Dark field image of sample A358

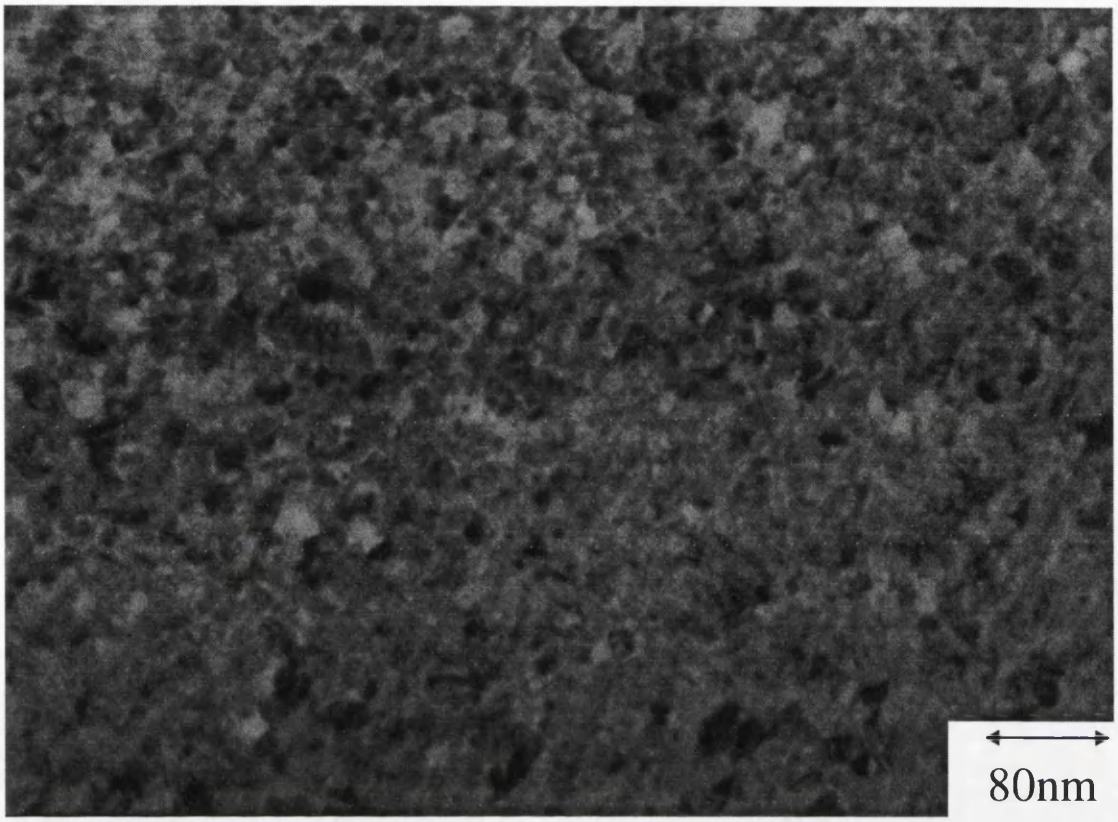

figure 4.2i: Bright field image of sample A359

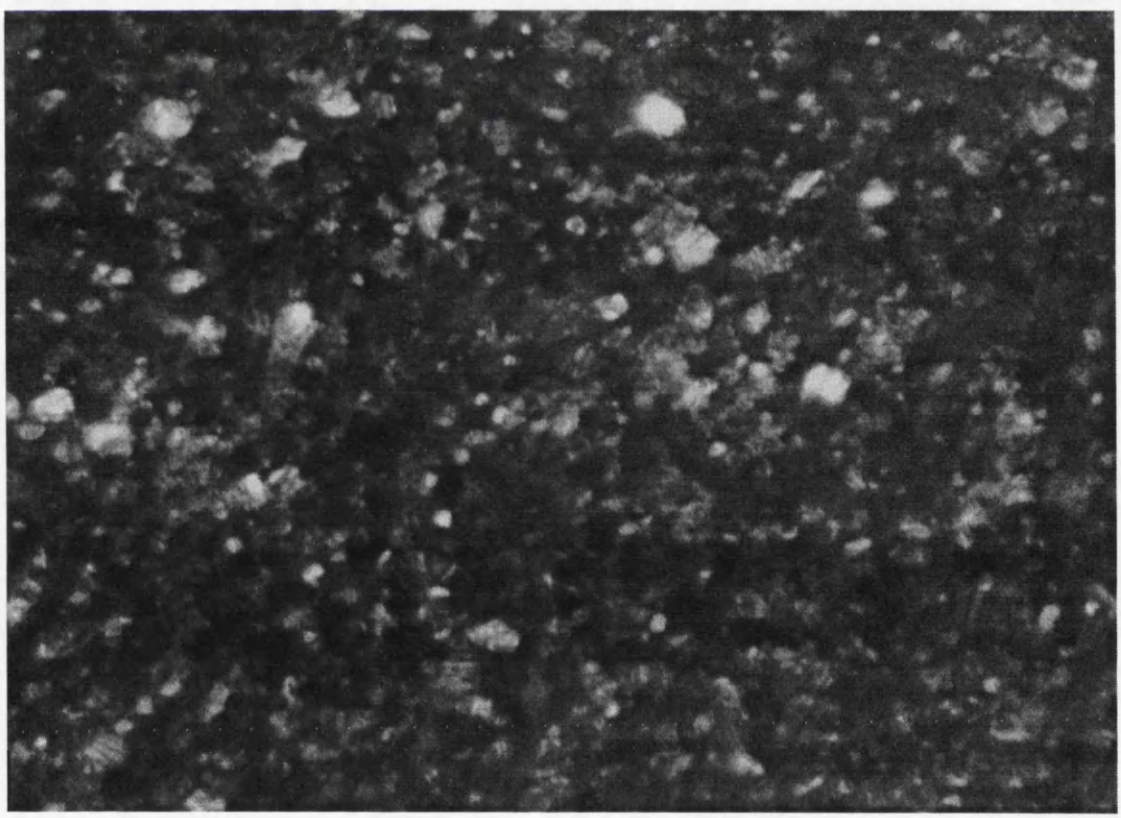
figure 4.2j: Dark field image of sample A359

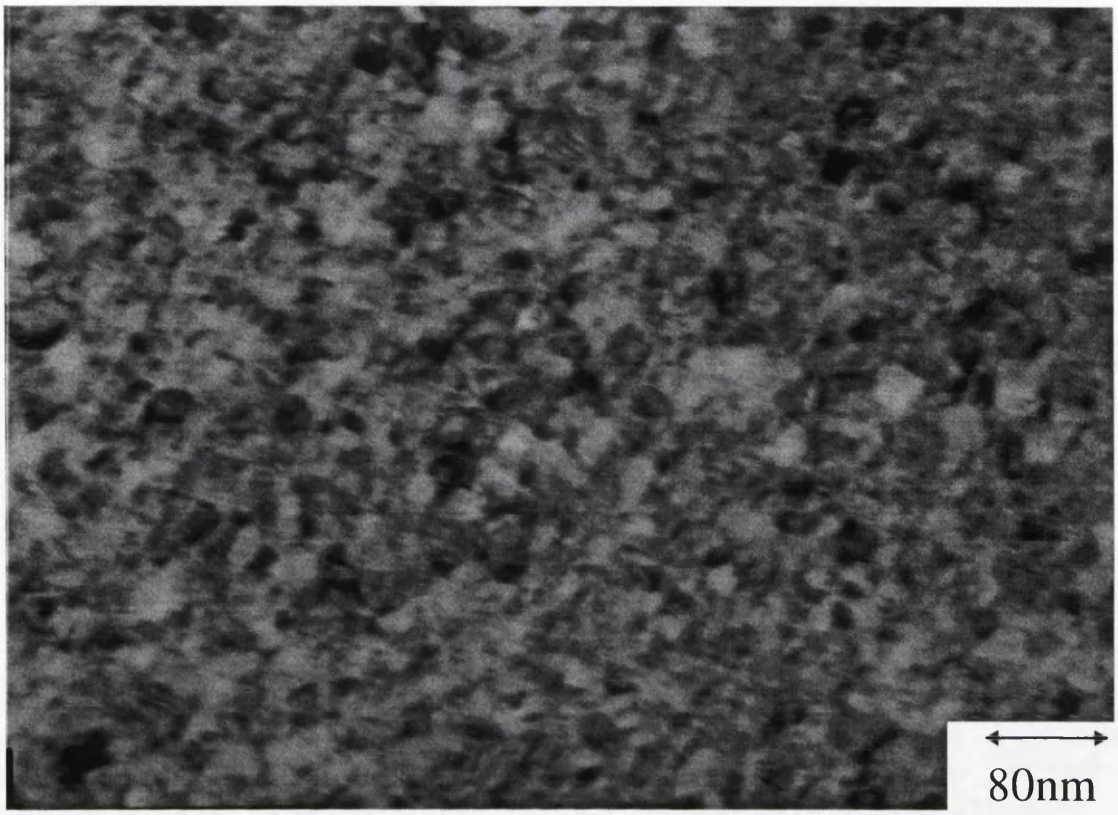

Figure 4.2k: Bright field image of sample A338

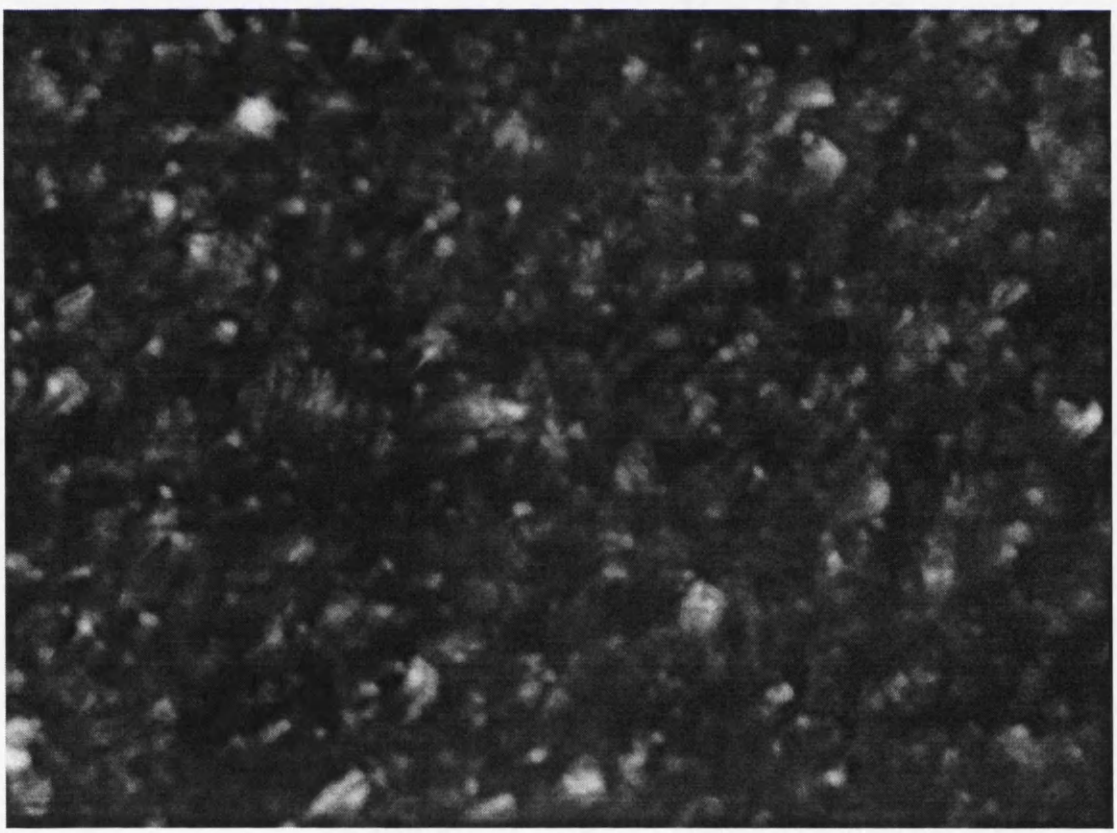
Figure 4.2l: Dark field image of sample A338

the samples were micropolycrystalline. Grain sizes varied over the range 5-30nm. There is no discernible difference between the specimens and it would be impossible to distinguish them on the basis of this set of images.

Diffraction patterns were recorded with the specimen plane (i) normal to the electron beam and (ii) inclined at an angle of 30° (figure 4.3). No significant differences were observed between the tilted and untilted patterns. In particular rings of uniform circumferential intensity were observed on all occasions. Hence no evidence at all is seen for texture in the films and a 3D-random distribution of crystallites orientations is a reasonable first approximation. However, the ring patterns recorded from the different samples did differ. To help with the analysis we show diffraction patterns (computed using DIFFRACT) for hcp Ru, fcc Cu, fcc Co and hcp Co are shown (figure 4.4) as well as the diffraction ring radii (in arbitrary units) for each of the above (table 4.2). Ru and Cu will always, under standard conditions, be found as hcp and fcc respectively whilst Co has been observed in a number of forms dependent on its thickness and the conditions under which it was deposited. It should also be noted that the inter-atomic spacings of fcc Cu and fcc Co are essentially indistinguishable using standard electron diffraction techniques.

It is instructive to examine diffraction patterns from A332 and A338 initially (figure 4.5); the former has the lowest Co content and the latter the greatest. All lines in the diffraction pattern for A332 can be fitted to hcp Ru and fcc Co/Cu. In particular, strong reflections such as Co $(01\bar{1}1)$, which would not overlap with any Ru or Cu lines, appear to be

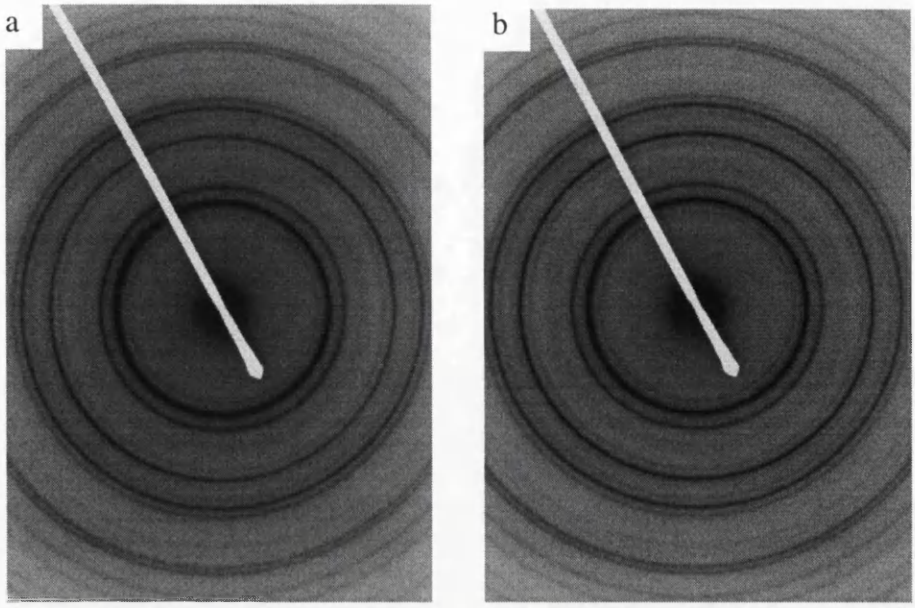

Figure 4.3 a and b: Diffraction patterns for sample A332 both tilted (a) and untilted (b)

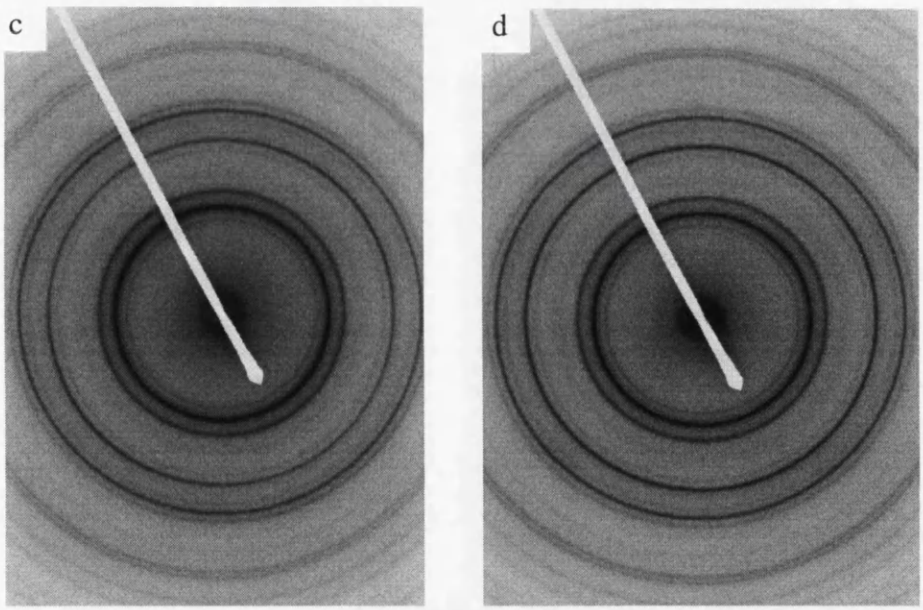

Figure 4.3 c and d: Diffraction patterns for sample A333 both tilted (c) and untilted (d)

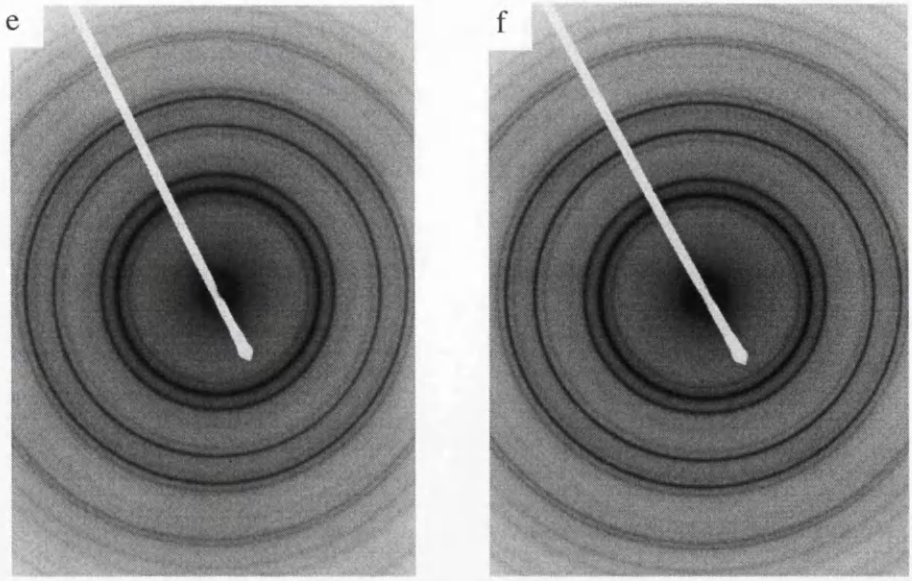

Figure 4.3 e and f: Diffraction patterns for sample A337 both tilted (e) and untilted (f)

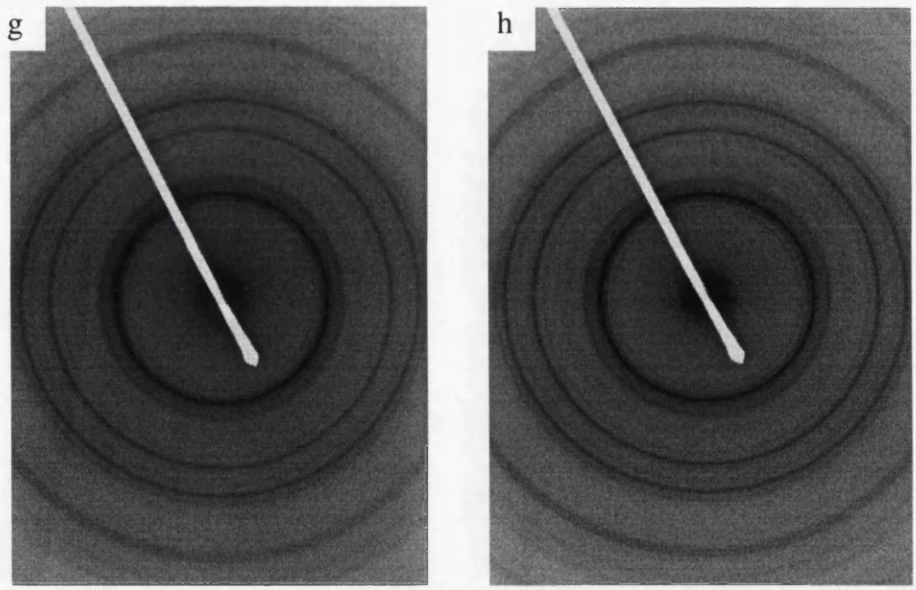

Figure 4.3 g and h: Diffraction patterns for sample A358 both tilted (g) and untilted (h)

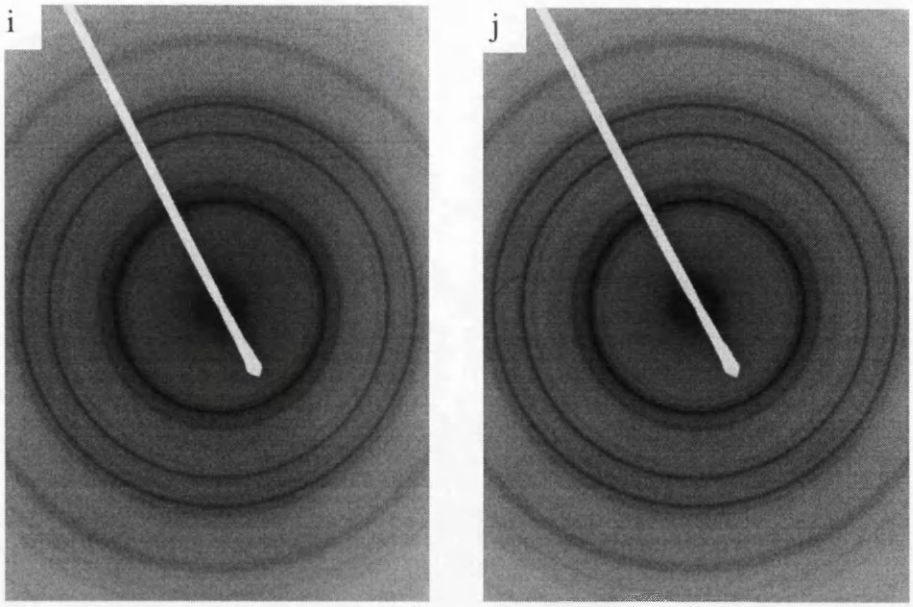

Figure 4.3 i and j: Diffraction patterns for sample A359 both tilted (i) and untilted (j)

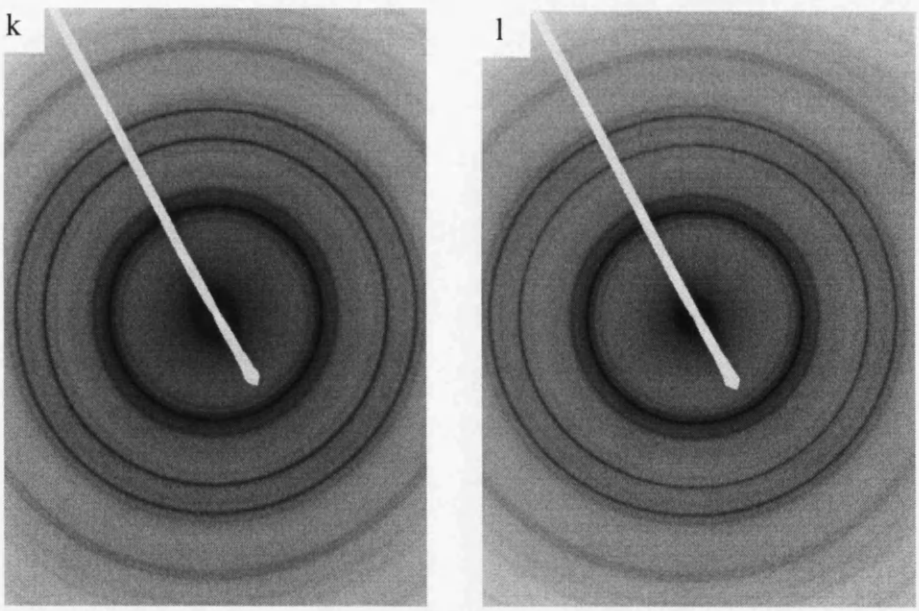

Figure 4.3 k and l: Diffraction patterns for sample A338 both tilted (k) and untilted (l)

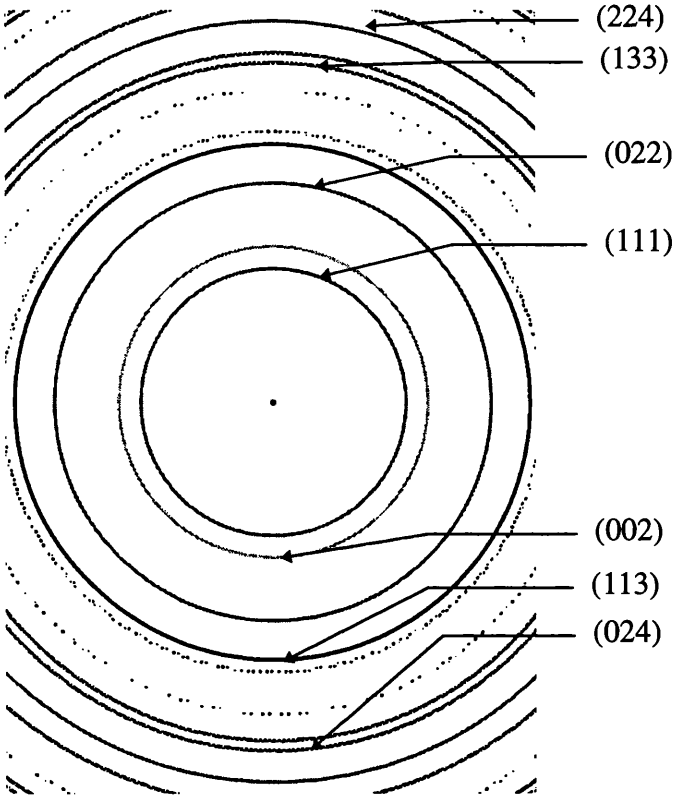

Figure 4.4a: The diffraction pattern for FCC cobalt calculated using DIFFRACT.

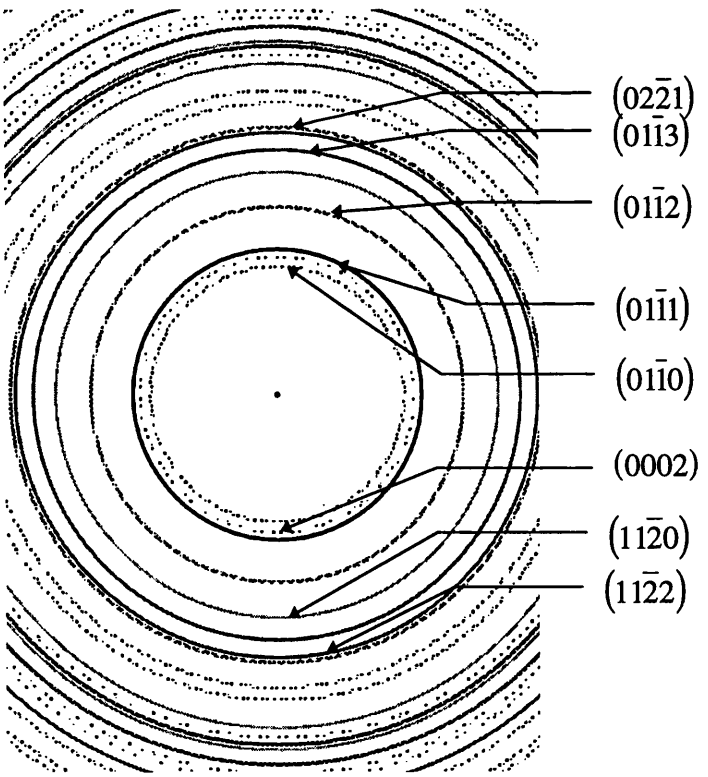

Figure 4.4b: The diffraction pattern for HCP cobalt calculated using DIFFRACT

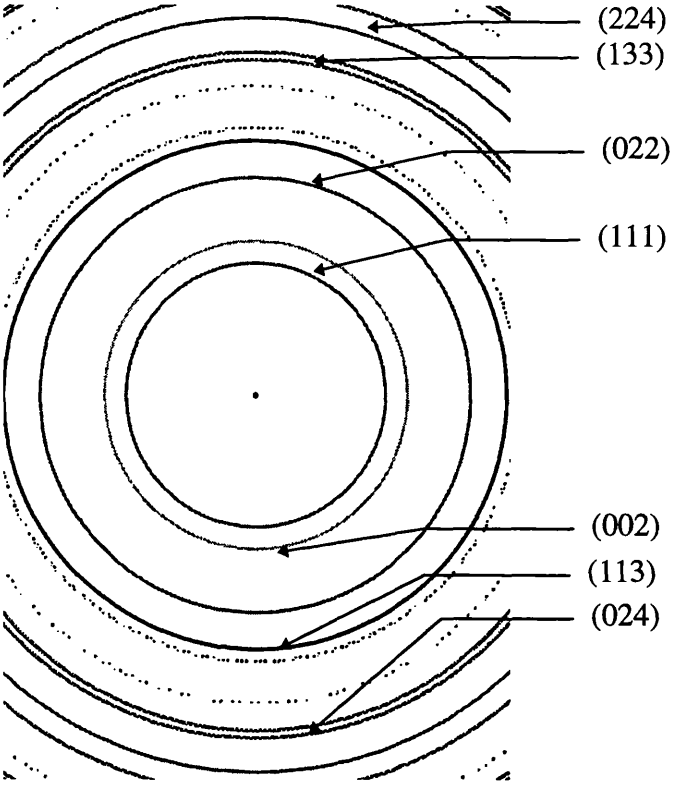

Figure 4.4c: The diffraction pattern for FCC copper calculated using DIFFRACT

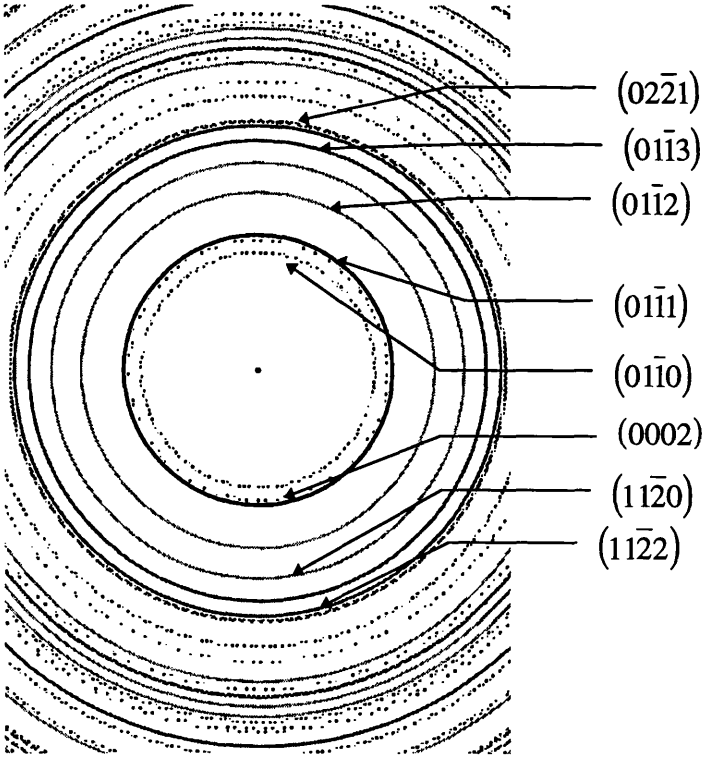

Figure 4.4d: The diffraction pattern for HCP ruthenium calculated using DIFFRACT

Ruthenium HCP	Copper FCC	Cobalt FCC	Cobalt HCP	Radius
$(01\bar{1}0)$				5.13
			$(01\bar{1}0)$	5.52
(0002)				5.61
	(111)			5.76
$(01\bar{1}1)$		(111)		5.85
			(0002)	5.9
			$(01\bar{1}1)$	6.26
	(002)			6.65
		(002)		6.76
$(01\bar{1}2)$				7.6
			$(01\bar{1}2)$	8.08
$(11\bar{2}0)$				8.82
	(022)			9.4
		(022)	$(11\bar{2}0)$	9.56
$(01\bar{1}3)$				9.85
$(11\bar{2}2)$			$(01\bar{1}3)$	10.43
$(02\bar{2}1)$				10.6
	(113)			11.02
		(113)		11.21
			$(11\bar{2}2)$	11.23
			$(02\bar{2}1)$	11.4
	(222)			11.52
$(02\bar{2}2)$				11.65
		(222)		11.71
$(01\bar{1}4)$				12.33
			$(02\bar{2}2)$	12.45
			$(01\bar{1}4)$	13.03
$(02\bar{2}3)$				13.27
	(004)			13.3
		(004)		13.52
$(12\bar{3}0)$				13.55
$(12\bar{3}1)$				13.9
			$(02\bar{2}3)$	14.15
$(11\bar{2}4)$				14.31
	(133)			14.49
			$(12\bar{3}0)$	14.61
$(12\bar{3}2)$				14.65
		(133)		14.73
	(024)			14.87
			$(12\bar{3}1)$	14.9

Table 4.2: Diffraction ring radii for Co/Cu multilayers in arbitrary units

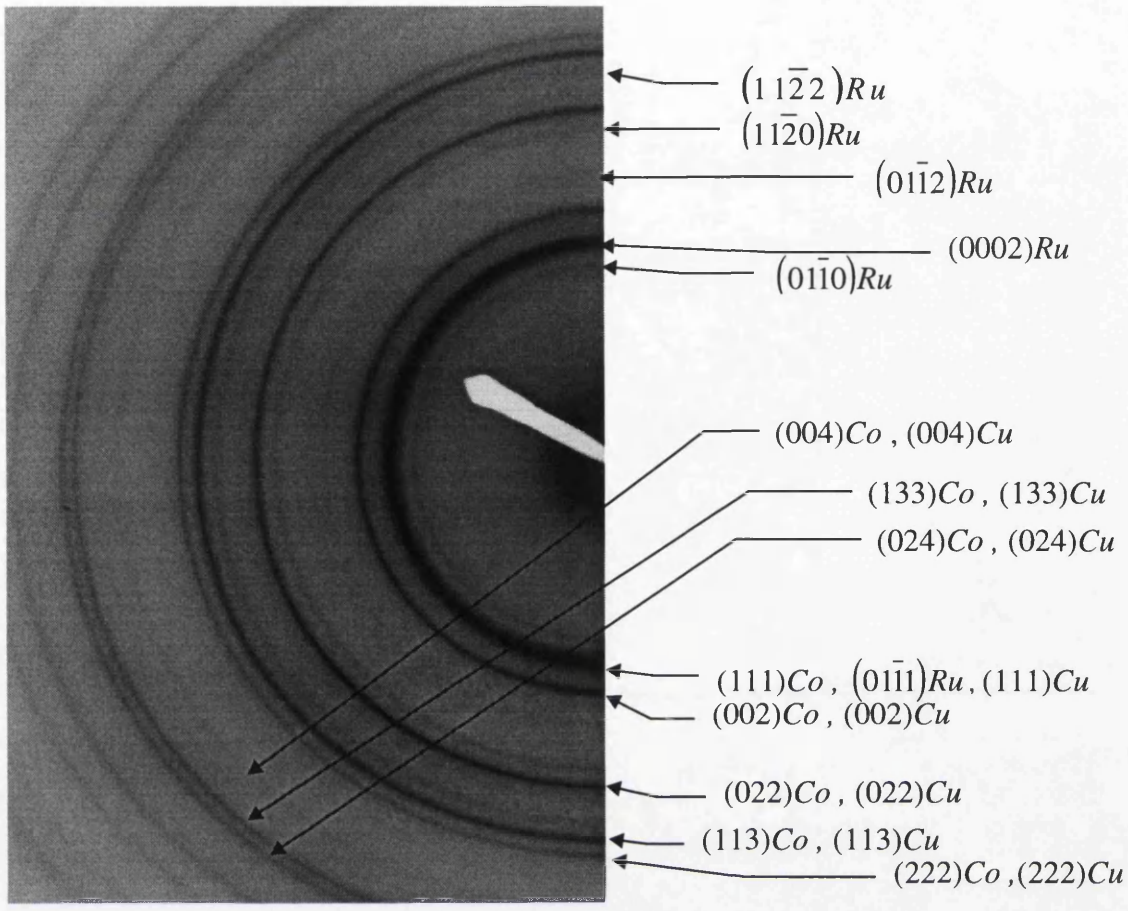

Figure 4.5a:Indexed diffraction pattern for sample A332

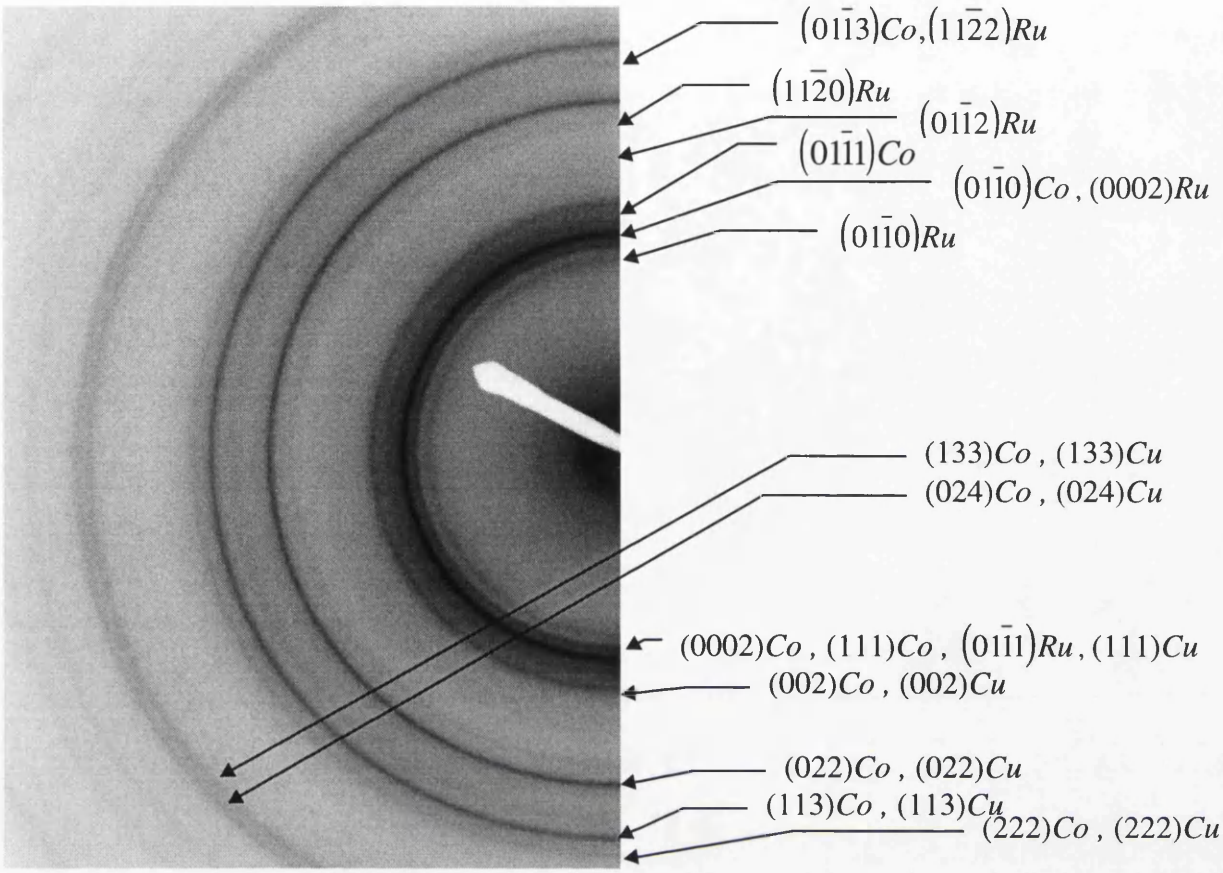

Figure 4.5b: Indexed diffraction pattern for sample A338

absent. By contrast the diffraction pattern from A338 does show a line where the Co $(01\bar{1}1)$ reflection is expected but it is only weak. Furthermore, the lines associated with the fcc Co/Cu systems are still present and are the strongest rings.

The diffraction patterns from A333 and A337 (where Co layers never exceed 2.0nm) are similar to that of A332. Indeed that from A337 is in many ways the clearest diffraction pattern and there is no sign of rings whatsoever in positions appropriate to hcp Co. Diffraction patterns from A358 and A359 more closely resemble that from A338 with at least a suggestion of a ring at the expected position of the hcp Co $(01\bar{1}1)$ reflection.

The results suggest that Co layers of thickness <2.0nm are predominantly fcc in structure and only beyond that thickness does hcp start to emerge. Even then, up to 3.0nm, the ring intensities suggest that fcc remains the dominant phase.

4.3 Magnetic studies of Co/Cu multilayers

Sample A338 was only studied structurally. Foucault images were recorded for each of the other specimens in its as-received state, i.e. before the sample was subjected by me to a magnetic field. In all cases magnetic contrast could be seen (figure 4.6) although in the case of A337 (with low Co content) it was very low. Magnetic contrast from samples A332 and A333 suggested a rather isotropic structure whilst strong directionality was apparent in A337, A358 and A359. These samples were then taken through their magnetisation cycles while being imaged in the Fresnel mode of Lorentz microscopy. The

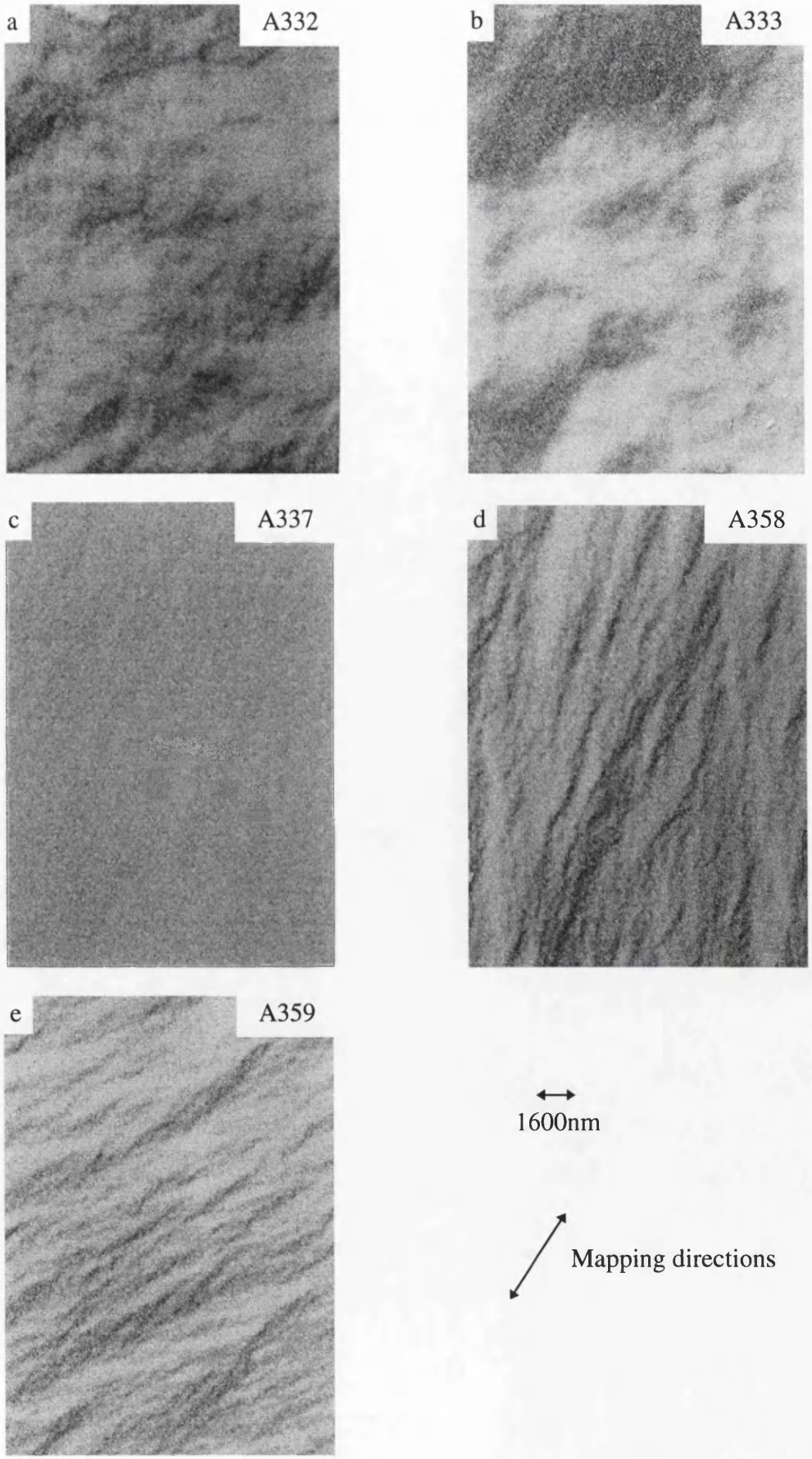

Figure 4.6: Foucault images of the samples in the as received state.

magnetisation sequences were recorded on the low light level TV camera. It is not possible to display these sequences here but upon repeated examination the basic reversal mechanism of the sample could be determined. More detailed examination of the reversal mechanism is deferred until later when CCD images of the reversal mechanism are discussed. (It should be noted that at no time during these sequences or during the following investigations were the samples exposed to a field which would definitely be high enough to saturate them.) The reversal mechanism appeared to be as follows:

(i) the orientation of the field is important in determining the detailed magnetisation reversal process and this may relate to hysteresis in the MR, especially when the specimens are only subjected to a limited field range (minor loops).

(ii) the behaviour of films at the first and second AFMs are quite different and A337 also differs significantly from A332 and A333. There appear to be instances where well-defined walls run throughout the thickness of the multilayer stack which are involved in the reversal (seen in A358 and A359), instances where low contrast walls which we assume only exist in a few layers (the peripheral ones?) appear part way through a reversal process that otherwise occurs predominantly by rotation (seen in A337) and instances where complex small scale structures but no well defined walls are observed (seen in A332 and A333). The directionality observed in the as-received state in A358, A359 and A337 seems to be important, however, the origin of this uniaxial anisotropy is unknown. Following these results, some of the samples were studied more closely, using

the Fresnel and DPC modes of Lorentz microscopy along with low angle diffraction. The images were recorded using the slow scan CCD camera.

The domain patterns which had been observed for samples A332 and A333 were similar to those observed for other Co/Cu multilayers [10]. The samples which for this reason have been studied in greatest detail are A358 and A359 where the Cu thickness is close to the first AFM and the alloy sample A337 (with Cu thickness close to the second AFM). In a typical experiment a specimen tilted through 30° is subjected to a large vertical field by exciting the objective lens to its maximum value (~6kOe). The field is then reduced to a lower value, 350Oe, and the tilt angle is slowly changed until the specimen is inclined at an angle of -30°. Hence the in-plane component of field to which the sample is subjected varies from +175Oe to -175Oe. This is a much smaller range of magnetic field than is required to observe saturation in the MR signal as seen in figure 4.1. Nonetheless, as the images show, much of the magnetisation reversal takes place over this range and what happens beyond is simply that the angle between the magnetisation vectors in alternate layers reduces steadily. Justification for this statement is given later.

It is important to recognise that for all transmission imaging and diffraction techniques the imaging conditions are sensitive to the magnetic induction component perpendicular to the electron beam and integrated along an electron trajectory. Thus contributions from individual layers in the multilayer stack can never be separated but variations in the averaged induction component orthogonal to the electron beam are seen. It follows that

for a sample with perfect AF coupling the resultant deflection of the electron beam would always be zero and no magnetic contrast would ever be observed.

For each of the Fresnel sequences shown the ripple direction is perpendicular to the average magnetisation direction. In this way, magnetisation rotation is revealed by the rotation of the ripple direction. The strength of the ripple contrast indicates the degree to which the average magnetisation direction changes between neighbouring crystallites, with larger changes being indicated by ripple with larger contrast. Domain walls are represented by continuous dark or light lines.

The magnetic structures in samples A358 and A359 show a pronounced directionality along the applied field direction. This was noted previously when images were recorded in the as-grown state (that is, before the specimen was subjected to an applied field) and is confirmed in the experiments recorded here. Figures 4.7 and 4.8 show sequences of Fresnel images for sample A359. In the former case, the field was applied parallel to the easy axis (judged as being perpendicular to the ripple direction observed in the remanent state) whilst in the second case the field was applied parallel to the hard axis. In figure 4.7 ripple is apparent through much of the sequence; it intensified somewhat as the field was reduced and at a field of $\approx$-10 Oe a single domain wall, approximately parallel to the applied field direction, ran across the field of view. Thereafter the intensity of magnetisation ripple decreased monotonically.

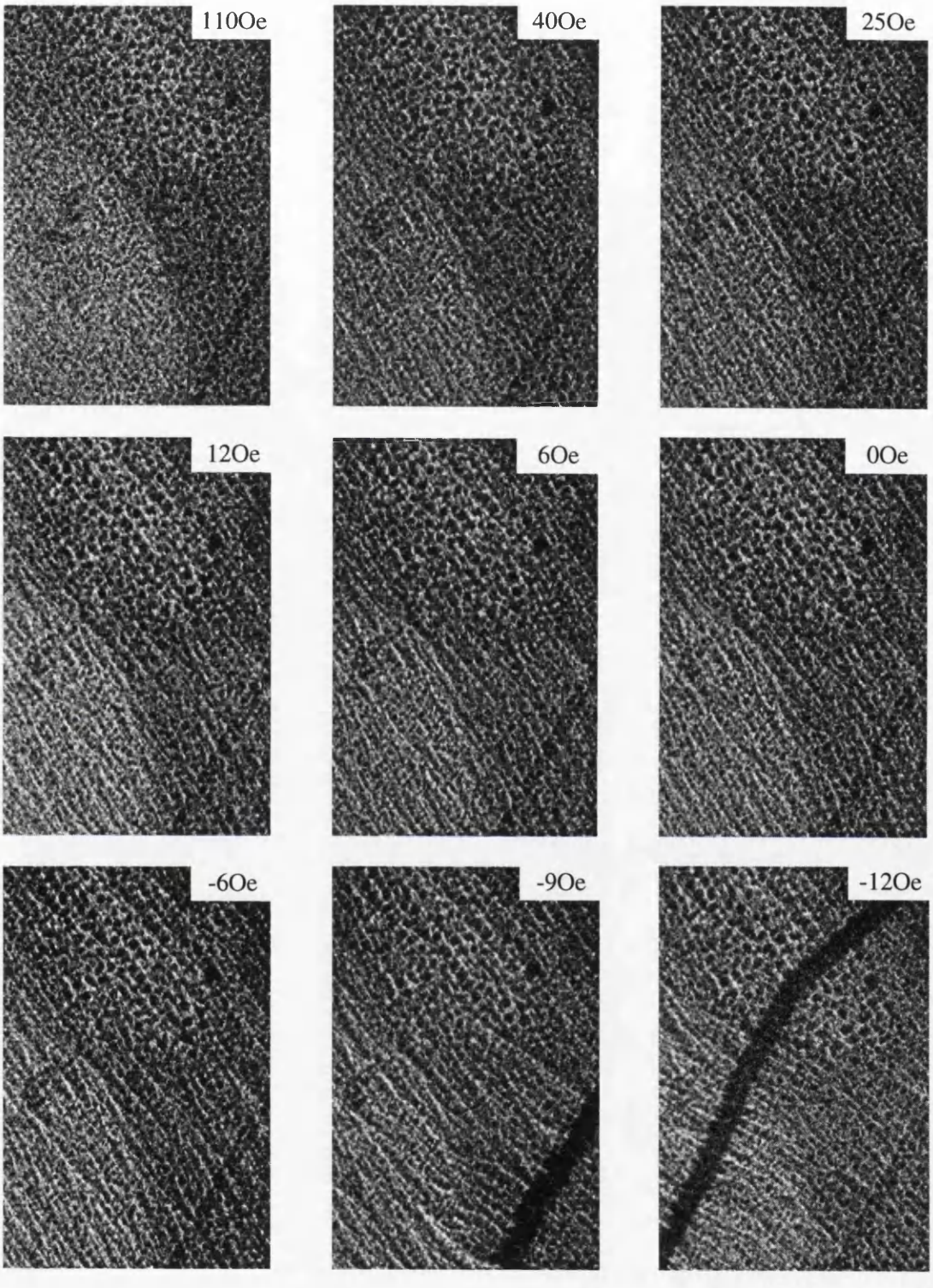

Figure 4.7: Fresnel images of sample A359 with field applied along easy axis. A domain wall can be seen at -9Oe and -12Oe.

Field direction:  4μm: 

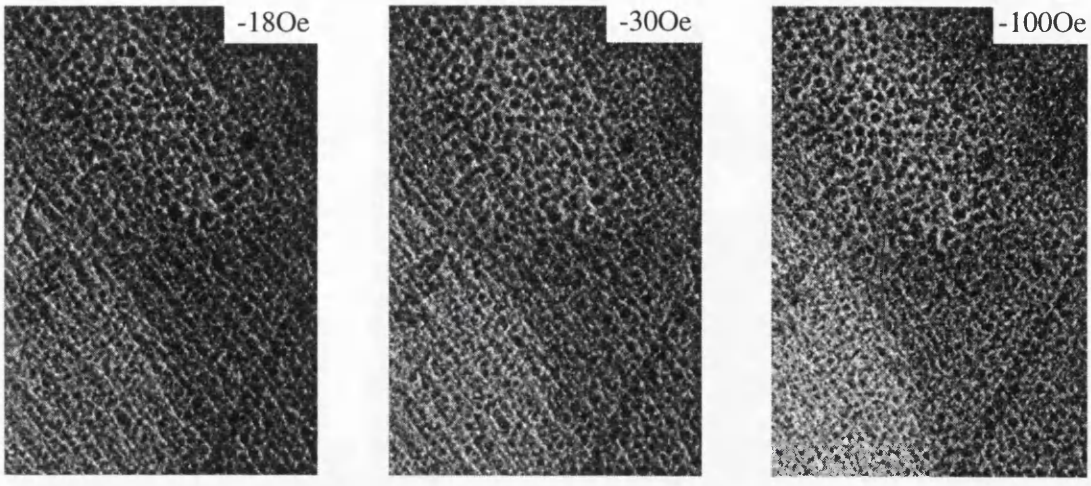

Figure 4.7(cont.): Fresnel images of sample A359 with field applied along easy axis.

Field direction:  4μm: 

When a field applied parallel to the hard axis was reduced, ripple contrast again increased but the ripple also began to rotate. The images (figure 4.8) show that in different areas of the film rotation of the magnetisation ripple occurred in different senses leading to the formation of a number of low angle domain walls. As the field passed through zero and increased in the negative sense the wall angle increased until the ripple was perpendicular to the walls and, indeed, to the initial direction of the ripple. Further increase in negative field gave rise to little wall motion but there was a gradual decrease in wall angle with ripple eventually returning to lie parallel to its original direction. Figure 4.9 shows a corresponding series of low angle diffraction patterns. Initially a single near-circular spot was seen but as the field was reduced this broadened into an arc. The arc extended as the field changed sign with a notable increase in electron intensity at the extremities of the arc and diminution of intensity at the centre. At a field of ≈-20 Oe, the intensity distribution changed rapidly with a downwardly-directed arc turning to an upwardly-directed arc. As the negative field was increased the intensity towards the centre of the arc also grew whilst the overall arc length shrank until once again a single undispersed spot was observed. It should be noted that the position of the undeflected spot was not reliably known due to slight electronic drifts within the microscope. The results of the imaging and diffraction experiments are clearly consistent. Increase in the intensity of magnetisation ripple is accompanied by increased spreading of the central diffraction spot whilst rotation of magnetisation ripple is associated with rotation of the averaged component of induction orthogonal to the electron beam. Fuller analysis of these results is deferred to the next section.

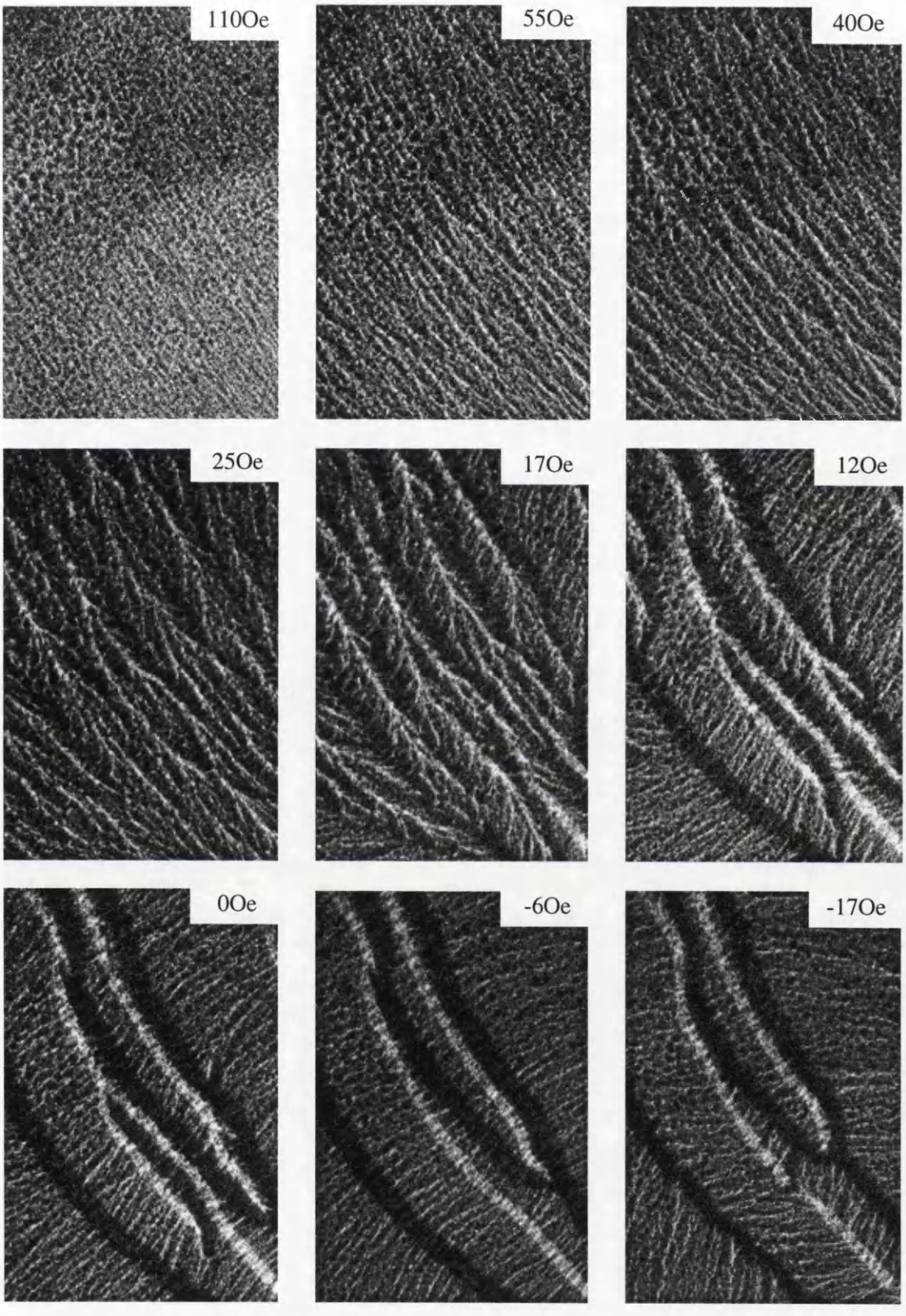

Figure 4.8: Fresnel images of sample A359 with field applied along hard axis. The increase in dispersion can be seen which results in the formation of low angle domain walls at 12Oe.

Field direction:  4μm: 

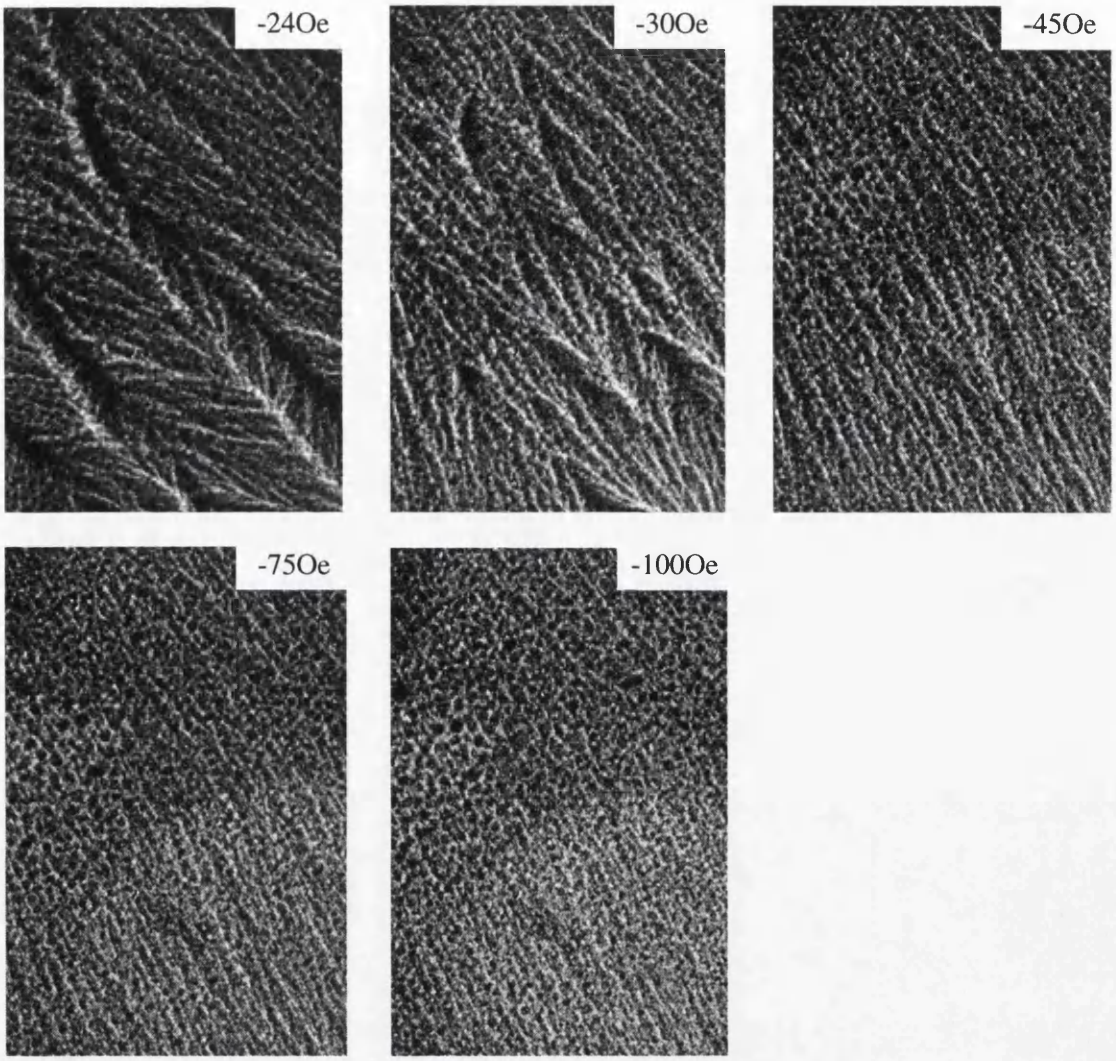

Figure 4.8(cont.): Fresnel images of sample A359 with field applied along hard axis. The decrease of the domain wall contrast as the magnetisation rotates round to the field direction can be seen from -24Oe onwards.

Field direction: 

4μm: 

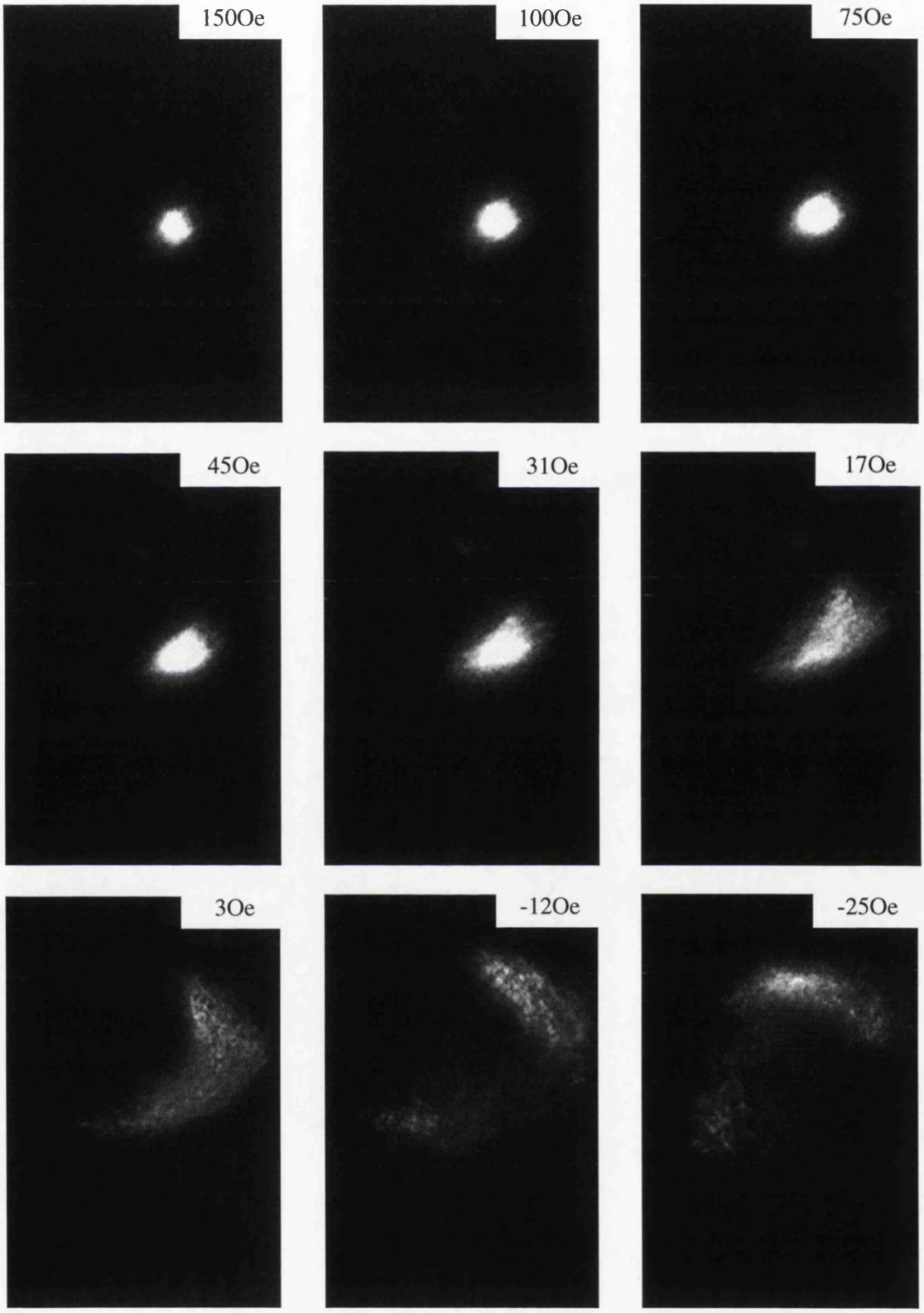

Figure 4.9: Low angle diffraction patterns of sample A359 with field applied along hard axis. The increase in dispersion of the spot can be seen up to 3Oe, where the spot splits as the magnetisation rotates round in two different senses.

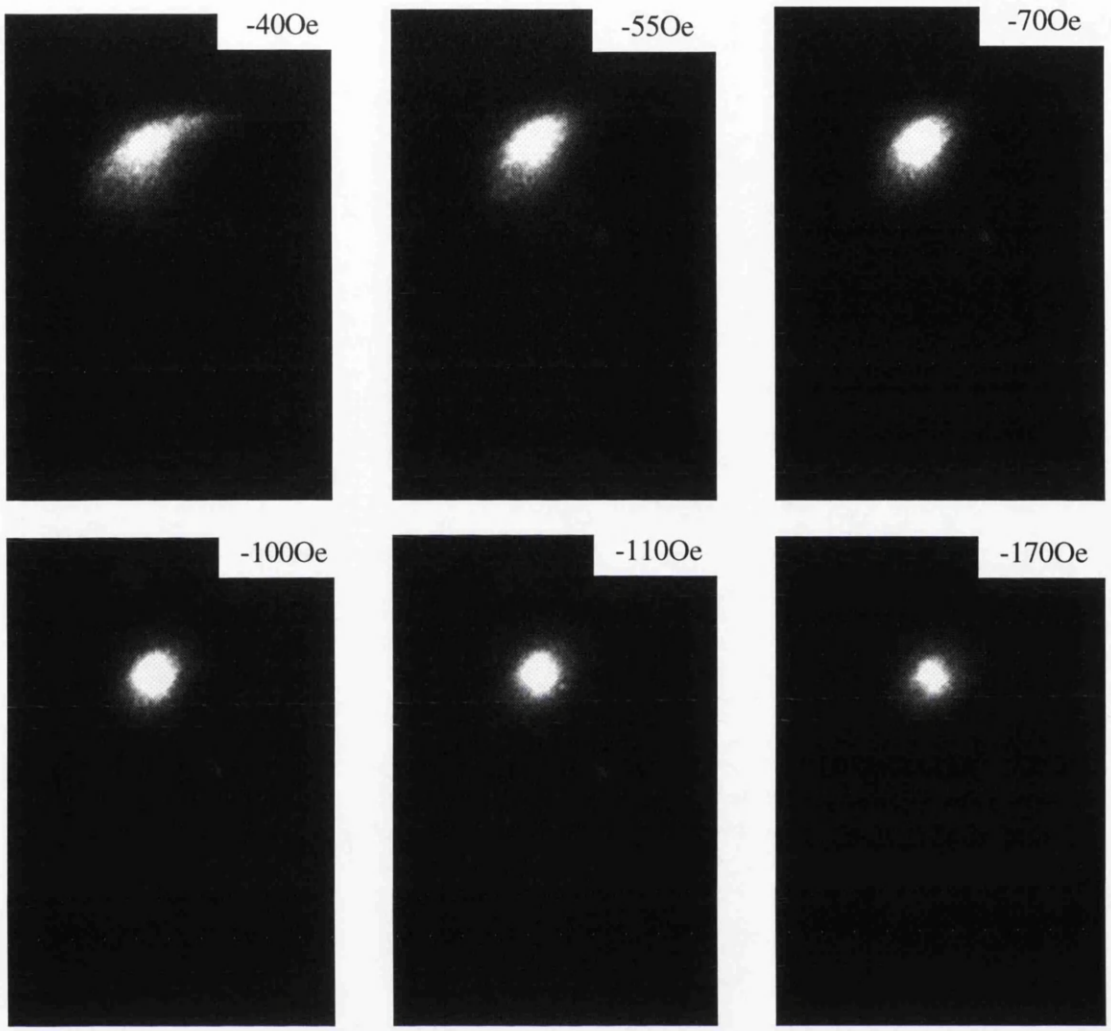

Figure 4.9(cont.): Low angle diffraction patterns of sample A359 with field applied along hard axis. The dispersion of the spot decreases until the average magnetisation is aligned with the field at -170Oe.

Figures 4.10 and 4.13 show Fresnel sequences for sample A358. With the field applied parallel to the easy axis, a wall passed through the sample very rapidly at a field close to -16 Oe. This was not captured on the CCD camera although it could be seen on the microscope viewing screen and is apparent in the video sequences. It left behind it a section of 360° wall (first observed in the image recorded in a field of -17 Oe) which decreased in length as the field became increasingly negative and eventually disappeared (in this sequence) at a field of ≈-105 Oe. DPC images (figure 4.11) show more clearly the scale of the magnetisation ripple and how it intensified up to the point where the rapid switch occurred. That there was a substantial change in the induction component parallel to the applied field direction is apparent from the change in average signal level in the appropriate images before and after the wall swept through. Confirmation that the "residual" wall left behind is a 360° wall is also obtained by noting the similarity of the signal levels on either side of it in the DPC images. The low angle diffraction sequence (figure 4.12) shows that as the field is reduced the undispersed spot steadily broadened into an arc. On one occasion I was fortunate to catch the sample in a partly reversed state and here it is possible to discern intensity lying over a substantial fraction of the circumference of an approximate circle. The regions of highest intensity were diametrically opposed and perpendicular to the applied field direction. Recalling that electron deflections due to the Lorentz force are orthogonal to the induction direction, this observation is as expected and is consistent with the DPC images. With minimal increase in negative field a single arc, now curving downwards rather than upwards, resulted.

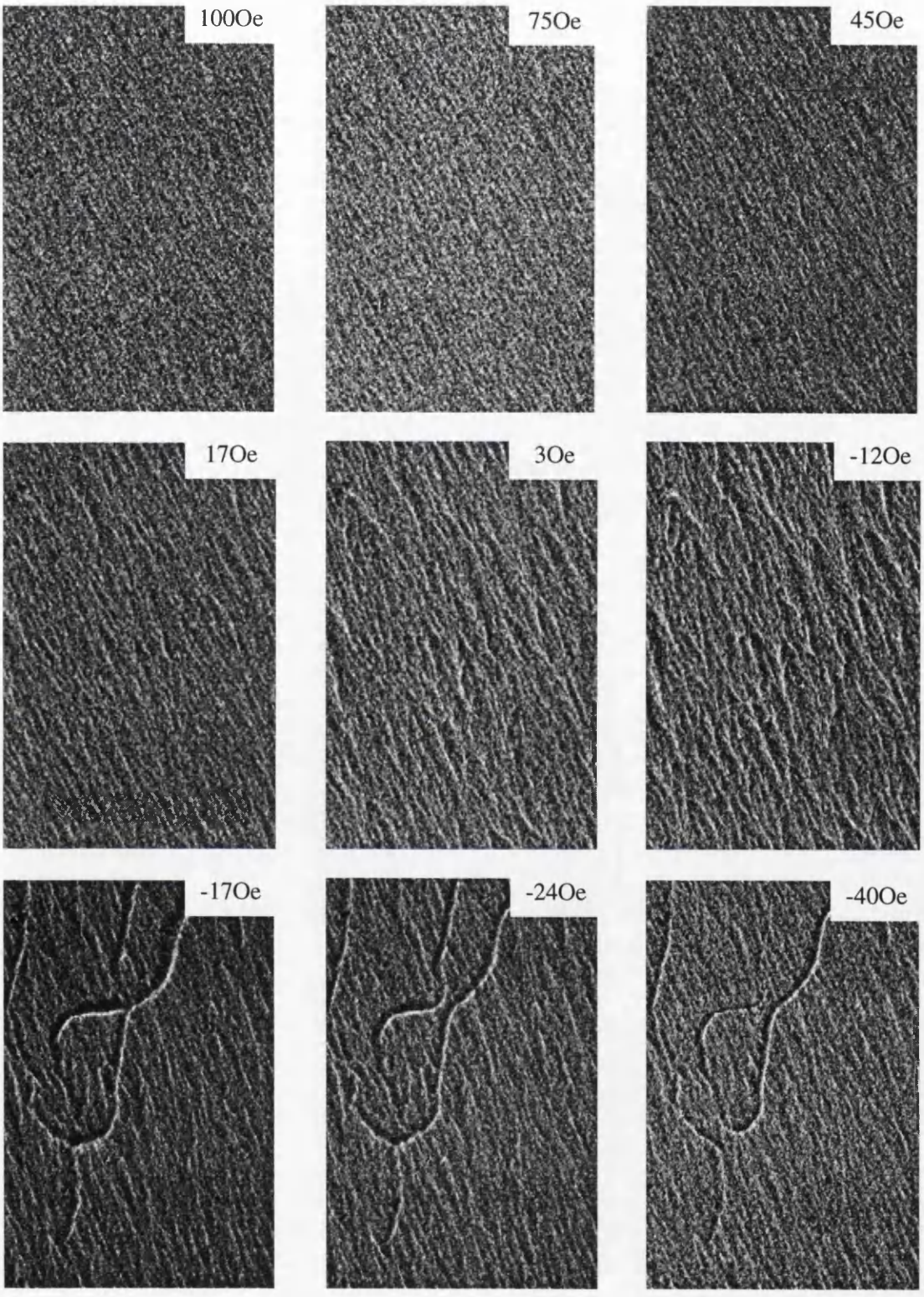

Figure 4.10: Fresnel images of sample A358 with field applied along easy axis. A 360^0 wall is formed between -12 and -17Oe as an unseen domain wall sweeps through the sample.

Field direction:  4μm: 

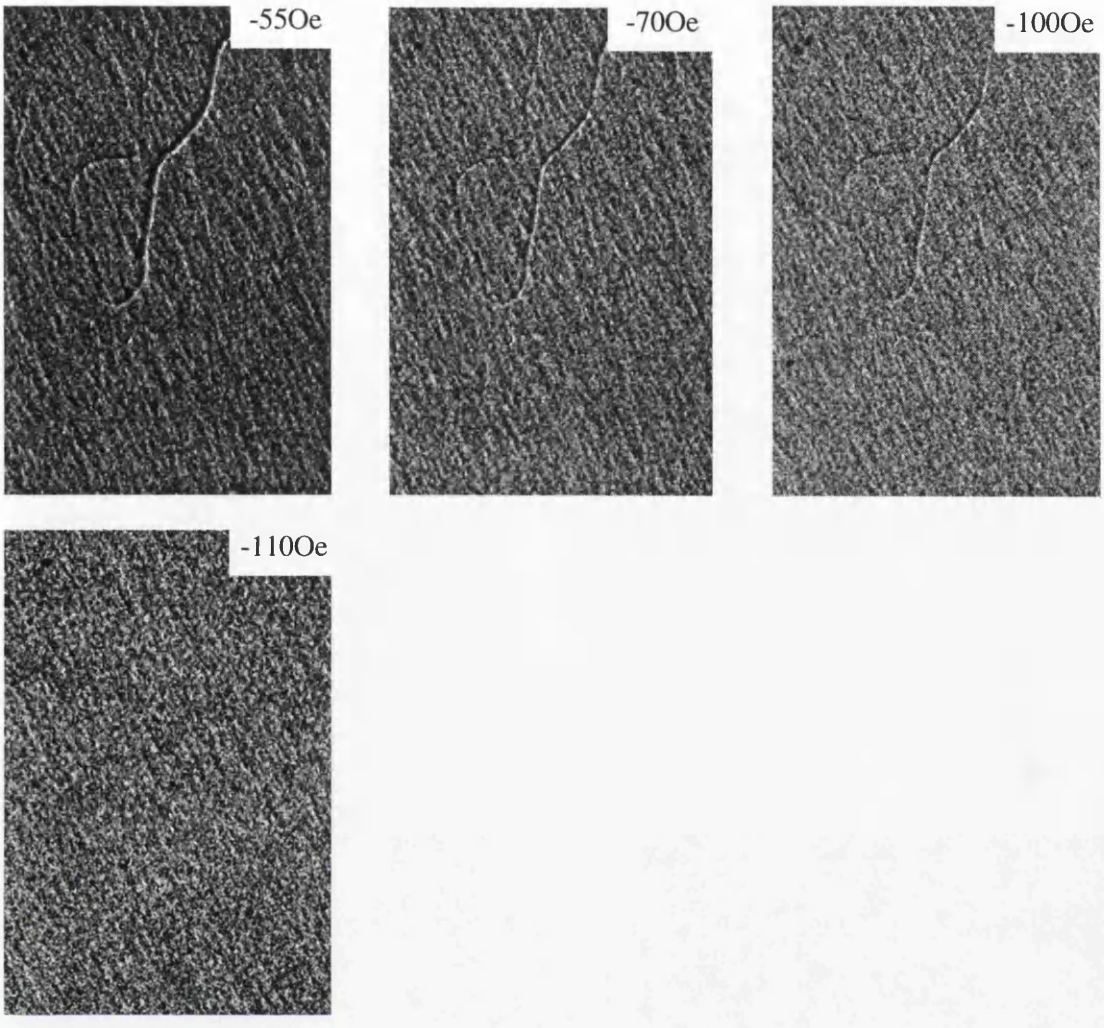

Figure 4.10(cont.): Fresnel images of sample A358 with field applied along easy axis. The 360^0 wall decreases in contrast as it shrinks in the applied field, and eventually disappears from view at -110Oe.

Field direction:  4μm:

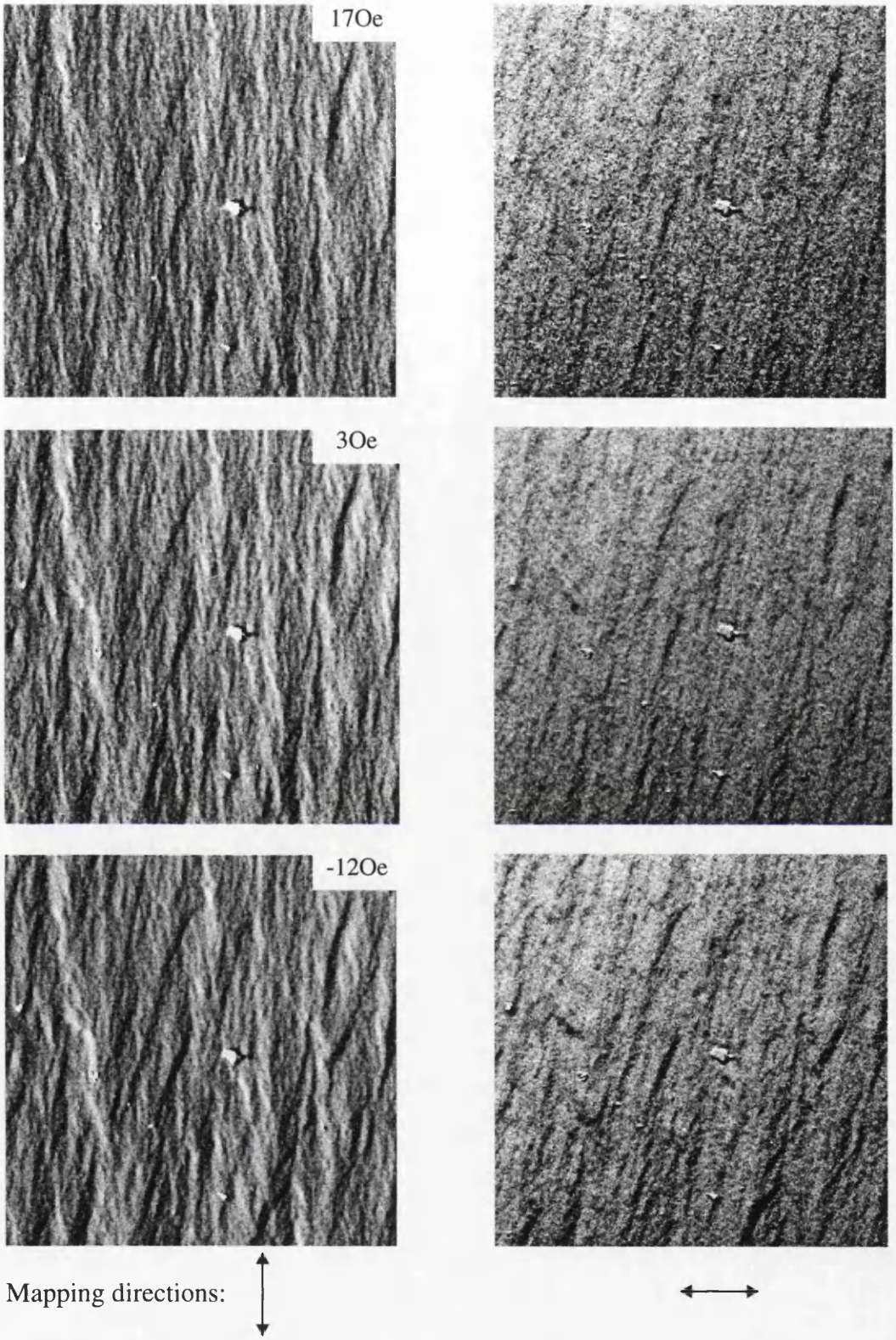

Figure 4.11: DPC images of sample A358 with field applied along easy axis. The increase in dispersion as the switching field is approached can be seen.

field direction: ⟷ 3.5μm: ⟷

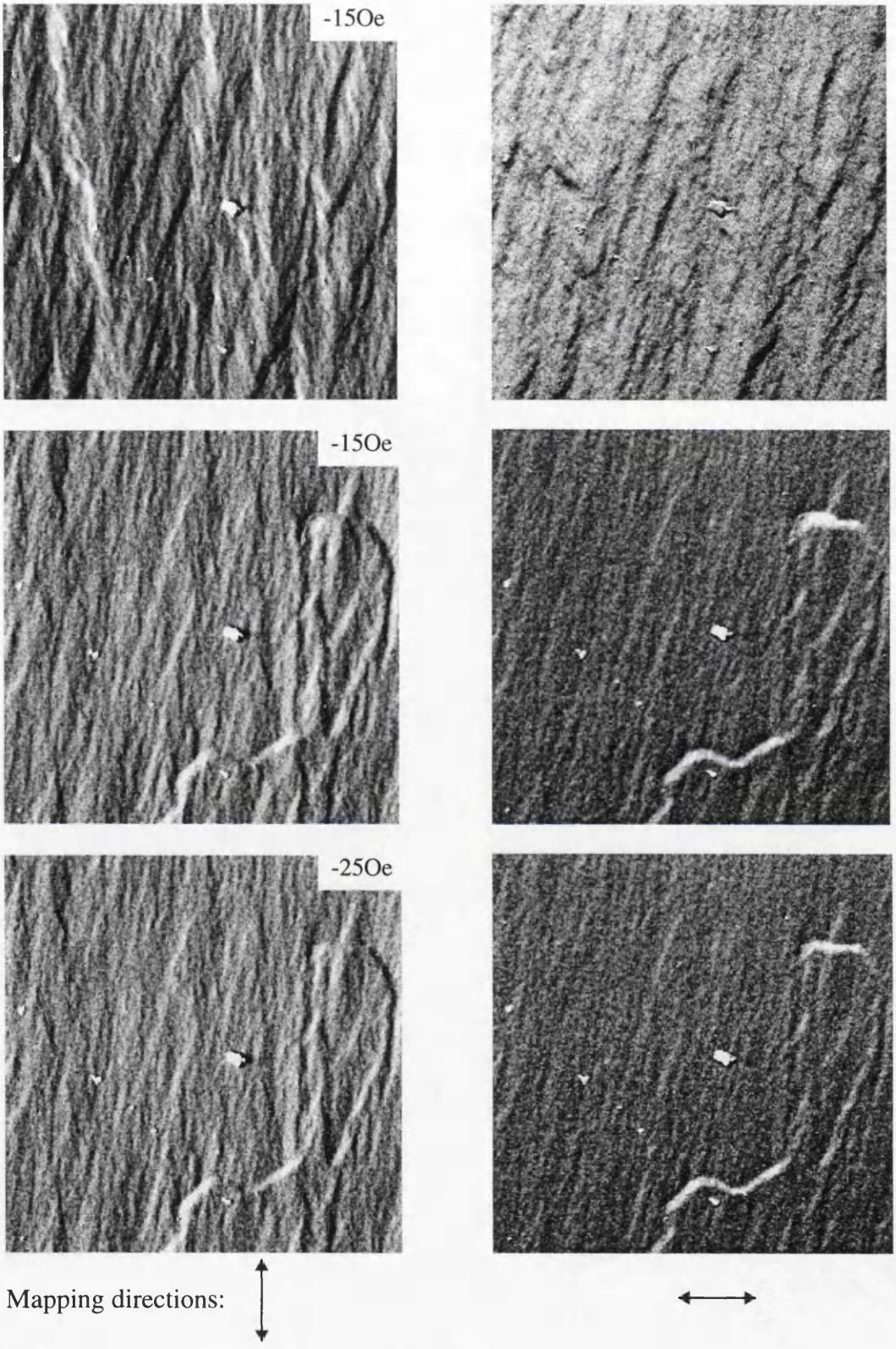

4.11(cont.): DPC images of sample A358 with field applied along easy axis. Switching occurs at -15Oe. This can be seen by the change in brightness of the right hand image and the formation of a 360^0 wall

field direction: ⟷ 3.5μm: ⟷

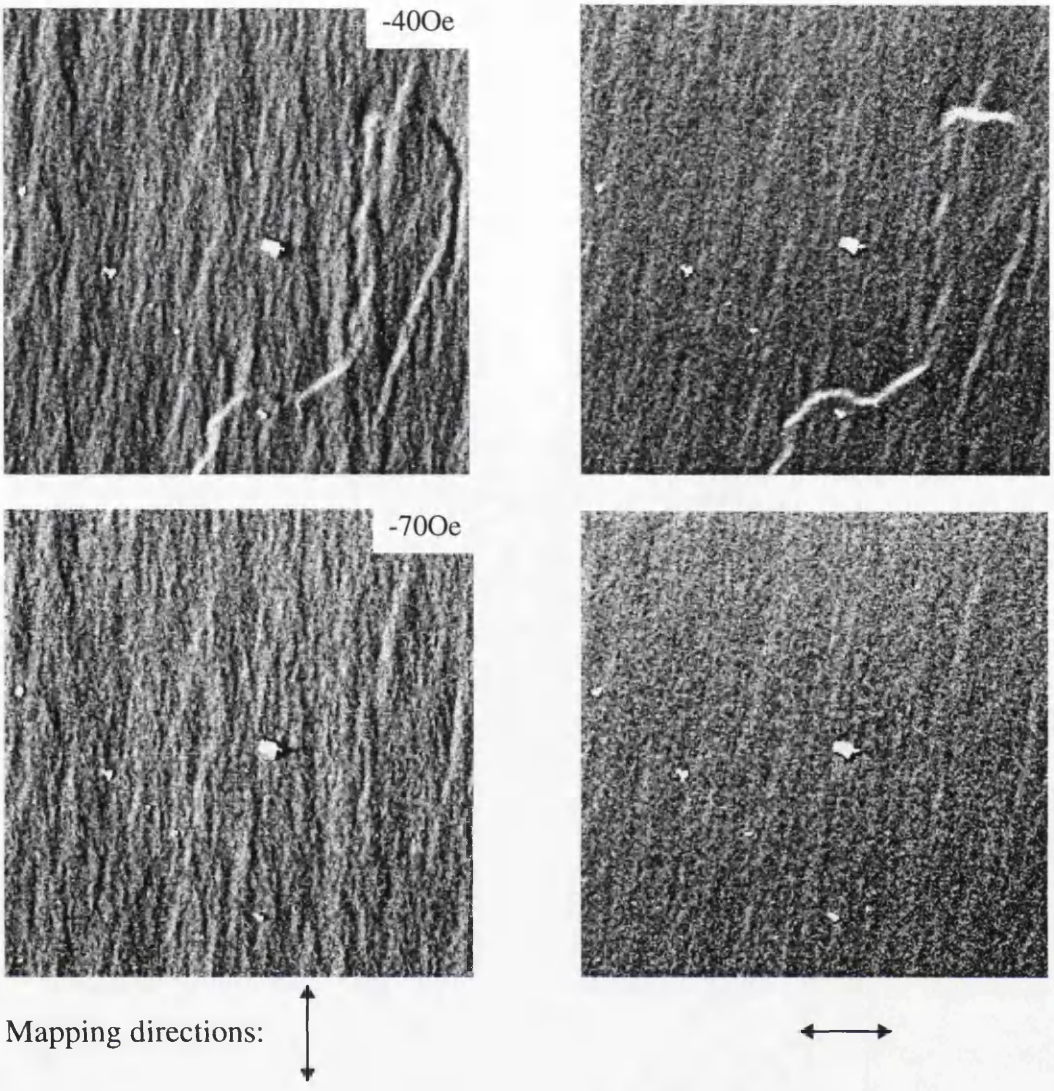

Figure 4.11(cont.): DPC images of sample A358 with field applied along easy axis. The 360^0 wall disappears from view between -40 and -70Oe.

field direction: ⟷ 3.5μm: ⟷

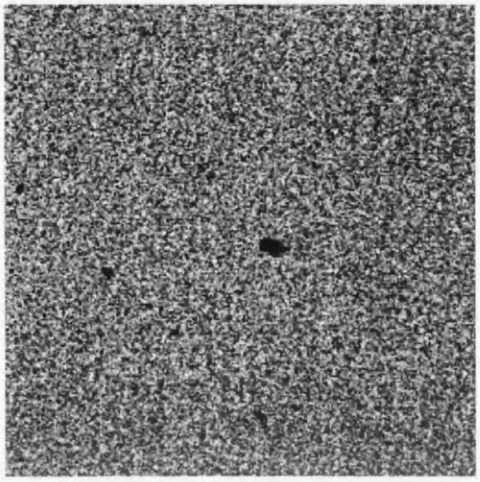

Bright field image of same area at same scale

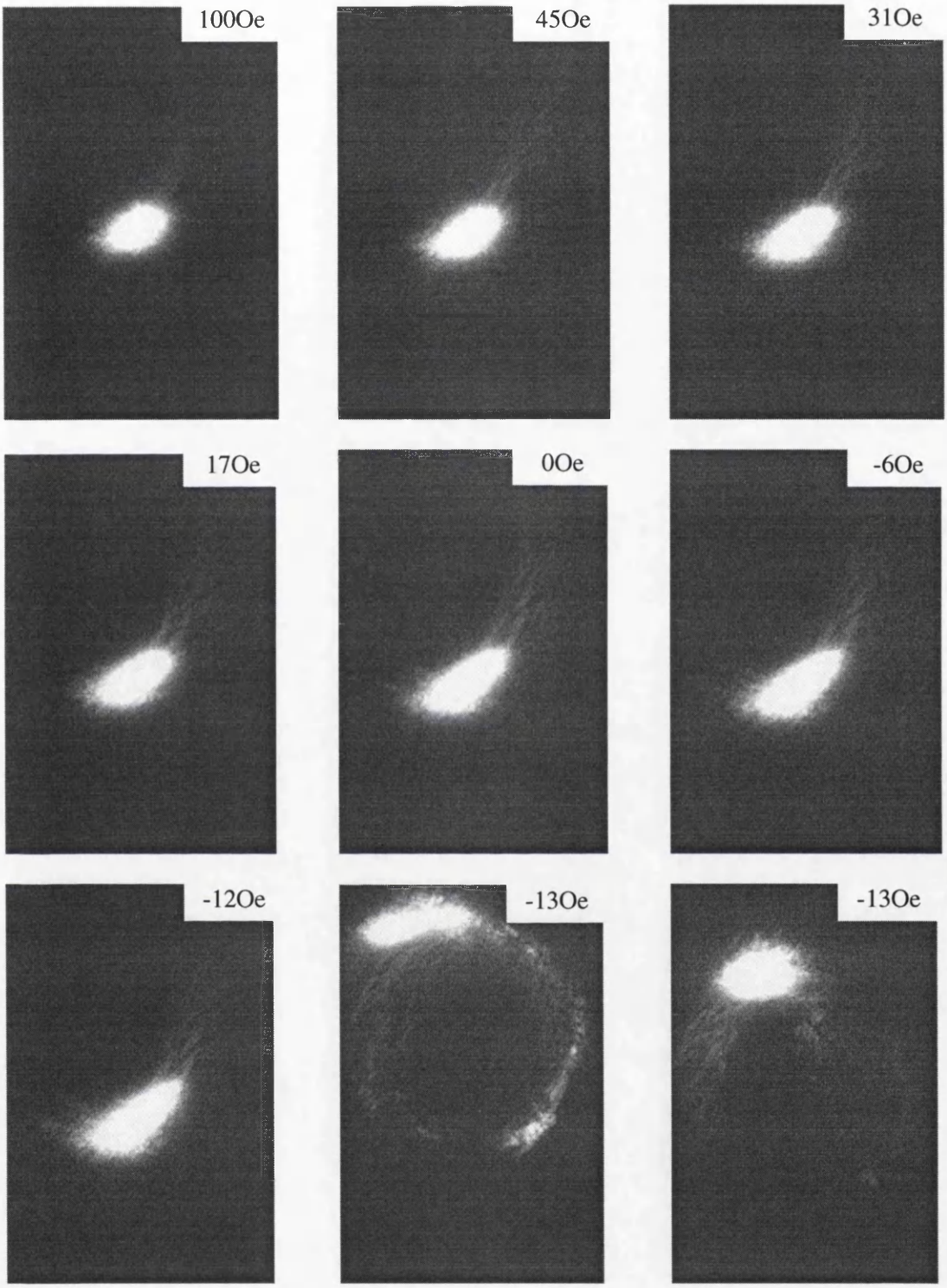

Figure 4.12: Low angle diffraction patterns of sample A358 with field applied along easy axis. The increase in dispersion of the spot can be seen up until -12Oe. The magnetisation reverses at -13Oe.

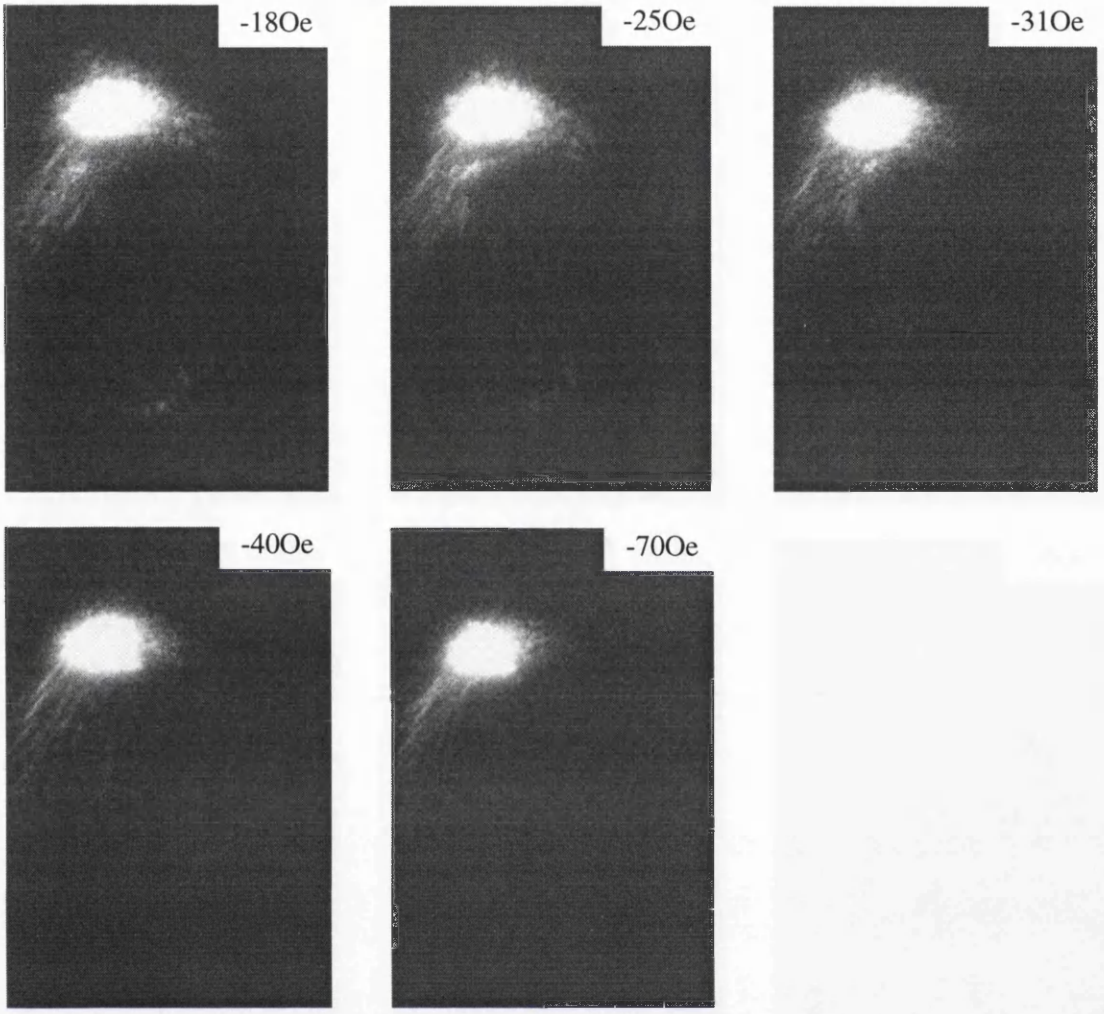

Figure 4.12(cont.): Low angle diffraction patterns of sample A358 with field applied along easy axis. The decrease in dispersion of the spot can be seen as the average magnetisation direction aligns with the field as the field increases.

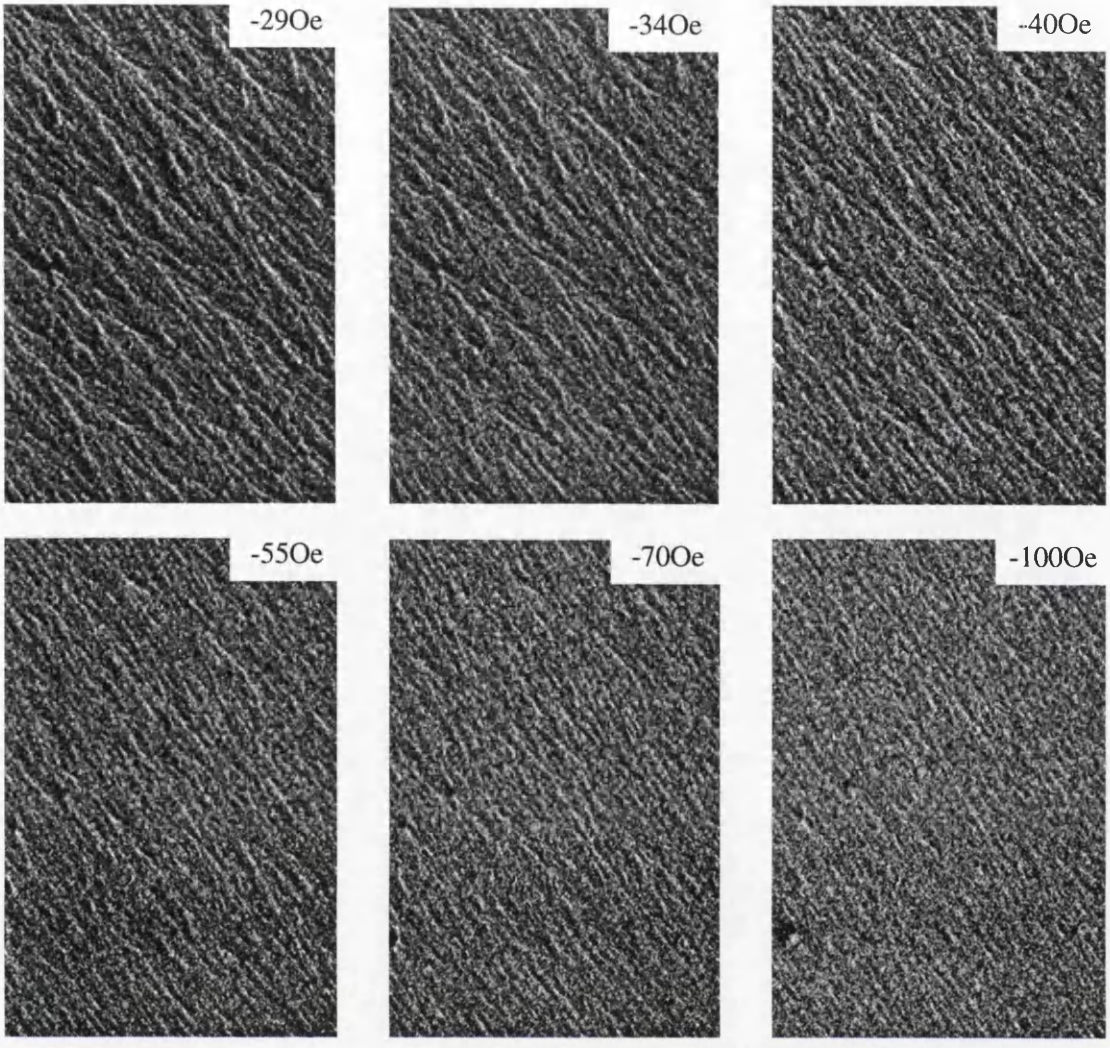

Figure 4.13(cont.): Fresnel images of sample A358 with field applied along hard axis. The magnetisation is aligned with the field but the dispersion decreases as the magnetisation of the individual crystallites becomes aligned with the field.

Field direction: 

4μm:

Further increase in negative field led to the arc length decreasing to leave an undistorted spot.

When the field was applied parallel to the hard axis (figure 4.13) magnetisation rotation was observed and dispersion once more increased. At a small negative field a rapid change took place leaving, once again, only magnetisation ripple which rotated until it lay approximately perpendicular to the applied field direction. Thereafter only a gradual decrease in ripple intensity was observed as the applied field became increasingly negative.

Figures 4.14 and 4.15 show Fresnel sequences for sample A337, the former parallel to the easy axis and the latter orthogonal to it. Contrast levels in the images are lower throughout reflecting the reduced total Co content of this sample. With the field lying close to the easy axis, magnetisation ripple intensified and the directionality became much less pronounced as the field was reduced to zero. Thereafter there was a monotonic decrease in ripple intensity whilst directionality, parallel to the original orientation, was re-established. At a field of ≈-34 Oe, when ripple contrast was already very low, domain walls running approximately parallel to the field direction moved through the sample. With the field applied parallel to the hard axis, rotation as well as ripple intensification was observed. As before, under the influence of a negative field, the ripple attained its original orientation and ripple intensity was much reduced when domain walls again appeared. In this instance the mean wall direction was approximately perpendicular to the applied field and the walls were present over only a small field range close to -70 Oe. A

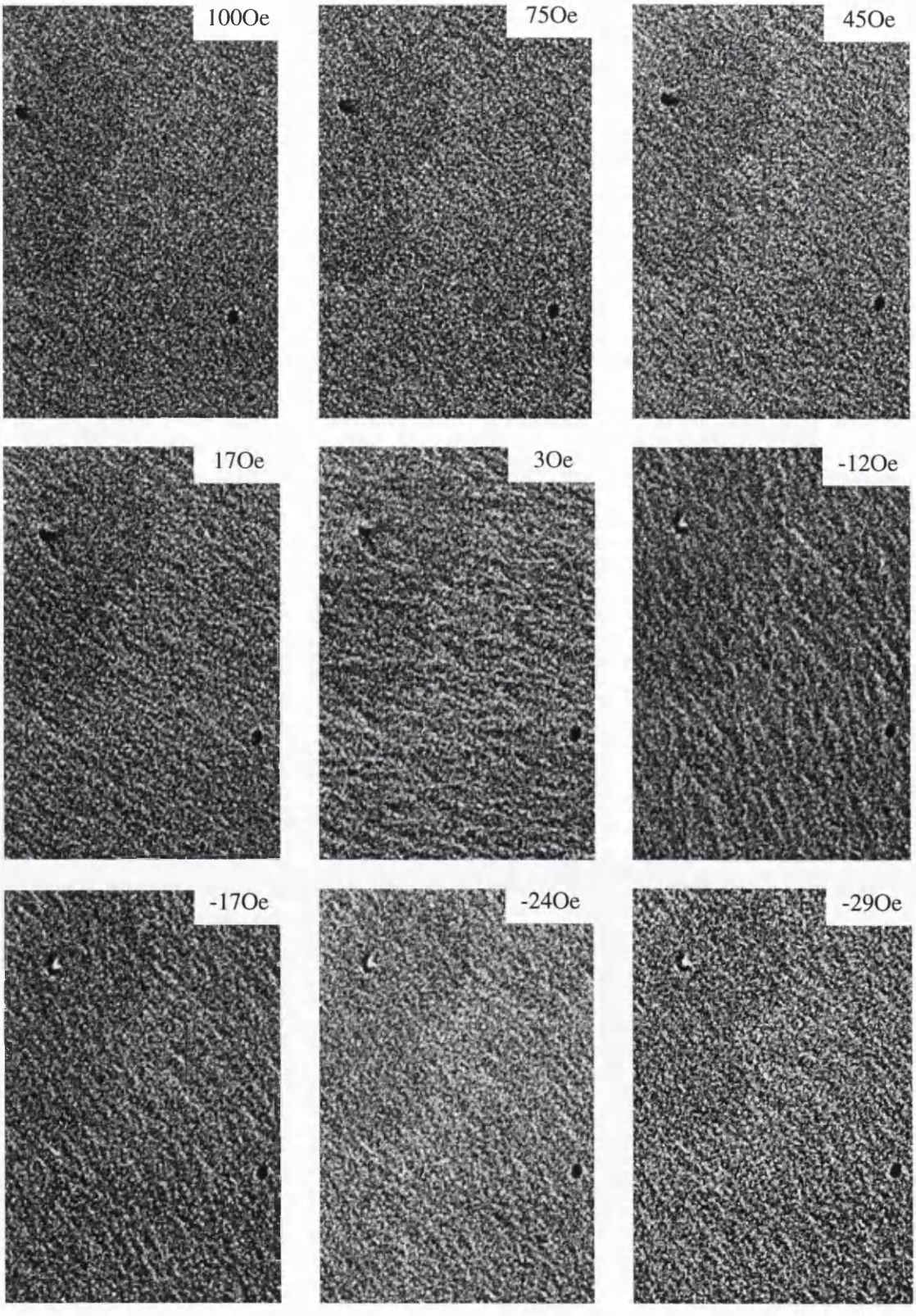

Figure 4.14: Fresnel images of sample A337 with field applied along easy axis. Magnetisation rotation can be seen between 45Oe and -17Oe.

Field direction: 

4μm: 

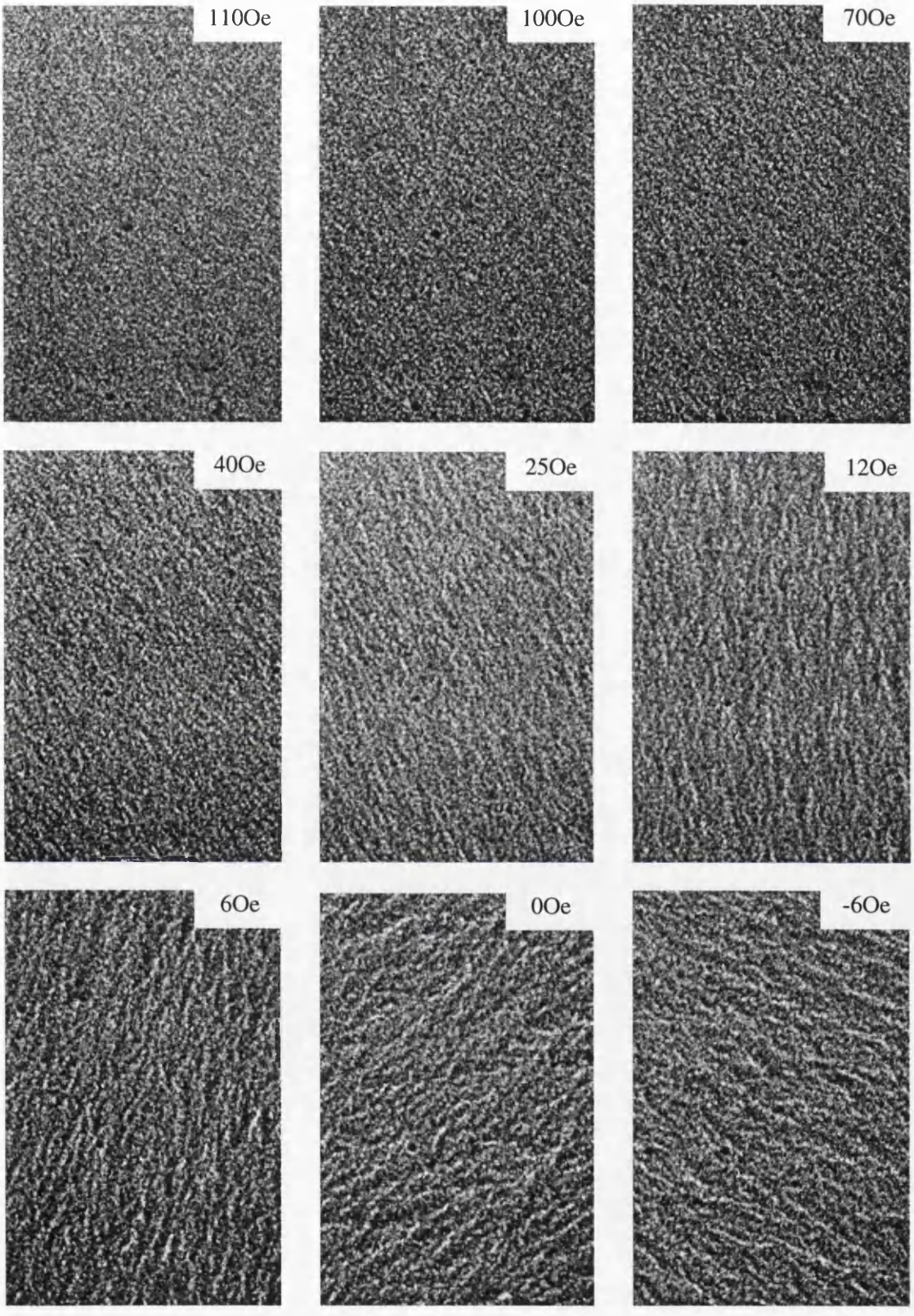

Figure 4.15: Fresnel images of sample A337 with field applied along hard axis. Magnetisation rotation can be seen from 40Oe onwards.

Field direction:  4μm: 

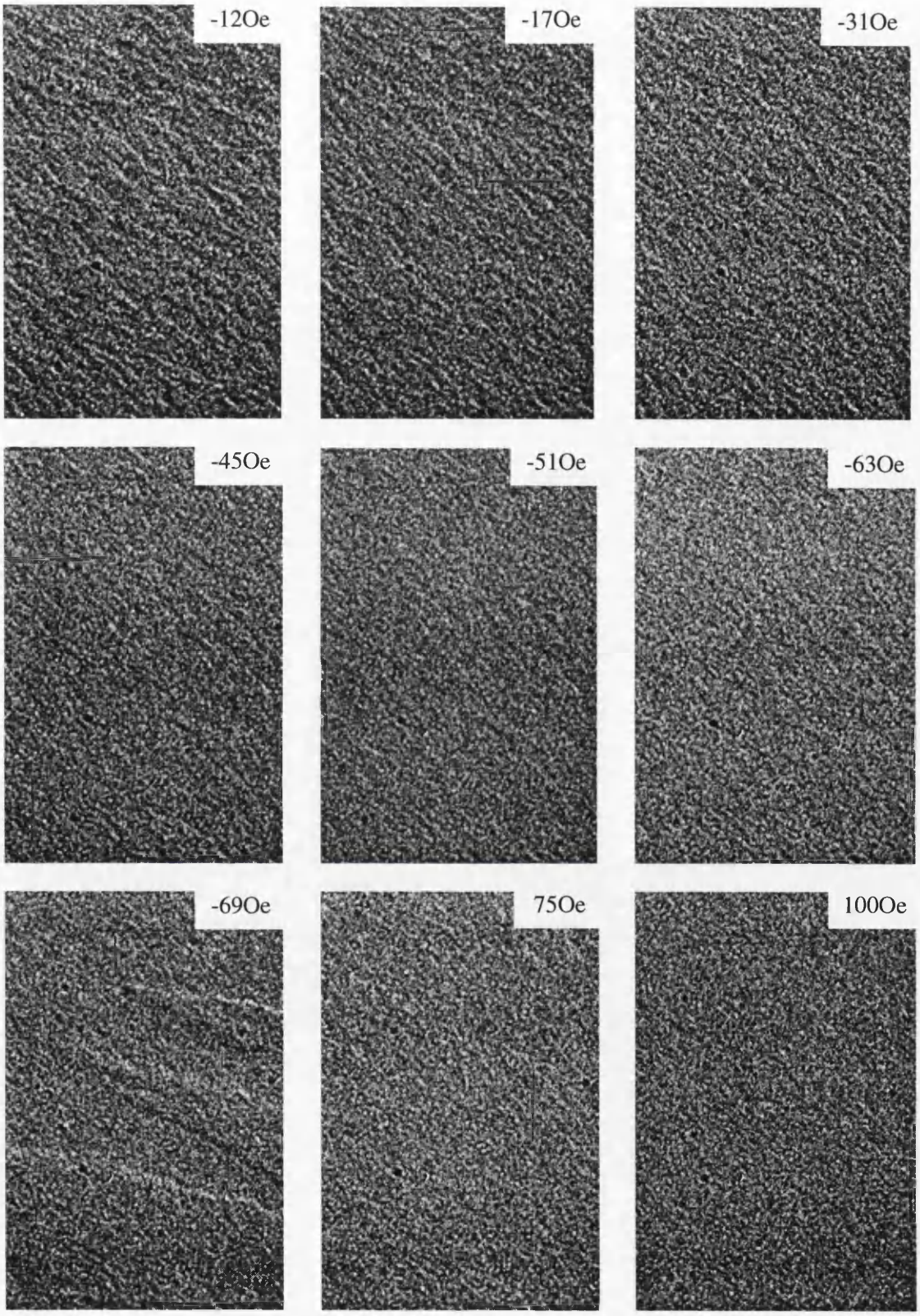

Figure 4.15(cont.): Fresnel images of sample A337 with field applied along hard axis. There is no magnetisation rotation and domain walls appear at -69Oe.

Field direction: ↗ 4μm: ⟷

low angle diffraction sequence for the hard axis is shown in figure 4.16. The varying orientation of the arc associated with the slightly broadened central diffraction spot attests to the fact that a component of induction does indeed rotate under the influence of the hard axis field. Furthermore the central spot split into two parts when, and only when, the domain walls were present in the specimen. I comment on the magnitude of this splitting later. The results observed for sample A337 differ markedly from the results of any other Co/Cu multilayer with any Cu thickness that I am aware of. It appears that two essentially independent reversal processes take place, presumably at different depths within the multilayer stack. Furthermore the required field for the process involving domain wall motion is substantially higher than that for reversal by magnetisation rotation. Again this is not expected a priori and seems most likely to be associated with properties of some layers within the stack differing markedly from others.

4.4 Analysis of magnetisation sequences

The analysis of the magnetisation sequences was performed by J.N.Chapman, P.Aitchison and myself.

Much of what is happening can be understood by considering an energy function of the form shown in equation 4.1.

$$\varepsilon = -\mu_o M H (t_1 \cos\theta_1 + t_2 \cos\theta_2) - J \cos(\theta_1 + \theta_2) + K (t_1 \sin^2\theta_1 + t_2 \sin^2\theta_2) \qquad [4.1]$$

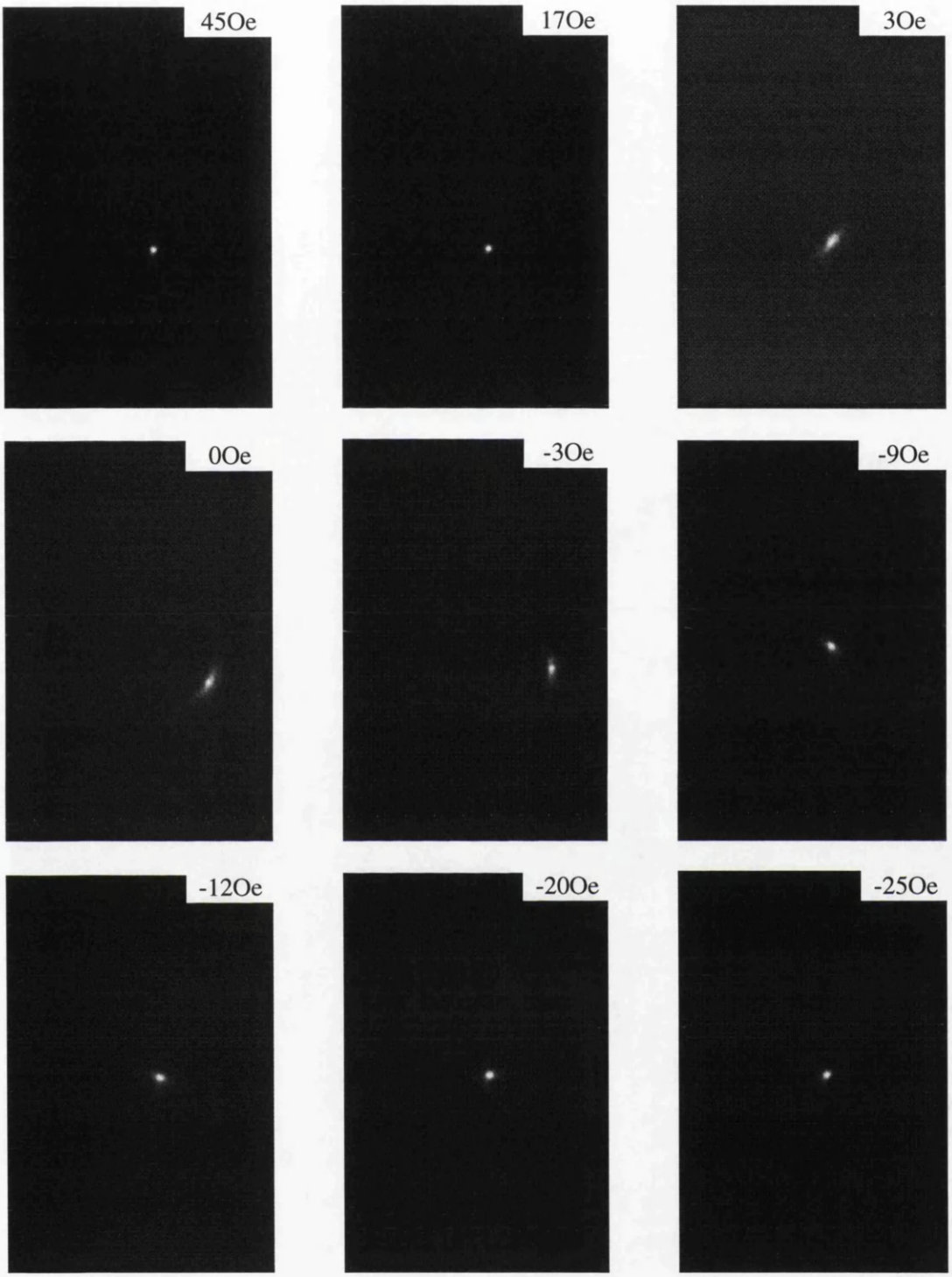

Figure 4.16: Low angle diffraction patterns of sample A337 with field applied along easy axis. Rotation of the dispersed spot can be seen between 3 and -12Oe. By -25Oe the dispersion has decreased.

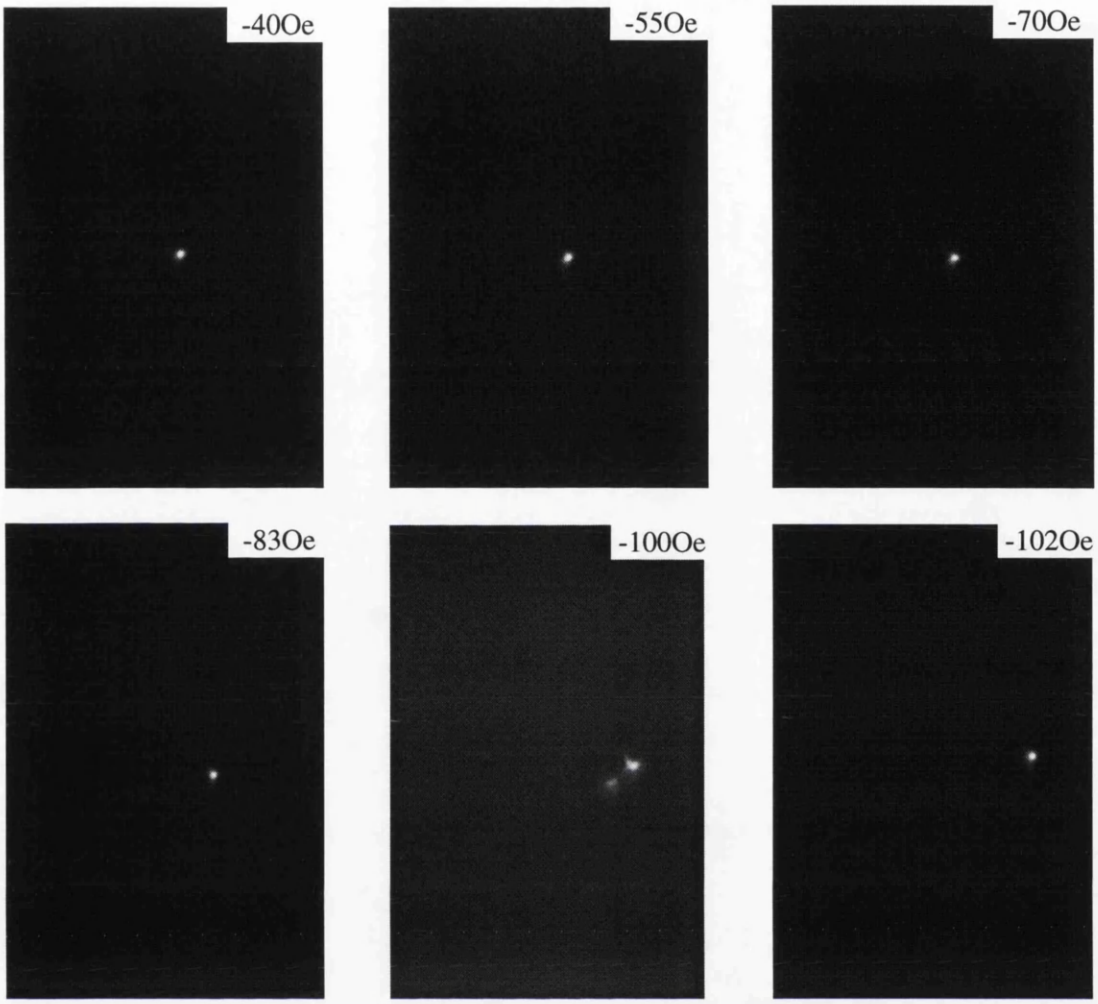

Figure 4.16(cont.): Low angle diffraction patterns of sample A337 with field applied along easy axis. Splitting of the spot as a domain wall moves through the sample can be seen at -100Oe.

ε is the energy per unit area per bilayer where the thicknesses of the alternating layers are t_1 and t_2, μ_o is the permeability of free space, M is the magnetisation, H is the applied field, J is the interlayer coupling and K is the uniaxial anisotropy constant. θ_1 and θ_2 are the angles the magnetisation vectors in each layer make with the applied field direction (figure 4.17). It is assumed that the bilayer stack is infinite in extent so that the energy per bilayer characterises the whole system; thus this model ignores end effects where the first and last layers are coupled to only one rather than two neighbouring layers. For a system with AF coupling $J < 0$ and we further restrict our attention to cases where the anisotropy axis lies either parallel or orthogonal to the field. For the former case, $K > 0$ and for the latter $K < 0$.

The orientations of the magnetisation vectors in alternate layers at equilibrium can be determined by differentiating equation 4.1 to yield:

$$\partial\varepsilon/\partial\theta_1 = \mu_o M H t_1 \sin\theta_1 + J \sin(\theta_1 + \theta_2) + K t_1 \sin 2\theta_1 = 0 \qquad [4.2]$$

$$\partial\varepsilon/\partial\theta_2 = \mu_o M H t_2 \sin\theta_2 + J \sin(\theta_1 + \theta_2) + K t_2 \sin 2\theta_2 = 0 \qquad [4.3]$$

Whilst it is possible to solve these equations numerically we can learn a lot by studying special cases. We begin by looking at remanent states and take the case where $t_1 = t_2$ (as appropriate for sample A359). Under these conditions equations 4.2 and 4.3 yield $\sin 2\theta_1 = \sin 2\theta_2$, the possible solutions to which are:

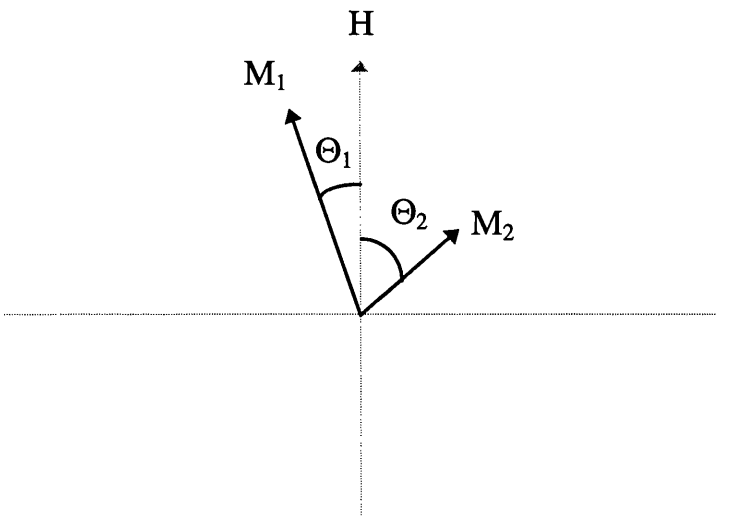

Figure 4.17: Schematic showing magnetisation vectors and angles as used in the model.

$$\theta_2 = \theta_1$$

$$\theta_2 = \pi - \theta_1$$

$$\theta_2 = \pi/2 - \theta_1$$

With further recourse to equation 4.2 or 4.3, it can then be shown that energy density extrema, and the corresponding values for ε, occur as follows:

$\theta_1 = 0$	$\theta_2 = 0$	$\varepsilon = -J$	[4.4]
$\theta_1 = \pi/2$	$\theta_2 = \pi/2$	$\varepsilon = J + 2Kt$	[4.5]
$\theta_1 = \pi$	$\theta_2 = \pi$	$\varepsilon = -J$	[4.6]
$\theta_1 = 0$	$\theta_2 = \pi$	$\varepsilon = J$	[4.7]
$\theta_1 = \pi$	$\theta_2 = 0$	$\varepsilon = J$	[4.8]
$\sin 2\theta_1 = -J/Kt$	$\theta_2 = \pi/2 - \theta_1$	$\varepsilon = Kt$	[4.9]

In many ways the most interesting of these is the last one which only occurs if $|Kt| > |J|$, that is in samples with sufficiently large anisotropy. Furthermore, for such samples and the case where $K < 0$, the state represents a lower energy solution than conditions 4.7 and 4.8. Indeed, as we shall explain shortly we believe we see direct evidence for state 4.9 in the images and low angle diffraction sequences of figures 4.8 and 4.9 respectively. Before this, however, it is worth exploring the bounds over which state 4.9 exists; we refer to these as "weak" and "strong" anisotropy cases.

Given that $|\sin 2\theta_1| \leq 1$, the value that θ_1 assumes in the "weak" anisotropy limit is $3\pi/4$ so that θ_2 takes the value $-\pi/4$. In the "strong" limit, by contrast, the asymptotic values for θ_1 and θ_2 are $\pi/2$ and 0 respectively. These two cases are represented schematically in figure 4.18. Also shown in figure 4.18 is the resultant magnetisation vector, which is what determines the Lorentz deflection angle, and we note that equivalent minima exist on either side of the magnetic field direction. Thus if on removal of the magnetic field the magnetisation in some parts of the sample rotated clockwise and in other parts counterclockwise, we would see two spots in the low angle diffraction pattern, also shown in figure 4.18. Expressed in terms of $(\beta_L)_{max}$ the separation of the spots would be $\sqrt{2}\times$ and $1\times$ for the "weak" and "strong" cases respectively.

Based on the above we now offer an explanation for the observations in figures 4.8 and 4.9. What happens as the field is reduced is shown schematically in figure 4.19. Initially the magnetisation in all layers is parallel to the applied field direction. As the field strength is reduced, the magnetisation vectors in alternate layers begin to separate and to rotate towards the easy axis. Net rotation may be clockwise (figure 4.19a) or counterclockwise (figure 4.19b). Given that individual crystallites have their axes randomly oriented we expect there to be some dispersion of magnetisation so that instead of simply seeing two gradually separating spots in the low angle diffraction patterns, we see small circular arcs. At remanence the spots have their maximum separation. Under the influence of a negative field we would expect a jump in the magnetisation vectors in the two layers for the case of "strong" anisotropy so that the resultant magnetisation vector

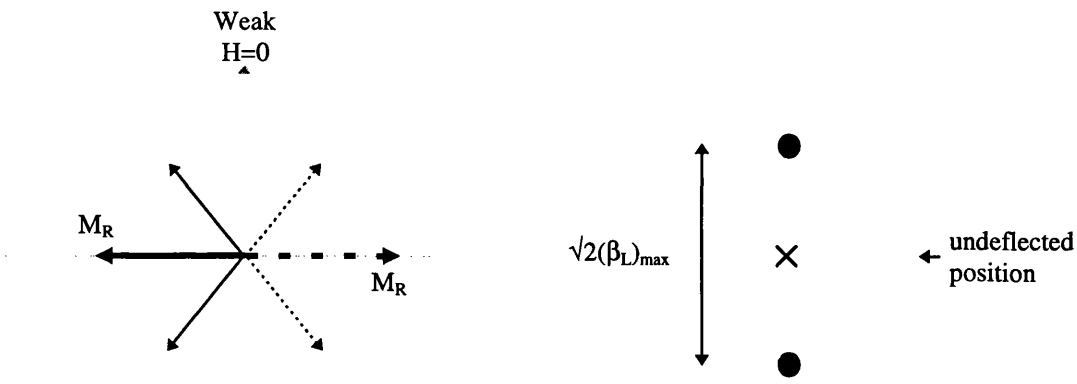

Figure 4.18a:Schematic showing the magnetisation vectors in a zero field for the weak anisotropy case. M_R is the resultant magnetisation vector. Right hand diagram shows the expected spot splitting from this magnetisation configuration.

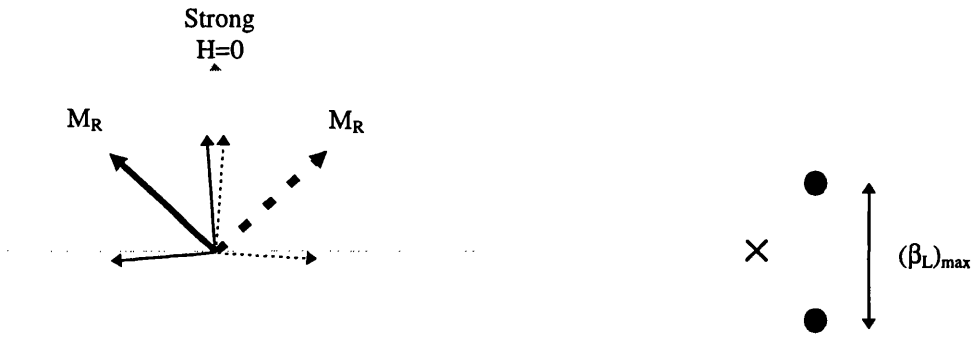

Figure 4.18b: Schematic showing the magnetisation vectors in a zero field for the strong anisotropy case.

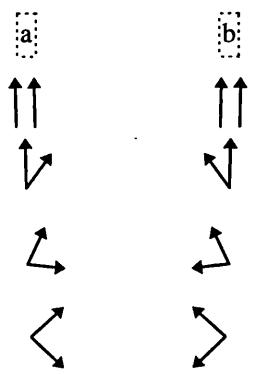

Figure 4.19:Schematic showing the magnetisation vectors on alternate layers for weak anisotropy case as the field is increased.

changed its orientation from $\pi/4$ with respect to the original field direction to $3\pi/4$. For the "weak" anisotropy case no such jump would occur as the resultant is already at $\pi/2$ to the field direction and the rotation of the resultant should continue smoothly.

The experimental observations are broadly in agreement with the model just described. Rotation occurs in different senses in different parts of the film. At a small negative field rather than zero, the result of a small amount of hysteresis, both images and low angle diffraction patterns attest to the resultant magnetisation vector in different regions of the film being anti-parallel. Furthermore, on increasing the field in a negative sense, whilst the diffuse intensity in the arcs in the low angle diffraction pattern changes rapidly, no large jump in resultant magnetisation direction has been observed. This suggests that our films are close to the "weak" anisotropy limit where $|K| \approx |J/t|$. As no anisotropy has been introduced deliberately and as the films themselves show no discernible microstructural texture, it is more surprising that condition 4.9 is fulfilled at all than that the multilayers are towards the "weak" limit.

Based on the above, the predicted separation of the principal spots is $\sqrt{2}\,(\beta_L)_{max}$. Using a saturation induction of 1.7T, appropriate for fcc Co, the predicted separation is 58 μrad compared with an experimental measurement of 65 μrad. Agreement is thus seen to be good. If the saturation induction is underestimated (more reliable measurements on hcp Co yield 1.8T) the agreement would be even closer. Furthermore, our model is for an infinite stack whereas in reality the coupling of the extremal layers of a finite stack is

weaker and these are more likely to align more closely with the preferred easy axis. Hence, the model is likely to underestimate the maximum spot splitting.

For the case where the field is applied parallel to the easy axis ($K > 0$) condition 4.9 represents an energy maximum and is of little interest. For this case there is no incentive for the resultant magnetisation from a pair of layers to move away from the easy axis during the reversal process. Thus the net ripple direction does not change and little of interest is seen in the low angle diffraction pattern.

It must be emphasised that a single unsplit spot in the low angle diffraction pattern does not imply that the magnetisation vectors in all layers in the multilayer stack are parallel. It simply means that the net dispersion is less than the angular divergence of the electron beam. Thus substantial angles can still exist between vectors in alternate layers at the stage where we no longer see magnetisation ripple nor distorted diffraction spots. To see what is happening in this regime through diffraction we would need an absolute reference against which to measure the position of the spot. In a continuous film there is no convenient intrinsic reference and the absolute position of the spot on the detector is of limited use because of small drifts in the microscope electronics.

We now turn our attention to films where $t_1 \neq t_2$ (as appropriate for sample A358). In this instance we expect the response to the applied field to be dominated by the thicker layers (say t_1) and the rapid switch referred to in connection with figures 4.10 to 4.12 seems likely to be associated with a near complete reversal of the magnetisation in the these

layers. With the field applied parallel to the easy axis, the images and diffraction patterns suggest that the behaviour of the magnetisation vector in the two layers as a function of field is as shown schematically in figure 4.20. From the diffraction pattern with the specimen in a partly reversed state, we can determine the magnitude of the angular splitting and hence the change in net induction vector when the switch takes place. The former quantity is found experimentally to be 70 μrad and we denote this by 2 $(\beta_L)_s$. From figure 4.20 we can deduce that:

$$(\beta_L)_s = (3 \cos \theta_1 + \cos \theta_2) (\beta_L)_{max} /4 \qquad [4.10]$$

Using the same values as before to calculate $(\beta_L)_{max}$ and the experimentally determined value for $(\beta_L)_s$ equation 4.10 reduces to:

$$(3 \cos \theta_1 + \cos \theta_2) = 3.4 \qquad [4.11]$$

To proceed further we note that the switch takes place close to zero field and is essentially between two equivalent remanent states. These can be explored through the equilibrium equations 4.2 and 4.3 which for a multilayer with layers of unequal thickness become:

$$\sin 2\theta_2 = \tau \sin 2\theta_1 = \eta \sin (\theta_1 + \theta_2) \qquad [4.12]$$

where $\tau = t_1/t_2$ and $\eta = -J/Kt_2$. For sample A358, $\tau = 3$ and the solution to equations 4.11 and 4.12 yields values of 7.5°, 65° and 0.8 for θ_1, θ_2 and η respectively. From the value of

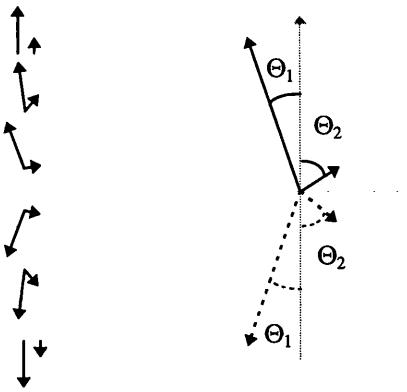

Figure 4.20: Schematic showing the magnetisation vectors and angles in samples with different layer thicknesses.

η we deduce that $|K| \approx 1.25\ |J/t_2|$, a factor approximately 2.5× larger than the "weak" anisotropy limit deduced for specimen A359. As the origin of the anisotropy is unknown we have no reason to assume that the values for the two films should be identical but the fact that similar magnitudes are obtained suggests a satisfactory level of consistency and lends credence to the model.

It is difficult to deduce useful additional information from the hard axis sequence shown in figure 4.13. The rotation of ripple is consistent with the application of a field marginally misaligned from the hard axis so that rotation in a particular sense is favoured for the thicker layers. Indeed, the dominance of the thicker layers in determining the overall behaviour is expected to increase as the magnitude of τ increases.

For sample A337 the magnitude of the central spot splitting observed in the low angle diffraction pattern when walls are present in the sample is 3.4 μrad. This is equivalent to 1.65 nm of fcc Co reversing in direction. If we assume that the moment of Co in the CoCu alloy is reduced simply in proportion to the Co concentration our result is consistent with the reversal of 3 FM coupled layers from the 20 in the multilayer stack.

The modelling of these two systems is still underway. Initial results using MAPLE, however have shown that is is not possible to get a stable set of solutions for the equations using only the energy terms detailed above. While it is still believed that the reversal mechanisms outlined are still valid, attempts are being made to achieve stable solutions of the energy equations by adding a bi-quadratic coupling term to the equation.

Bi-quadratic coupling causes an angle of 90 degrees between the magnetisation vectors in adjacent layers to be favoured and is of the form:

$$j\cos^2(\Theta_1 + \Theta_2) \qquad [4.13]$$

This investigation is still ongoing.

4.5 Conclusions

The reversal of a number of Co/Cu multilayers has been studied using a range of Lorentz microscopy techniques. The combination of techniques has proved extremely powerful and in the most favourable cases a clear picture of the behaviour of the magnetisation distribution in the multilayer stack as a function of applied field strength and orientation has been obtained. The results are particularly encouraging for multilayers with Cu thicknesses appropriate to the first AFM. The simple model we have applied fits the experimental observations well and has allowed us to extract much useful quantitative information. The low angle diffraction patterns in particular have proved a useful source of information. With this technique the central spot of the diffraction pattern is seen to be split or broadened if the net magnetic induction is other than uniform over the illuminated area, and when taken in connection with the Fresnel images, this gives excellent insight into the overall magnetisation process. Calibration of the camera length is important if we are to determine absolute deflection angles. This was achieved using a replica diffraction

grating of known periodicity and experimentally determined deflections are accurate to ±5%.

The magnetisation processes have been described in detail for samples A358 and A359, and these results appear to indicate the presence of an anisotropy. The source of this anisotropy is not clear but possible sources are: introduction during deposition, or a layer which is pinned in that direction during the recording of the MR loops. If the anisotropy results from the deposition conditions, then it is not clear why samples A358, A359 and A337 have an anisotropy, whilst samples A332 and A333 do not. This is especially confusing when it is considered that the antiferromagnetic coupling for these two samples should be less since their copper layer thicknesses correspond to the second AFM maxima, whereas, in chapter one it can be seen that the coupling will be stronger at the first antiferromagnetic maxima. The reduced coupling should make the effect of any anisotropy more pronounced. The presence of an anisotropy does also present the problem that it is not known whether the GMR loops were recorded along the easy or hard axes, or whether the recording of the GMR loops exposes the field to a high enough field to define the hard axis as seen in the microscope. This could have a significant effect on the hysteresis and the sensitivity of the response.

From the GMR loops provided, sample A337 (the alloy sample) appears to have the best GMR properties for the proposed applications, with little hysteresis and high sensitivity. This sample does however have the least well understood magnetic properties, with two distinct processes occuring: magnetisation rotation in some layers, and domain wall

motion in the others. It must be noted that it was possible during the magnetisation experiment to reduce the field once a domain wall had appeared and hence get both domains and magnetisation rotation processes visible at the same time. These two processes appeared to be completely independent. More work will have to be done on this sample before it is completely understood.

References

[1] S.S.P.Parkin, N.More and K.P.Roche, Phys. Rev. Lett. **64** (1990) 2304.

[2] S.S.P.Parkin, Z.G.Li and D.J.Smith, Appl. Phys. Lett. **58** (1991) 2710.

[3] D.H.Mosca, F.Petroff, A.Fert, P.A.Schroeder, W.P.Pratt and R.Laloee, J.Magn. Magn. Mater. **94** (1991) L1.

[4] S.S.P.Parkin, R.Bhadra and K.P.Roche, Phys. Rev. Lett. **66** (1991) 2152.

[5] D.J.Kubinski and H.Holloway, J.Appl. Phys. **79** (1996) 7395.

[6] D.J.Kubinski and H.Holloway, J.Appl. Phys. **79** (1996) 1661.

[7] D.J.Kubinski and H.Holloway, J. Magn. Magn. Mater. **165** (1997) 104.

[8] D.J.Kubinski and H.Holloway, J.Appl. Phys. **82** (1997) 322.

[9] E.Jedryka, M.Wojcik, S.Nadolski, D.J.Kubinski, H.Holloway and P.Panissod, accepted for publication 1997.

[10] P.R.Aitchison, J.N.Chapman, D.B.Jardine and J.E.Evetts, J. Appl. Phys. **81** (1997) 3775.

Chapter 5

Magnetisation processes in magneto optic media

5.0 Introduction

Magneto optic (MO) recording has been described in chapter one. In this chapter I present and discuss the results of characterisation experiments carried out on proposed new magneto optic media. The experimental procedures have been previously detailed in chapters two and three.

Before we can evaluate the materials described in this chapter we need to know what makes good magneto optic media. There are three main requirements for good magneto optic media:

i: **Large perpendicular anisotropy and coercivity.**

The shape effect calculations detailed in chapter three show that in thin film media the magnetisation will lie in the plane of the film if there are no further forces to cause the magnetisation to lie perpendicular to the plane of the film. For magneto optic media the perpendicular magnetic anisotropy ($K_\perp$) must be larger than the shape anisotropy ($\frac{1}{2}\mu_0 M_s^2$) to achieve the perpendicular magnetisation which is required for magneto optic recording. Furthermore the perpendicular M vs. H loop must show a large coercivity at room temperature, so that written marks are stable, and 100% remanence so that the marks do not degrade in a zero field. It should also be noticed

that the H_c should decrease rapidly with increasing temperature to allow for high writing sensitivity and sharp mark boundaries.

ii: **Large polar Kerr rotation.**

A large polar Kerr rotation (Θ_k) is a basic demand for a sufficient readout signal. Indeed the figure of merit that is quoted for magneto optic media is related to Θ_k by:

$$F.O.M.= R(\Theta_k^2+\varepsilon_k^2) \qquad [5.1]$$

where R is the reflectivity of the surface of the media, which should be above 20% for MO recording and ε_k is the ellipticity of the polar Kerr rotation, which is often negligable. The Θ_k for rare earth-transition metal amorphous alloys and cobalt/platinum multilayers is of the order of 0.4° at λ=800nm [13].

iii: **Suitable Curie temperature.**

For a high data writing rate, the thermomagnetic switching temperature should be as low as possible, without being too low, as it takes time to heat up the material. This property is dominated by the Curie temperature (T_c). A low Curie temperature will also allow lower laser powers to be used, which will reduce the degradation of the media and allow more read/erase cycles. The lower thermomagnetic switching temperature will also mean that a laser power which is low enough to cause minimal degradation of the media will be high enough to completely write or erase a mark, giving better mark definition. If the thermomagnetic switching temperature is not low enough to allow this, these two requirements will have to be balanced for best

performance. It should, however, be noted that if the Curie temperature is too low the mark will be degraded at room temperature, giving an unsatisfactory lifespan for the mark.

The materials described in this chapter are two different types of magneto optic media: rare earth-transition metal (RETM) amorphous alloys, and cobalt nickel/platinum (CoNi/Pt) multilayers.

Current commercial magneto optic media are based on RETM thin film alloys such as TbFeCo and GdFeCo since they fulfil all the requirements for a successful magneto optic media. These types of media were first recognised as magneto optic media in 1973 [1]. Since they are amorphous they have no crystallite boundaries, which helps to increase the carrier to noise ratio (CNR). However they do suffer from a poor chemical stability, which necessitates the application of a protective coating, increasing the expense of the material, and a relatively low Kerr rotation at shorter wavelengths (≈400nm). The materials described in this chapter compare a film which has been doped with a light rare earth element in an attempt to increase the Kerr rotation at shorter wavelengths and one which has not.

Co/Pt type multilayers have been investigated as suitable magneto optic media since perpendicular magnetic anisotropy was discovered in Co/Pt and Co/Pd multilayers in 1985 [2][3]. Their large polar Kerr rotations at shorter wavelengths [4][5], superior chemical stability and reflectivity has increased their interest as a future magneto optic media. They do, however, suffer from a high Curie temperature. The media

described in this chapter have had nickel added to the magnetic layer in an attempt to reduce the Curie temperature.

5.1 The magnetisation processes in CoNi/Pt multilayers

Co/Pt multilayers are attractive as future magneto optic recording media for several reasons. The constituent metals are chemically stable, and therefore the whole multilayer is resistant to oxidation and corrosion (unlike RETM alloys). They can be deposited at room temperature either by electron beam evaporation or sputtering. Their high reflectivity means that their figure of merit for magneto optic recording is high enough that their typical carrier to noise ratio is generally higher than current media despite their crystalline nature [6]. Their figure of merit is also still high enough at short wavelengths (≈400nm) to allow magneto optic recording [6]. They do however suffer from a Curie temperature which is too high for practical magneto optic recording (between 300C and 400C). Nickel however can be added to the magnetic layers to reduce the Curie temperature [7][8][9], and much work is ongoing in this area.

Past work on CoNi/Pt and Co/Pt multilayers has shown that the magnetic properties of the system depend very heavily on the exact film parameters. The perpendicular magnetic anisotropy (PMA) arises from the interfaces between the layers, so any parameter which affects these interfaces affects this [10][11][12]. In particular as the magnetic layers are increased in thickness from zero, the anisotropy energy increases until it reaches a maximum value at ≈0.7nm thick, and then decreases. The same happens when the platinum layers are increased from zero, with the maximum here

being at ≈0.9nm. The anisotropy energy is also affected by the number of bilayers, with it being largest for between six and twelve bilayers. The anisotropy energy becomes less as the number of bilayers lies outside this range [13]. Another aspect of the multilayer which affects the PMA is the degree of texturing, with the anisotropy energy being enhanced for systems with strong <111> texturing. This texturing can be partially controlled by depositing a platinum underlayer, the thickness of which affects the final anisotropy energy [13].

All these changes result in different shapes of M vs. H loops. These loops fall into two basic categories: the first category being where the reversal of the magnetisation occurs over a small field range, with the precise shape of the loop being determined by the magnetic viscosity of the sample. The second category is where the reversal process occurs at several different fields ranges. This results in kinks in the M vs. H loops. Samples were chosen for study which fall into each of these two catagories. The first pair of samples, with a magnetic layer consisting of $Co_{50}Ni_{50}$ has a multi stage reversal process. The other multilayer sample, with a magnetic layer consisting of $Co_{40}Ni_{60}$ has a reversal process which occurs at a single field. It should be noted that the different properties are more likely to be caused by the different layer geometries than the slightly different compositions.

In addition to modifying the anisotropy energy, the Kerr rotation can also be enhanced by annealing the sample at temperatures up to 470C. The Θ_k is thought to be controlled by the polarisation of the platinum [14] which is enhanced by the annealing [13]. Annealing at temperatures up to 400C also has the effect of increasing the coercivity of the sample. This is thought to be caused by silicon

diffusion into the metallic layers (or oxygen diffusion if annealing is carried out in air) and the formation of non-metallic phases at the boundaries of the crystallites. These act both as pinning sites and to decouple the crystallites. These effects are found to be larger for samples with thicker magnetic layers, and for this reason one of the $Co_{50}Ni_{50}$/Pt samples was annealed in a vacuum to look at the effects of annealing on the micromagnetics of the system.

This work was carried out in collaboration with Q.Meng and J.C.Lodder at the University of Twente, where all the multilayers were deposited by Q.Meng. The multilayers were sputter deposited onto silicon wafers with silicon nitride windows suitable for TEM investigation at an argon gas pressure of $1.6x10^{-2}$mbar.

5.1.1 $Co_{50}Ni_{50}$/Pt multilayers

The first pair of samples consisted of a 27.5nm platinum seed layer followed by 17 bilayers of 0.9nm $Co_{50}Ni_{50}$ and 1.1nm Pt. Following deposition some of the samples were annealed in a vacuum at 300C. The samples were characterised in the TEM as described in chapter three, and on the AGFM as described in chapter two. Minor loop experiments on a vibrating sample magnetometer and cross section images were also recorded to characterise the samples further.

The diffraction patterns (figure 5.1) showed that the layers were polycrystalline, with both the platinum layer and the magnetic layer having a FCC structure. By comparing points w and x on figure 5.1 it can be seen that as the samples were tilted, the (022) planes start to diffract less perpendicular to the tilt axis, showing that there is a

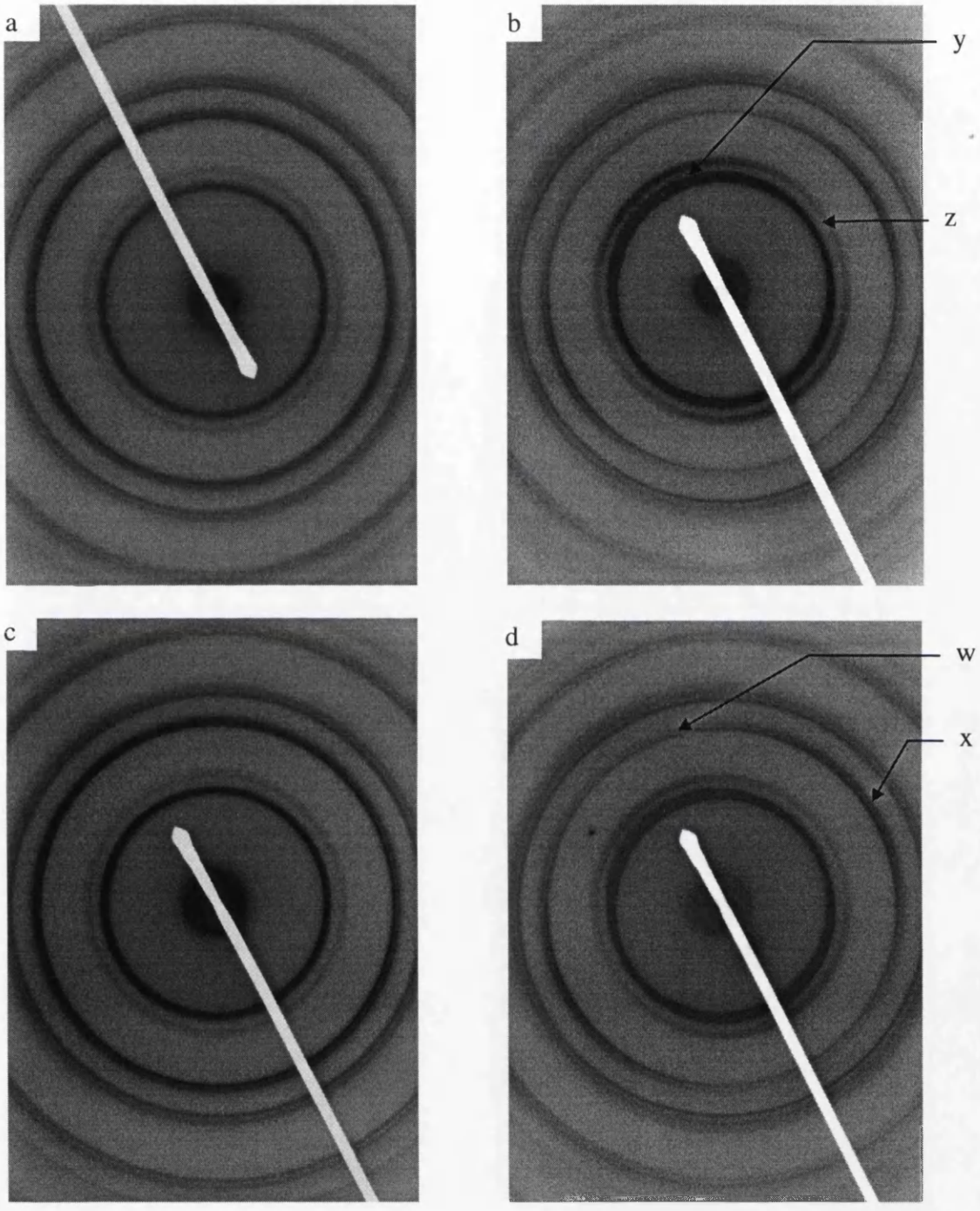

Figure 5.1: diffraction patterns of CoNi/Pt multilayers in the as grown state both perpendicular to the electron beam (a) and tilted 20° from perpendicular (b) and in the annealed state both perpendicular to the electron beam (c) and tilted 20° from perpendicular (d). Tilt axis is in direction shown below.

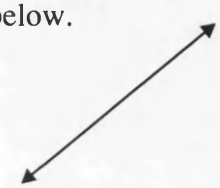

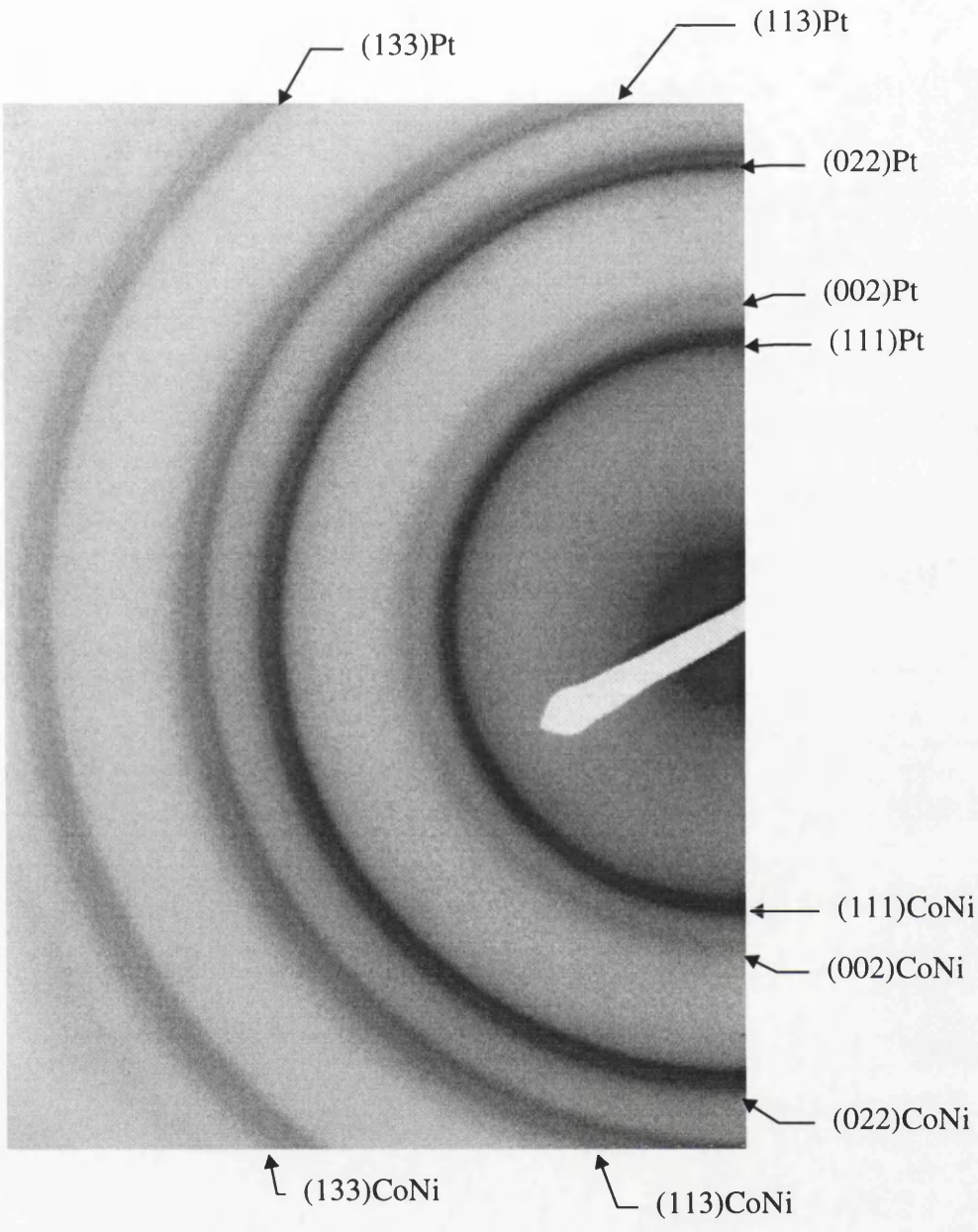

Figure 5.1e: An indexed diffraction pattern for a CoNi/Pt multilayer showing the FCC structure for both the cobalt nickel layers and the platinum layers

tendency for this plane to lie perpendicular to the plane of the film. However by comparing points y and z on figure 5.1, it can be seen that the (111) CoNi plane starts to diffract more under the same conditions, showing that there is a tendency for this plane not to be perpendicular to the plane of the film. Both these results suggest that these films are textured in the <111> direction. The crystallites, as observed in the bright field images (figure 5.2), are 10-15nm across while the cross section image (figure 5.3) shows that the crystal growth tends to be columnar, with the columns having a width of 10-15nm. There is no apparent change in this following annealing.

Fresnel images (figure 5.4) of the samples show that both have a complex dendritic structure, where the seperation of domains in regions where they are tightly packed is in the range 150-250nm.

Hysteresis loops for both the as grown and annealed sample (figures 5.5) show that reversal begins with an initial sharp fall in the magnetisation followed by a more gradual increase to saturation in the reverse direction. The principal effect of annealing the sample is an increased coercivity, 500Oe compared to 300Oe.

In the VSM experiment the samples were subjected to a saturating field in the positive direction followed by a negative field whose magnitude lay between the nucleation and saturation fields. On removal of the reverse field the magnetisation rises and continues to rise in a non-linear fashion as the field is increased in the positive direction (figure 5.6), showing that reversible processes were far from negligible.

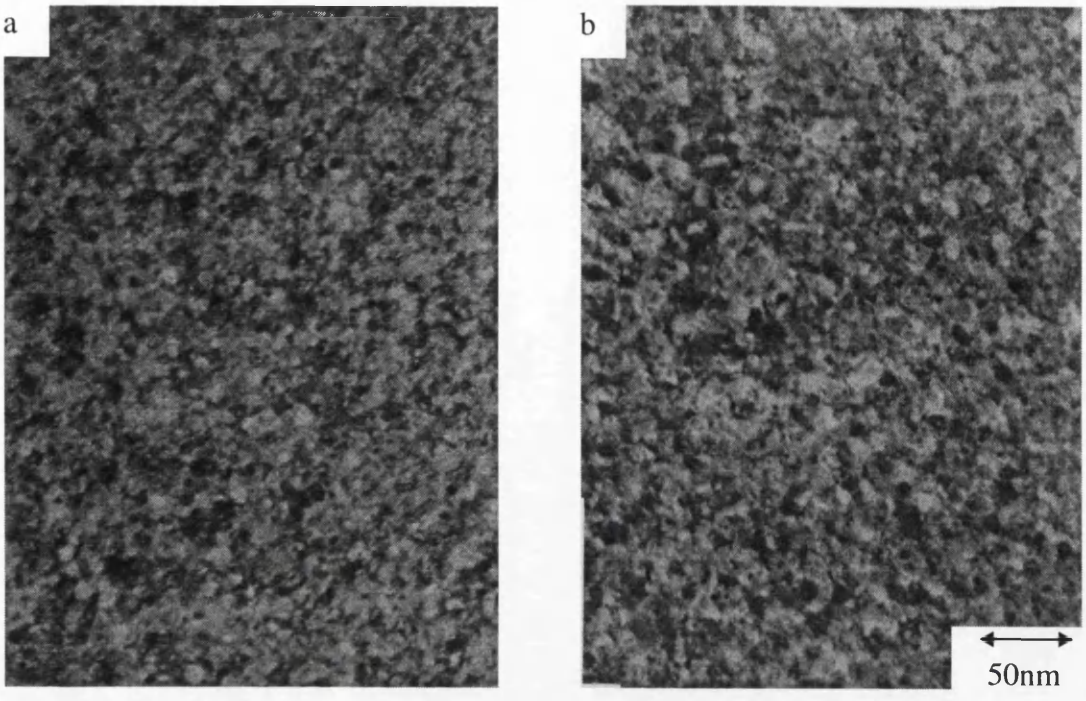

Figure 5.2: Bright field images of CoNi/Pt multilayers in as grown state (a) and annealed state (b).

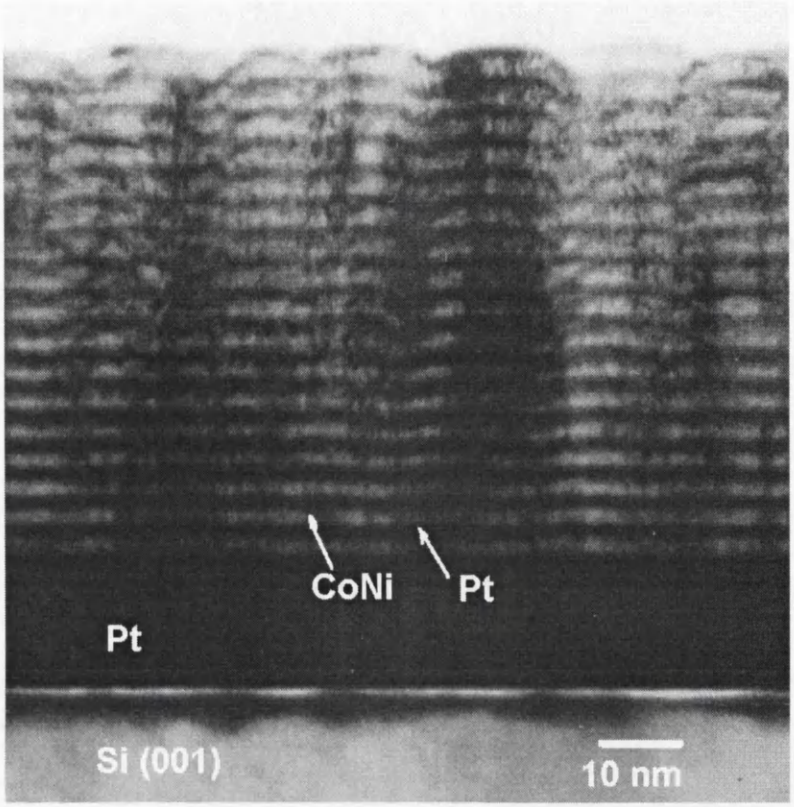

Figure 5.3: A bright field image of a cross section of a CoNi/Pt multilayer (courtesy Q.Meng)

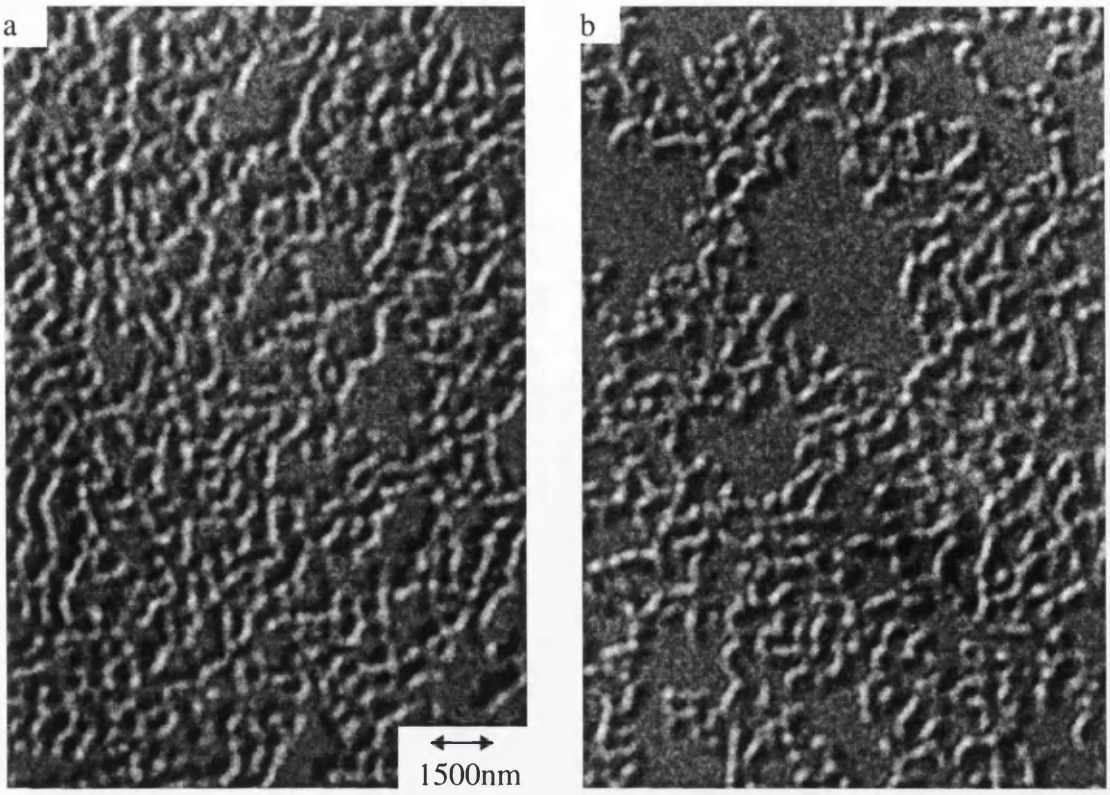

Figure 5.4: Fresnel images of CoNi/Pt multilayers in the as grown state (a) and annealed state (b).

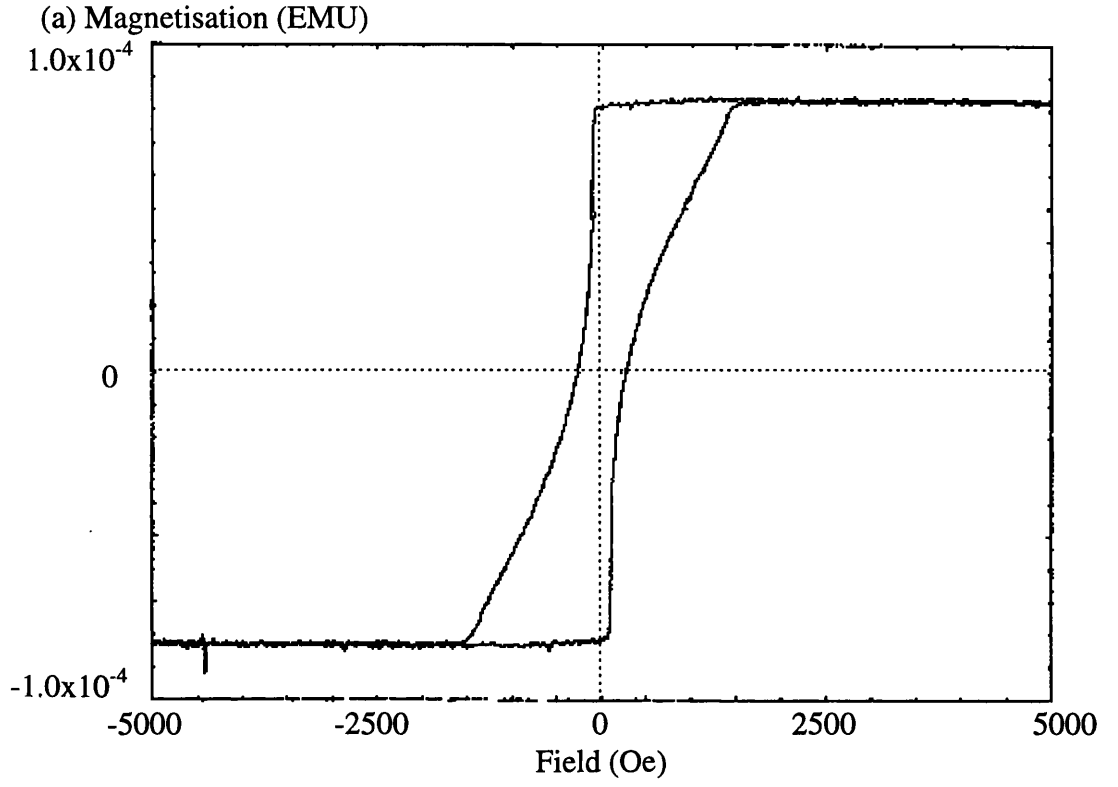

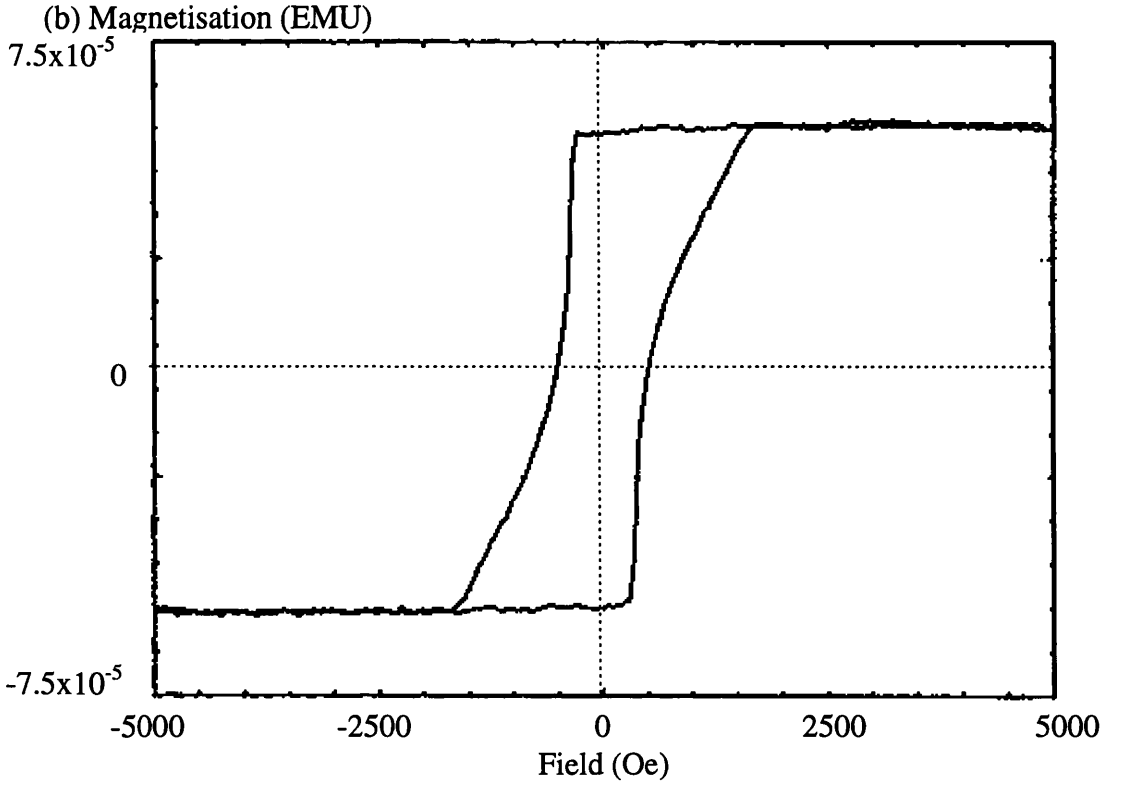

Figure 5.5: Magnetisation versus field plots for CoNi/Pt multilayers in the as grown (a) and annealed (b) states, showing the slight increase in coercivity as the sample is annealed.

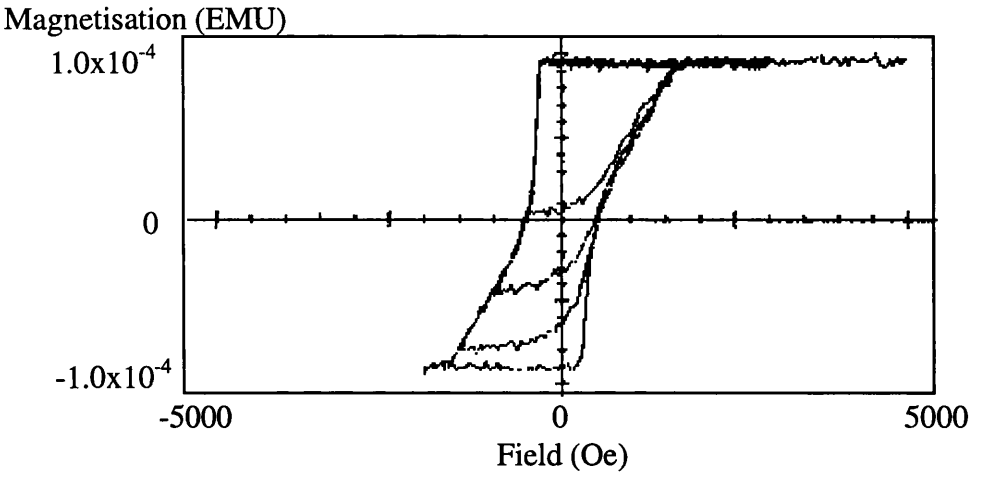

Figure 5.6: Minor loops recorded for CoNi/Pt multilayer on a VSM. The shape of the magnetisation curve and the increase in the magnetisation as the field is increased from a value less than negative saturation indicates the presence of reversible processes.

Remanence (DCD and IRM) curves were taken for both the samples as described in chapter two. The differentiated DCD and IRM curves show the switching field distributions for the sample, with the differentiated IRM curve showing the fields at which irreversible changes occur in the domain structure, and the differentiated DCD curve showing the effect of nucleation on this distribution.

The differentiated remanence plots (figure 5.7) for these two samples are similar and much more complicated than those for the other samples in this chapter. The differentiated DCD plot shows a fairly sharp peak at 100 or 350Oe depending on the sample. Another, lower, peak is observed on both the IRM and DCD plots at around 1500Oe and in between these two peaks the switching field distribution appears to be fairly constant but greater than zero. In an attempt to understand these sequences a similar field sequence to a DCD curve was applied to the sample in the TEM and Fresnel images were taken at the relevant points on the curve. This sequence will not be the same as the magnetisation sequence detailed later since the field is removed before any images are taken. This has the effect of highlighting only irreversible changes to the micromagnetic structure.

To highlight the changes that occurred along the DCD plot, the Fresnel images were taken after the field had been increased to a chosen value then reduced to zero, as in a DCD curve. The Fresnel images were then subtracted from the Fresnel images of the sample after a slightly higher field had been applied. The resulting image is of predominately low contrast with high contrast areas where the magnetisation had changed.

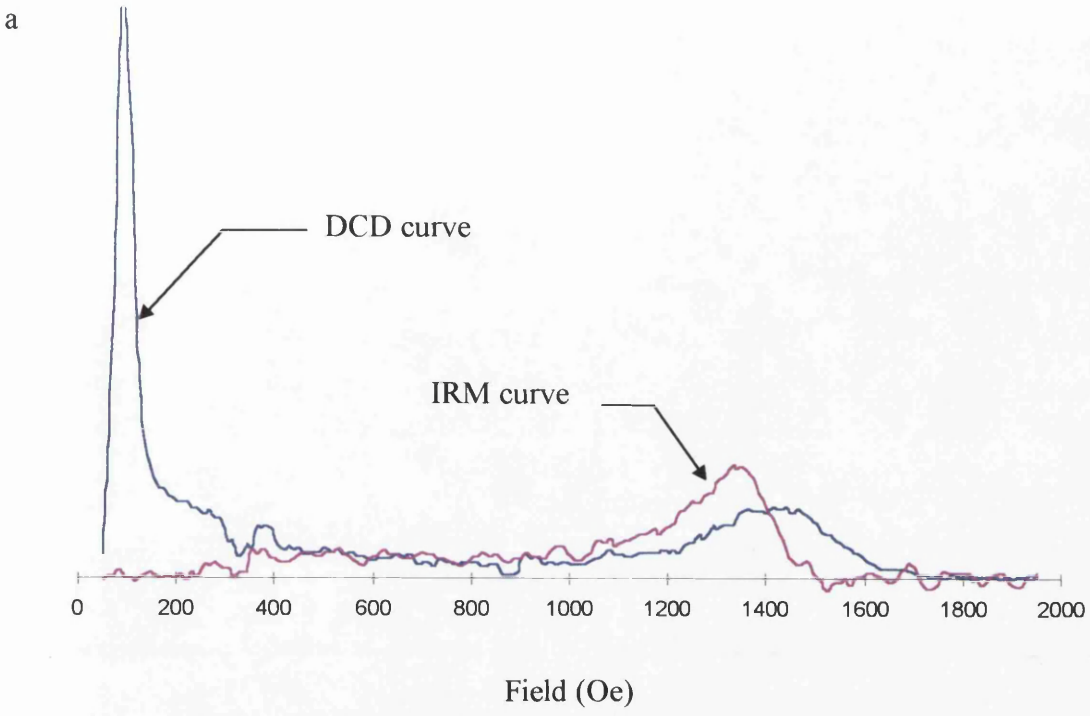

Figure 5.7a: Differentiated remanence curves for CoNi/Pt multilayer in the as grown state.

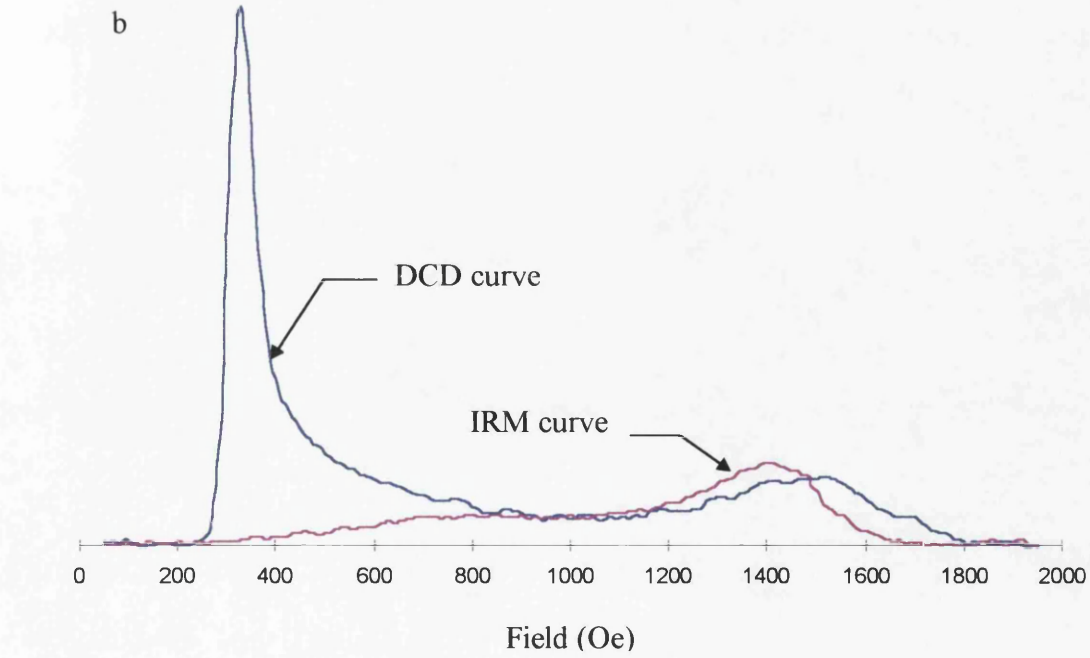

Figure 5.7b: Differentiated remanence curves for CoNi/Pt multilayer in the annealed state. This shows the increase in the domain nucleation field (left hand peak on differentiated DCD curve) if the sample is annealed, while the right hand peak remains at the same field.

These difference images (figure 5.8) show that the differentiated DCD peak at 250Oe results from the initial nucleation (figure 5.8a), and spread of the maze like domain structure, the back side of this peak representing the "filling in" of small areas which were bypassed in the initial nucleation (figure 5.8b). This filling in process continues until the sample is covered in a dense maze like domain structure. This happens at a field larger than the coercive field of the sample and since you would expect this maze like structure to have an almost zero nett magnetisation in a zero applied field it suggests that changes to this domain structure in the magnetisation process are reversible, and that the domain structure relaxes to this state as the field is removed.

The fields between the two peaks on the differentiated DCD curve appear to represent small jumps in the magnetisation pattern (figure 5.8c), possibly as groups of domains rearrange their geometries in order to achieve a more dense domain structure. The noise level for this figure is also notably higher than for the other images, this could indicate wall motion. The final peak (at ≈1500Oe) represents the destruction of these domains as the walls collapse together under the influence of the reverse field and annihilate each other. This stage of the process was difficult to capture on the difference images since as the field was increased from the large negative values, the unreversed domains would grow in a way which made the resulting domain pattern almost independent of that of the previous remanent state (figure 5.8d).

The time delay plots of the two samples (figure 5.9) show that the magnetisation against log(time) is non-linear at the fields represented by the sharp peak. This would

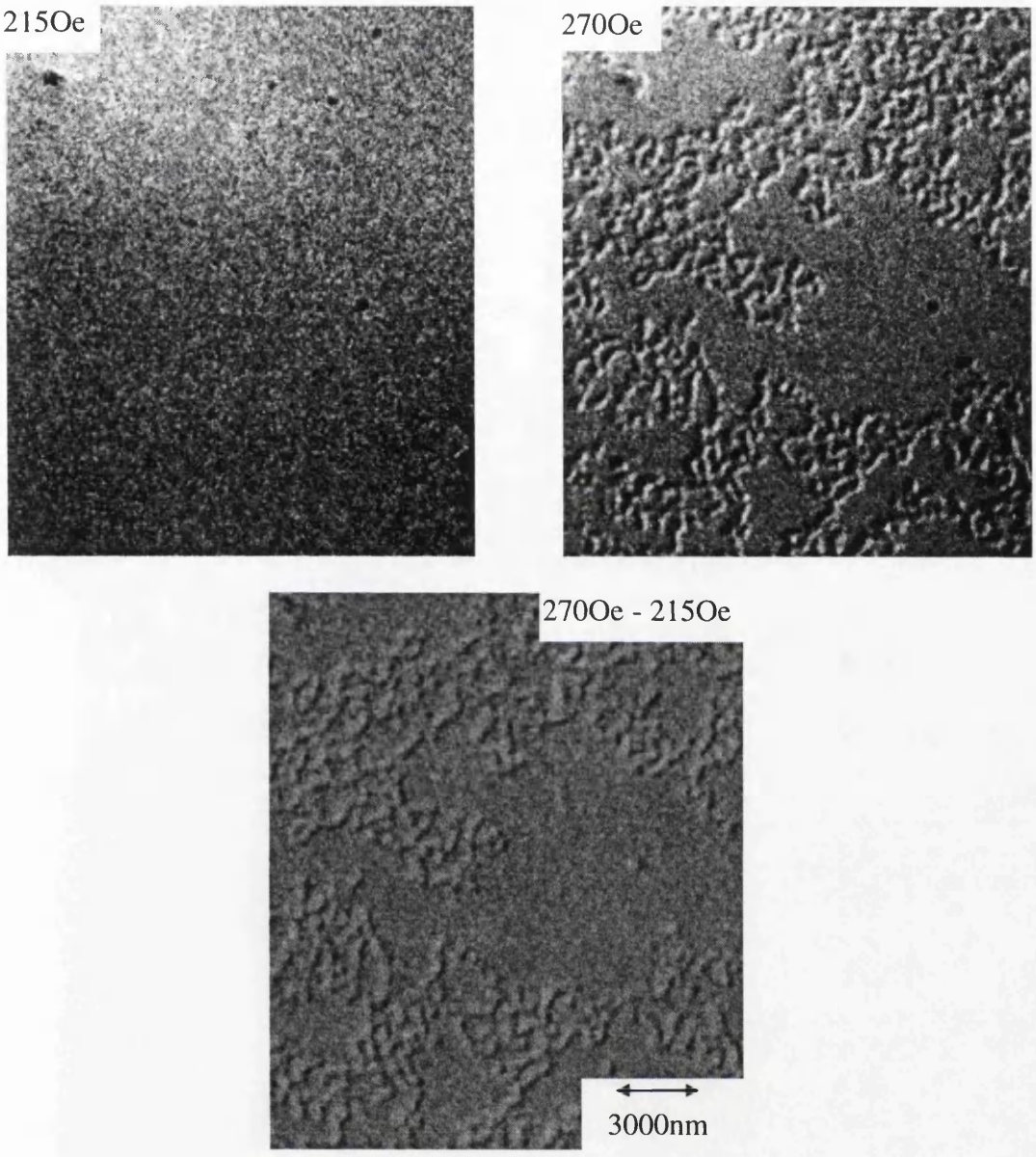

Figure 5.8(a): A set of images containing two Fresnel images recorded after the annealed CoNi/Pt multilayer had been exposed to reversing fields of 215Oe and 270Oe, and a difference image. The difference image was calculated from Fresnel images by subtracting one image from the other. While the difference image is not necessary here, it is shown here for comparison with the other difference images later on in the figure.

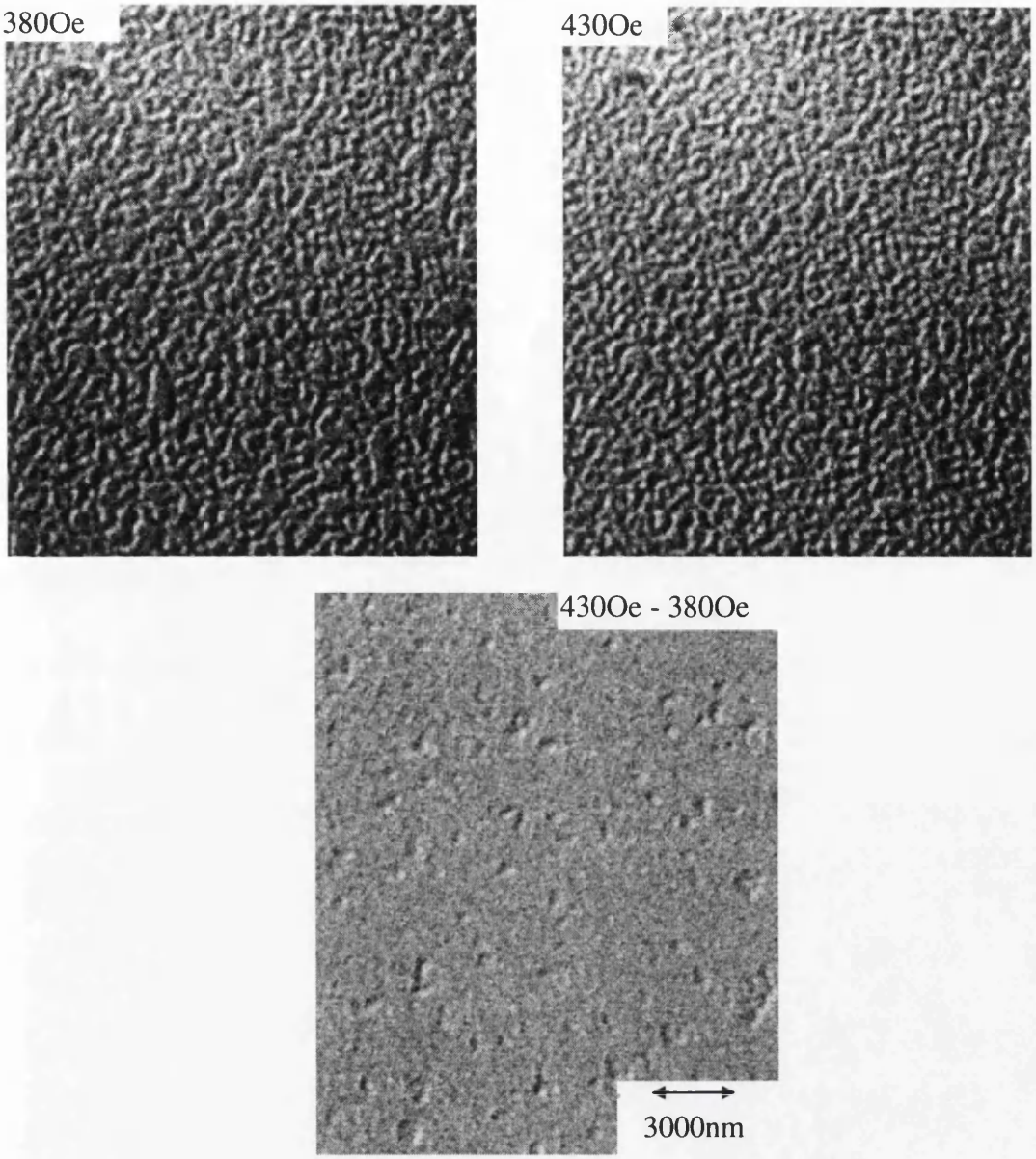

Figure 5.8(b): Fresnel images and a difference image for the annealed CoNi/Pt multilayer. The Fresnel images were recorded after the sample had been exposed to reversing fields of 380Oe and 430Oe. This shows the small changes that are taking place at this point on the DCD curve.

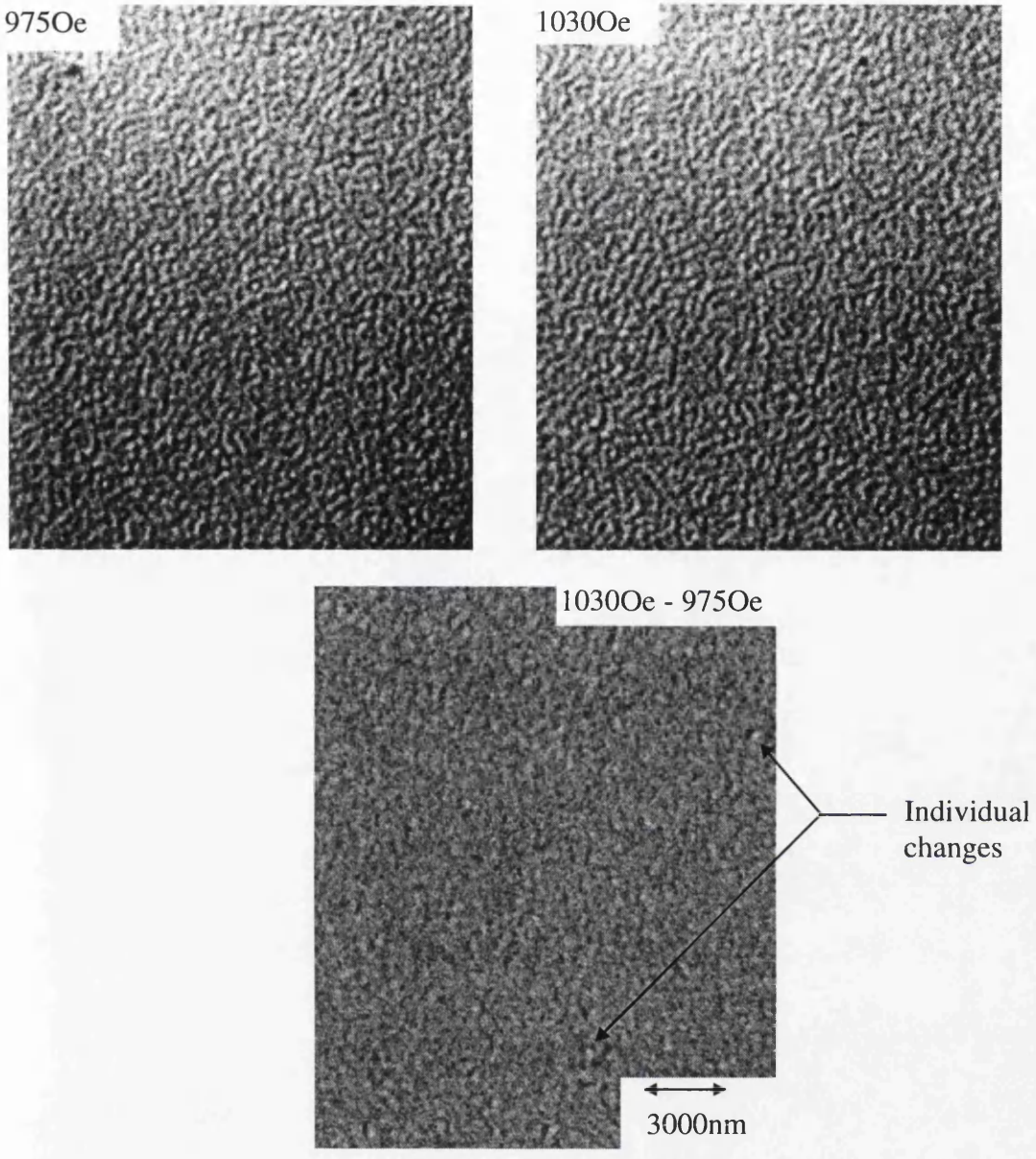

Figure 5.8(c): Fresnel images and a difference image for the annealed CoNi/Pt multilayer. The Fresnel images were recorded after the sample had been exposed to reversing fields of 975Oe and 1030Oe. This difference image is generally noisier, this may reflect the small number of changes that are taking place, or may be indicative of domain wall motion.

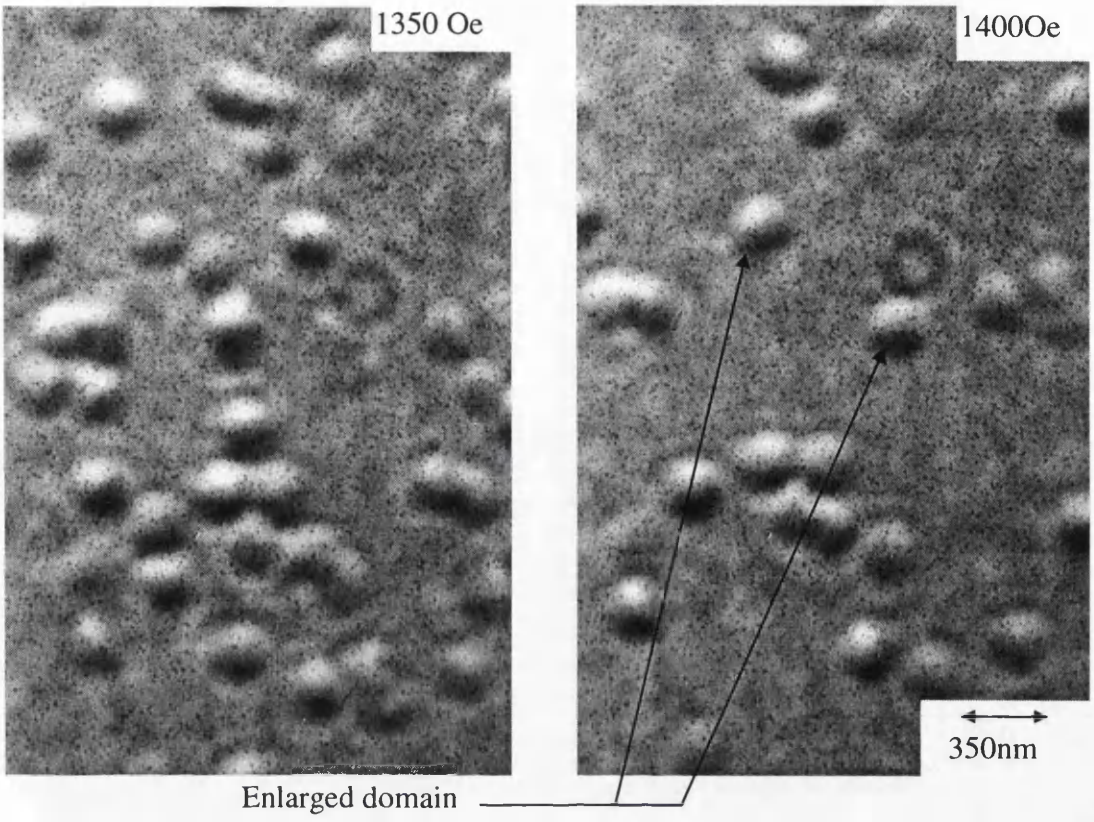

Figure 5.8d: Fresnel images of annealed CoNi/Pt multilayer after it had been exposed to reversing fields of 1350Oe and 1400Oe in turn. The arrows indicate areas which have unreversed despite being exposed only to reversing fields.

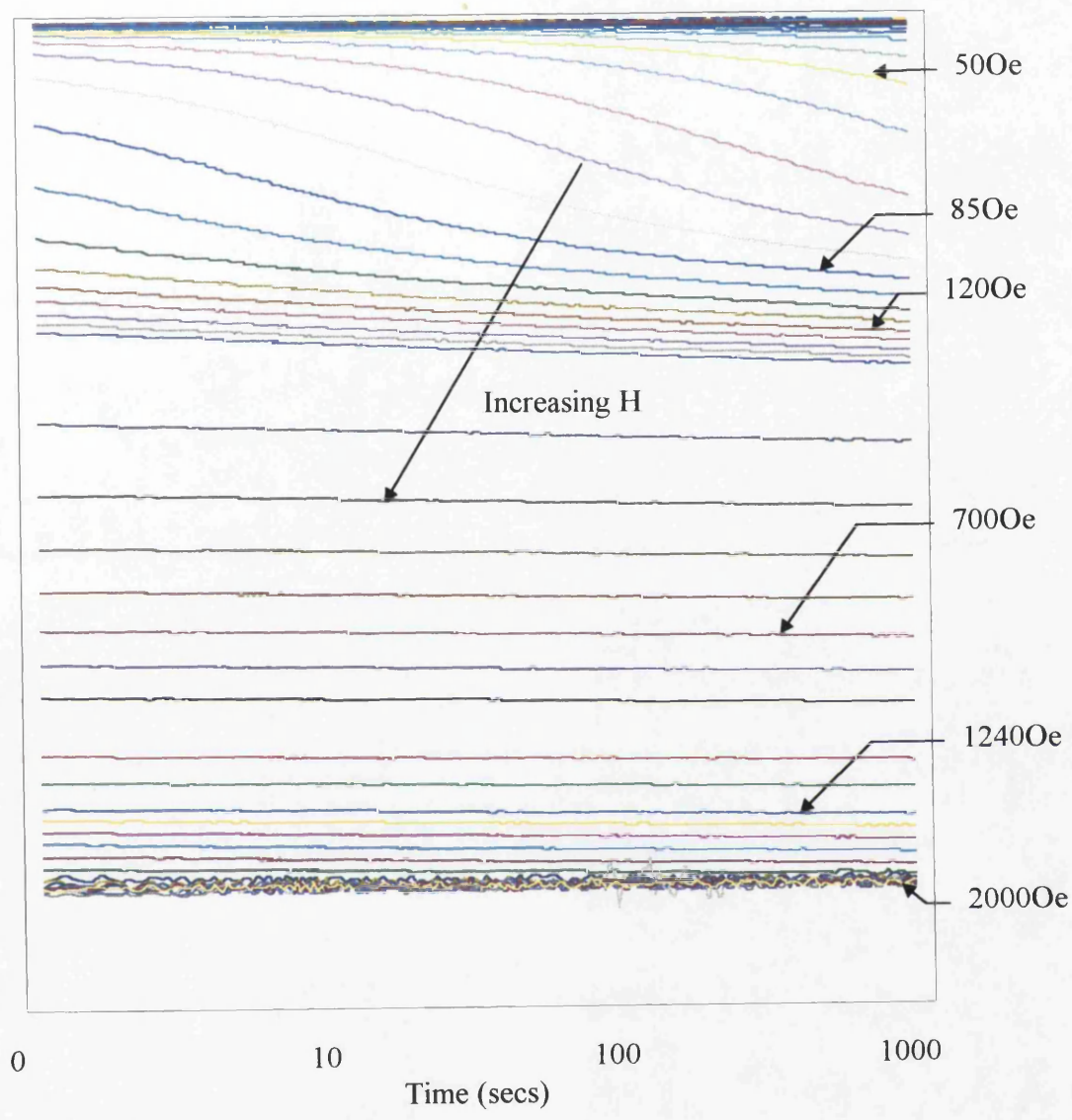

Figure 5.9(a): Magnetisation versus time plots for CoNi/Pt sample in the as grown state recorded on an AGFM. The vertical scale goes from $+m_s$ to $-m_s$. Selected field values are indicated on the right hand side.

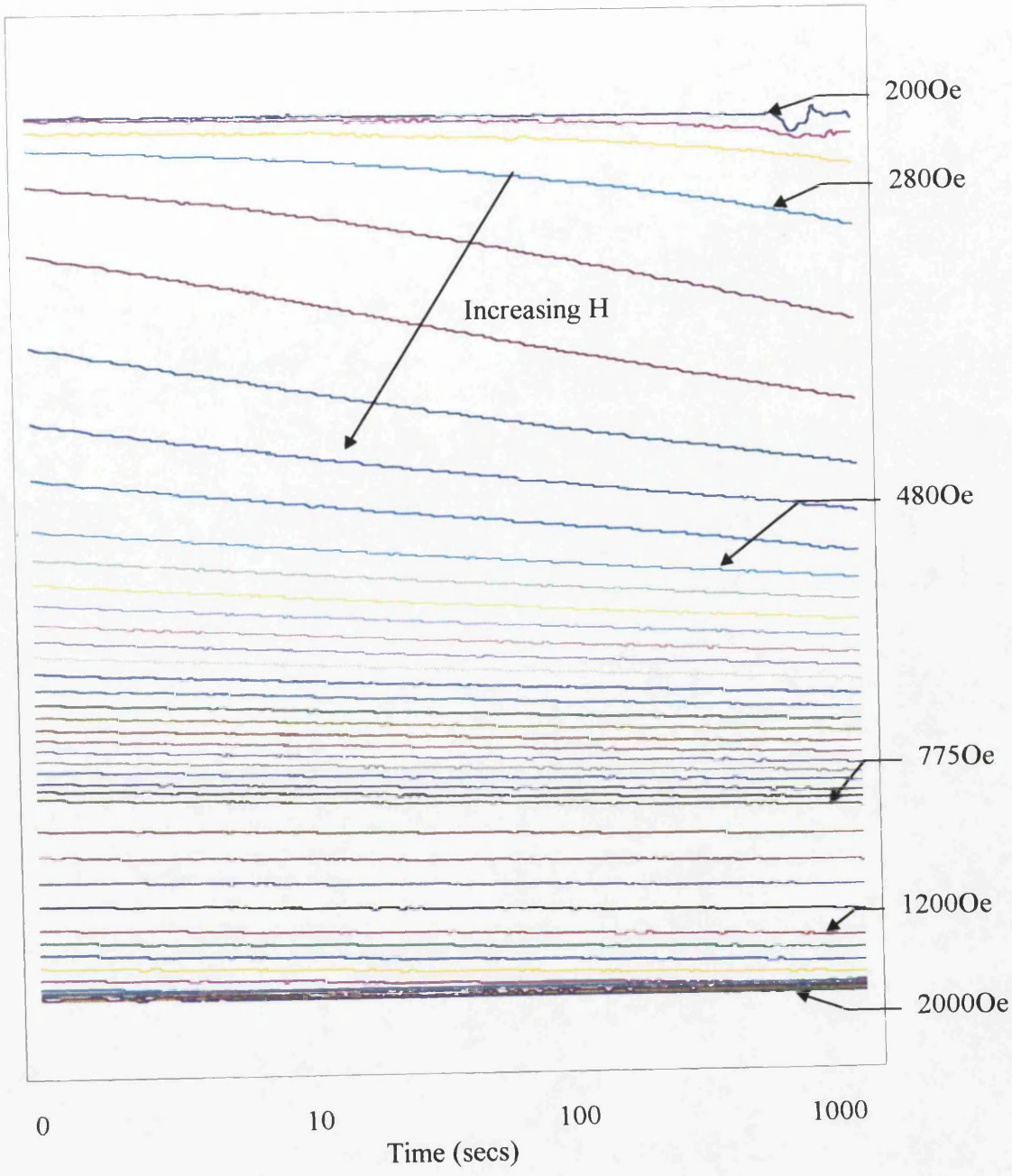

Figure 5.9(b): Magnetisation versus time plots for CoNi/Pt samples in the annealed state recorded on an AGFM. The vertical scale goes from $+m_s$ to $-m_s$. Selected field values are indicated on the right hand side.

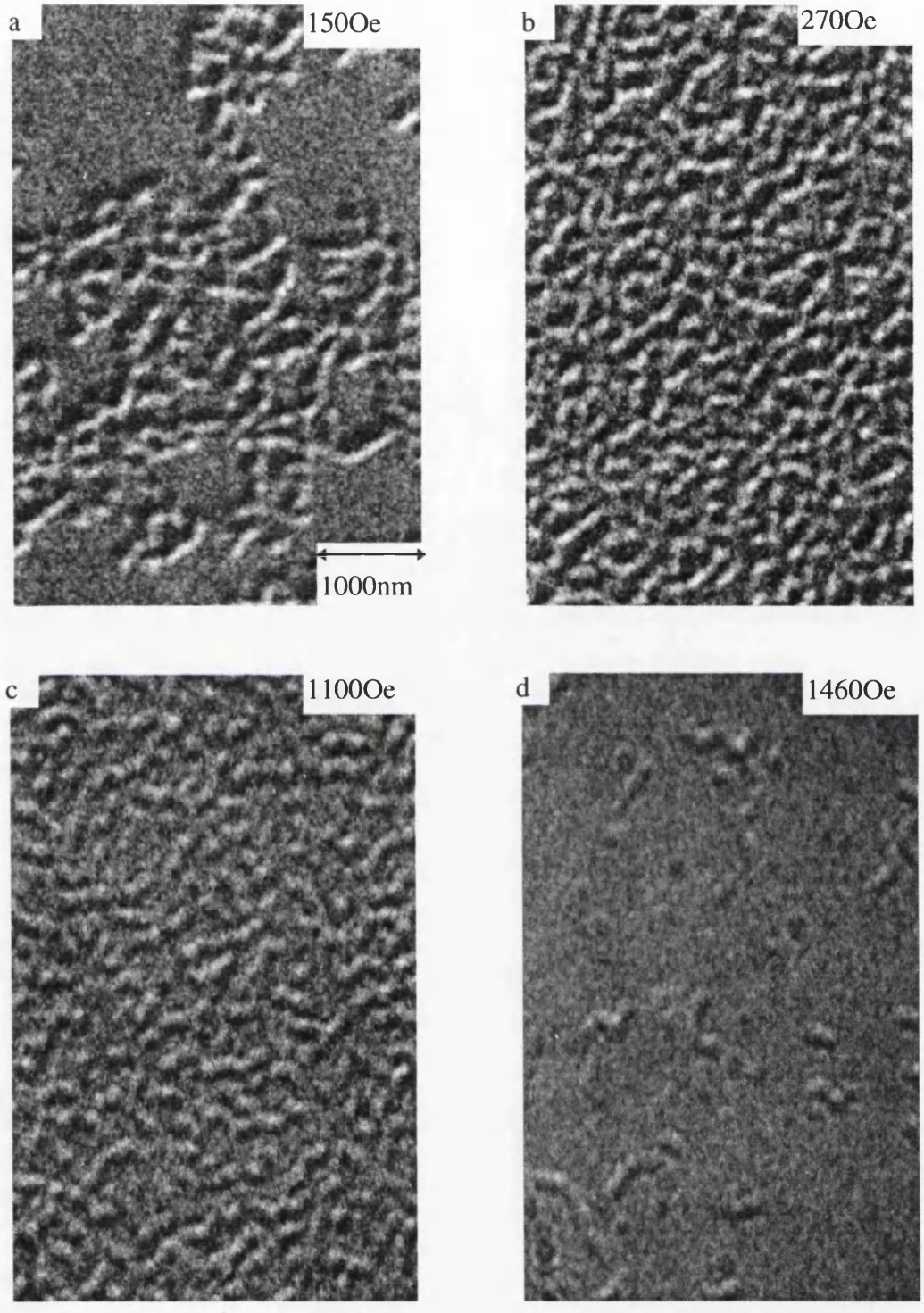

Figure 5.10:Fresnel images of the magnetisation processes in the as-grown CoNi/Pt taken at field values of: 150Oe (a); 270Oe (b); 1100Oe (c); 1460Oe (d).

be expected from a sharp switching field distribution [21]. However unlike the other samples in this chapter, the magnetisation tends towards a value well above negative saturation at fields above the coercive field rather than negative saturation as in the other samples. This suggests that there is a strong demagnetising field which controls part of the reversal mechanism for this sample. The time dependent plots where the field applied is larger than the coercive field are linear with log(time). This would be expected from a broad switching field distribution [21].

To give a more complete picture of the mechanisms involved, the magnetisation process was recorded on the CCD camera (figures 5.10). The initial nucleation of reverse domains was never seen so it can be assumed that this occured in a very small number of sites. Reversal went on to involve the growth of irregular domains (figure 5.10a). As the field was increased slightly the irregular domain structure grew to cover a greater fraction of the specimen (figure 5.10b). Observations of the process in real time showed that growth involved multiple branching of existing domains to form the complex dendritic structures seen in the figures and was strongly time dependent. A further increase of the field of around 100Oe led to the complete coverage of the sample with tightly packed irregular domains, and once coverage was complete, further changes required the application of substantially larger fields (figure 5.10c). The remainder of the magnetisation process took place over a larger field range and involved the steady shrinking of unfavourably orientated domains with the appearance of increased areas of reversed magnetisation separated by local regions supporting narrow irregular domains. As the reverse field was increased the number of regions supporting a domain structure decreased (figure 5.10d) until reverse saturation was attained. The fact that extremely narrow domains existed up to

substantial fields suggested that annihilation was difficult and may reflect the existence of wall structures of the kind predicted previously for multilayers supporting perpendicular magnetisation [15].

The observation of the early stages of domain evolution is complicated considerably by the presence of time dependent effects. Here I found the most useful procedure was to subject the film to a field very close to that at which domain nucleation occurs and then to record image sequences at regular time intervals without changing the field. The extremely high stability of the objective lens (≈1ppm) makes it an ideal source of magnetic field for such experiments. The resulting sequences of the growth of the domain structure tell us a lot about the initial stages of the reversal mechanism and confirm the importance of thermally activated processes. Advantage can also be taken of the fact that the images are digitally recorded on the slow scan CCD camera which is connected to the Philips CM20 TEM. This allows the subtraction of adjacent images in the sequence from each other to highlight the changes which occur in the time between each image was recorded (figure 5.11). In this way very small changes in the domain structure can be highlighted which would otherwise be missed. Some of these areas are indicated with arrows in figures 5.11 f and h. The difference images also highlight the fact that once a domain wall system has formed it remains essentially unchanged as the domain structure evolves. This is indicative of large energy barriers which would have to be overcome, and could indicate highly stable wall structures or strong domain wall pinning sites. Care was also taken to ensure that the temperature was as stable as possible. This was in view of the fact that the processes being investigated were thermal in nature. It was not possible to

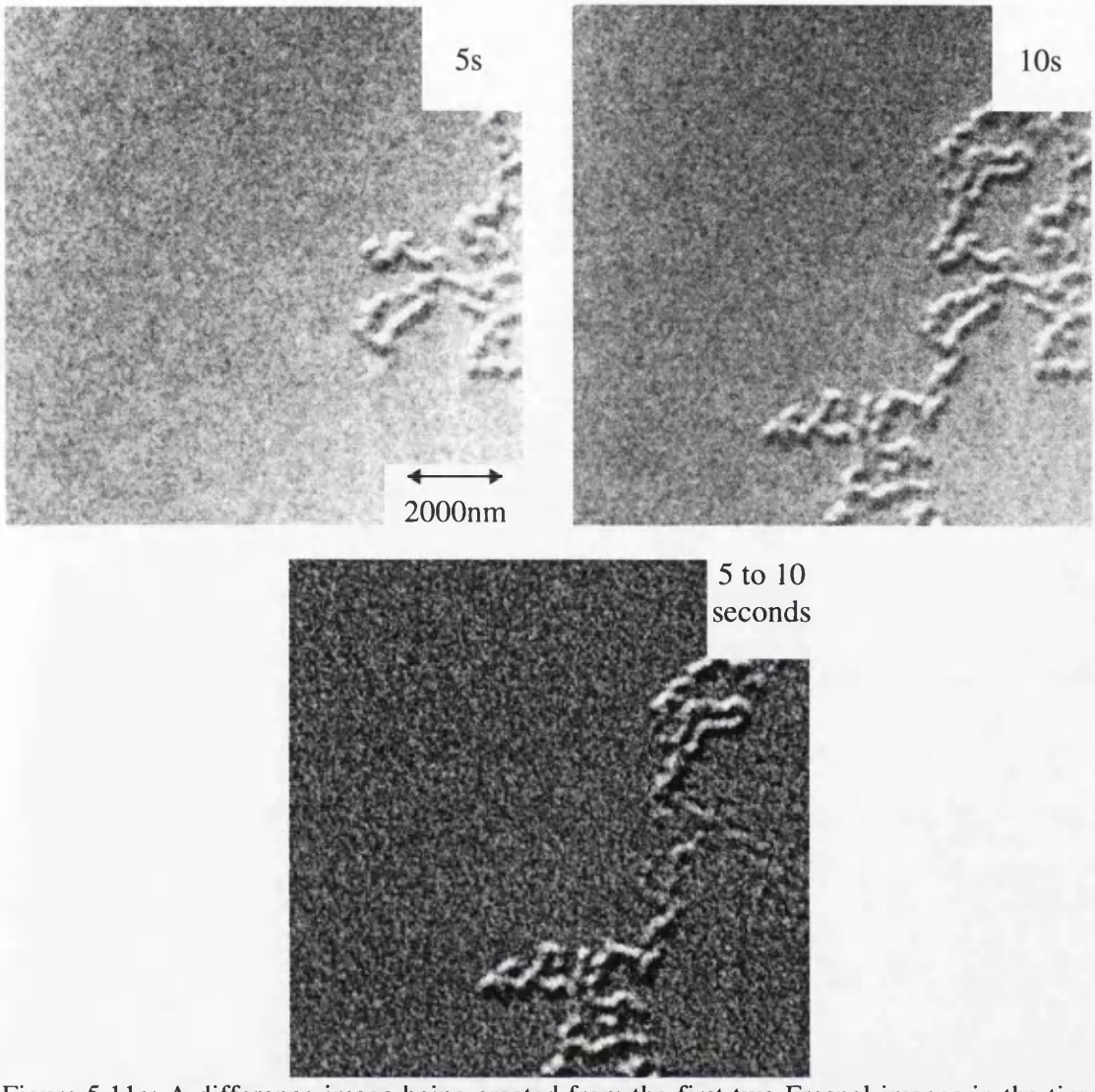

Figure 5.11a: A difference image being created from the first two Fresnel images in the time dependent sequence. This shows the domains which appeared between 5 and 10 seconds.

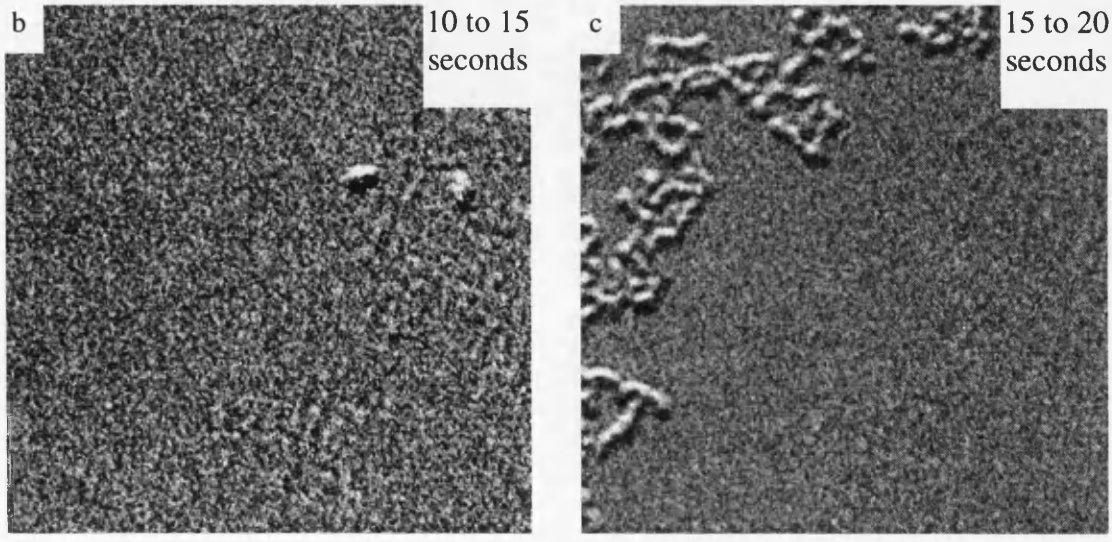

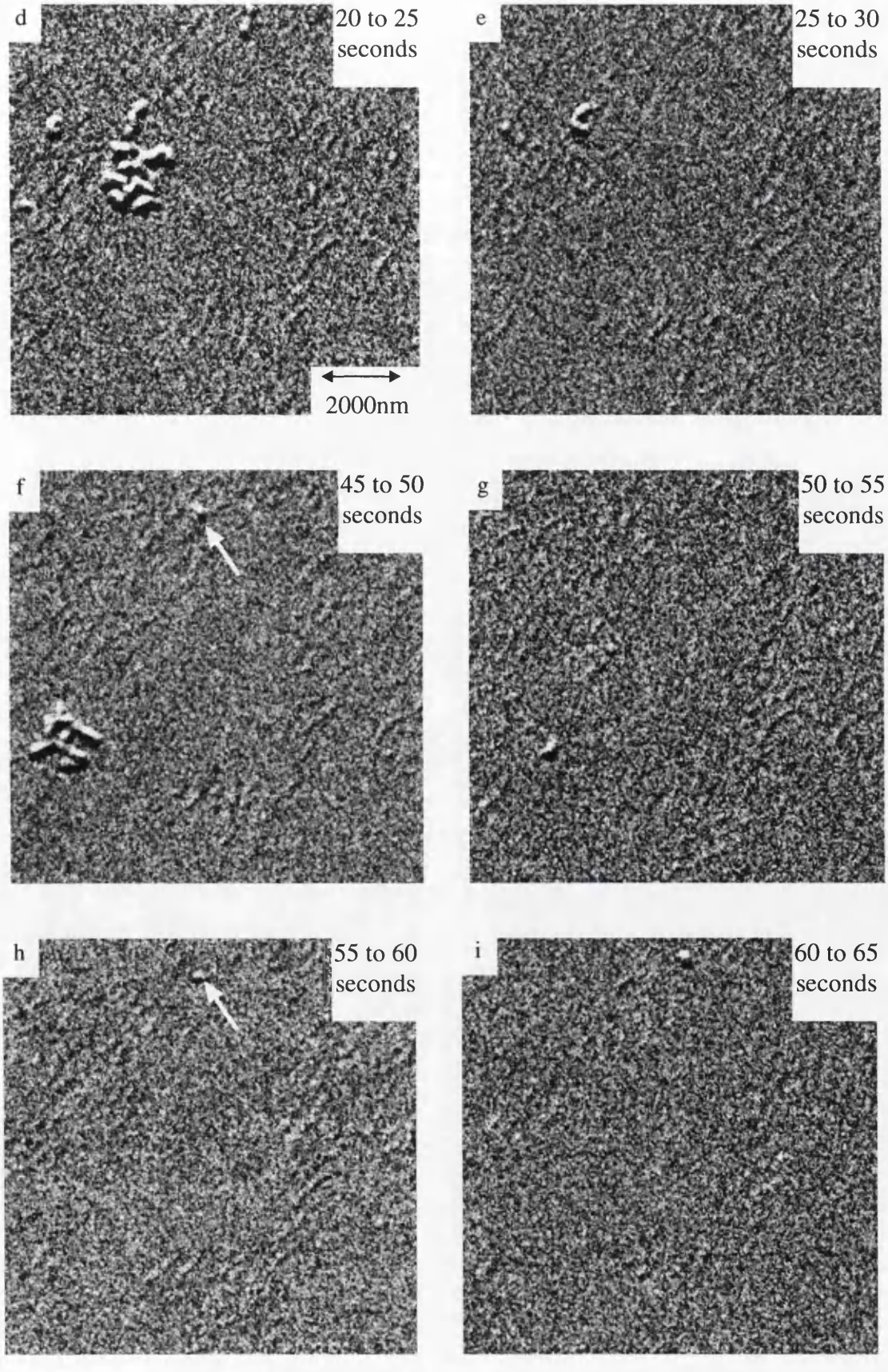
d
20 to 25 seconds
2000nm
e
25 to 30 seconds
f
45 to 50 seconds
g
50 to 55 seconds
h
55 to 60 seconds
i
60 to 65 seconds

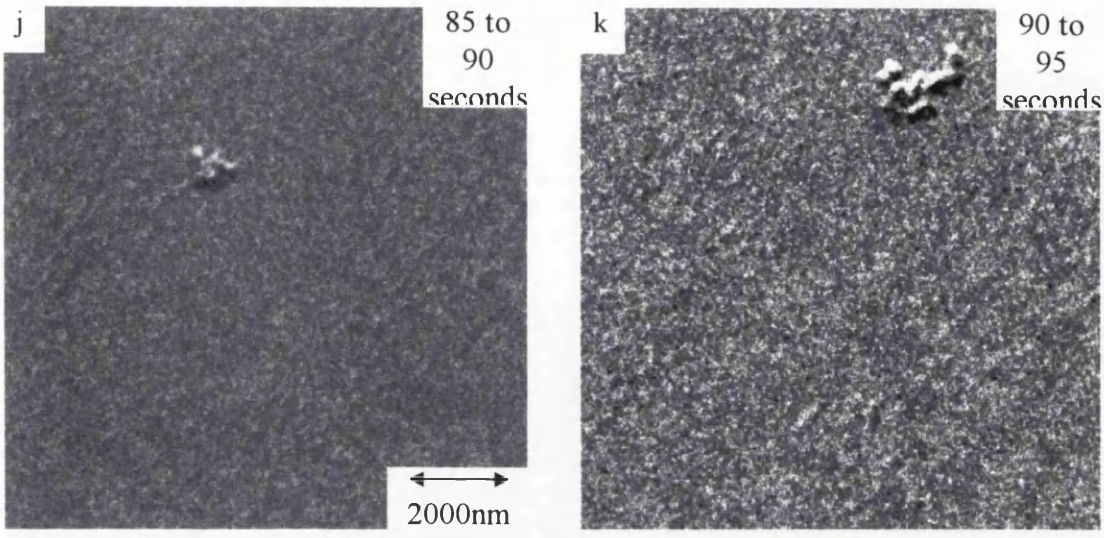

Figures 5.11 b to k: Difference images showing domains which appear in the time interval indicated. There were no new domains in time intervals which are not present in the sequence.

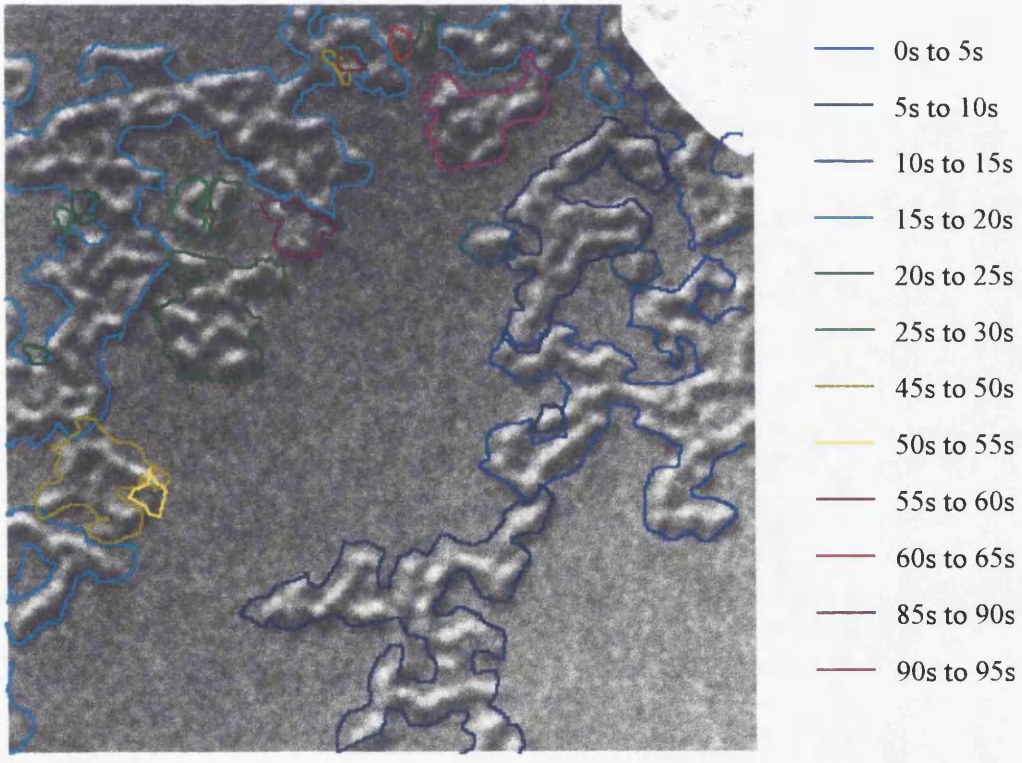

Figure 5.11l: The evolution of the magnetisation pattern with time for CoNi/Pt.

reproduce the alternating field of the AGFM for direct comparison, although this is expected to have a minimal influence.

The observed reversal process begins with domains appearing at the edge of the field of view. The fact that the initial nucleation site was never observed in the area of the film ($\approx 10^{-2}mm^2$) suggests that there are only a very few nucleation sites, and that the entire domain structure evolves from these sites. The reversal then proceeds with a series of domain expansions to form a dendritic domain structure. These jumps occur at irregular intervals and are irregular in size. The size of the smallest jump can be estimated from the difference images to be $\approx 10^{-2}\mu m^2$, while the larger jumps can be several μm^2. These estimates of the area of the smallest jumps are inherently inaccurate since the domains are viewed in Fresnel mode, which is a defocus mode. The esimate of this size will however represent the upper limit for the size of that jump. Viewing the nucleation process on the low light level TV camera shows that these jumps generally proceed between the frames of the video recording system, hence the domain growth process does not proceed at even a nearly uniform rate.

The above results show the magnetisation and time dependent micromagnetic patterns for the sample in the as grown state. The results for the sample in the annealed state were very similar (figure 5.12) and did not appear to be affected by the annealing process. The only differences between the two processes was the higher fields required to nucleate domains ($\approx$250 Oe compared to $\approx$80Oe), however the sample does reach reverse saturation at approximately the same field ($\approx$1400Oe).

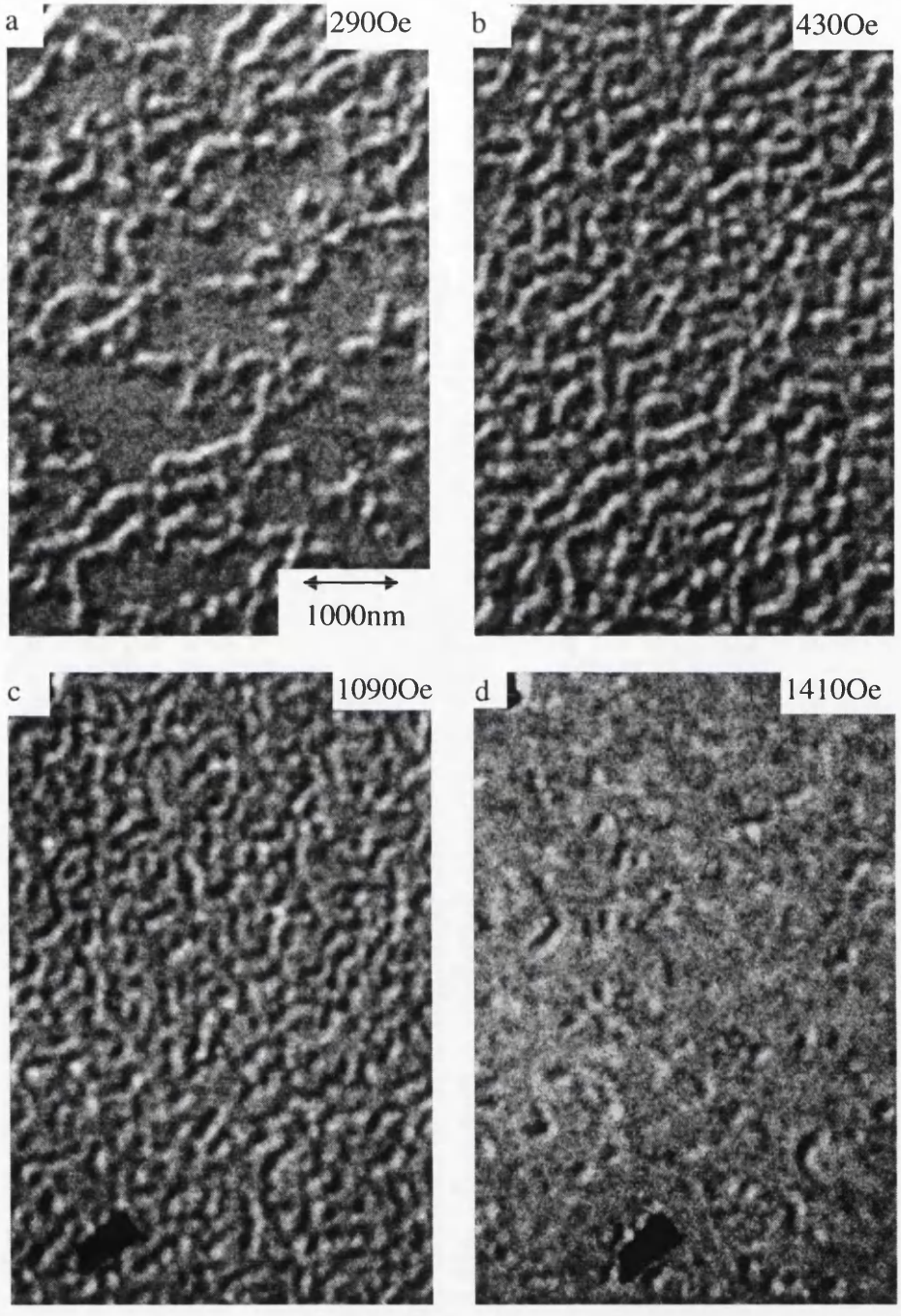

Figure 5.12: Fresnel images of the magnetisation processes in the annealed CoNi/Pt taken at field values of: 290Oe (a); 430Oe (b); 1090Oe (c); 1410Oe (d).

5.1.2 $Co_{40}Ni_{60}$/Pt multilayers

This sample was deposited onto a silicon nitride window suitable for TEM investigation and consists of ten bilayers of 0.4nm thick $Co_{40}Ni_{60}$ and 0.9nm thick Pt deposited on top of a platinum seed layer which is 10nm thick. The samples were prepared by sputter deposition in an argon gas pressure of $1.6x10^{-2}$mbar.

The bright field images and diffraction patterns (figures 5.13 and 5.14) show a structure similar to the previous two sets of multilayer, with the most prominent difference being there is almost no texturing evident in these multilayers. The reason for this difference is unknown. Fresnel images (figure 5.15) show a complex domain structure which is unlike the previous two samples. The larger features which can be clearly seen on the Fresnel images are not magnetic and are probably dirt particles. While they do not appear to affect or obscure the magnetic contrast, they are certainly the most prominent features on the Fresnel images. The hysteresis loop (figure 5.16) is of the type where the reversal process occurs at essentially a single field.

As with the other samples, remanence curves and time delay plots were recorded for these samples on an AGFM (figures 5.17 and 5.18), along with magnetisation and time delay sequences (figures 5.19 and 5.20) on the TEM.

The differentiated remanence curves (figure 5.17) show that nucleation occurs at on average a slightly higher field than that required to sweep domains through the system. This would suggest that once domains had been nucleated they would spread throughout the sample if the field was held steady. This is borne out by the time

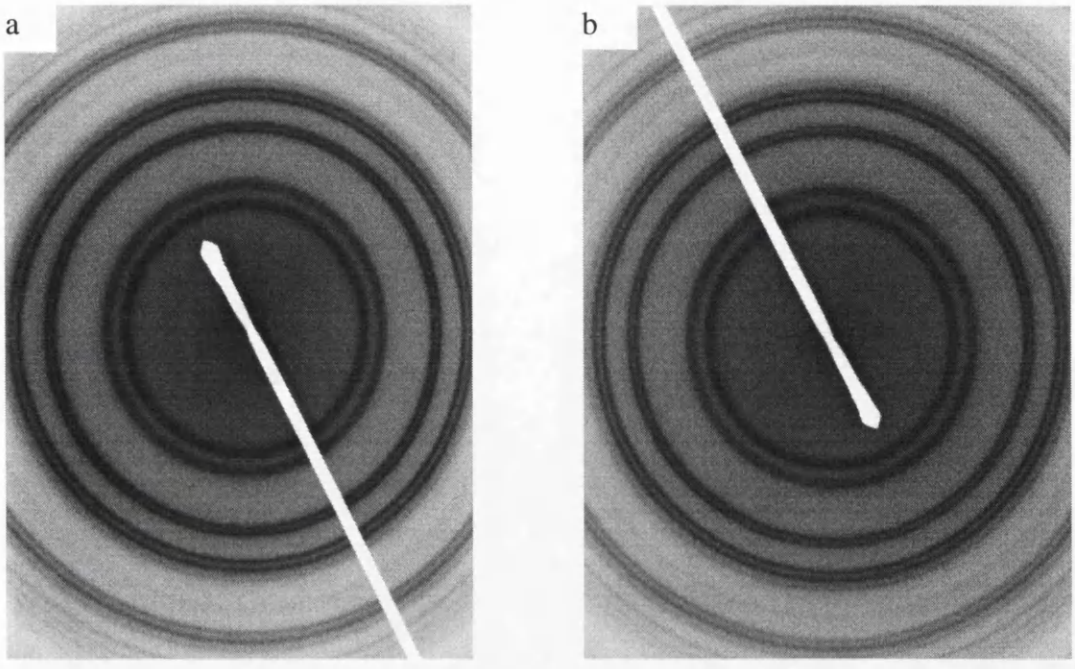

Figure 5.13: Diffraction pattern of $Co_{40}Ni_{60}$/Pt multilayers both perpendicular to the electron beam (a) and tilted to an angle of 20° from perpendicular (b), showing the lack of texturing.

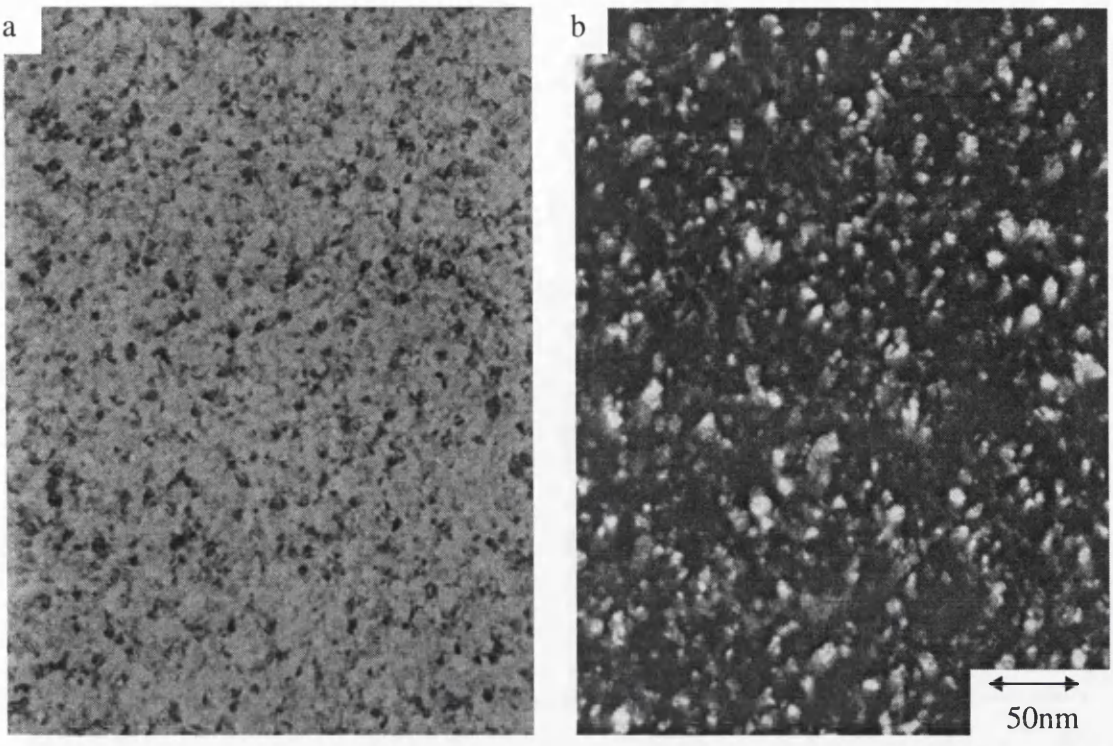

Figure 5.14: Bright field (a) and dark field (b) images of $Co_{40}Ni_{60}$/Pt multilayers.

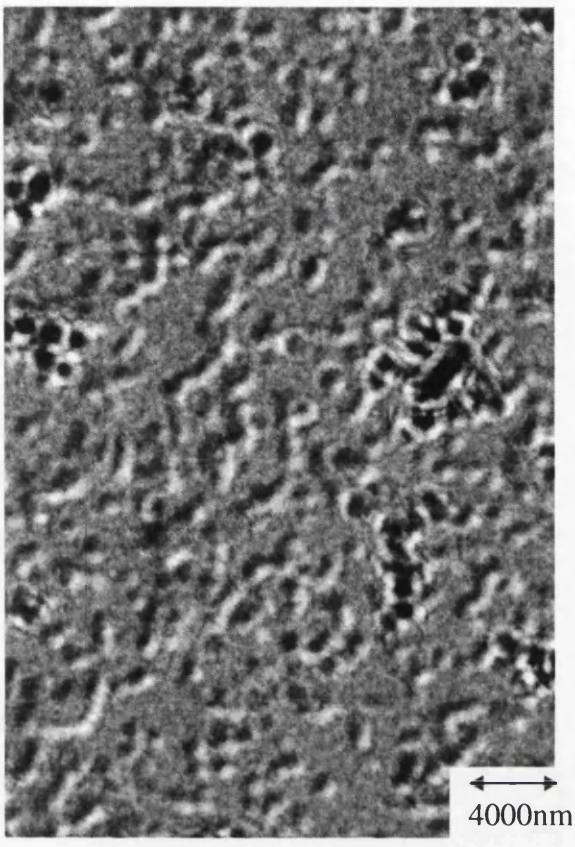

Figure 5.15: A Fresnel image of $Co_{40}Ni_{60}$/Pt multilayer in the as received state.

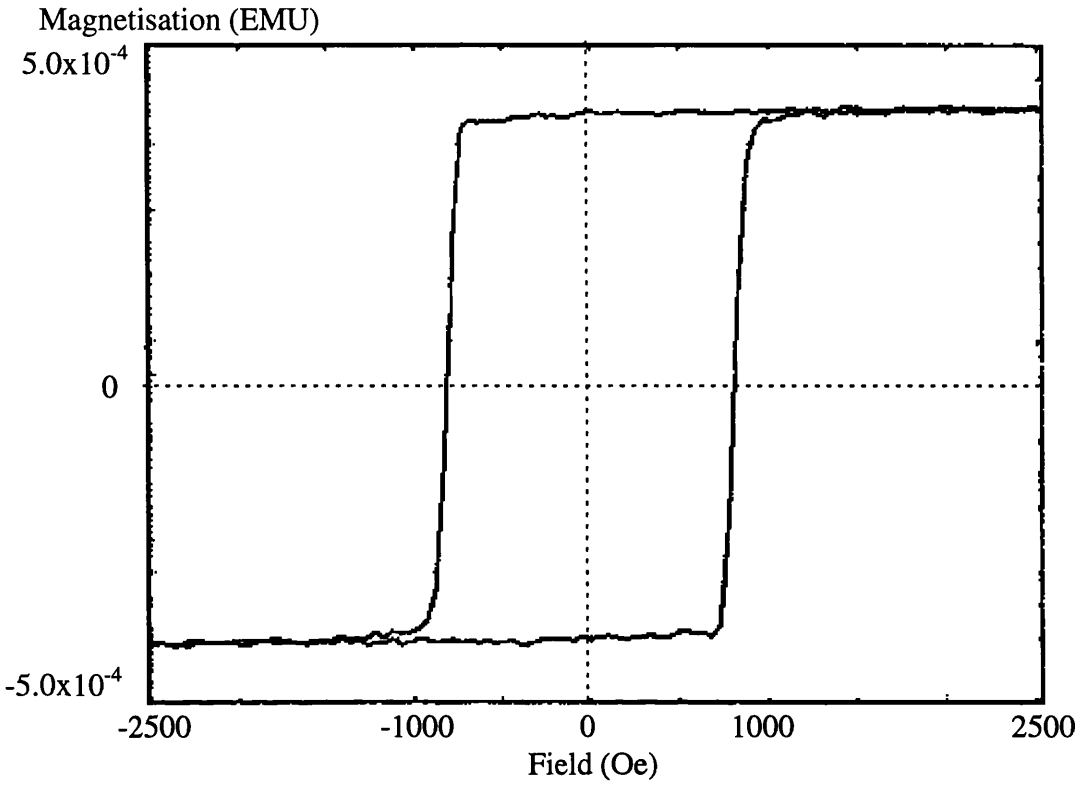

Figure 5.16: Magnetisation against field plot for $Co_{40}Ni_{60}$/Pt multilayer.

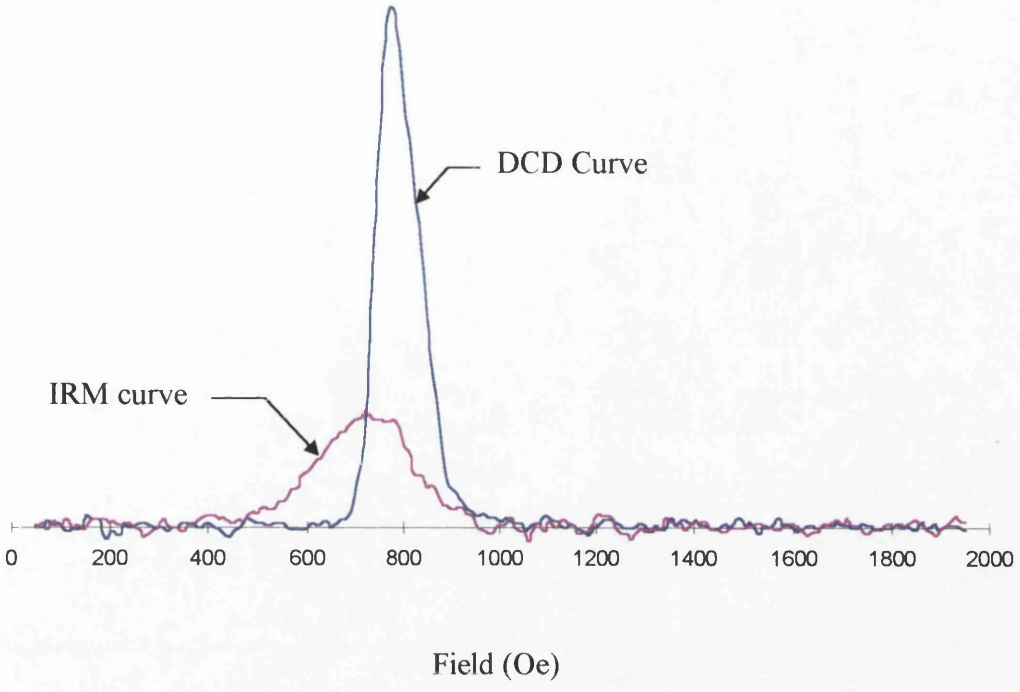

Figure 5.17: Differentiated remanence curves for $Co_{40}Ni_{60}$/Pt multilayer, showing that the domain nucleation field is higher than the domain wall motion fields.

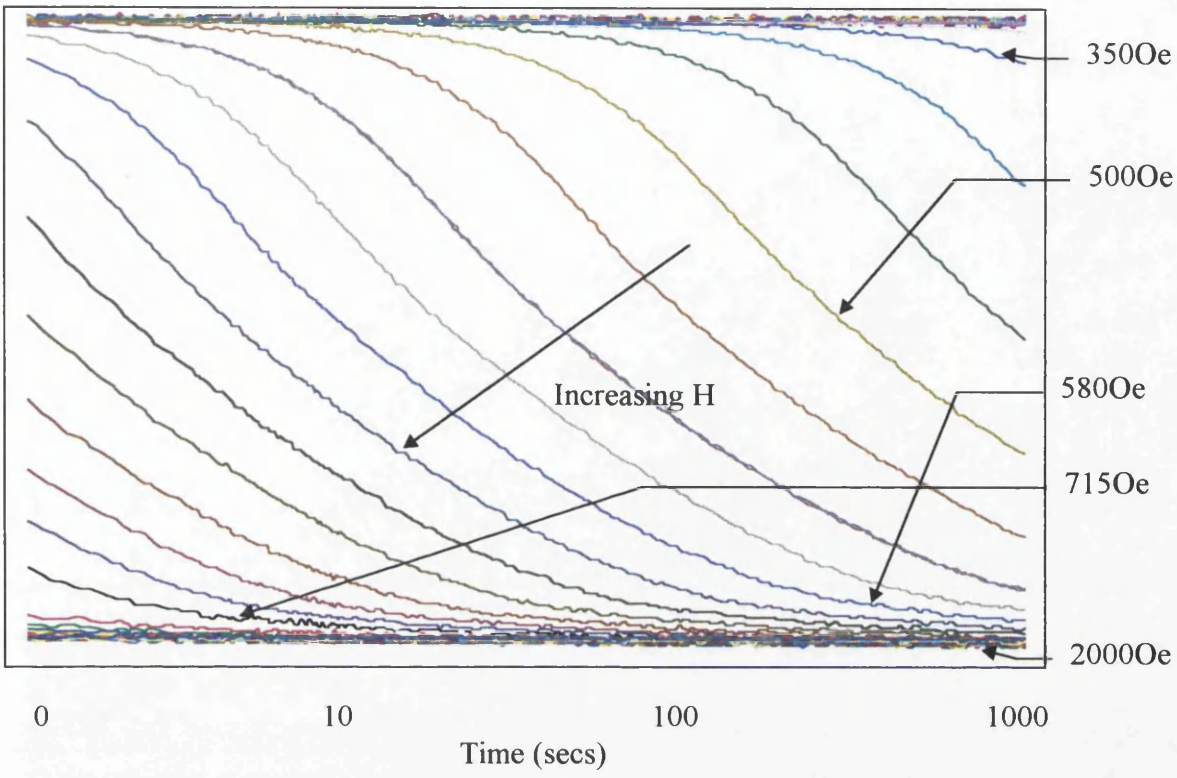

Figure 5.18: Magnetisation versus log(time) plots for $Co_{40}Ni_{60}$/Pt multilayer. The vertical scale goes from $+m_s$ to $-m_s$. Selected field values are indicated on the right hand side.

dependent studies on the AGFM which show just this.

The change in micromagnetic structure with the applied field is shown in figure 5.19. Each figure was taken at the same time after the field was increased (≈5 seconds) since time dependent effects were present.

The reversal started at only a few points, none of which were in the field of view during any of the experiments. These nucleated domains were irregular in shape (figure 5.19a), with the seperation of the domain walls having no fixed value which suggests that they were probably being defined by pinning sites. These domains grew to cover the field of view and evolved at the same time, leaving isolated areas of unreversed magnetisation in the form of irregular elongated domains (figure 5.19b). These unreversed regions continued to shrink and disappear as the field was increased (figure 5.19c). These small unreversed domains eventually disappeared as the time or the field was increased.

The time dependent sequences and difference images (figure 5.20) show in more detail the growth of the domains, and show that the sample can be almost completely reversed in a steady field under the effect of time alone. The difference images here also highlight the fact that as with the other multilayer samples described in this chapter, the areas which are reversing vary greatly in size. The shape of the domains observed for this sample, however, are considerably different from the other multilayers described in this chapter, having a more variable width.

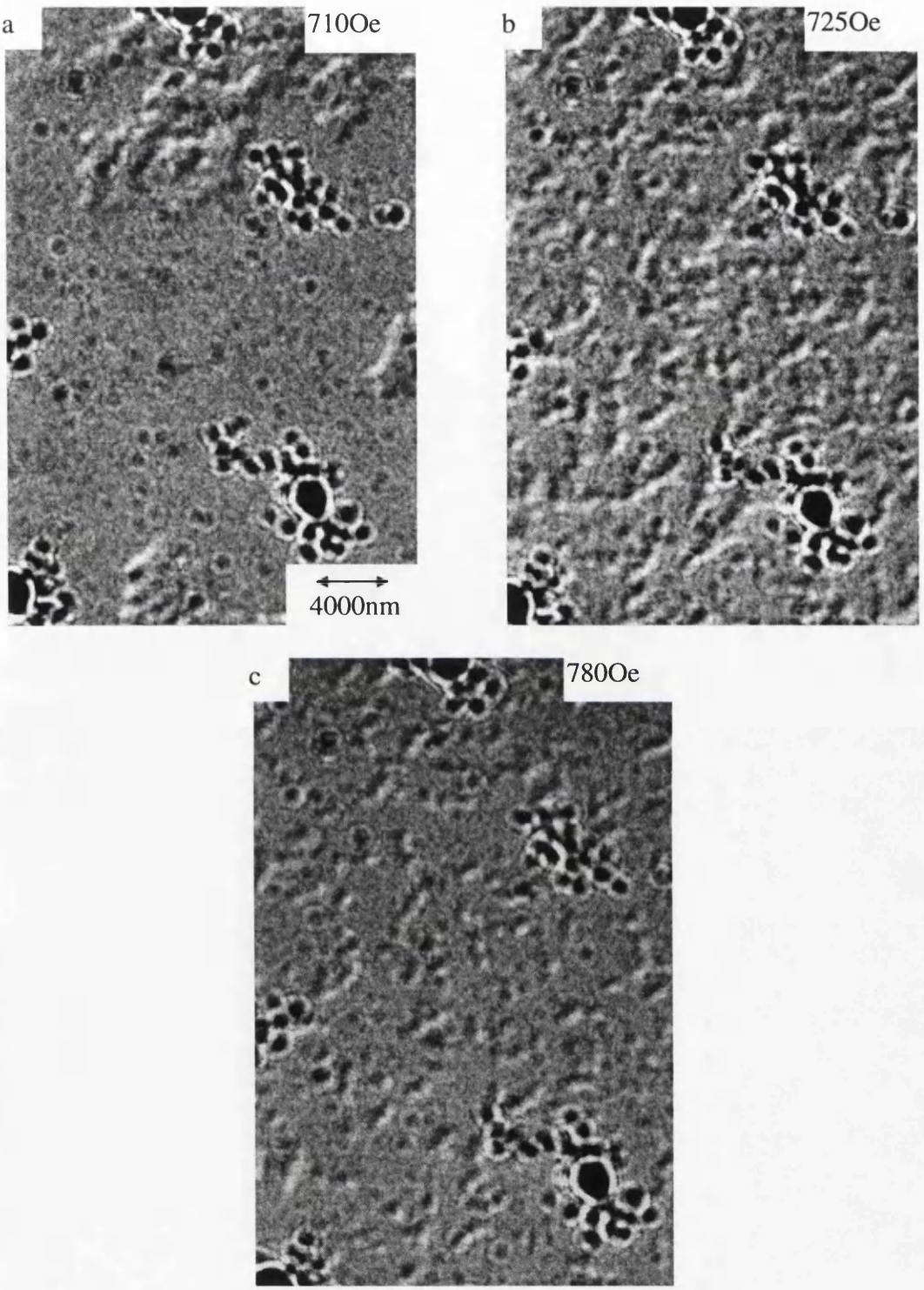

Figure 5.19: Fresnel images of the micromagnetic structure of $Co_{40}Ni_{60}$ multilayer changing with an applied field.

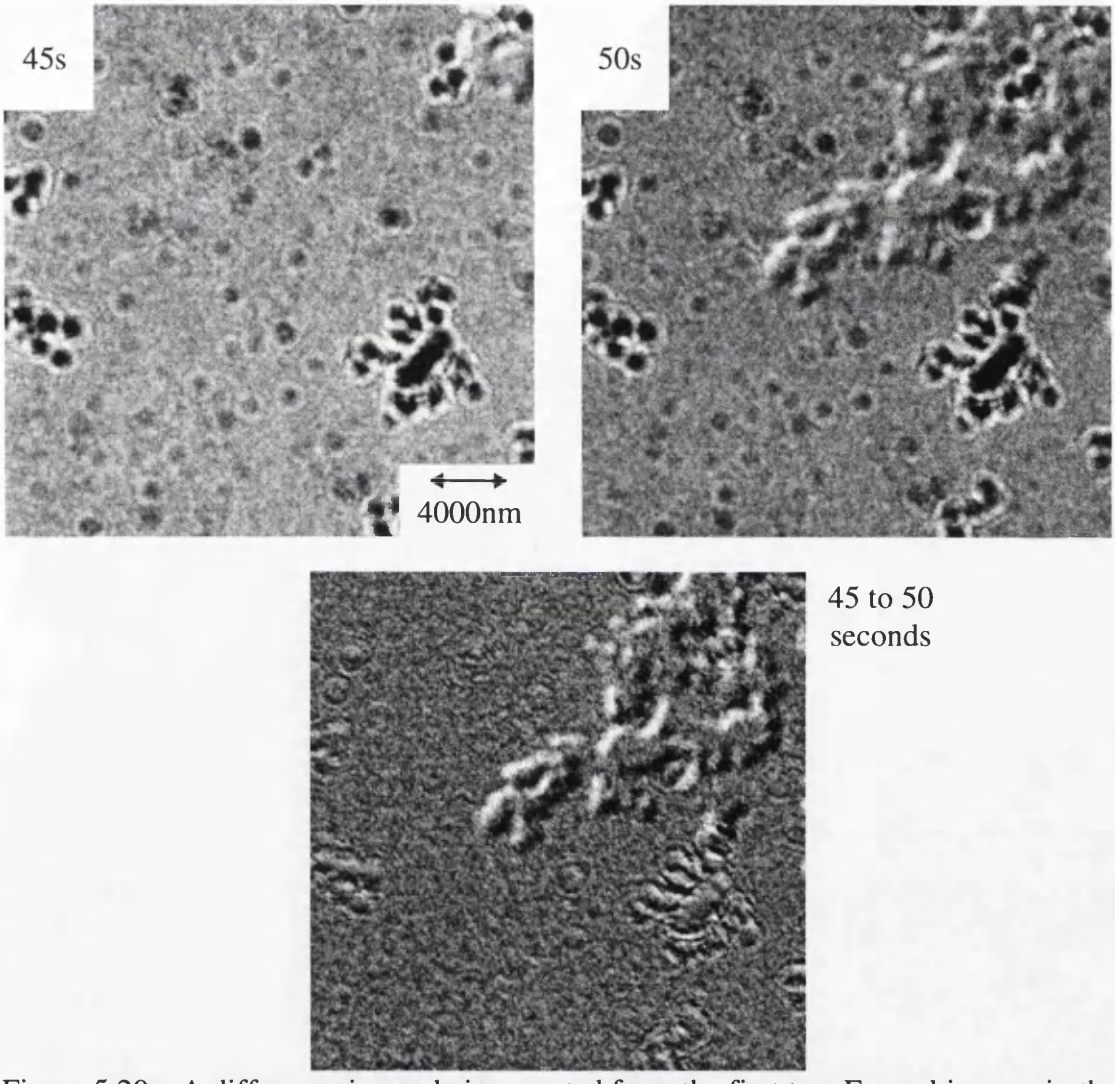

Figure 5.20a: A difference image being created from the first two Fresnel images in the time dependent sequence. This shows the domains which appeared between 45 and 50 seconds.

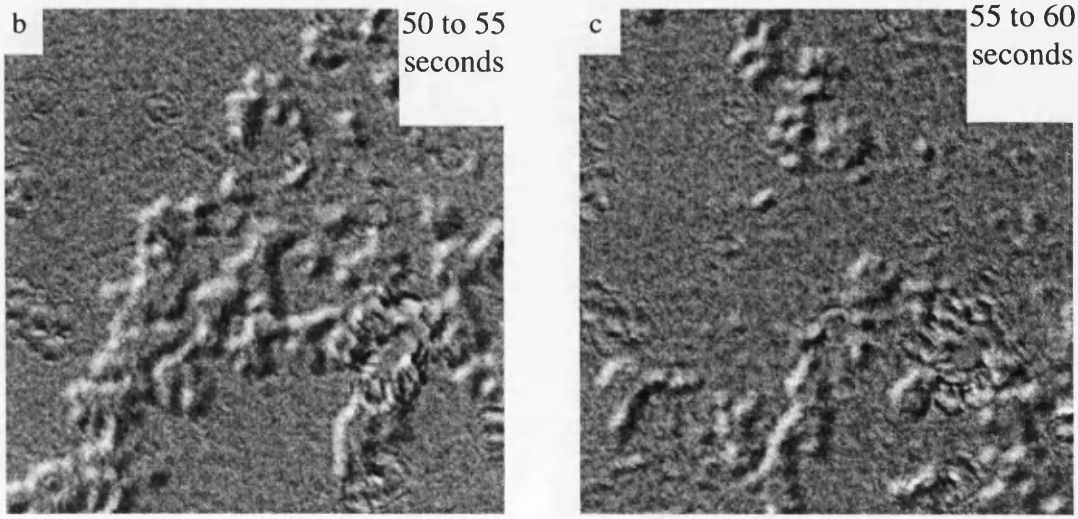

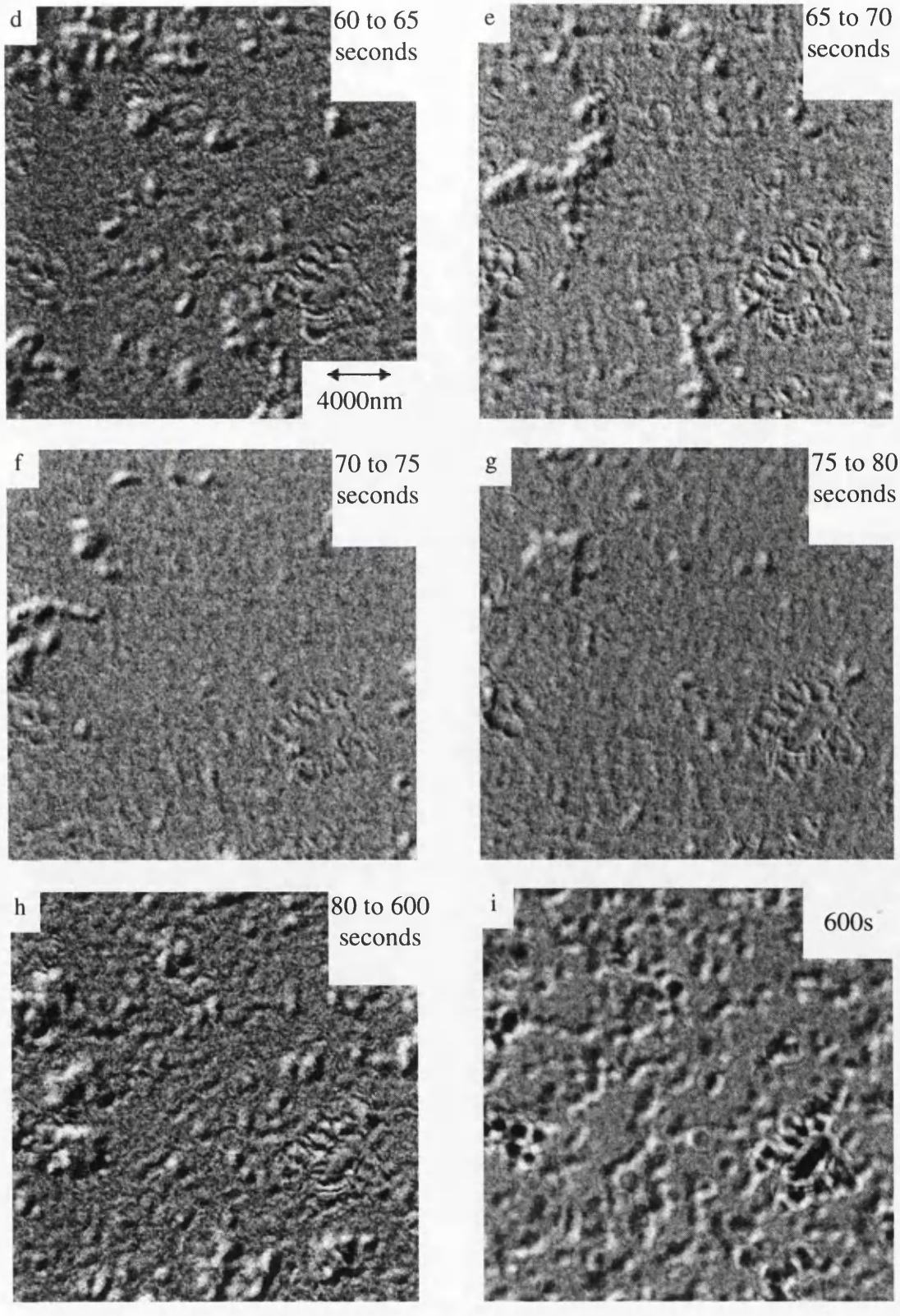

Figures 5.20b to h: difference images showing domains which appeared in the time intervals indicated.
Figure 5.20i: The domain pattern after 600s.

5.2 The magnetisation processes in amorphous Tb(Nd)FeCo alloys

Current magneto optic media are based on rare earth-transition metal (RETM) amorphous alloys such as TbFeCo, since they fill all the requirements for magneto optic media at current laser wavelengths (≈800nm). RETM alloys were first described as magneto optic media in 1973 [1] when GdCo and GdFe were used. It is not fully understood how the perpendicular magnetic anisotropy arises, although it has been suggested that it is caused by elongated areas of local ordering which are present in the media [16]. The properties of the thin films do however depend strongly on the concentration of the rare earth element(s) (Tb, Nd) present [17]. Furthermore the RETM alloys do suffer from poor corrosion resistence, with the rare earth metal(s) diffusing towards the surface of the thin film forming oxides [18] even after a protective overlayer has been applied, and poor Kerr rotations at the shorter wavelengths which will be used for magneto optic recording in the future. In an attempt to increase the Kerr rotation at short wavelengths, lighter rare earth metals like Nd have been added to the alloy. These attempts have been largely unsuccessful [19].

Two samples are described in this section: $Tb_{19}Nd_{14}Fe_{48}Co_{19}$ (sample A) and $Tb_{30}Fe_{46}Co_{24}$ (sample B). This work is being carried out in collaboration with D.Raasch at Philips in Aachen, Germany, who deposited these samples. Both these samples were evaporated onto silicon substrates with silicon nitride windows suitable for TEM investigation, and were covered with a 20nm Al overlayer. Sample A is 43nm thick whilst sample B is 22nm thick. Characterisation carried out by Dr. Raasch showed that the Curie temperature for sample A is 227C and 287C for

sample B. Both samples were characterised on the TEM, as described in chapter 3, and on the AGFM as described in chapter 2. In addition a magnetisation sequence was recorded for sample A.

The diffraction patterns for both samples are similar and show the broad band of reflections that you would expect from an amorphous material (figures 5.21). The sharp lines which are visible are probably from the 20nm thick aluminium overlayer, which is shown to be a textured polycrystalline coating.

The contrast present in both the bright field images is the same (figures 5.22). The scale of the "features" is ≈20nm, and this will be the size of the crystallites in the overlayer.

The Fresnel images (figures 5.23) are quite similar for both the samples, showing an irregular maze like domain structure with domain periodicity of around 400nm, although the scale of the magnetic features in sample A is slightly smaller than this. The larger features which can be clearly seen on the Fresnel images are not magnetic and are probably dirt particles.

The hysteresis loops (figures 5.24) show that while the coercivity for sample A is suitable for investigation in the TEM, the coercivity of sample B is over 8000Oe, which is larger than the largest field that can be applied in situ in the microscope (≈6000Oe). The irregularities on the hysteresis loops of sample B can not be fully explained, but are probably artefacts of the AGFM.

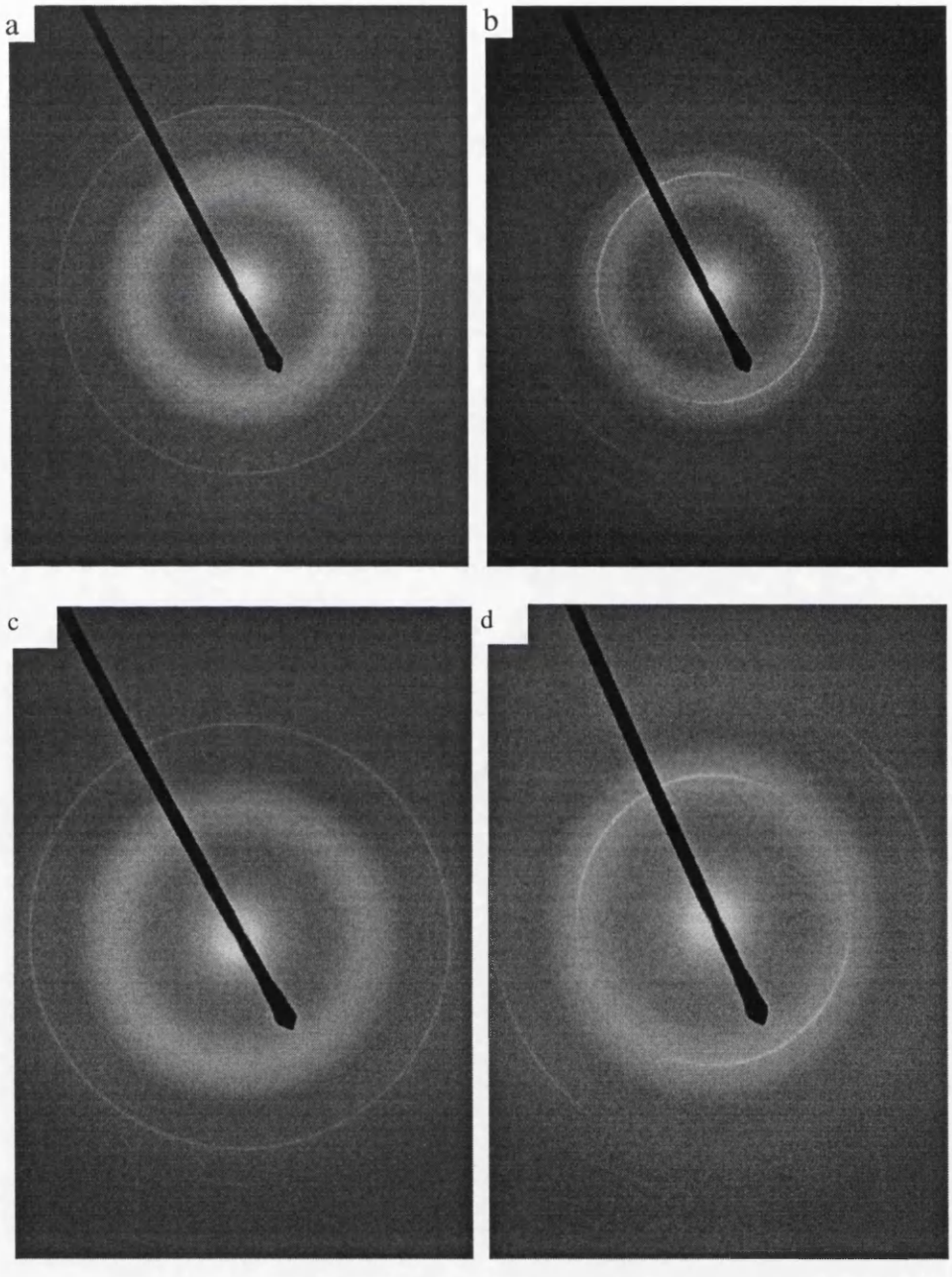

Figure 5.21: Diffraction patterns of NdTbFeCo (sample A) perpendicular to electron beam (a) and tilted to an angle 20° from perpendicular (b) and TbFeCo (sample B) perpendicular to the electron beam(c) and tilted to an angle of 20°from perpendicular (d). The broad band of reflections caused by the amorphous nature of the sample can be clearly seen in all images, along with the crystallite contrast from the aluminium protection layer.

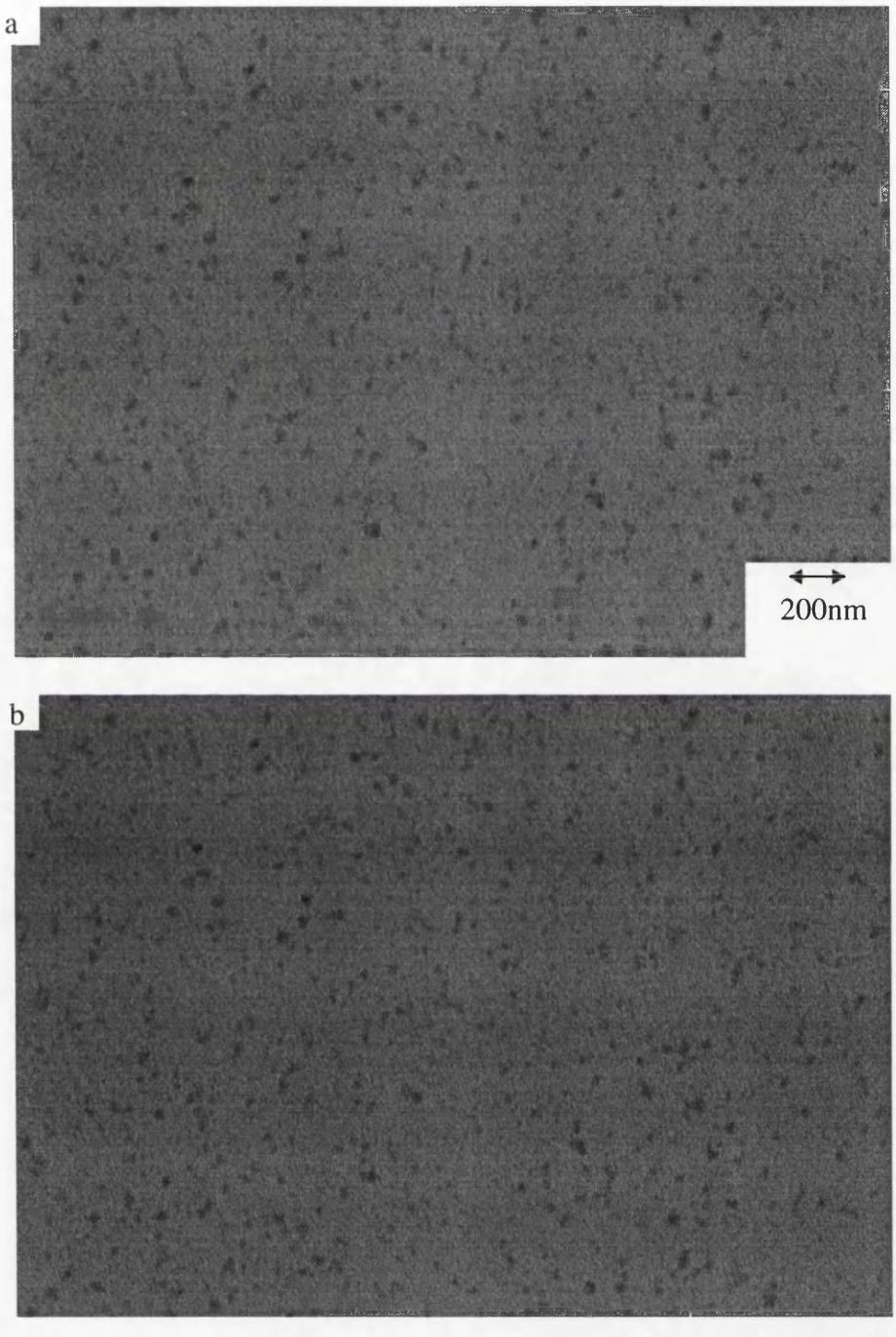

Figure 5.22: Bright field image of NdTbFeCo (sample A) (a) and TbFeCo (sample B) (b) showing the low contrast and the crystallites in the aluminium layer.

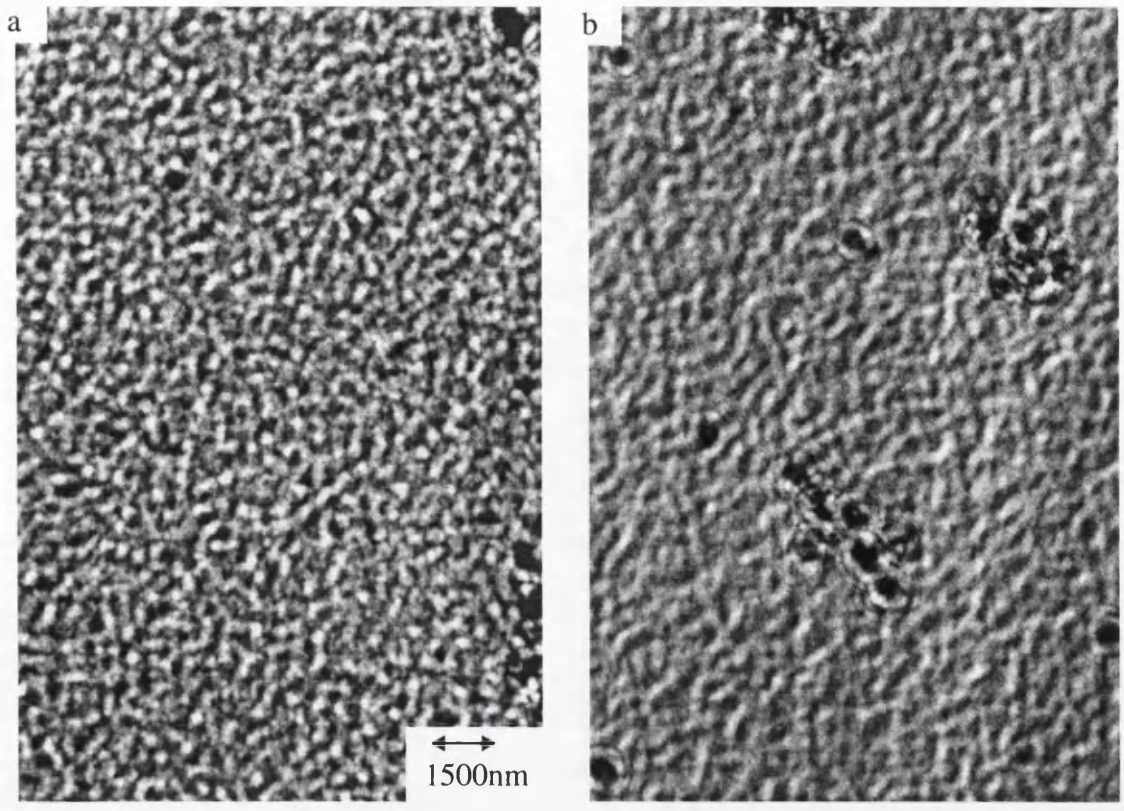

Figure 5.23: Fresnel images of NdTbFeCo (sample A) (a) and TbFeCo (sample B) (b).

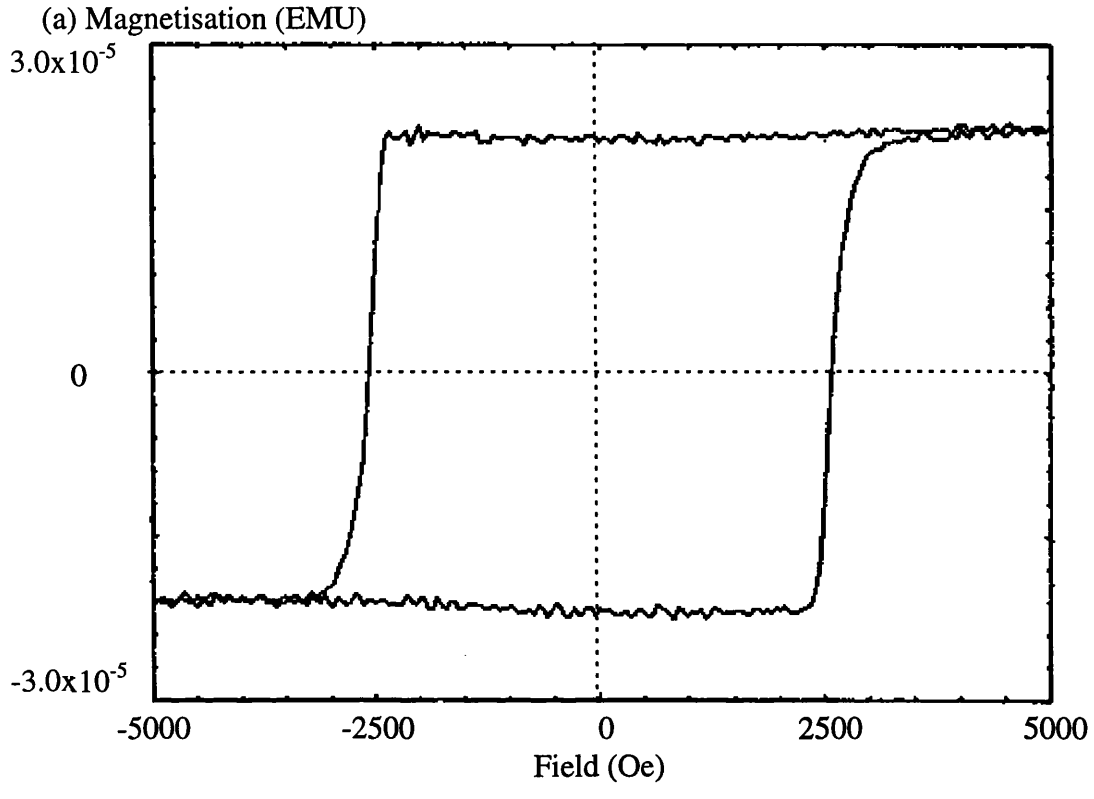

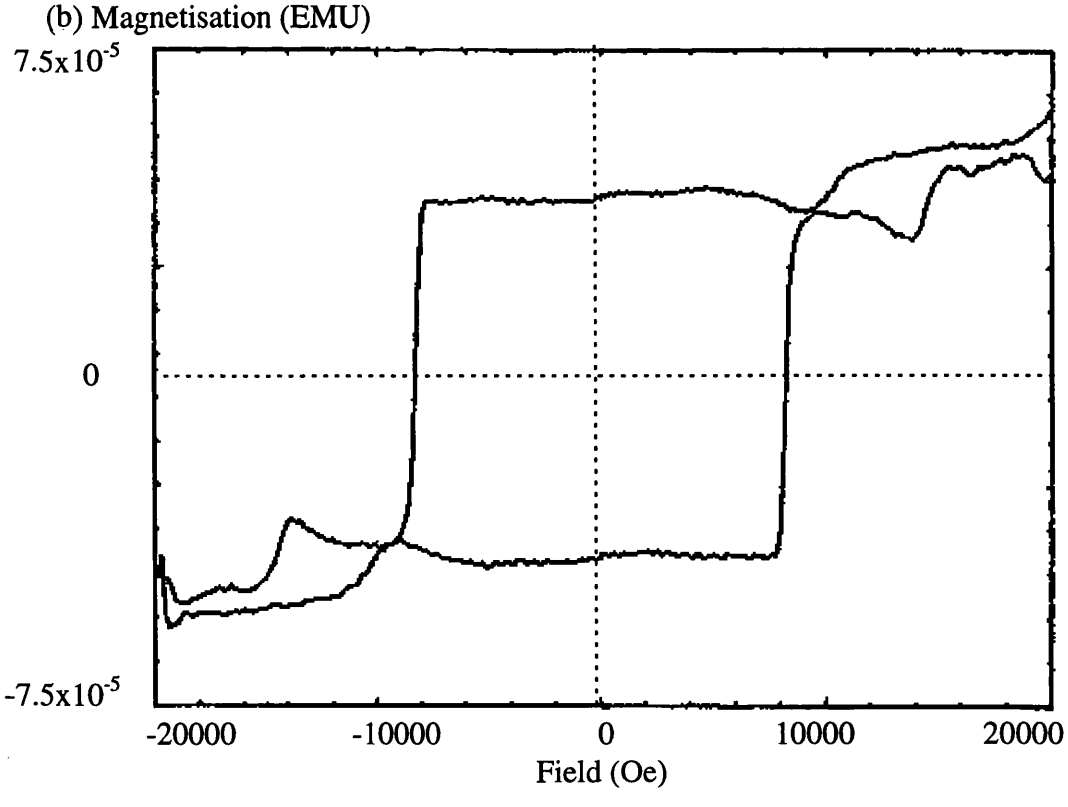

Figure 5.24: Hysteresis loops for NdTbFeCo (sample A) (a) and TbFeCo (sample B) (b), recorded on an AGFM.

The differentiated remanence curves (figure 5.25) show that, for sample A, the nucleation occurs at approximmately the same fields as domain wall motion, and for sample B, nucleation occurs at on average a slightly higher field than domain wall motion. From these switching field distributions we would expect any domains, which are formed at nucleation, to grow rapidly with no further increase in field. We would also expect this to be faster for sample B than sample A [13].

The time dependent curves (figure 5.26) for both samples show that once nucleation has occurred, the sample continues reversing when immersed in a steady field, although for sample A this is more gradual.

The change in micromagnetic structure with the applied field is shown in figure 5.27. Each figure was taken at the same time after the field was increased (≈5 seconds) since time dependent effects were present.

Once again the reversal never started in the field of view during any of the experiments, so it has to be assumed that it started at only a few points. These nucleated domains were irregular in shape and elongated (figure 5.27a). The nucleated domains did not appear to have a well defined width, which suggests once again that they were being defined by pinning sites. This domain structure continued to grow to cover the field of view. As this grew the domains evolved, reducing the areas between each domain (figure 5.27b). Eventually the reversed areas coalesced together leaving only small unreversed domains (figure 5.27c). These small unreversed domains would eventually disappear as the time or the field was increased

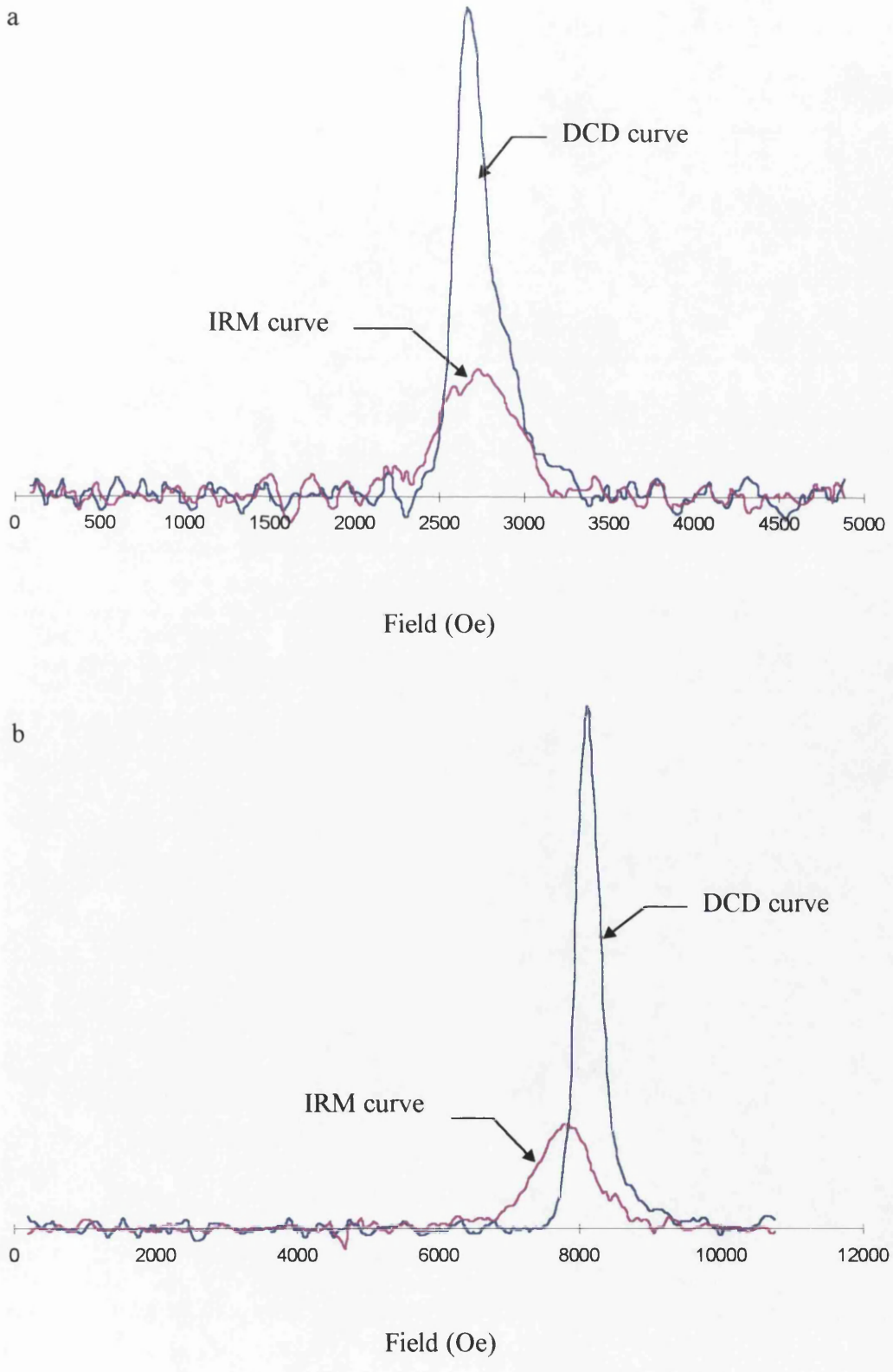

Figure 5.25: remanence curves for NdTbFeCo (sample A) (a) and TbFeCo (sample B) (b), showing that the domain nucleation field is similar to the domain wall motion field in both cases.

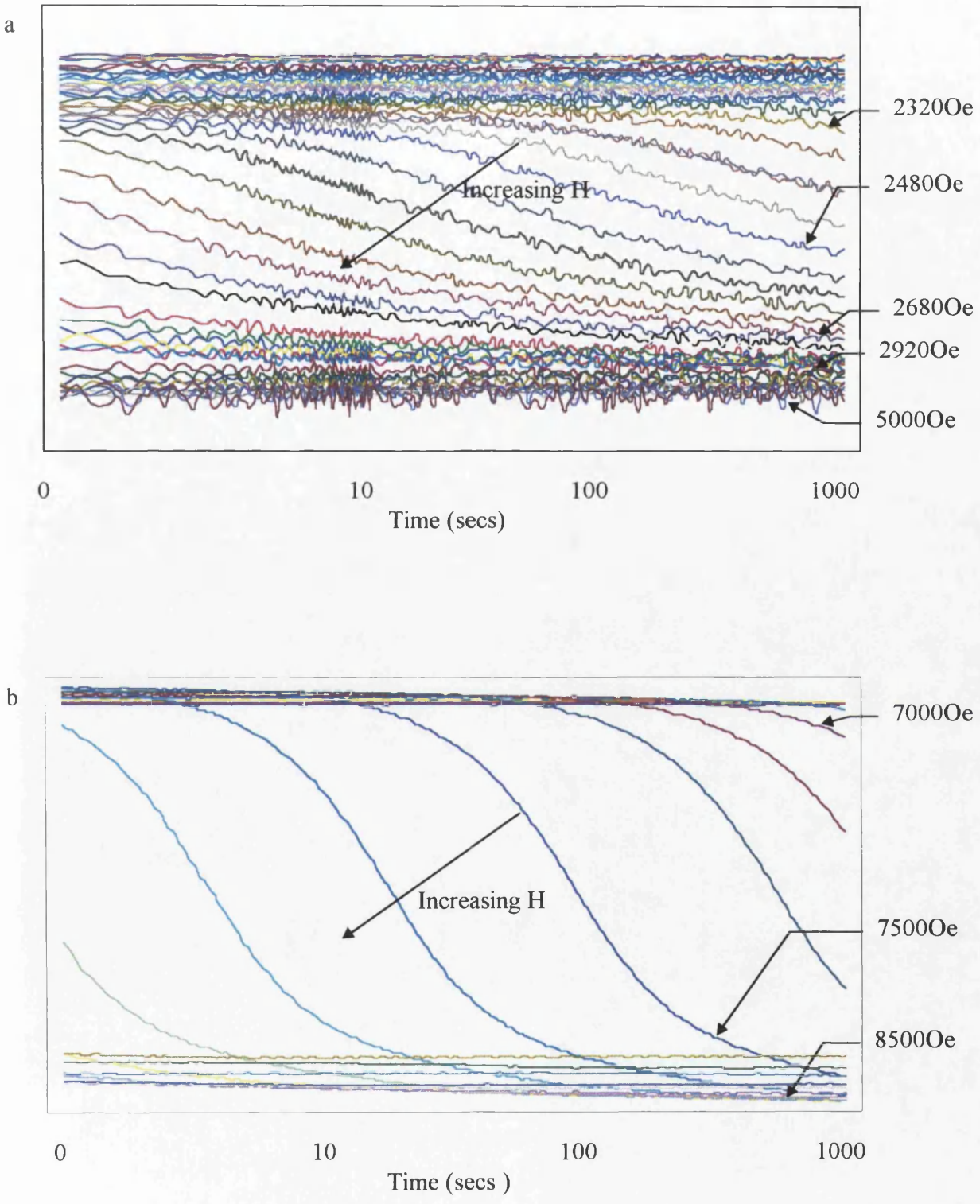

Figure 5.26: Magnetisation versus time plots for NdTbFeCo (sample A) (a) and TbFeCo (sample B) (b) taken on an AGFM. The vertical scale goes from $+m_s$ to $-m_s$. Selected field values are indicated on the right hand side.

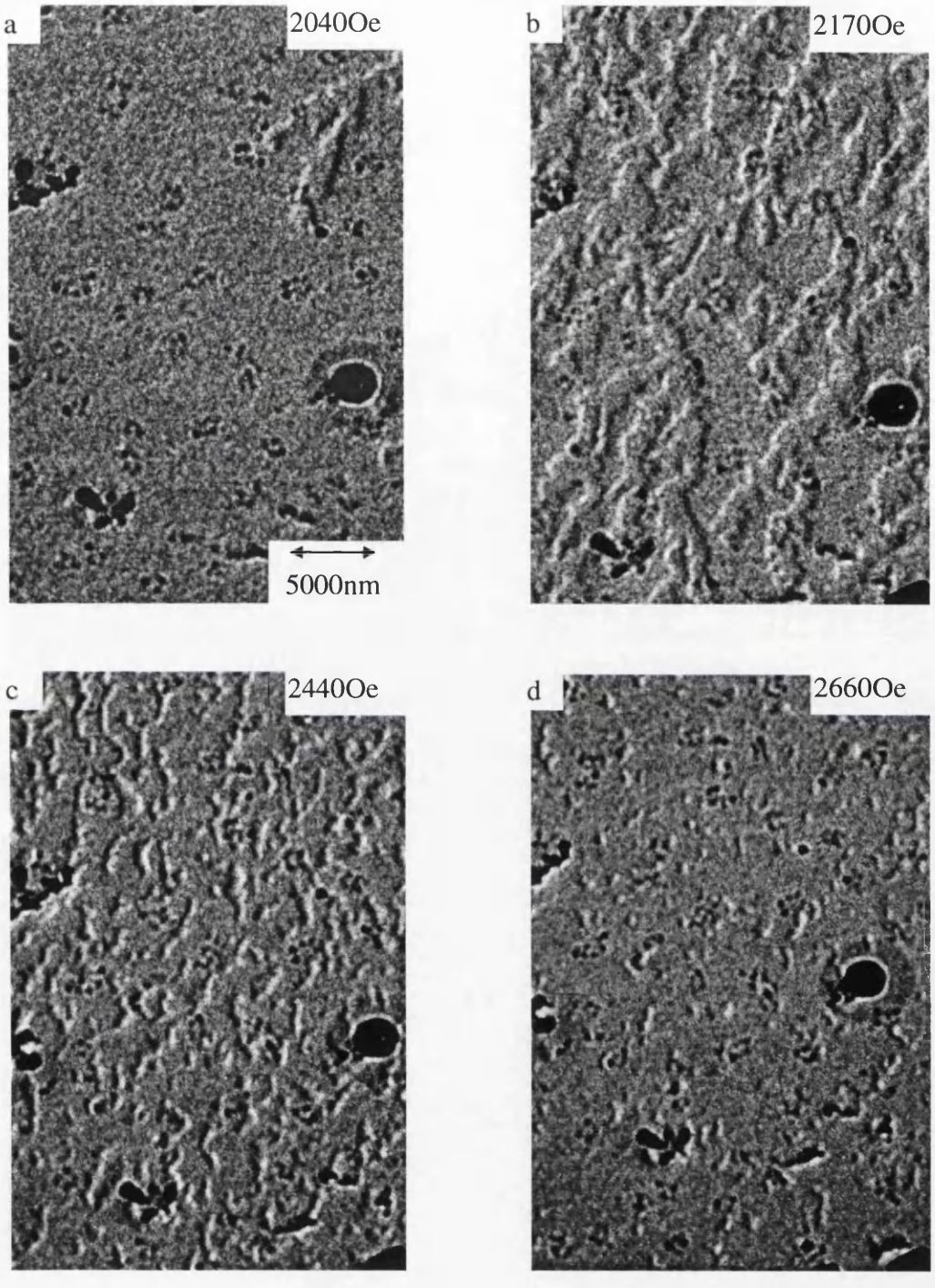

Figure 5.27: Fresnel images of the micromagnetic structure of NdTbFeCo (sample A) changing with the field applied.

(figure 5.27d). The only effect of increasing the field was to increase the rate of change of the magnetic microstructure. There are similarities between this process and that for the $Co_{40}Ni_{60}$ multilayers. There is a difference however in the shape of the domains which extend across the sample. The domains in this media are more elongated and directional.

5.3 Discussion

The use of several different experimental techniques has proved very useful in the examination of the magnetisation processes of the samples described in this chapter. In particular the ability to image the sample in a field of the experimenter's choosing was essential. This ability was enhanced by being able to record and play back a real time video of the reversal and time dependent phenomena which occurred. The technique reveals much information about the growth of the domains which could not otherwise have been deduced.

The domains observed during the magnetisation process were qualitatively similar to those previously described for Co/Pt multilayers and RETM alloys [20][21]. This is encouraging for their future use as MO media. The magnetisation process itself has been modelled using several different strategies.

The first model is that of Draaisma and de Jonge [23]. They use an updated version of the Kooy and Enz [22] model for a single magnetic layer, and apply it to multilayer systems. This model considers the balance of the magnetostatic, domain wall and Zeeman energies and from these considerations calculated the most stable

domain configuration for perpendicularly magnetised multilayers. Hysteresis and domain growth processes are ignored in this model since the domain walls are assumed to be freely mobile, and the global minimum energy state is always reached. This model predicts an idealised magnetisation curve which can be related to the magnetisation curves for the samples studied in this chapter.

The idealised M vs. H loop without hysteresis predicted by this model is shown in figure 5.28, the slope is drawn as a straight line but in actual fact the calculated slope deviates slightly from this, becoming less steep, near saturation, nonetheless for the purpose of my analysis, a straight line suffices. The two shapes of hysteresis loop described in section 5.1 can then be imagined to arise due to different values of the domain nucleation field. If domains were nucleated at field H_a on figure 5.28 then the most stable configuration is for the sample to reverse completely. The domains would then spread through the sample in a steady field until negative saturation was reached. This is similar to what appears to happen in the RETM alloys and $Co_{40}Ni_{60}$/Pt samples described in this chapter. If, however, domains are nucleated at field H_b in figure 5.28, the most stable state for the sample would be a magnetic moment somewhere between positive and reverse saturation. The magnetisation would then relax towards this stable state and the M vs. H curve would then follow the idealised curve if there are no additional energy barriers to be overcome. This is similar to what happens in the $Co_{50}Ni_{50}$/Pt multilayers described in this chapter.

Further energy barriers do, however, exist so the experimental curve will not follow the idealised curve exactly, but instead the system will relax into a local minimum state. The deviation of the actual hysteresis loop from the idealised curve through the

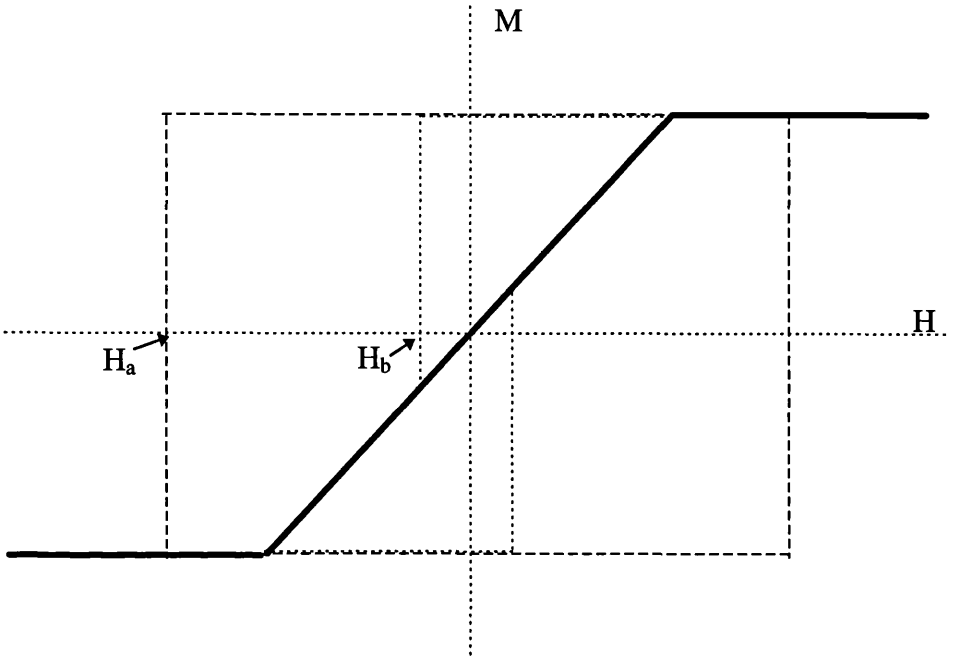

Figure 5.28: An idealised M vs. H loop for a perpendicularly magnetised sample, showing also ideal loops if domains nucleated at fields H_a and H_b.

origin may be indicative of the height of the energy barriers to be overcome. This can be seen in the hysteresis loops for the two multilayer samples with $Co_{50}Ni_{50}$ magnetic layers in particular. After initial nucleation the curve then closely follows the idealised curve until fields of around 1000Oe are reached; at these fields the slope of the M vs. H curve decreases. This can be seen to correspond with the "bump" in the switching field distributions seen for these samples at this field (figure 5.7).

The second model is an enhanced version of the Monte Carlo model developed by Lyberatos et al. [24], which has been applied to the $Co_{50}Ni_{50}$/Pt samples characterised in this chapter. The modelling was carried out by I.S.Weir, I.S.Molchanov and D.M Titterington in the Statistics Department at the University of Glasgow in conjunction with J.N.Chapman and myself. In this model the sample is given a starting condition, then exposed to a field. This model assumes that there will be energy barriers present so the final magnetic state reached could be a local minimum instead of the global minimum energy state reached in the Kooy and Enz and Draaisma and de Jonge models.

The model is based on a wrap around array of hexagonal crystallites in a steady applied field of the modellers' choosing. Wrap around array means that any structures leaving the array at one edge will be continued at the opposite edge as if the area of the array formed a continuous surface. The magnetic events are assumed to be thermally activated, and after each step one crystallite, selected on the basis of a probability distribution, reverses its magnetisation. This continues until any further reversals do not decrease the total energy of the system. The starting condition for this model assumes a single nucleation point. Account is taken in the model of

anisotropy, Zeeman, demagnetising and domain wall energy densities and these all contribute to the local field that is effective during the thermal activation. For the multilayer films of interest here, discreteisation was not only in the plane of the film but also in a vertical direction to allow for the number of magnetic layers in the stack. Key parameters in the model are: The intrinsic nucleation energy barrier, the intrinsic wall motion energy barrier, the wall energy, the activation volume, the saturation magnetisation, the cell dimensions, the single layer dimensions and the number of layers.

This model was run with parameters appropriate to the samples with $Co_{50}Ni_{50}$ in the magnetic layer. The aim was to determine the set of parameters which most closely matched the domain configuration imaged for these samples at the coercive field and whose time dependent growth most closely matched that observed. In figure 5.29 domain patterns at the coercive field (300Oe) for several simulations are shown and are compared with an image taken on the TEM at an applied field of 300Oe. The results show the dependence of the results on two parameters which are not well known: the activation volume (V_{act}) and the domain wall energy (σ_w). "The activation volume is the volume associated with the change in magnetisation between the maximum and minimum energy positions of the domain wall" [24]. The best match with the imaging results appears to be for a V_{act} which is 0.015 of the crystallite volume and a σ_w which is $1.8x10^{-3}Jm^{-2}$ [25]. V_{act} cannot be measured directly, but our value does not seem unreasonable. This volume represents a column through the multilayer approximately $5nm^2$ in area, or approximately ¼ of a crystallite on a single layer. The value for σ_w has been measured for Co/Pt multilayers as $7.9x10^{-3}$ Jm^{-2} [6],$12.3x10^{-3}$ Jm^{-2} and $12.9x10^{-3}$ Jm^{-2} [26]. Our value is

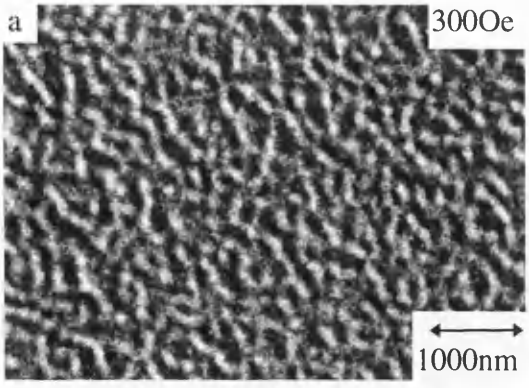

Recorded Fresnel image

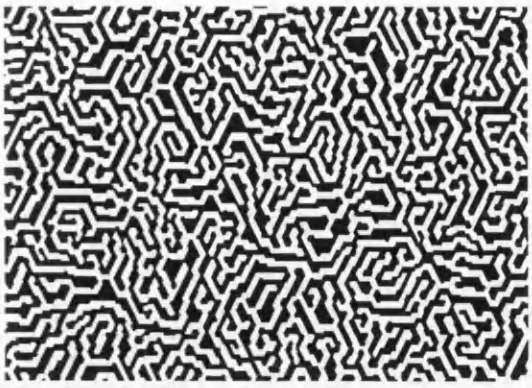

V_{act}=0.015V, σ_w=1.8

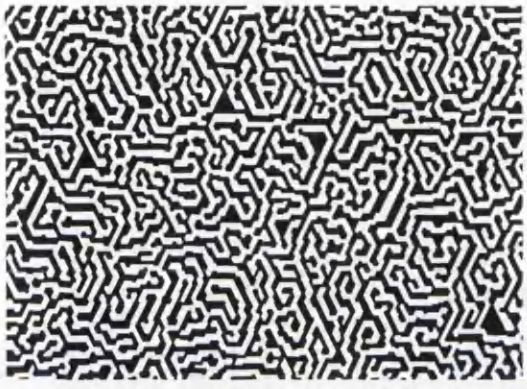

V_{act}=0.015V, σ_w=1.7

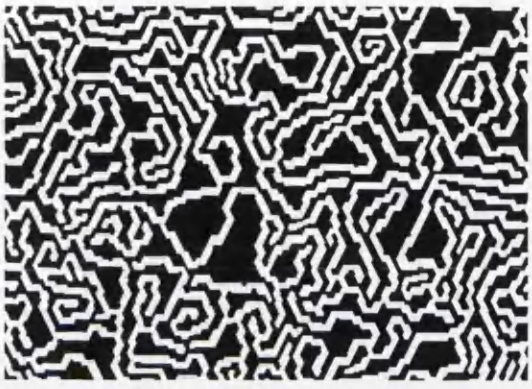

V_{act}=0.015V, σ_w=1.9

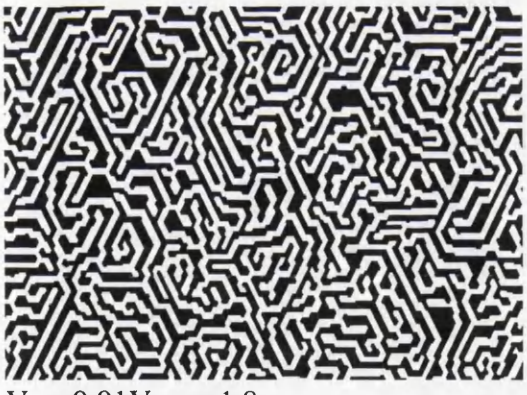

V_{act}=0.01V, σ_w=1.8

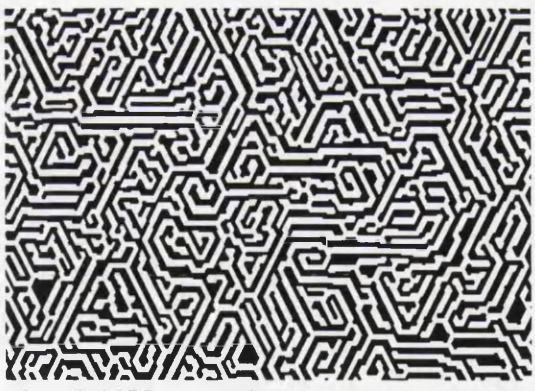

V_{act}=0.02V, σ_w=1.8

Figure 5.29: Recorded domain pattern at 300Oe compared to simulated domain patterns at same field and with parameters shown. V is the volume of a single crystal in the model.

between a factor of four and seven times smaller than the values quoted. This is reasonable since the M_s for $Co_{50}Ni_{50}$ (~1T) is about half that for pure Co (1.8T) and σ_w is related to M_s since the domain walls will have very few free poles compared to domains. This leads me to believe that while the modelled behaviour may not be exactly correct, it is close. The growth of the domain patterns could be matched reasonably well with these values (figure 5.30), however the time dependence of these results were not satisfactory since the growth of the domains was continuous, rather than in jumps as seen experimentally. The next stage of this project is to be the addition of pinning sites to the model in the hope that the time dependence of the behaviour is improved.

Looking at the energy barriers to domain wall motion, they will be predominately domain wall pinning [24]. There is however a second source of domain wall motion energy barriers, that is the forcing together and subsequent annihilation of two domain walls with an opposite chirality. This process will only occur towards the end of the reversal process as the unreversed domains shrink in size. This can be contrasted with domain wall pinning, which can be assumed to have an constant effect throughout the whole reversal process if the pinning sites are randomly positioned. This additional mechanism appears to apply to the $Co_{50}Ni_{50}$/Pt multilayers, and to a lesser extent the $Co_{40}Ni_{60}$ multilayers, where there are a set of energy barriers at high field as the sample approaches negative saturation. This again would support the presence of domain walls of the type mentioned previously [15].

The results in this chapter have shown the usefulness of using several different techniques to investigate the properties of thin film media and the extra information

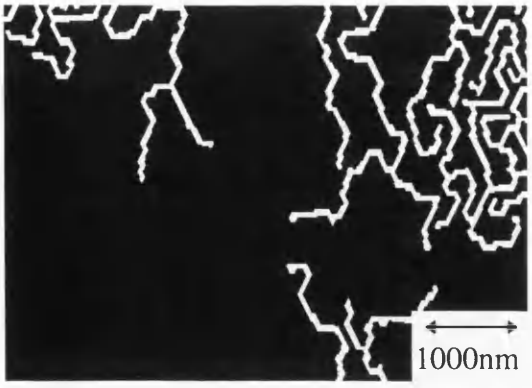

12.5% reversed

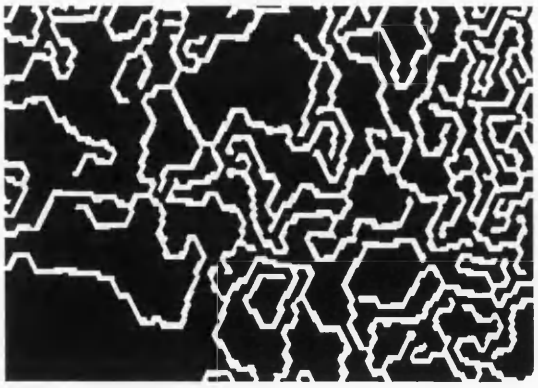

25% reversed

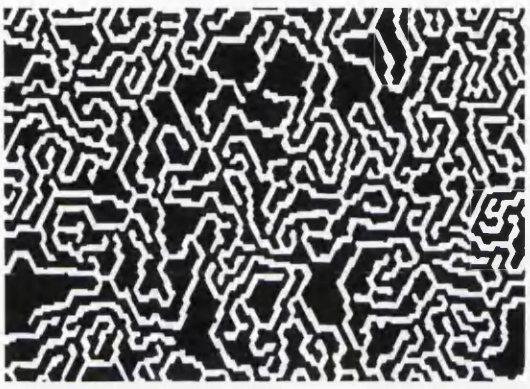

38% reversed

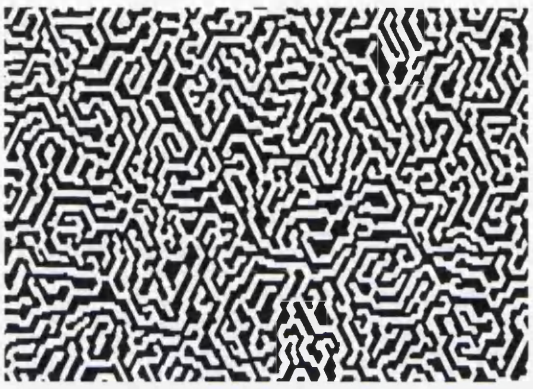

48% reversed (equilibrium)

Figure 5.30: Simulated domain growth for multilayer with $Co_{50}Ni_{50}$ in magnetic layer in a field of 300Oe. V_{act}=0.015V, σ_w=1.8x10^{-3}Jm^{-3}.

that can be gained if the experimental techniques are used in conjunction with modelling. The TEM techniques developed in this thesis in particular have been central to the understanding of the magnetisation process. In particular it would have been virtually impossible to describe the magnetisation processes in the multilayers with $Co_{50}Ni_{50}$ in the magnetic layer without the image sequences obtained on the TEM.

References:

[1] P.Chaudari, J.J.Cuomo and R.J.Gambino, Appl. Phys. Lett. **22**(1973) 337.

[2] P.F.Carcia, A.D.Meinhaldt and A.Suna, Appl. Phys. Lett. **47** (1985) 178.

[3] P.F.Carcia, J. Vac. Sci. Technol **A5** (1987) 1975.

[4] W.B.Zeper, F.J.A.M.Greidanus, P.F.Carcia and C.R.Fincher, J.Appl. Phys. **65** (1989) 4971.

[5] Y.Ochiai, S.Hashimoto and K.Aso, IEEE Trans. Mag. **25** (1989) 3755.

[6] W.B.Zeper, Ph.D Thesis, Philips research laboratories, (1991).

[7] M.Mes, J.C.Lodder, T.Takahata, I.Moritani and N.Imamura, MORIS '92, J. Mag. Soc. Jpn. **17-S1** (1993) 44.

[8] S.Hashimoto, A.Maesaka, K.Fujimoto and K.Bessho, J. Magn. Magn. Mater. **121** (1993) 471.

[9] S.Hashimoto, J. Appl. Phys. **75** (1994) 439.

[10] P.J.H.Bloemen, W.J.M. de Jonge, F.J.A. den Broeder and W.Hoving, J.Magn. Magn. Mater. **93** (1991) 105.

[11] P.Bruno, J. Magn. Soc. Jpn. **15-S1** (1991) 15.

[12] H.W. van Kesteren and W.B.Zeper, J. Magn. Magn. Mater. **120** (1993) 271.

[13] Q.Meng, Ph.D. Thesis, University of Twente, (1996).

[14] D.Weller, R.F.C.Farrow, R.F.Marks, G.R.Harp, H.Notarys and G.Gorman, Mast. Res. Soc. Symp. Proc. **313** (1993) 791.

[15] R.Ploessl, J.N.Chapman, M.R.Scheinfein, J.L.Blue, M.Mansuripur and H.Hoffmann, J. Appl. Phys. **74** (1993) 7431.

[16] A.G.Dirks and H.J.Leamy, Thin Film Solids **4** (1977) 219.

[17] D.Raasch, P.Hansen and D.Mergel, J. Appl. Phys. **76** (1994) 8022.

[18] M.Aeschlimann, G.L.Bona, F.Meier, M.Stampanoni, A.Vaterlaus, H.C.Seigmann, E.E.Marinero and H.Notarys, IEEE Trans. Mag. **Mag-24** (1988) 3180.

[19] C.J.Lin and H.V.Do, IEEE Trans. Mag. **26** (1990) 1700.

[20] C.J.Lin, J.C.Sui and R.H.Geiss, J. Appl. Phys., **63** (1988) 3835.

[21] D.M.Donnet, V.G.Lewis, J.N.Chapman, K.O'Grady and H.W. van Kesteren, J. Phys. D., **26** (1993) 1741.

[22] C.Kooy and U.Enz, Philips Res. Rep., **15** (1960) 7.

[23] H.J.G.Draissma and W.J.M.de Jonge, J.Appl. Phys., **62** (1987) 3318.

[24] A.Lyberatos, J.Earl and R.W.Chantrell, Phys. Rev. B. **53** (1996) 5493.

[25] J.N.Chapman, J.Rose, I.S.Weir, I.S.Molchanov and D.M.Titterington, J. Mag. Soc. Japan - accepted for publication 1997.

[26] D.M.Donnet, Ph.D Thesis, The University of Glasgow, (1992).

Chapter 6

TEM investigations of CoPt magnetic recording media

6.0 Introduction

In-plane magnetic recording has been described in chapter one. In this chapter I will present and discuss the results of characterisation experiments carried out on experimental magnetic recording media. This work was carried out in collaboration with S.Casey, E.W.Hill and J.J.Miles at the University of Manchester. The samples were deposited by S.Casey. The experimental procedures have been described previously in chapters two and three.

Magnetic in plane recording has been around for decades. During this time the recording media have changed frequently in an unrelenting drive for higher fidelity analogue and higher density binary recording. In recent years the rate of improvement has been such that the binary recording density has increased by an order of magnitude every ten years.

The density of a binary recording system is called the areal density. This is measured in gigabits per square inch (Gb/in^2). The areal density of a recording system is governed by two factors: the track density (measured in tracks per inch), and bit density (measured in bits per inch). To increase the track density, the recording head has to be narrow, with high sensitivity and an accurate positioning mechanism. Bit density is increased by decreasing the head to media spacing (without causing a head

crash) and both the media and head have to be capable of supporting the density of recording required. In this chapter I will concentrate on the recording media, and in particular CoPt thin film alloys.

In order to be suitable as magnetic recording media, a medium would have to be able to support as small domains as possible. Since domain walls themselves are in some materials up to 100nm in width, which is comparable with the size of domains required, domain walls of this scale would have to be avoided for the very highest density recording media [1][2][3]. This can be done by growing crystallites which are magnetically decoupled from their neighbours, allowing the magnetisation direction to change over a much smaller range. As well as supporting small domains, these media would have to have: coercivities which are high enough to avoid accidental erasure, chemical and thermal stability and be cheap to manufacture.

6.1 CoPt as a recording media

Bulk CoPt has been known as a high coercivity material for some time. Initial attempts to deposit it electrochemically as a thin film for magnetic recording purposes, however, resulted in films where the crystallites were magnetically coupled and the coercivities were too low for magnetic recording (≈350Oe) [4]. Once these films could be deposited where the individual crystallites were decoupled, it was found that there were two other factors, as well as the coupling of the grains, which affected the magnetic properties of the final thin film: the structure of the crystallites, and the orientations of the crystallites [5][6][7][8][9].

The crystallite structure for CoPt can be either face centre cubic (FCC) or hexagonal close packed (HCP). This depends on several factors: deposition parameters, annealing conditions (if sample is annealed), the layer thickness, the substrate and the cobalt to platinum ratio. Thin cobalt layers are known to be FCC in structure, reverting to HCP if conditions are right as the layer grows thicker. This was also found to be the case with CoPt alloys deposited under certain conditions [8]. The deposition of an underlayer, or a suitable choice of substrate, is known to promote the growth of a preferred crystal lattice for several thin film structures. The crystal structure is also strongly affected by the Co to Pt ratio [6][7][8]. For example, in the papers cited, films deposited with more than 25% platinum are either FCC, or a mixture of FCC and HCP in structure, while those with less platinum have an HCP structure.

The crystallites can have a preferred crystal growth direction over the whole volume of the film, this is called texturing, or the preferred growth direction can extend over only a localised volume, this is called clustering. The orientation of a crystallite has an effect on the magnetic properties since this determines the easy axis for that area of the sample. For HCP crystals the easy axis is the "c" axis. This means that if the whole thin film is textured and the structure is HCP then there will be an anisotropy direction for the film corresponding to the mean direction of the "c" axis. Clusters of crystallites where there is local texturing may be expected to appear more magnetically coupled within the cluster than to neighbouring clusters due to the common easy axis. This is because the edges of the clusters will be more likely to act as pinning sites for walls than grains within the cluster. This has the effect of increasing the effective crystallite size and hence the minimum magnetic feature size [10]. Clustering and texturing is

thought to be related to the cobalt to platinum ratio, the substrate and the deposition conditions, although the evidence for this is unclear [8][11].

In order to investigate the micromagnetic effects of these changes in the microstructural properties of the thin films, several groups of thin films were investigated: (i) A group with different Co to Pt ratios, but the same thickness. (ii) Two films, one grown onto a standard silicon nitride substrate, the other grown onto a silicon nitride substrate which had been etched in warm sodium hydroxide for 20 minutes. (iii) A group with the same composition but grown to different thicknesses. Each film in these groups was investigated to determine their crystallite structure, orientation, texturing and size as well as their micromagnetic properties. Suitable films were then chosen from these groups and their magnetisation processes were investigated more thoroughly. Finally a suitable film was chosen and magnetic bits were recorded onto the film at different frequencies and the structure of these recorded bits was compared with predicted structures obtained from computer modelling [10].

6.2 The effect of composition on micromagnetic and microstructural properties of CoPt

The samples studied in this chapter are detailed in table 6.1. The compositions and coercivities were determined by Siobhan Casey at the University of Manchester, who also deposited the samples. The samples were sputter deposited onto silicon wafers with silicon nitride windows, suitable for TEM investigation. They were grown over a period of months during which the deposition techniques were known not to be

reproducable. For this reason it can not be assumed that the deposition conditions for all the films was the same.

name	composition		coercivity	thickness
sample A	37%Co	63%Pt	1188Oe	30nm
sample B	66%Co	34%Pt	800Oe	30nm
sample C	72%Co	28%Pt	900Oe	30nm
sample D	73%Co	27%Pt	971Oe	30nm
Sample E	78%Co	22%Pt	958Oe	30nm
Sample F	85%Co	15%Pt	200Oe	30nm
Sample G	88%Co	12%Pt	950Oe	30nm

Table 6.1: The samples studied in this section

The bright field images (figure 6.1) show that the films have crystallite diameters in the range of 10-15nm, except sample C, which has crystallites which are noticebly larger at approximately 25nm in diameter. All the samples also have a degree of clustering except sample F. The degree of clustering for the other samples varies from sample D where clusters consist of 100's of crystallites to samples C and E where the clusters consist of the order of 10 crystallites. There also appears to be two different crystal structures present in sample A, with the right hand side of the area (x) being similar to the other samples, but the left hand side (y) appears to have a different structure with more elongated crystallites. This is investigated later.

The untilted and tilted diffraction patterns (figures 6.2) are shown for each of the samples (an indexed pattern is shown in figure 6.3). The diffraction patterns were all

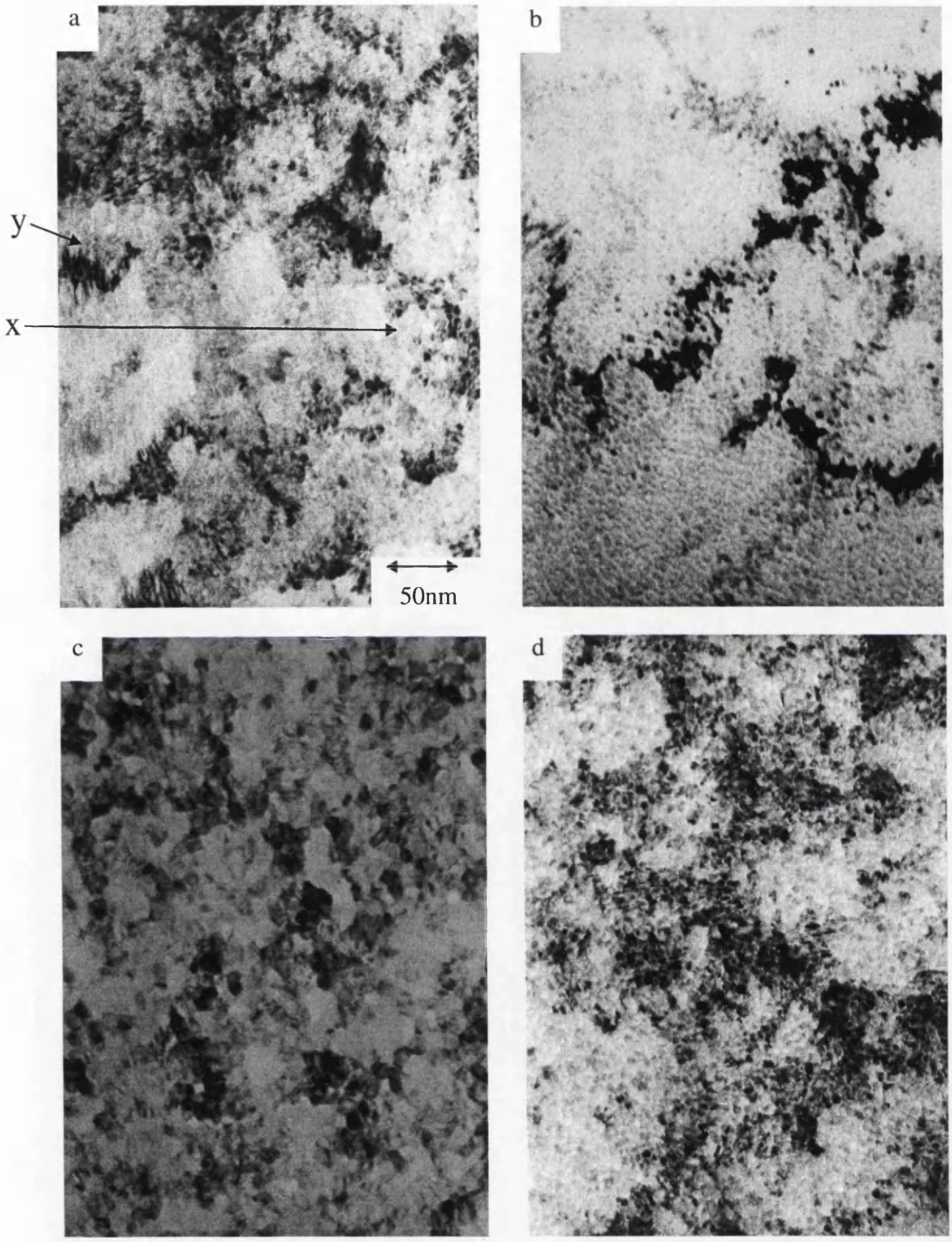

Figure 6.1: Bright field images of samples A to D, showing the crystalite size and clustering.

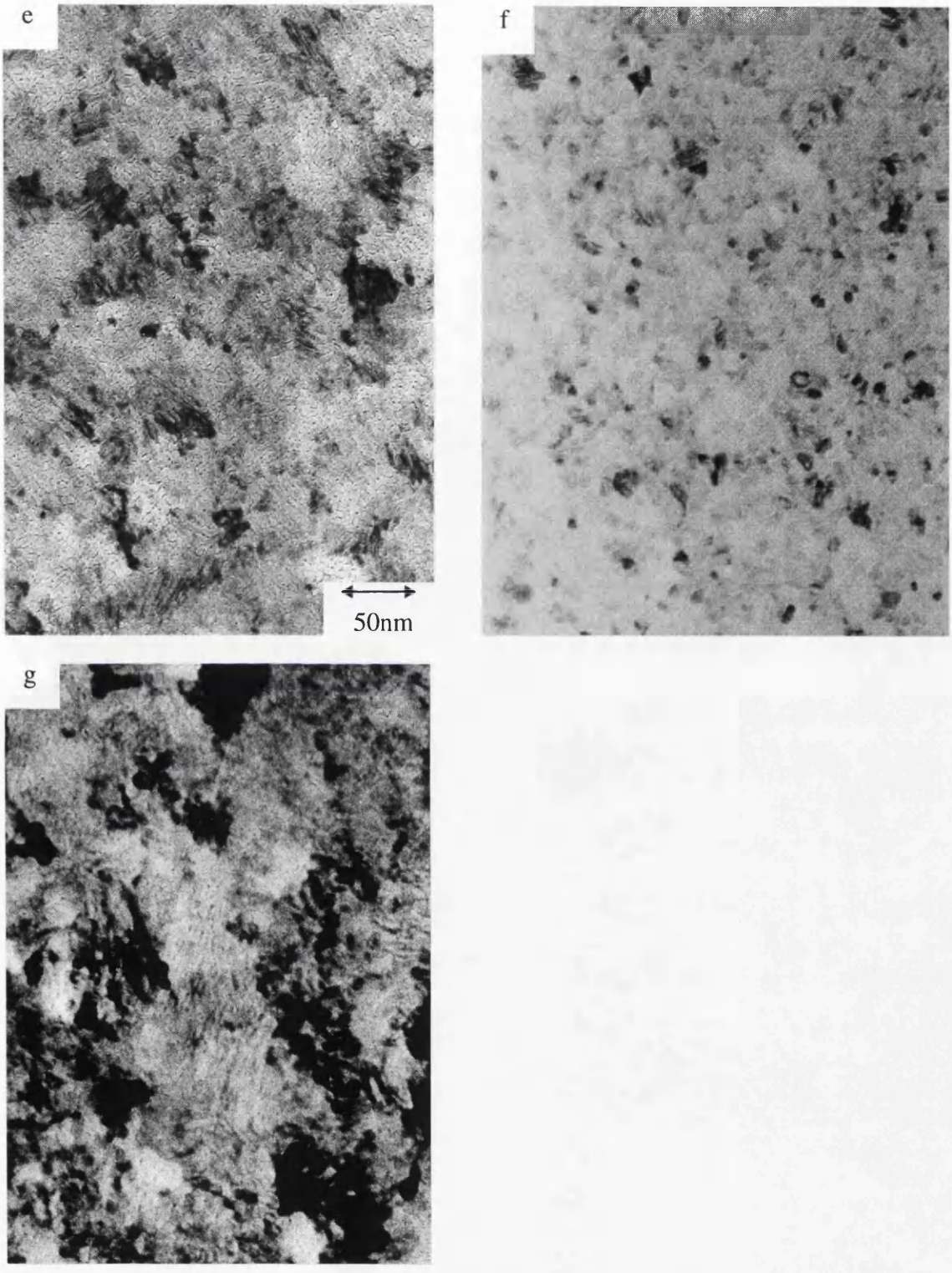

Figure 6.1(cont): Bright field images of samples E to G. Sample F shows no clustering, while samples E and G show extensive clustering.

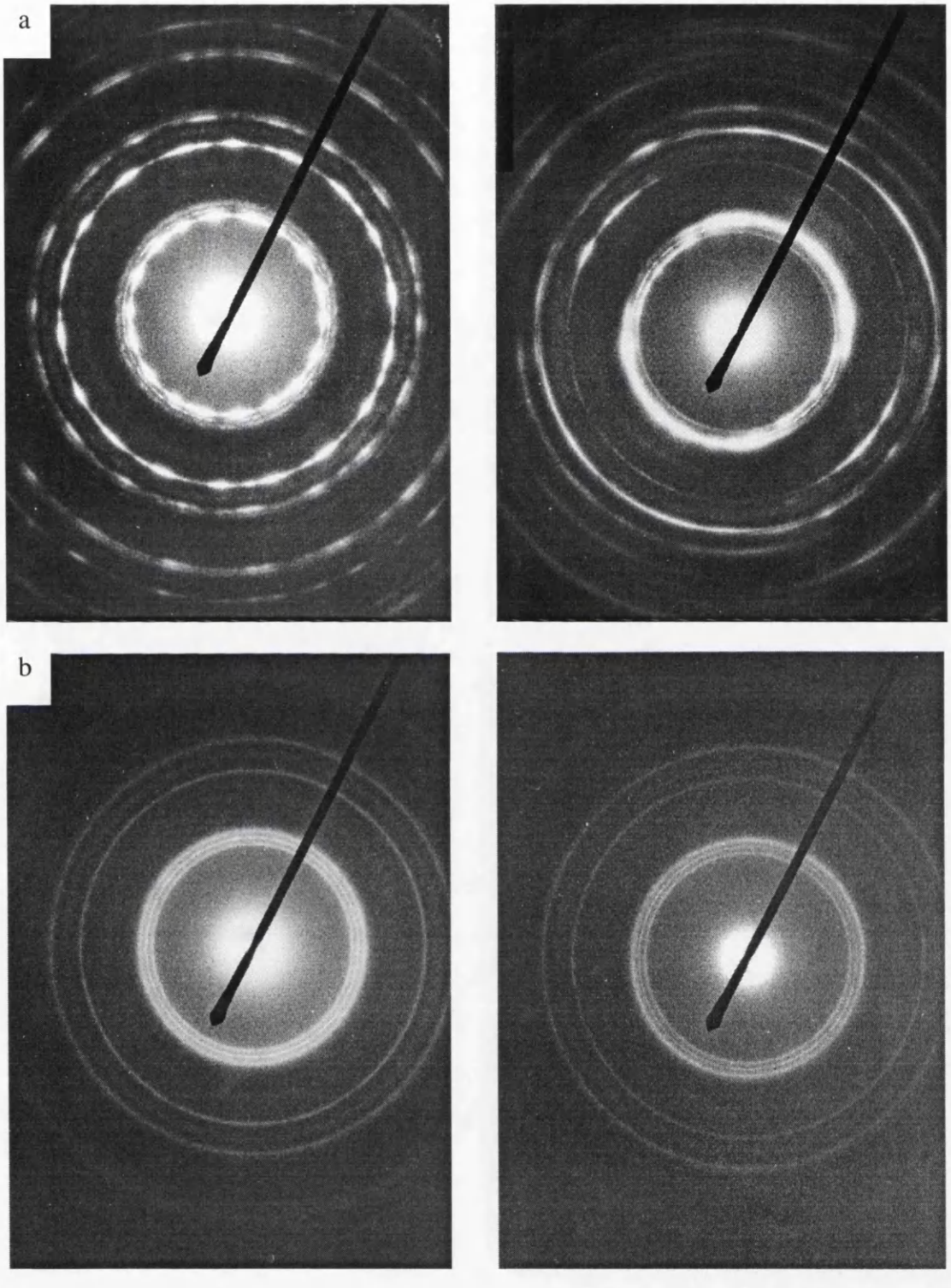

Figure 6.2 : Untilted and tilted diffraction patterns of samples A to B. The tilted diffraction pattern is on the right.

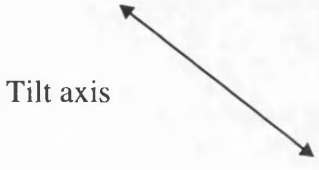

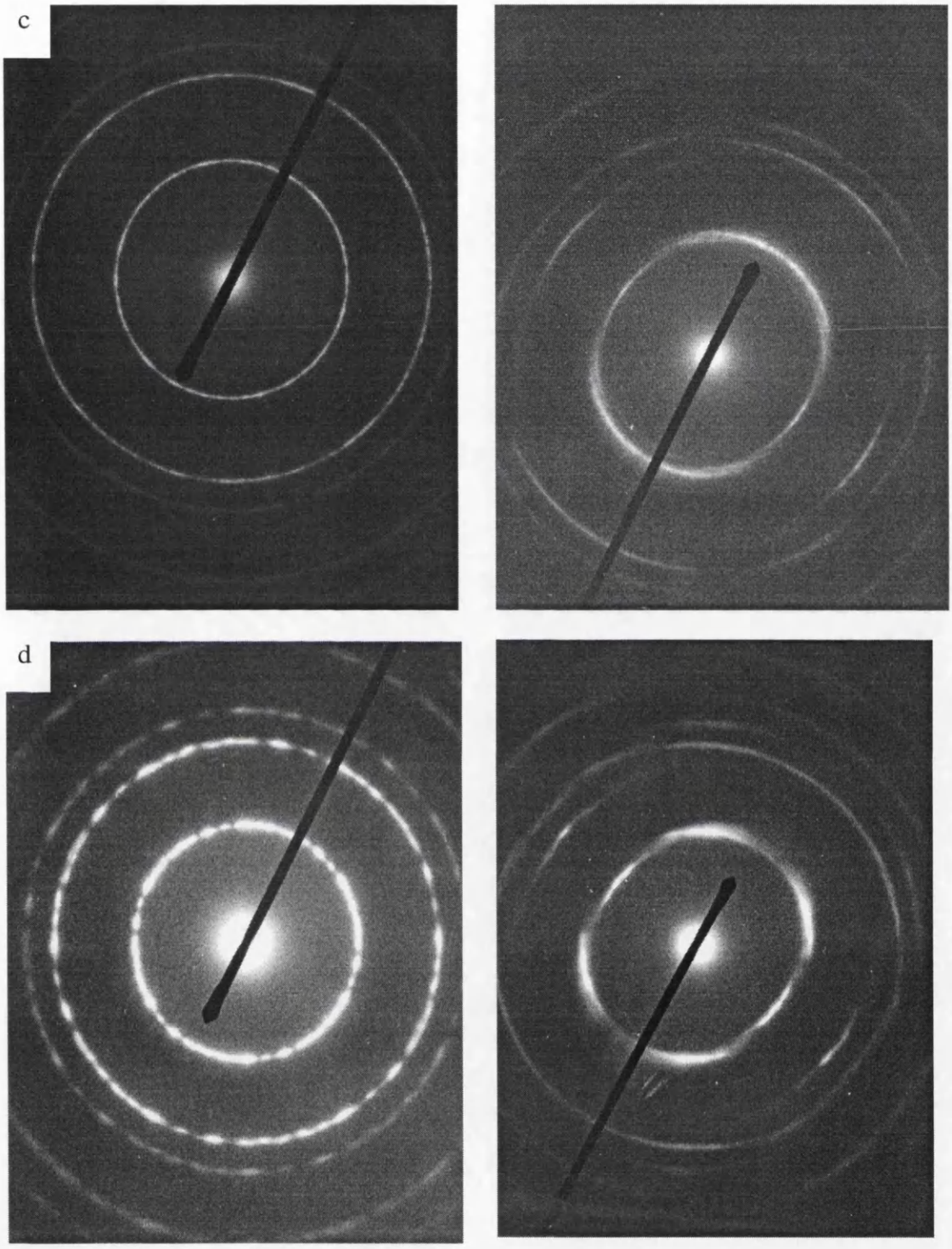

Figure 6.2 (cont): Untilted and tilted diffraction patterns of samples C to D. The tilted diffraction pattern is on the right.

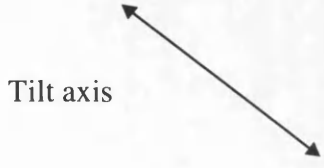

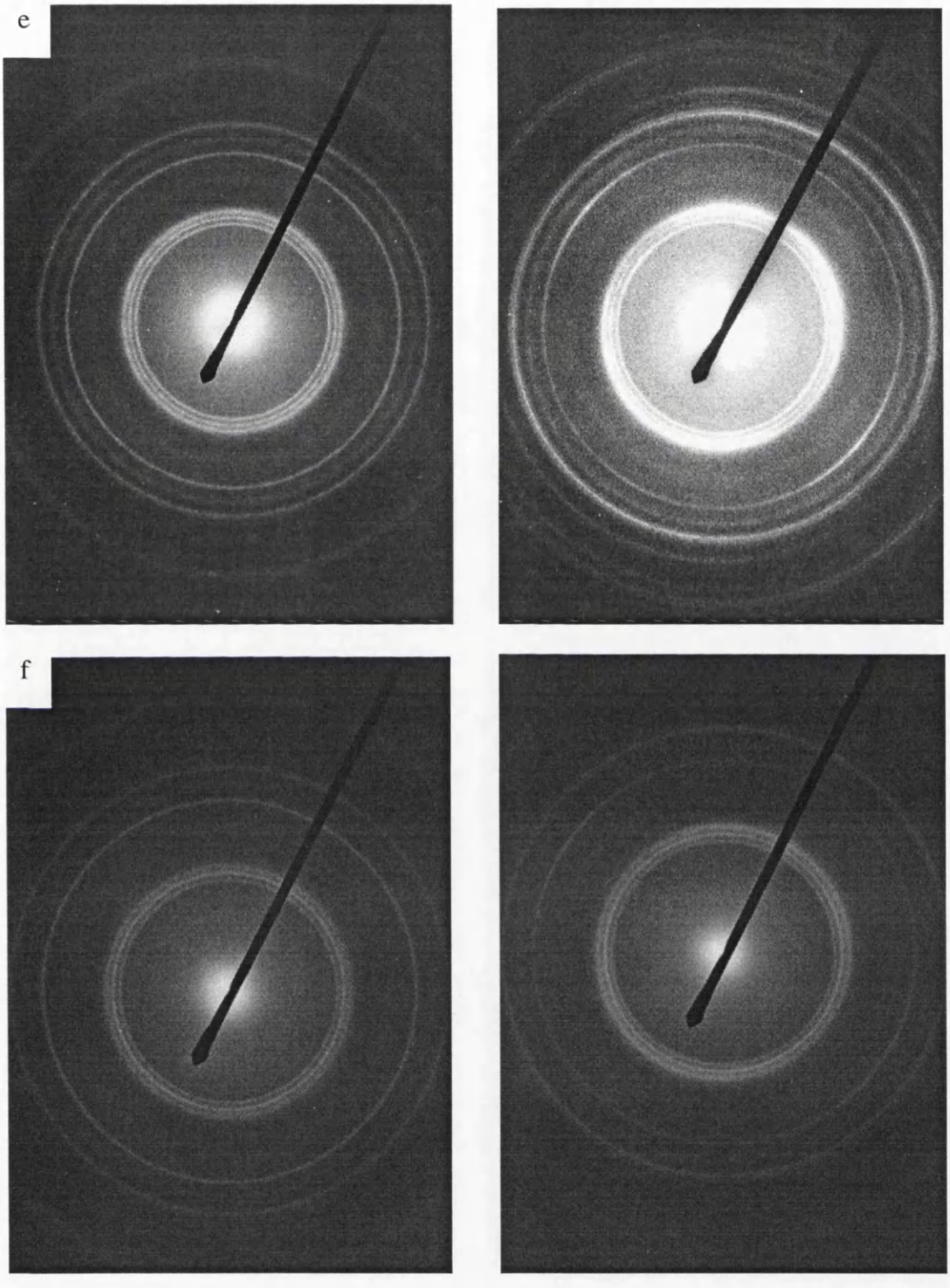

Figure 6.2 (cont): Untilted and tilted diffraction patterns of samples E to F. The tilted diffraction pattern is on the right.

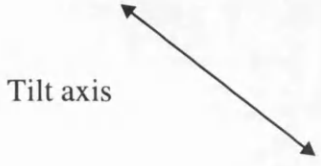

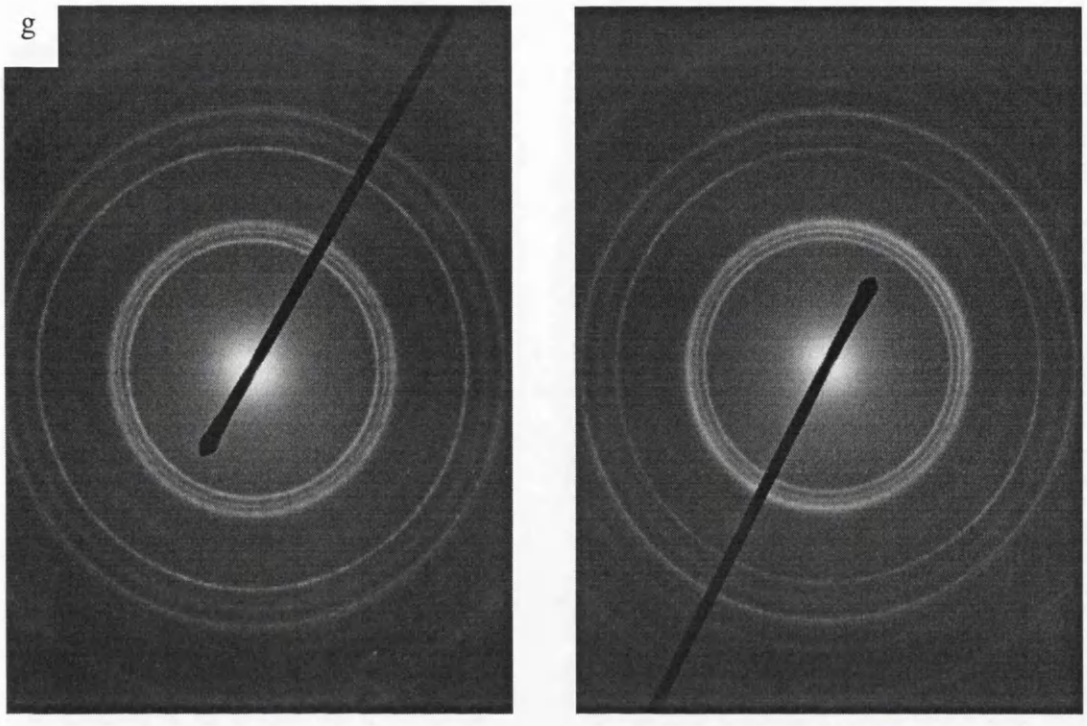

Figure 6.2 (cont): Untilted and tilted diffraction patterns of sample G. The tilted diffraction pattern is on the right.

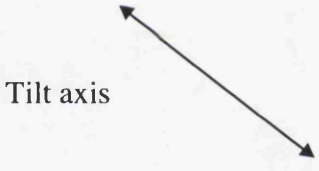

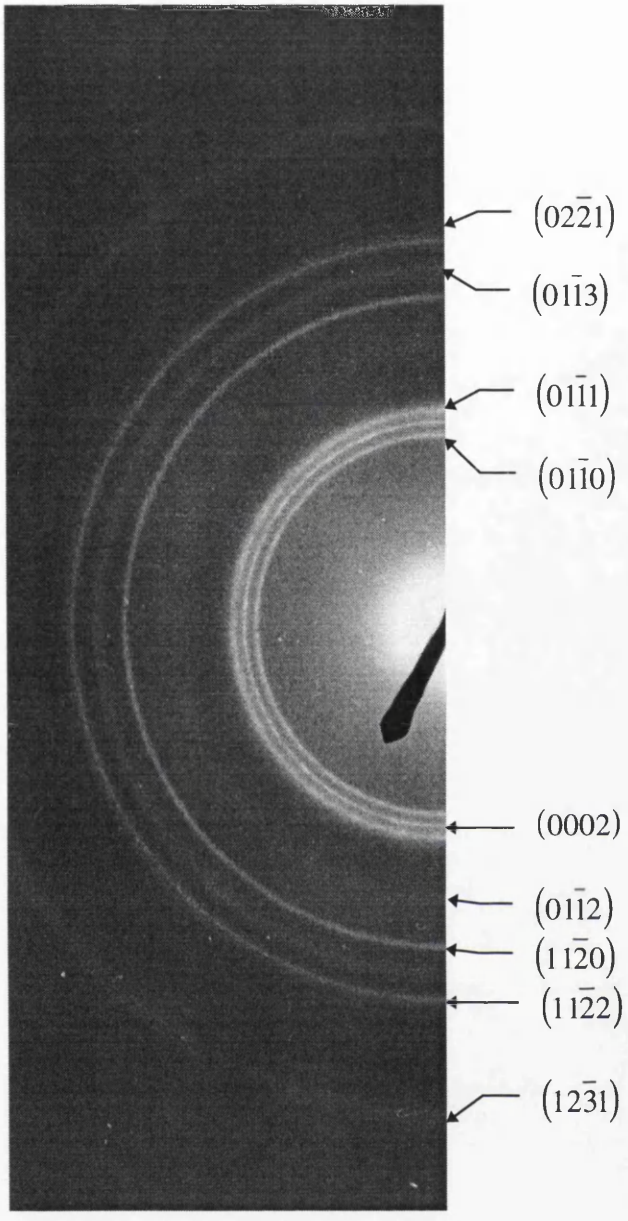

Figure 6.3: Indexed diffraction pattern for CoPt alloy.

taken from the same size of area ($\approx 65\mu m^2$). They show that all the samples are HCP in structure. Samples C and D show strong texturing with the "c" axis perpendicular to the plane of the film, while samples A and E show smaller degrees of texturing, also with the "c" axis perpendicular to the plane of the film. As the areas of the samples which contributed to the diffraction pattern were the same, the granularity of the rings can be attributed to there being fewer crystal orientations present for samples A and D. This could be indicative of the degree of clustering of the sample.

These structural results show no correlation with the composition of the samples. This is probably indicative of the different deposition conditions which were used for each sample, and shows the relative importance of the deposition conditions and the composition with respect to the final structure. Especially when it is noted that all the samples described here were HCP in structure, despite the fact that articles cited state that thin films with the same composition are FCC.

Lorentz (Fresnel and Foucault) images (figures 6.4) of the samples in the spin demagnetised state were taken. The spin demagnetised state was achieved by rapidly spinning the sample in a plane perpendicular to the plane of the sample and a magnetic field which was being reduced from 10000Oe to zero over the period of several seconds. The Fresnel images show that there was no directionality in the micromagnetic structure in the plane of the film. The magnetic structure could however be split into four groups: In-plane domains without ripple; In-plane domains with ripple; perpendicularly magnetised domains; and a mixture of all three. Ripple in domains is caused by crystallites within the domains having different easy axes, which

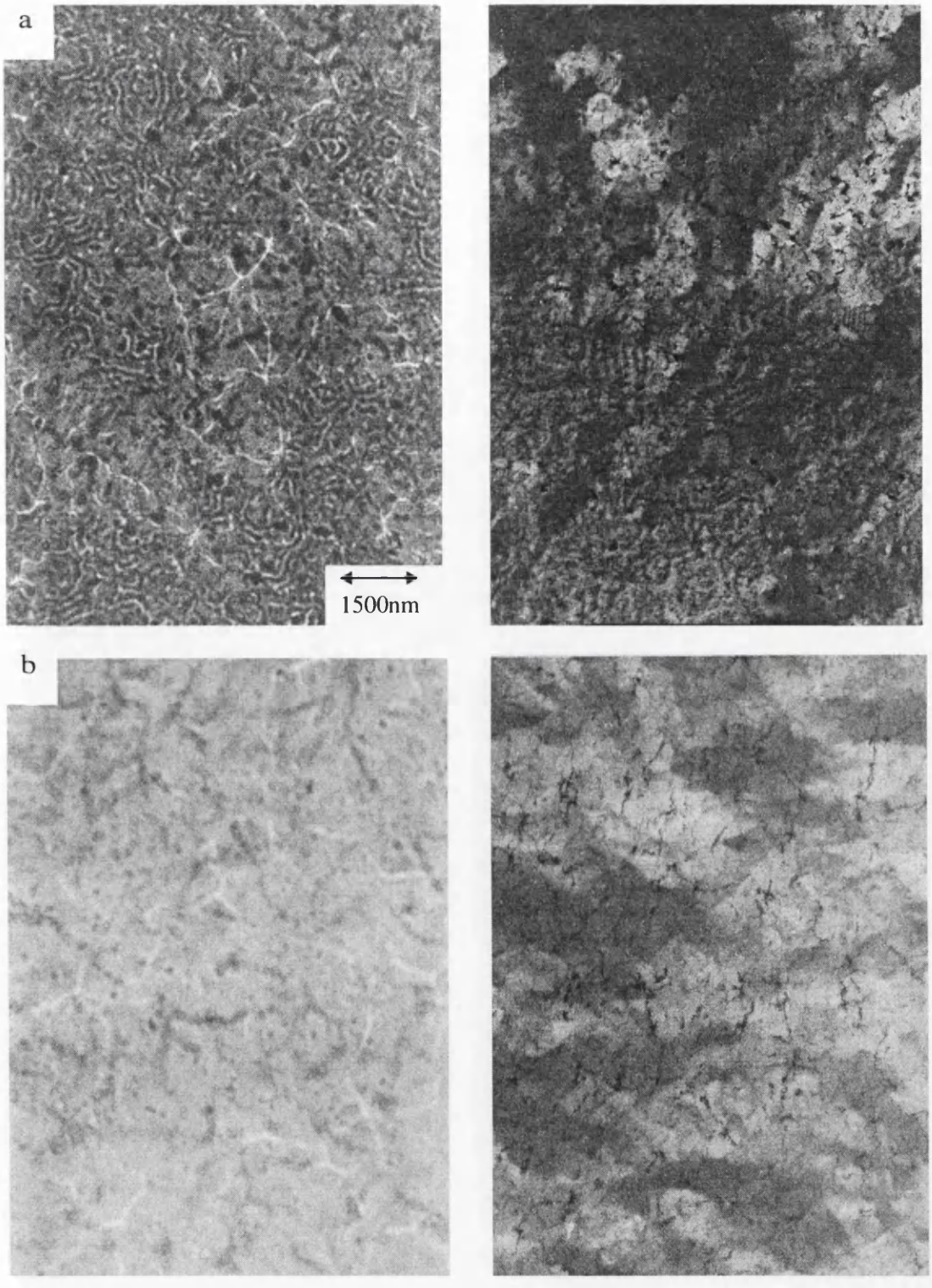

Figure 6.4 : Fresnel and Foucault images of sampls A and B. The Foucault image is on the right.

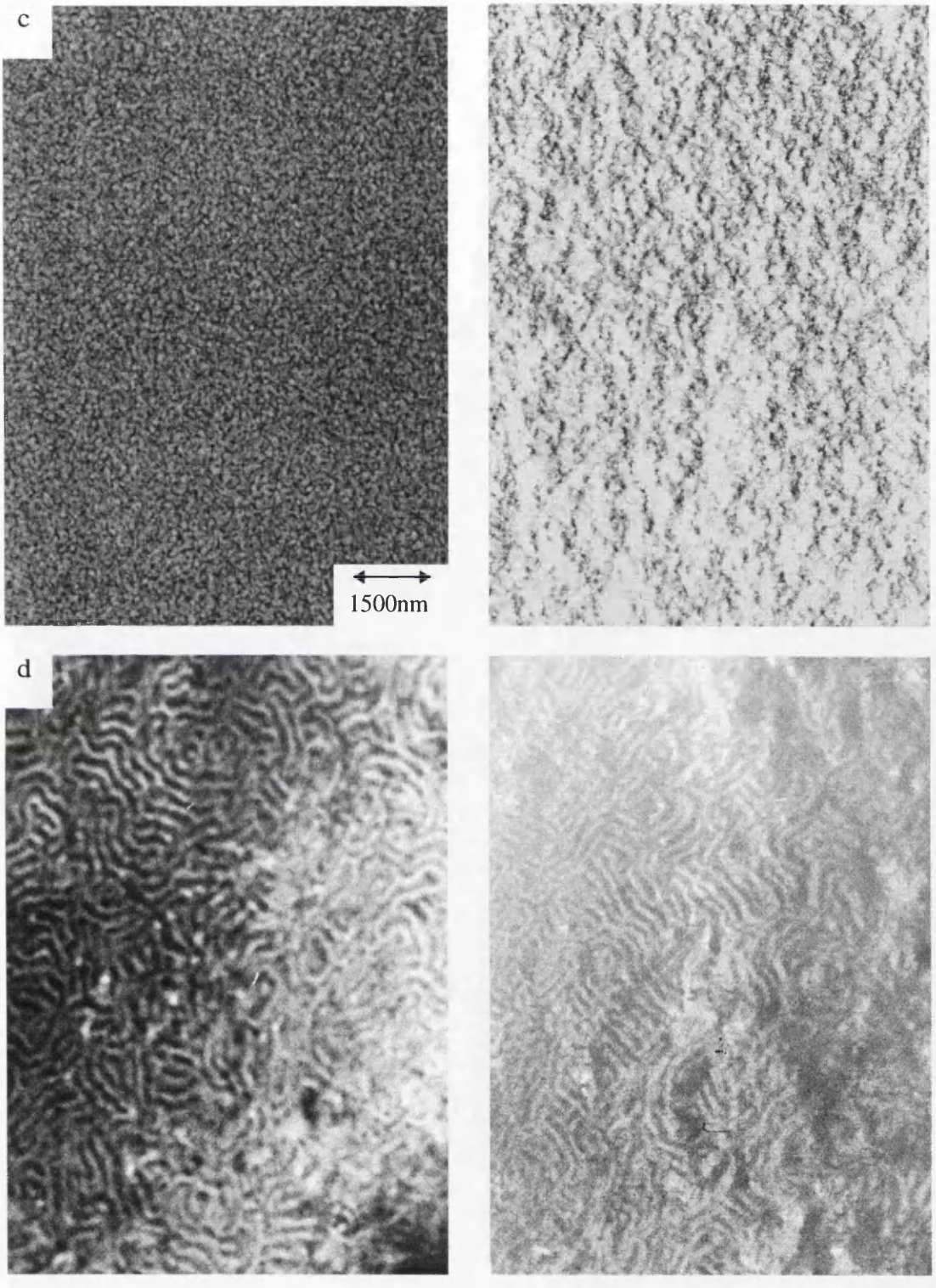

Figure 6.4 (cont): Fresnel and Foucault images of samples C and D. The Foucault image is on the right.

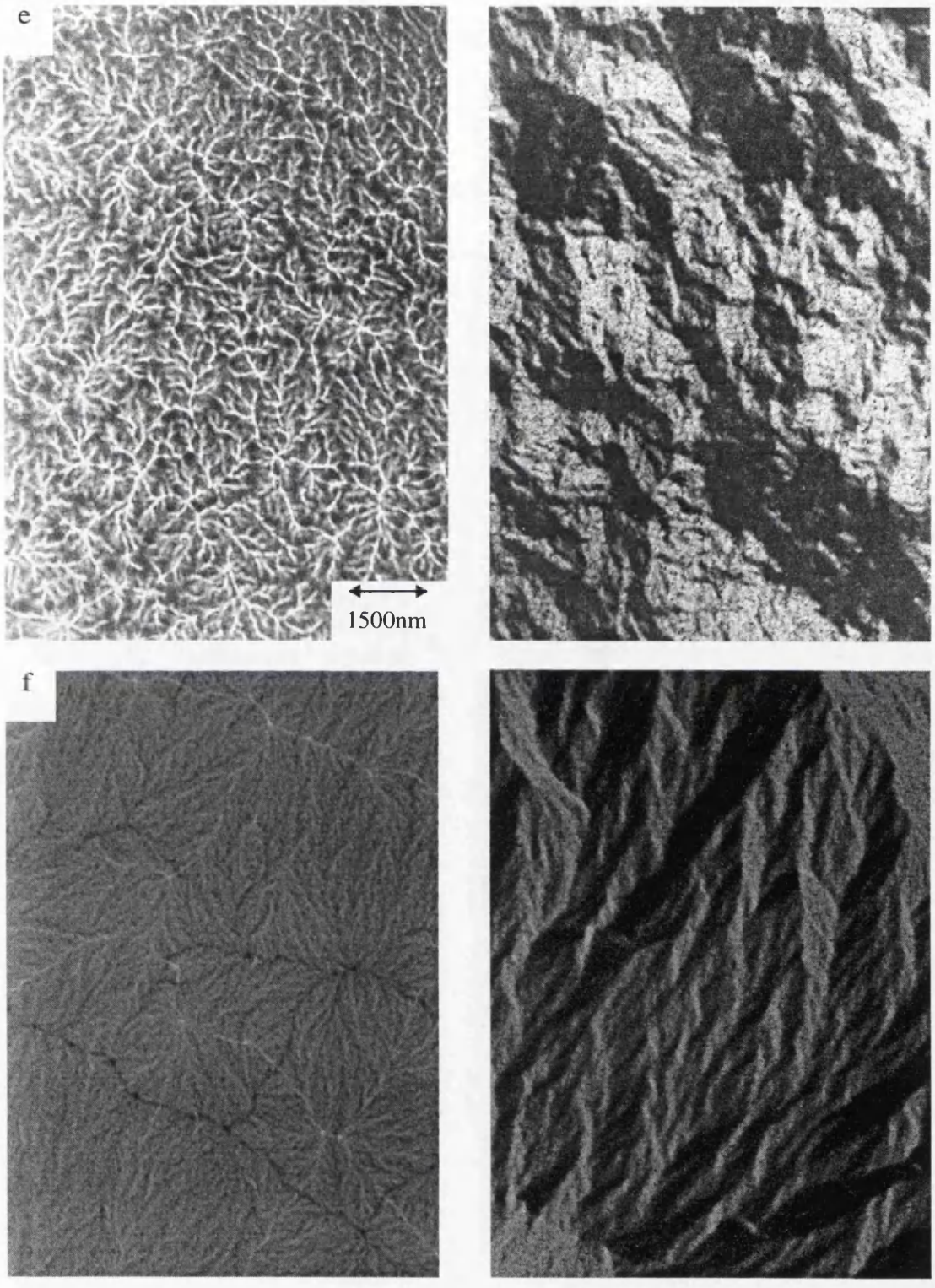

Figure 6.4 (cont): Fresnel and Foucault images of samples E and F. The Foucault image is on the right.

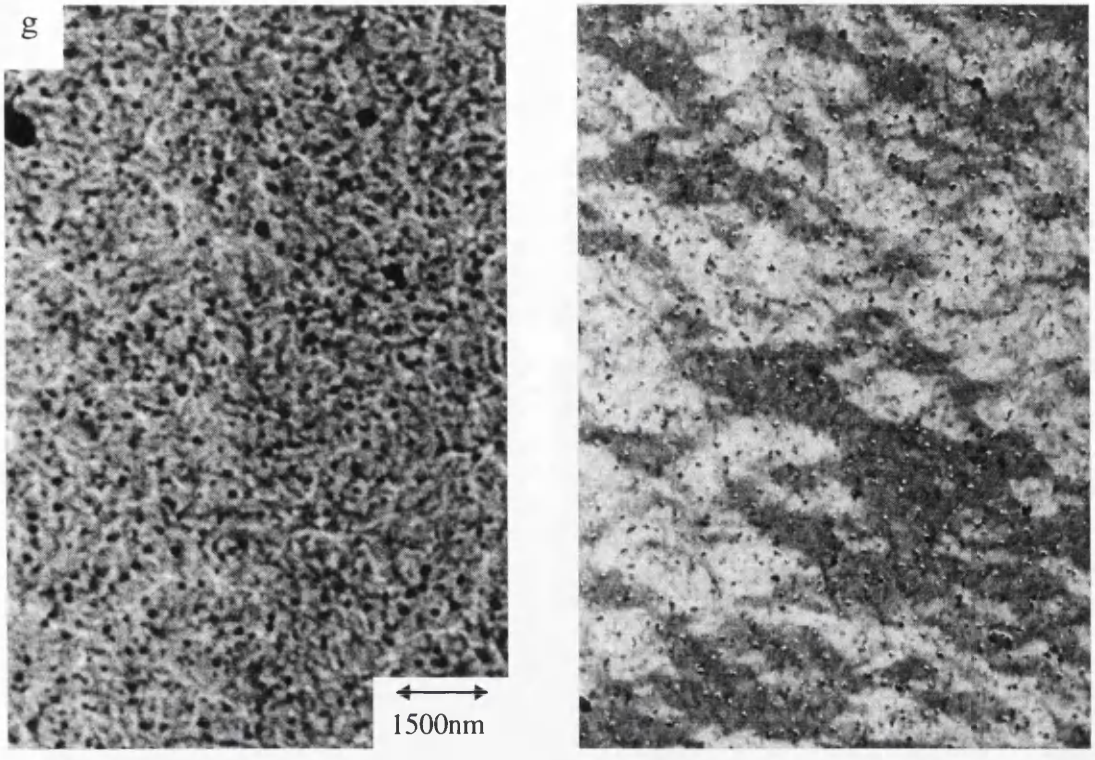

Figure 6.4 (cont): Fresnel and Foucault images of sample G. The Foucault image is on the right.

means that the local magnetisation direction within a single domain varies over a small angle.

The micromagnetic structure of samples B, C and G consisted of domains with no ripple. These domains were smallest for sample C (≈200nm in diameter) but were larger for samples B and G (≈500nm in diameter). These magnetic features are consistent with crystallites which are magnetically decoupled. This means that the magnetisation within a crystallite is less influenced by the exchange energy term, and, hence the energy balance in determining the micromagnetic behaviour will be between the anisotropy energy and the magnetostatic energy.

The domains in samples E and F extended over a larger distance (>1μm) and have ripple. The scale of the magnetic ripple in both samples is similar, with the magnetic features changing over a distance of 100nm. The scale of the extended domains is however different, with 1μm being the average diameter for domains in sample F, but for sample E this is the smallest diameter, with domains extending being as large as several μm. These magnetic features are consistent with crystallites which are magnetically coupled.

Sample D appears to have perpendicular magnetisation, with the domains forming a maze like domain structure. This is unsuitable for in-plane magnetic recording and could reflect a high perpendicular anisotropy caused by the "c" axis pointing predominately out of the plane of the film. The "c" axis is the easy axis for magnetisation in HCP cobalt. For this sample to be perpendicularly magnetised the

texturing in the "c" axis direction must be so large that the perpendicular magnetocrystalline anisotropy caused by this can overcome the shape anisotropy term described in chapter three.

Sample A shows regions of perpendicular and in-plane magnetisation. These features appear to vary as the crystallite structure varies on the same scale (figure 6.5). X-ray spectra were taken from points of the film, along with an x-ray map which mapped the intensity of the Cobalt K_α and Platinum L_α lines. These confirmed that the composition of the film did not vary spatially and that the different micromagnetic characteristics on this single film would appear to depend on the crystal structure alone. This is clearly undesirable in a single film intended for use as a hard disk recording medium.

The rather unpredictable magnetic properties of sample A, along with the varying properties of the other samples suggest that it is important to get a well defined deposition procedure which can be relied on for reproducable results. Overall the sample with the best apparent micromagnetic structure, from this evidence, for magnetic recording is sample C. This sample has a large degree of texturing, which will result in a perpendicular magnetocrystalline anisotropy term, which is obviously not large enough to cause perpendicular magnetisation as is the case in sample D, but could reduce the effect of the shape anisotropy, which causes the magnetisation to lie in the plane of the film. This may be the mechanism for the formation of the smaller domains.

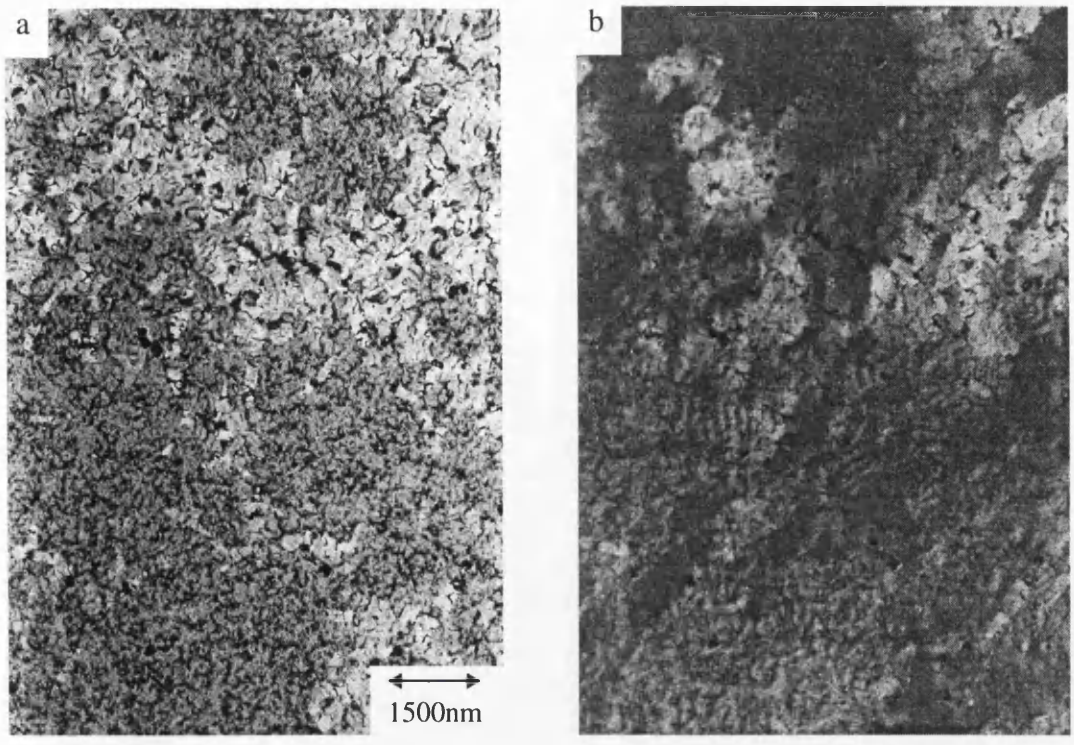

Figure 6.5: A bright field and Foucault image of the same area of sample A, showing the changing crystallite structure and the effect this has on the magnetic structure.

Samples F and G were chosen to study further, they represent both categories of in-plane magnetisation observed. The hysteresis loops for these samples are shown in figure 6.6. To study these samples further, magnetisation experiments as described in chapter three were carried out. Written bits were recorded on sample C and these are examined later.

The reversal mechanisms for both samples were recorded using the slow scan CCD camera and low light level TV camera. Only the results recorded on the CCD camera are shown here, although both sets of results proved invaluable in the interpretation. The centre of each of the LAD patterns was determined by fitting a circle to the pattern which displayed the largest arc, then fitting this circle to the other arcs. The centre of illumination was then determined by converting the image into an two dimensional array of values, and calculating the centre using the spreadsheet. From these two points, the mean deflection arrows were worked out. The magnetisation reversal process in samples F and G are shown in figures 6.7 and 6.8 and in figures 6.9 and 6.10 respectively. Under the influence of a reverse field there is a marked increase in dispersion in sample F, followed by the appearance of reverse domains which increase rapidly in size. Reversal takes place at relatively low fields (≈200Oe). The LAD patterns for sample F show that the electrons are deflected so that they lie on the circumference of a circle throughout the whole reversal process (figure 6.8). This indicates that the electrons are being deflected predominately by the magnetisation within the sample and that there are negligible stray field effects. The LAD patterns also show that the magnetisation within a particular area rotates until it is at an angle slightly less than perpendicular to the applied field before domain walls form which move through the sample, aligning the magnetisation with the field.

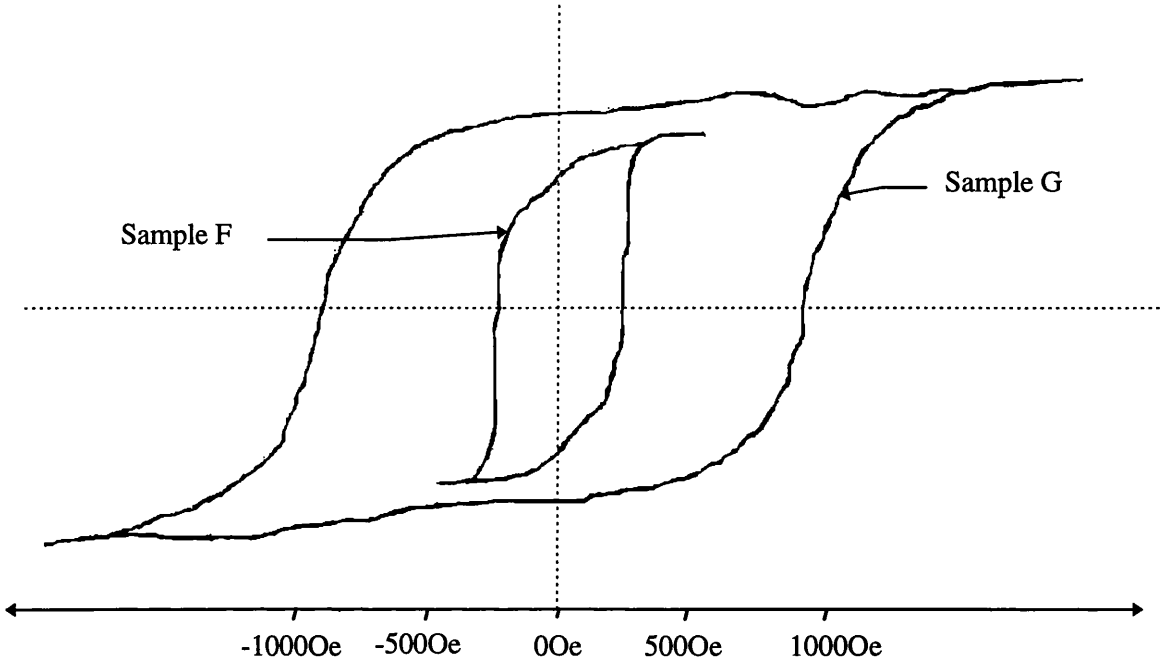

Figure 6.6: Hysteresis loops for samples F and G. The vertical scale is arbitrary .

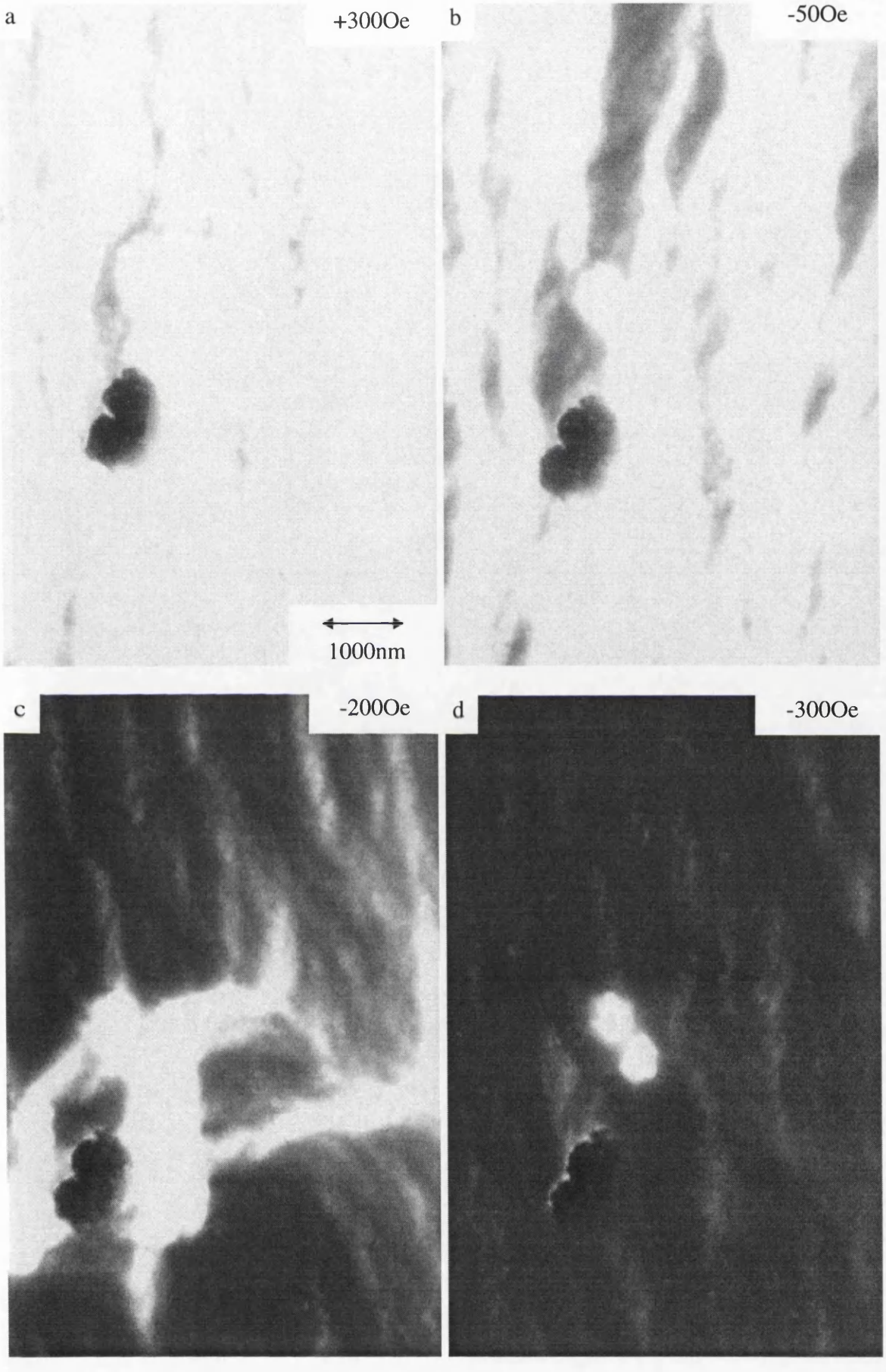

Figure 6.7:Foucault images of sample F in an applied field. Showing the domain wall sweeping through at -200Oe.

Field and mapping direction: ⟷

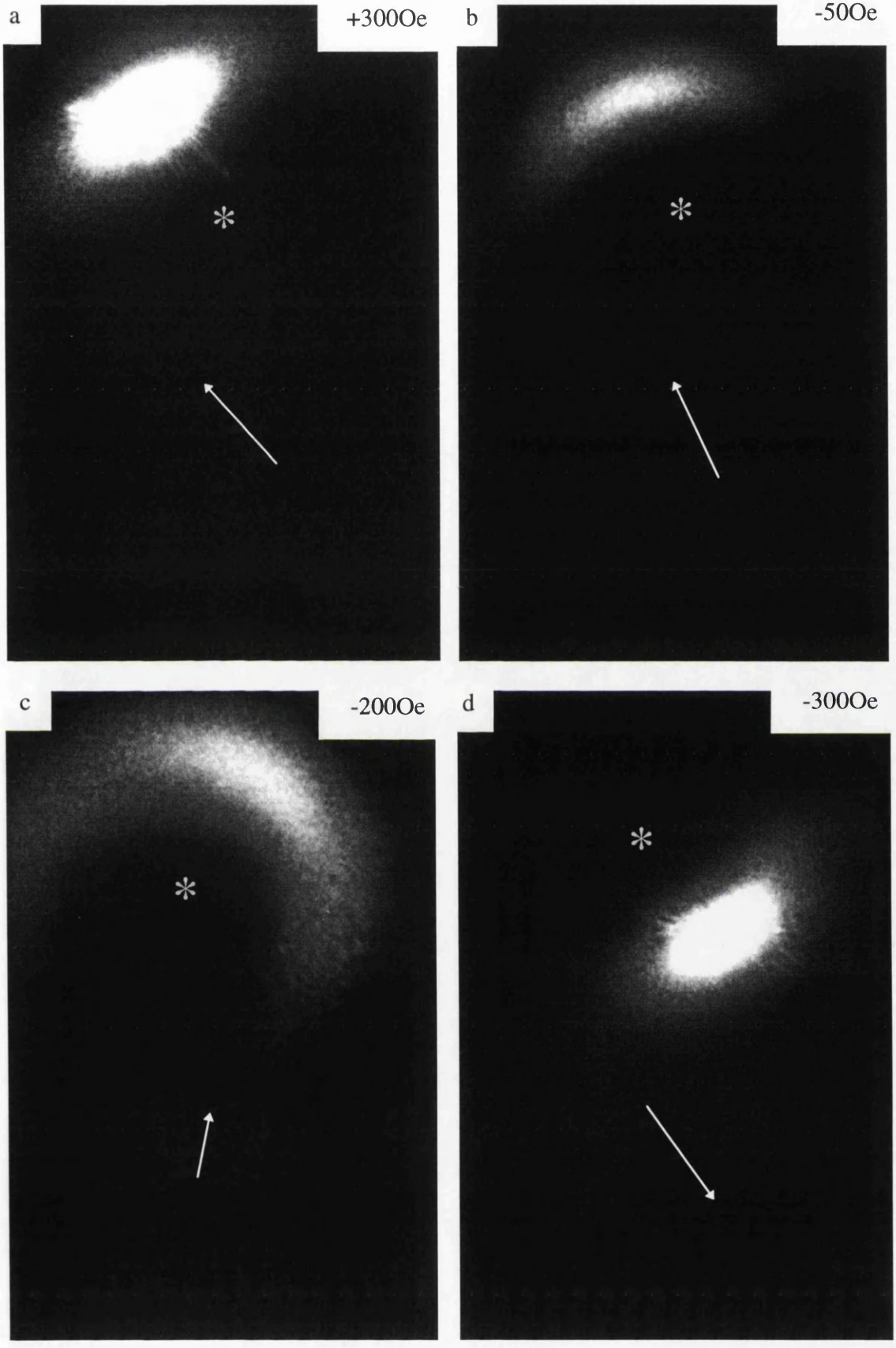

Figure 6.8: LAD patterns of sample F in an applied field. The white arrows represent the mean deflection. While the star represents the position of the undeflected beam.

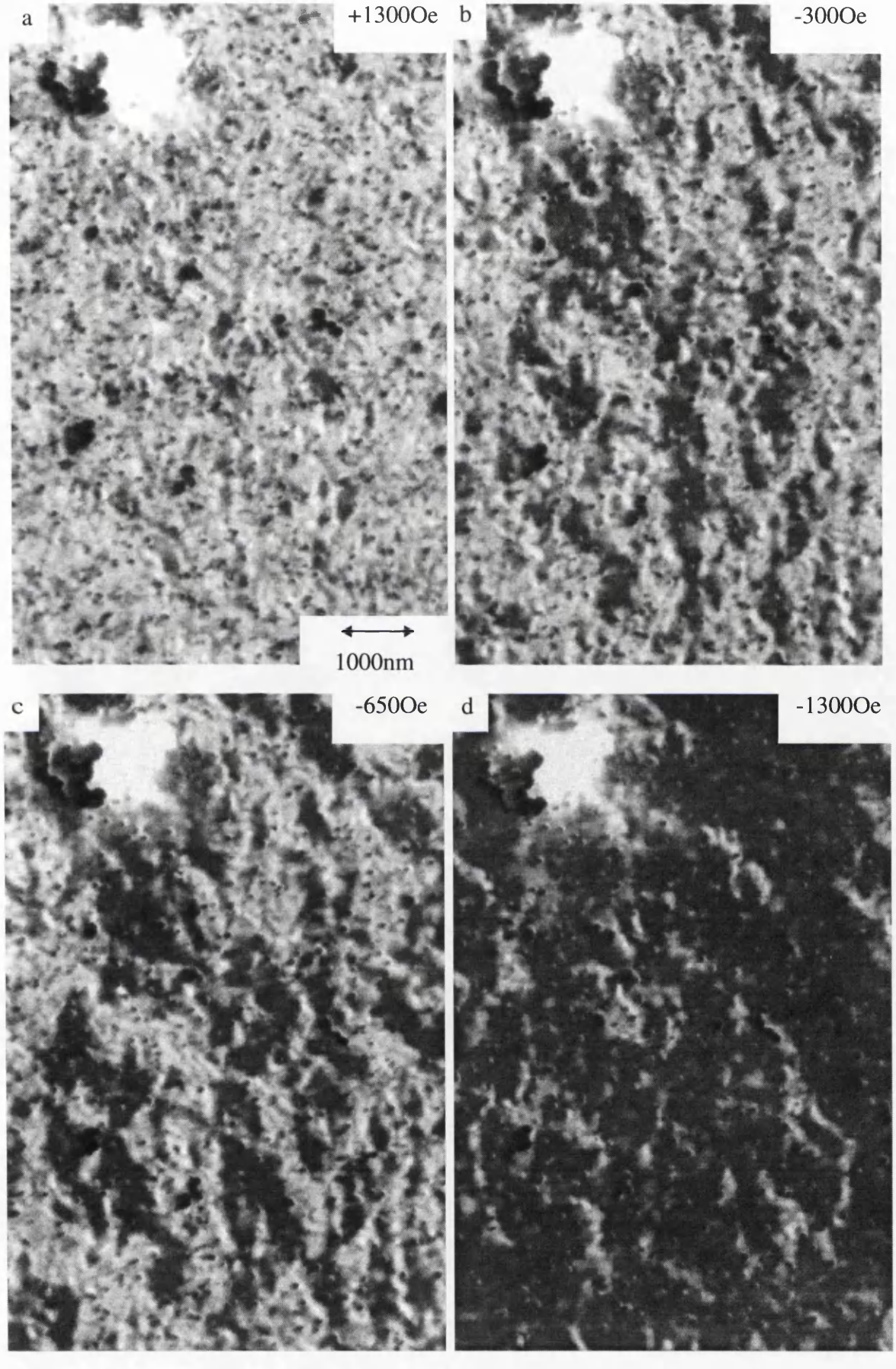

Figure 6.9: Foucault images of sample G in an applied field.
Field and mapping direction:

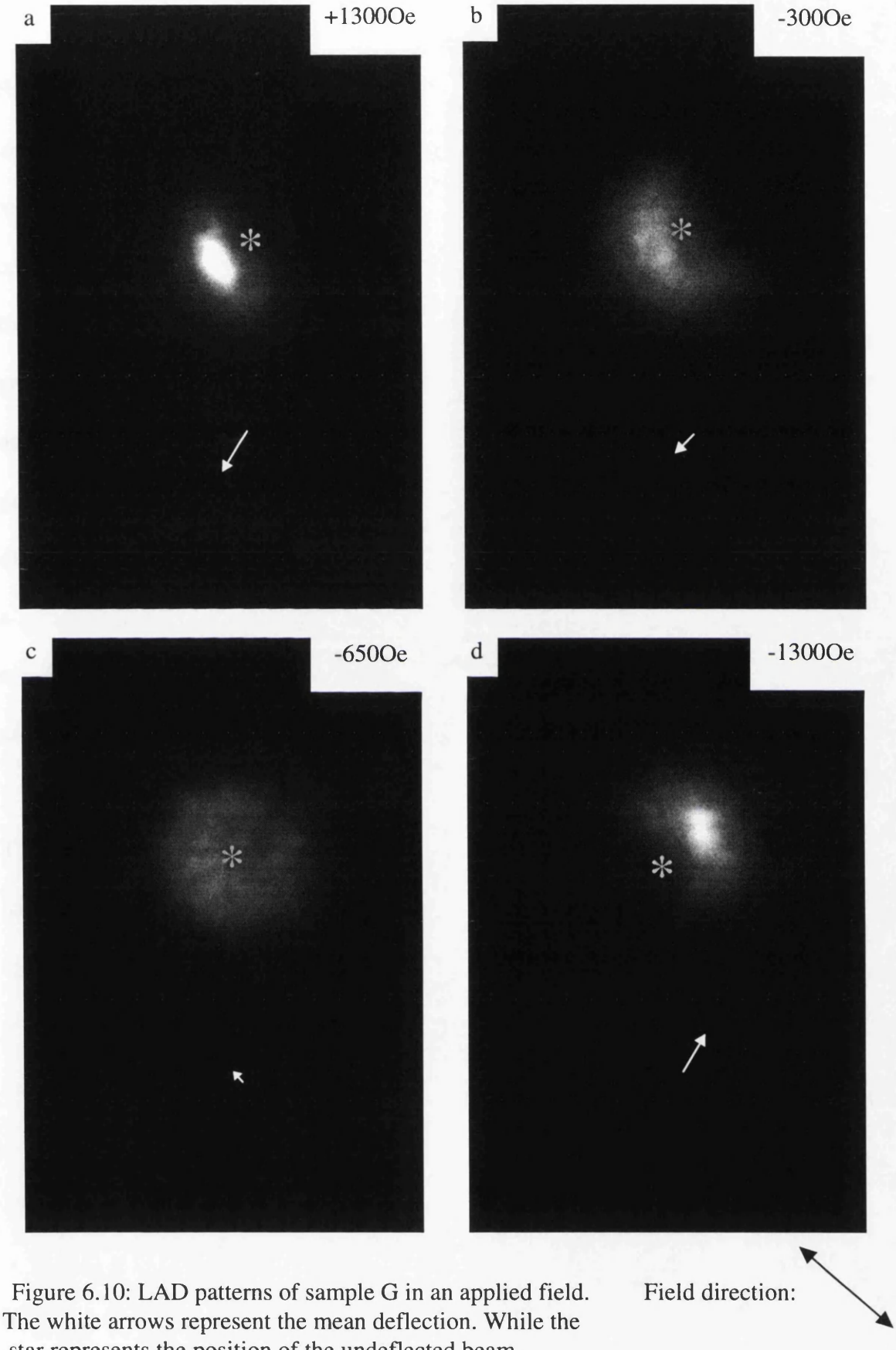

Figure 6.10: LAD patterns of sample G in an applied field. The white arrows represent the mean deflection. While the star represents the position of the undeflected beam.

For sample G reversal takes place over a much larger field range (≈2000Oe) and involves the formation of many small domains, the number of which grow as larger reverse fields are applied. The LAD patterns for sample G (figure 6.10) show the presence of stray fields by the fact that the intensity distribution is no longer in the form of an arc of a circle, when the magnetisation is reversing. The stray fields will be produced where the magnetisation in neighbouring domains meets head on, as described in chapter one, so the presence of large stray field effects suggests the presence of many large angle domain walls, and therefore domains. Furthermore observing the pattern as it changed in the microscope showed that the induction within a particular area moves from aligned against the field to aligned with the field in a series of jumps, with the initial jump often leaving a component of the induction aligned against the field.

The deflection angles caused by the Lorentz interactions between the specimen induction and the electron beam were measured from the LAD patterns. From these an approximate value for the saturation magnetisation (M_s) was calculated: for sample G M_s= $8.8x10^5 Am^{-1}$, and for sample F M_s= $6.6x10^5 Am^{-1}$. The error in each of these values will is ≈10%. The M_s value for pure cobalt is $1.4x10^6 Am^{-1}$.

Here I have demonstrated how the micromagnetic structure of thin film recording media can be imaged in the presence of applied fields sufficiently large to take them through a magnetisation cycle. The resolution in the magnetic image sequences shown here is approximately 50nm so that very small scale magnetic features can be identified clearly. Of the two CoPt specimens investigated in depth, only sample G has

the makings of a satisfactory recording medium. The observed reversal mechanism is compatible with there being substantial exchange-decoupling between grains. For sample F, by contrast, the low coercivity and the observation of walls moving through the sample suggest that inter-granular exchange coupling is substantial.

Finally, the LAD provides not only useful information (in conjunction Foucault imaging) of the reversal mechanism but also a microscopical means of determining the saturation magnetisation. In the case of the two samples under study here the values differ substantially but in a manner at least qualitatively consistent with the Pt content determined from x-ray microanalysis [7]. This paper shows that the M_s decreases sharply as the cobalt composition is decreased from 100% Co to around 70% Co, where the M_s was unrecordable. A direct comparison of the M_s values cannot be made since the microstructural make-up of the samples are different.

6.3 The effect of substrate condition on micromagnetic and microstructural properties of CoPt

To examine further the effect of the microstructure on the magnetic properties, another pair of samples (samples H and I) was deposited to a thickness of 30nm with the same deposition conditions and composition (80%Co 20%Pt) onto two different substrates: one (sample H) was deposited onto a standard silicon nitride window which had been exposed to concentrated, heated sodium hydroxide (NaOH) during the etching process for twenty minutes and the other (sample I) was deposited onto a silicon nitride substrate which was only exposed for two minutes. NaOH is highly corrosive and although silicon nitride is known as a mask for NaOH etching, there will be some

corrosion into the surface of the silicon nitride. The bright and dark field images (figure 6.11) and tilted diffraction patterns (figure 6.12) showed that although the crystallite size for the sample H is less, there is a clustering of the crystal orientations which made the number of crystallite orientations in a given area less than for the sample I. A low magnification dark field image was taken to determine the extent of the clustering (figure 6.13). This showed that clusters extended over several μm, a much larger range than for any of the previous samples. The crystallite texturing and structure however appeared to be the same for both samples, being HCP with the "c" axis lying out of the plane of the film. The magnetic properties of the sample H were however much harder to determine (figure 6.14), this was partly due to the increased crystallite contrast in the magnetic images and the apparent increase in complexity of the magnetic structure itself. The magnetic structure for sample I is reported in the next section as this sample is equivalent to sample N. These results confirm that the substrate surface conditions must be reproducible if consistent properties are required.

6.4 The effect of thickness on micromagnetic and microstructural properties of CoPt

A series of samples was deposited from the same target onto similar substrates with similar deposition parameters, but to different thicknesses. The sample composition was: 20%Pt 80%Co. The thicknesses were 5nm (J), 10nm (K), 15nm (L), 20nm (M) and 30nm (N). These samples were characterised in the same way as the samples with different compositions. The diffraction patterns (figure 6.15) showed a textured hexagonal close packed crystallite structure, with the "c" axis lying out of the plane of the film, in all the samples. Convergent beam diffraction patterns of a single crystallite

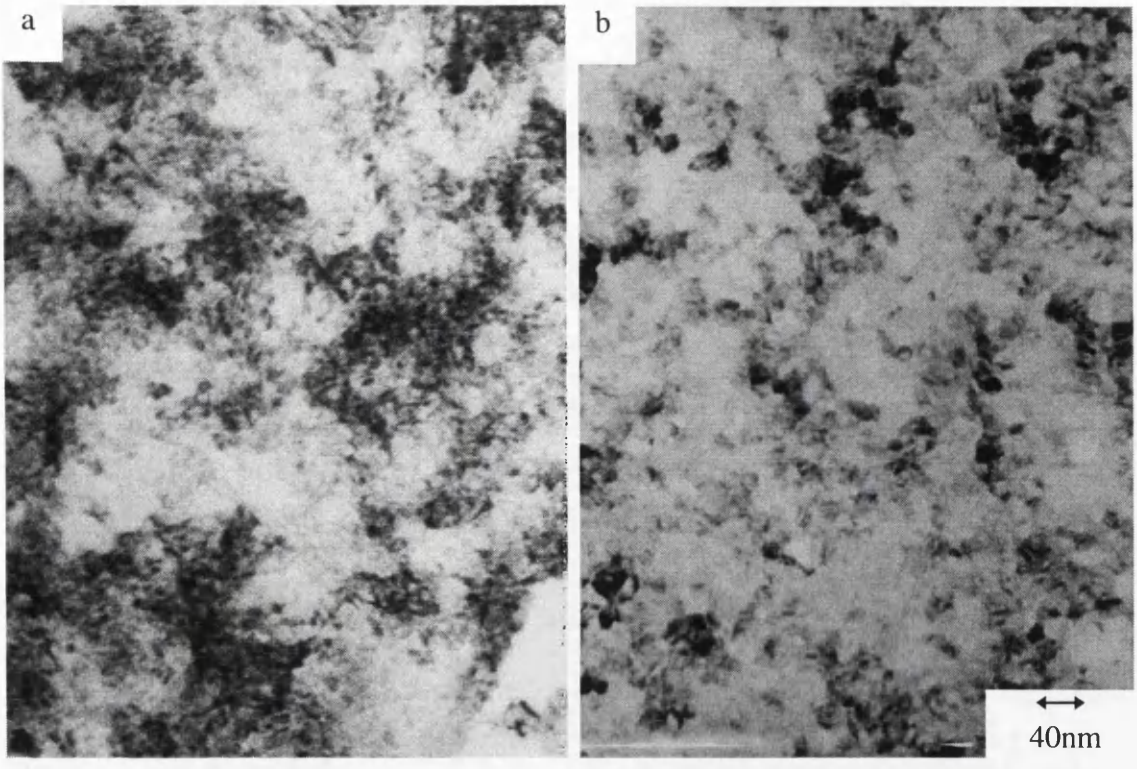

Figure 6.11: Bright field images of samples H (a) and I (b).

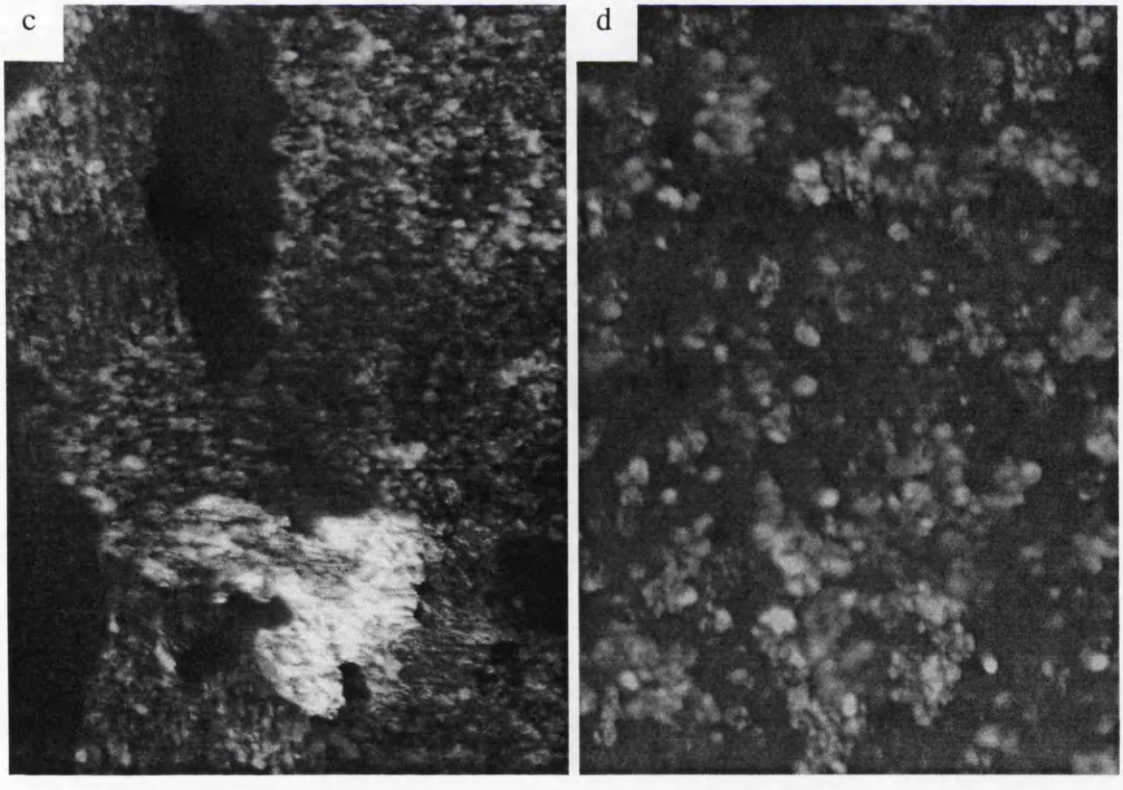

Figure 6.11 (cont.): Dark field images of samples H (c) and I (d) showing the changes in the clustering.

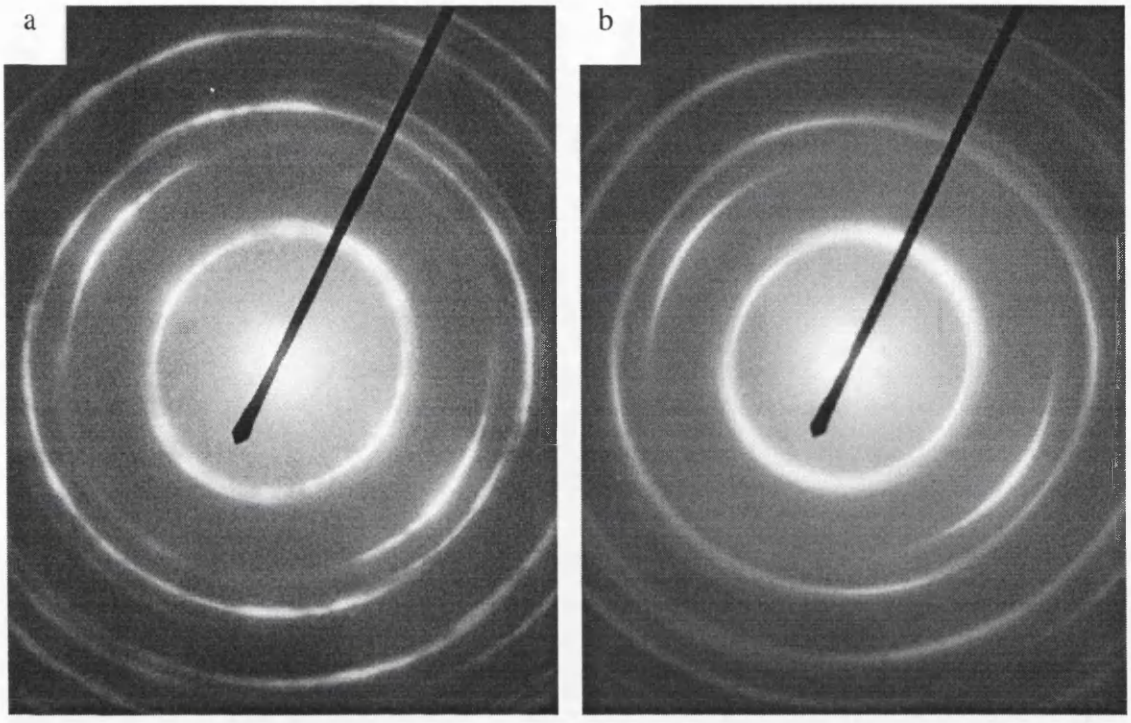

Figure 6.12:Tilted diffraction patterns of samples H(a) and I (b), showing the similar texturing.

Tilt axis

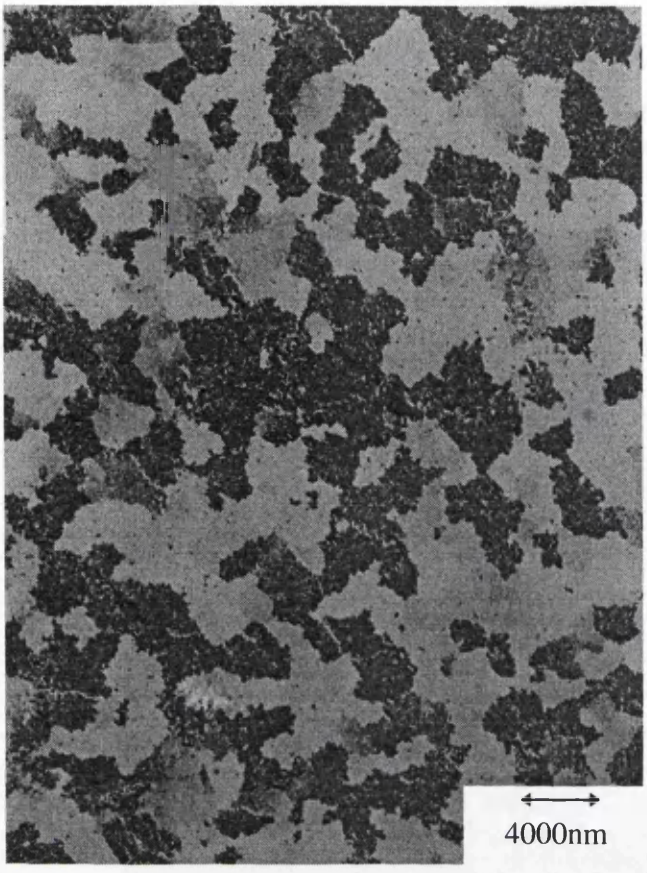

Figure 6.13: A dark field image of sample H showing large scale texturing.

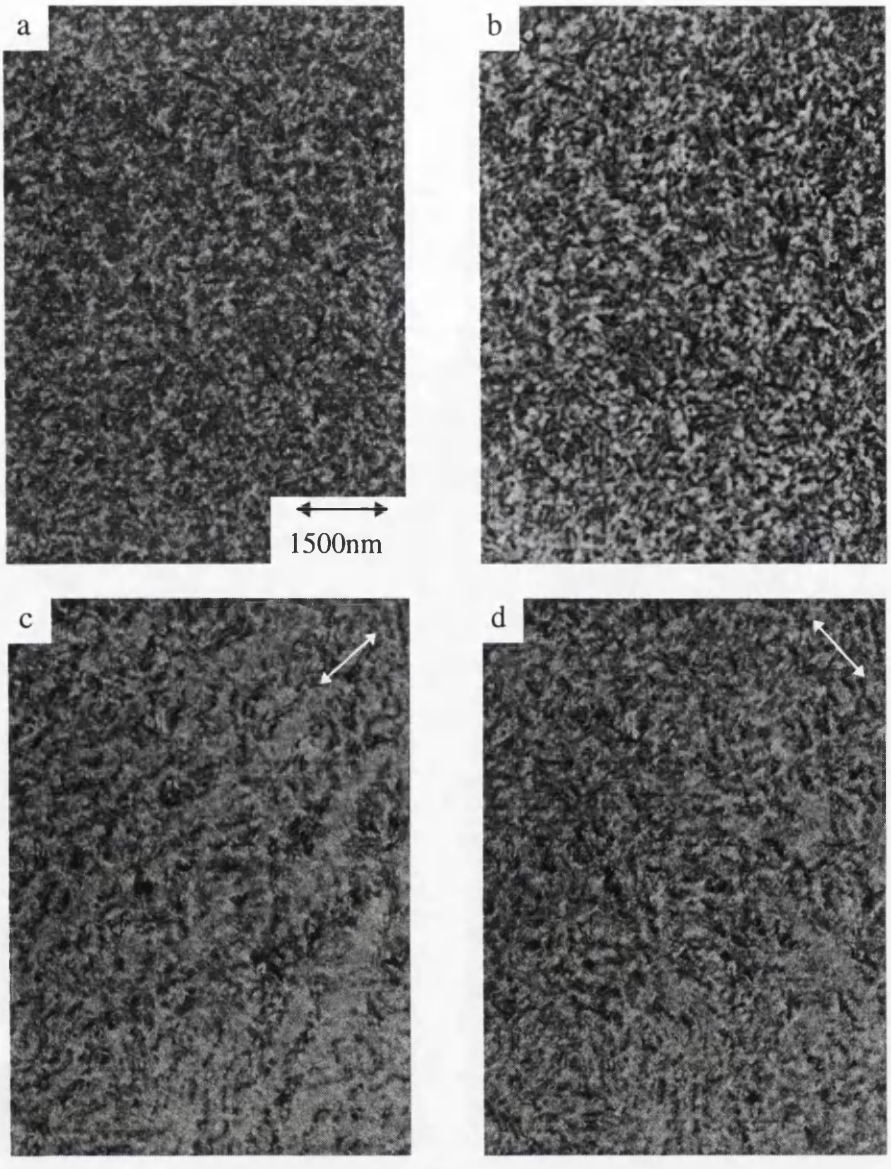

Figure 6.14: Bright field (a), Fresnel (b) and foucault pair (c),(d) images of same area of the sample H. This shows how the magnetic structure is hidden, to an extent, by the large crystallographic contrast. The white arrows represent the mapping directions in the Foucault images.

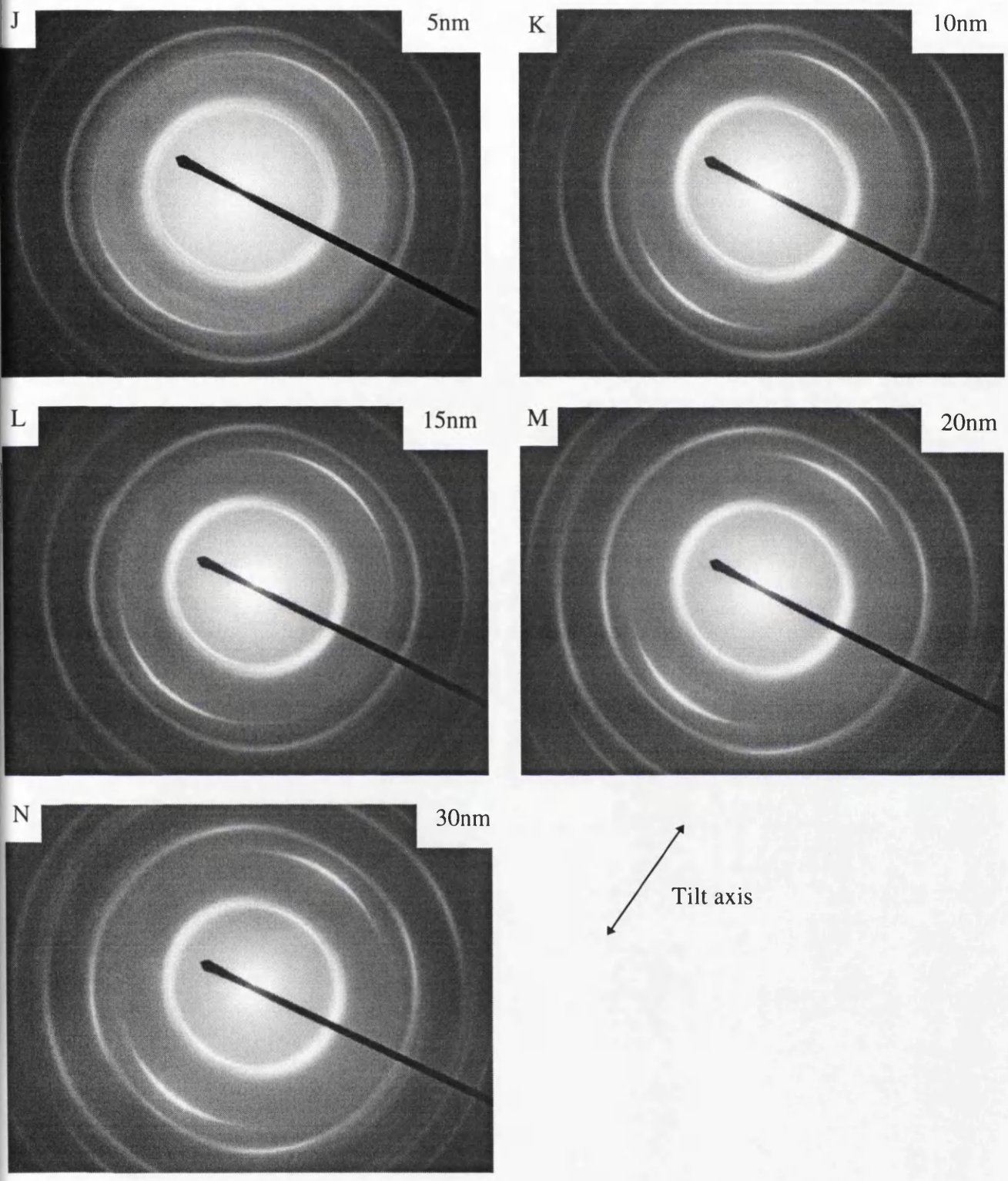

Figure 6.15: Tilted diffraction patterns for samples grown to different thicknesses, showing the similar crystal structure between the samples.

were taken of samples K and N (figure 6.16). These confirmed that they were indeed both HCP in structure. The bright field images (figure 6.17) showed more contrast as the sample thickness increased; this was thought to be due to the increased amount of diffraction from each crystallite rather than any changing structural characteristic. There is no apparent change in the average crystallite size, or clustering (which is of the order of 10 grains or less) as the sample thickness increases. In addition dark field images were taken of samples K and N (figure 6.18), these highlighted individual crystallites and allowed the crystallite size to be compared more readily. The two dark field images are essentially indistinguishable, confirming the similarity of the crystallite structure. The magnetic microstructure was recorded as Foucault images of the spin demagnetised state (figure 6.19) and appeared to change as the sample thickness increased. The prominant features on the Foucault images of the thinner samples are probably the features that can just be made out on the bright field images of these samples (figure 6.17J) and do not appear to be magnetic. The origin of these contaminants is not known. The most prominent change in the micromagnetic structure was between samples L and M. The magnetic microstructure of the sample L was made up of domains around 350nm in diameter, while those for sample M were around 150nm in diameter. As the sample thickness increased further to 30nm (sample N), the size of these domains decreased further to 100nm across. This is not an unreasonable observation, and will be due to the larger shape anisotropy in the thinner samples. As the samples thickness increases the ratio of the out of plane dimension to the in plane dimensions will increase, so the out of plane demagnetising will decrease. This will mean that the overall energy term forcing the magnetisation to lie in plane will be smaller. As with sample C, this suggests that the larger the force which forces the magnetisation to lie in plane, the larger are the domains which are formed.

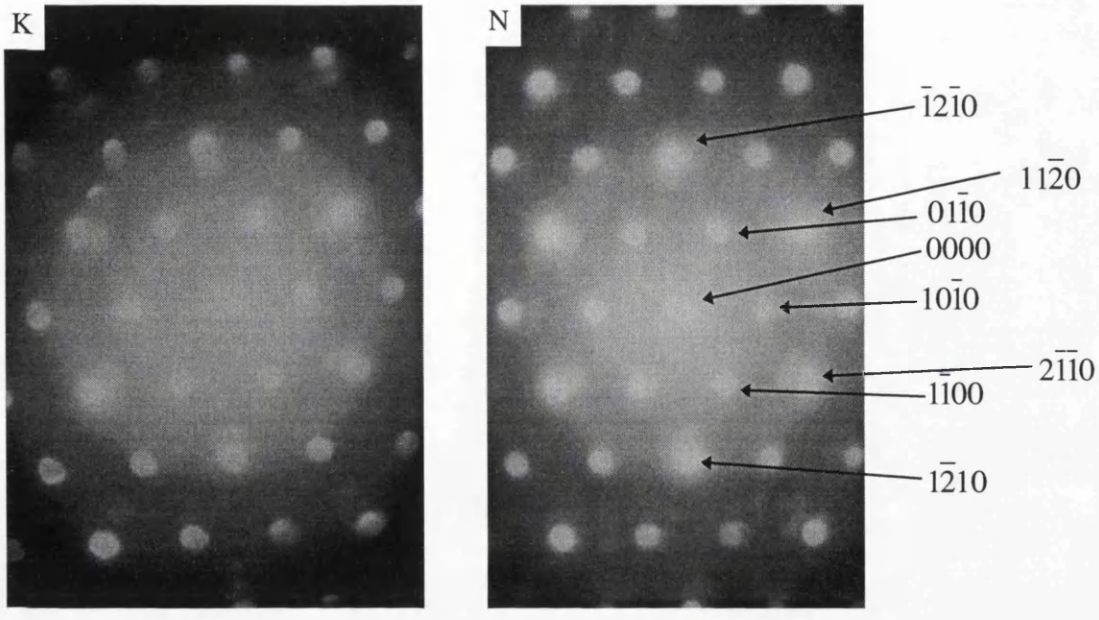

Figure 6.16: convergent beam diffraction patterns for samples grown to 10nm (K) and 30nm (N) showing the same (0001) diffraction pattern.

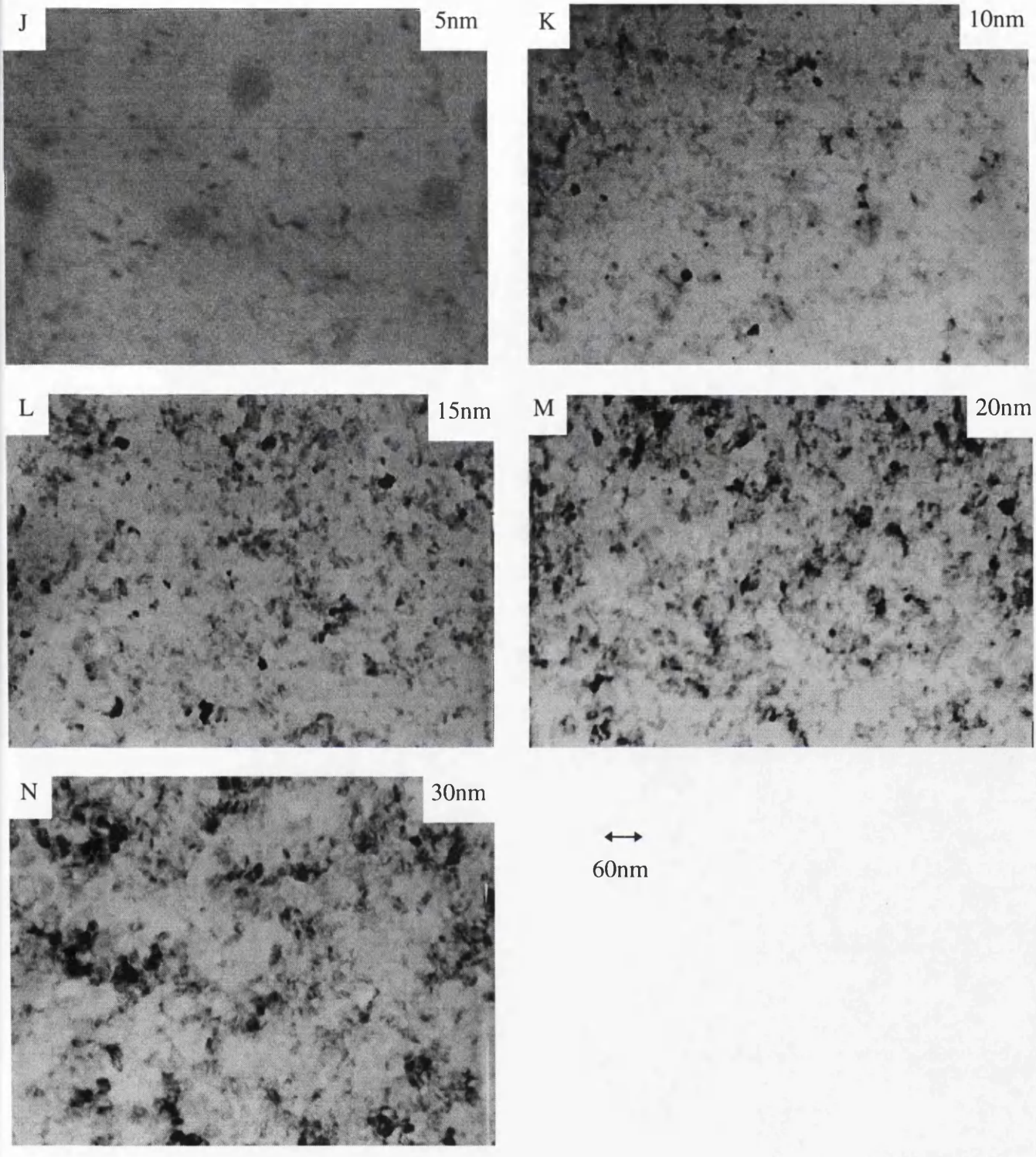

Figure 6.17: Bright field images of samples grown to different thicknesses showing the increase in contrast but the lack of any other changes.

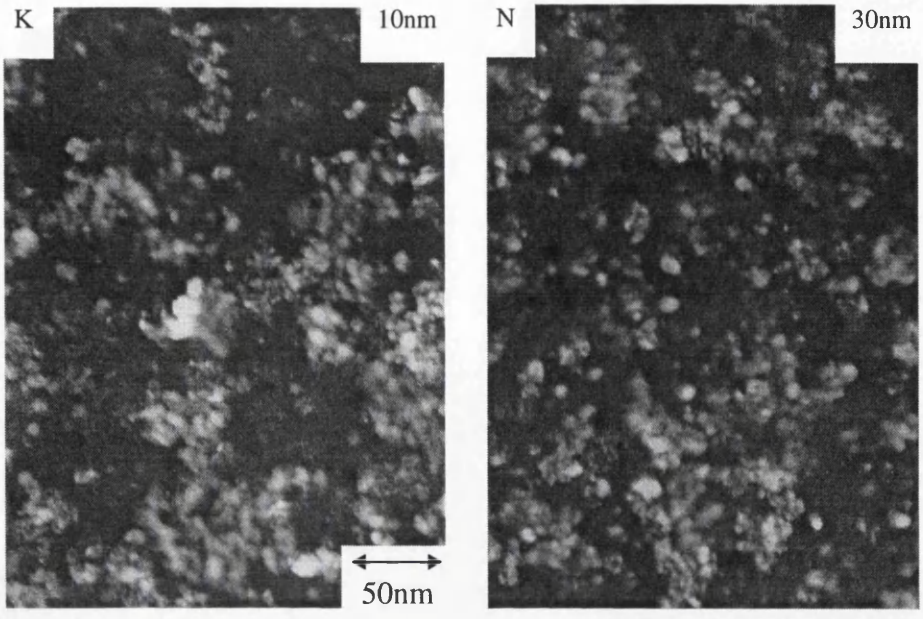

Figure 6.18: Dark field images of samples K and N, highlighting the similar nature of the two samples.

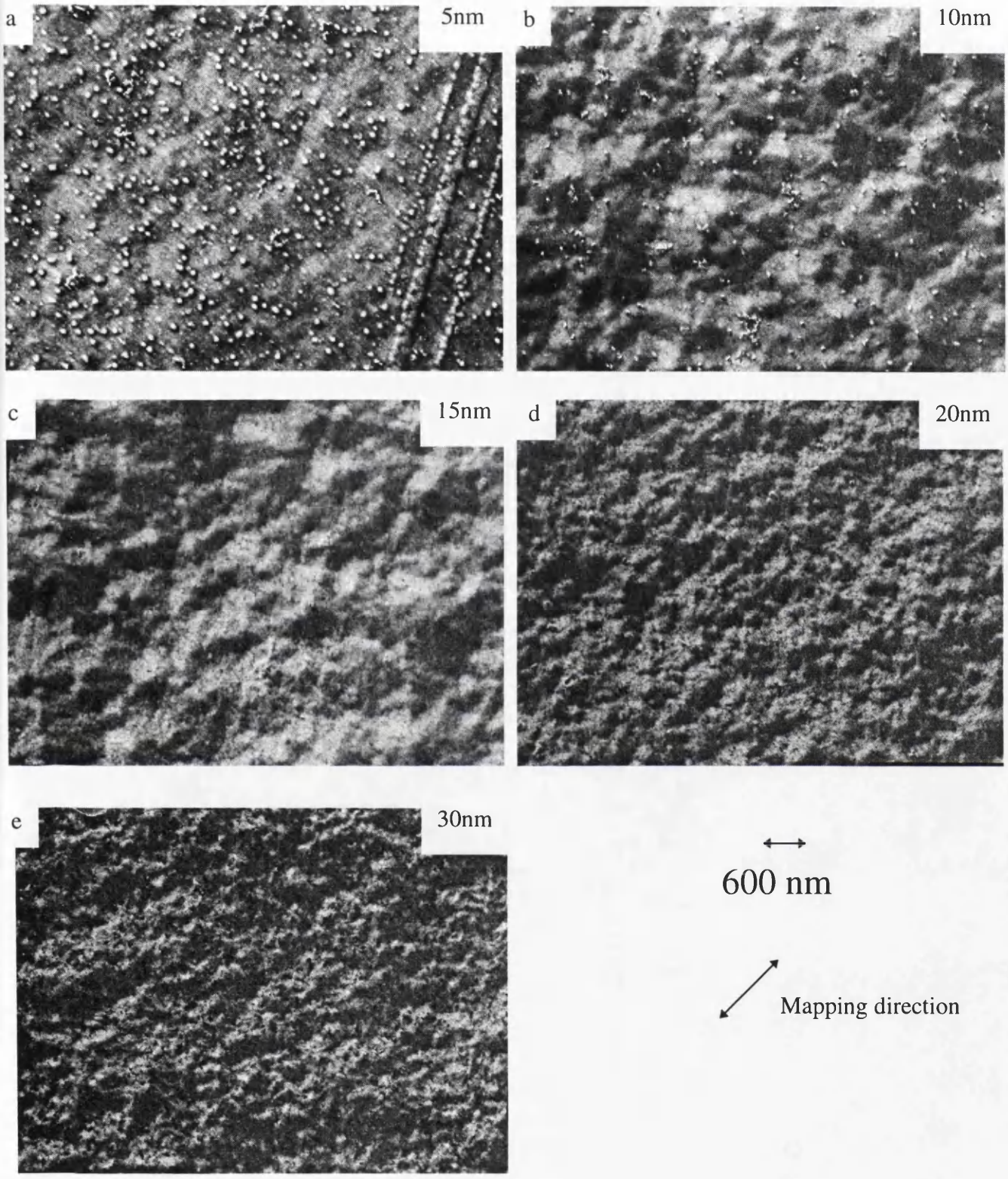

Figure 6.19: Foucault images of samples grown to different thicknesses in the spin demagnetised state. This sequence shows the decrease in scale of the magnetic features as the sample thickness increases.

Foucault images of the micromagnetic reversal process of the samples was recorded, which were all similar. The magnetisation process for the sample N is shown (figure 6.20) as it had the best contrast. The reversal process is very similar to that previously described for sample G, the size of the domains which are formed during the reversal process is of the order of 200nm in diameter.

6.5 Investigations of written bits in CoPt

Bit patterns have been recorded onto sample C at the University of Manchester at a density of 15 and 30 Mbits/in^2. The bits were written before the windows were etched into the substrate, and the write head was in contact with the substrate while the bits were being written. Sample C was chosen since it had the smallest in-plane domains and so should represent the highest density of recording possible on the samples studied. These bit patterns were studied using Fresnel and differential phase contrast (DPC) imaging to try to determine characteristics such as the transition width. The transition width is the width along the recording direction over which the magnetisation of the bit is not entirely in the intended direction (figure 6.21) and is related to the signal strength of the recoverred signal. The transition region is caused by the domain pattern attempting to reduce the magnetostatic energy.

The Lorentz images of the bits recorded at a density of 15Mbits/in^2 (figure 6.22) show that most of the contrast is at the edges of the tracks where there is less stray field to affect the contrast. The transition widths measured from the DPC images are

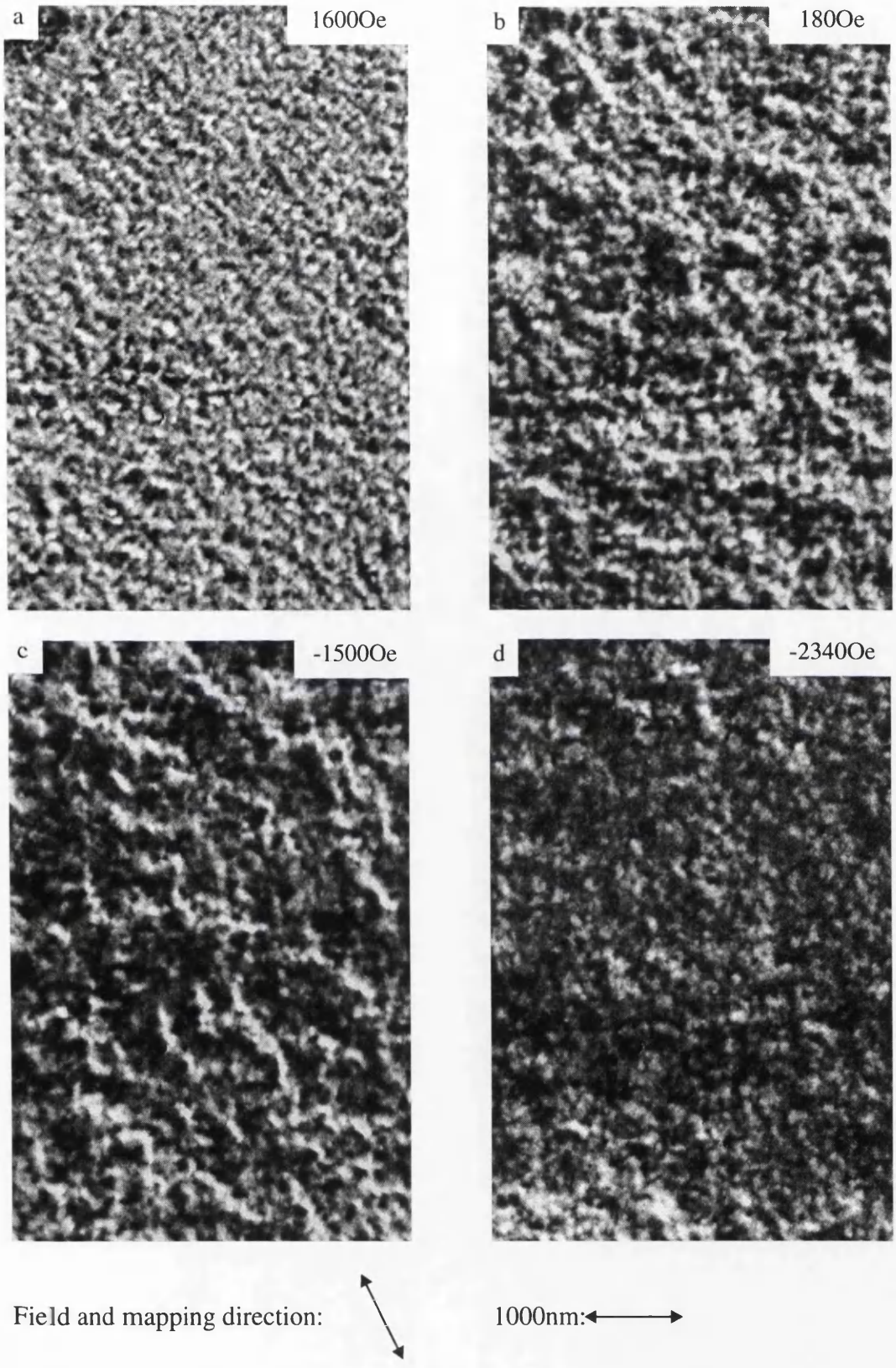

Figure 6.20: Foucault images of the magnetisation process of sample N.

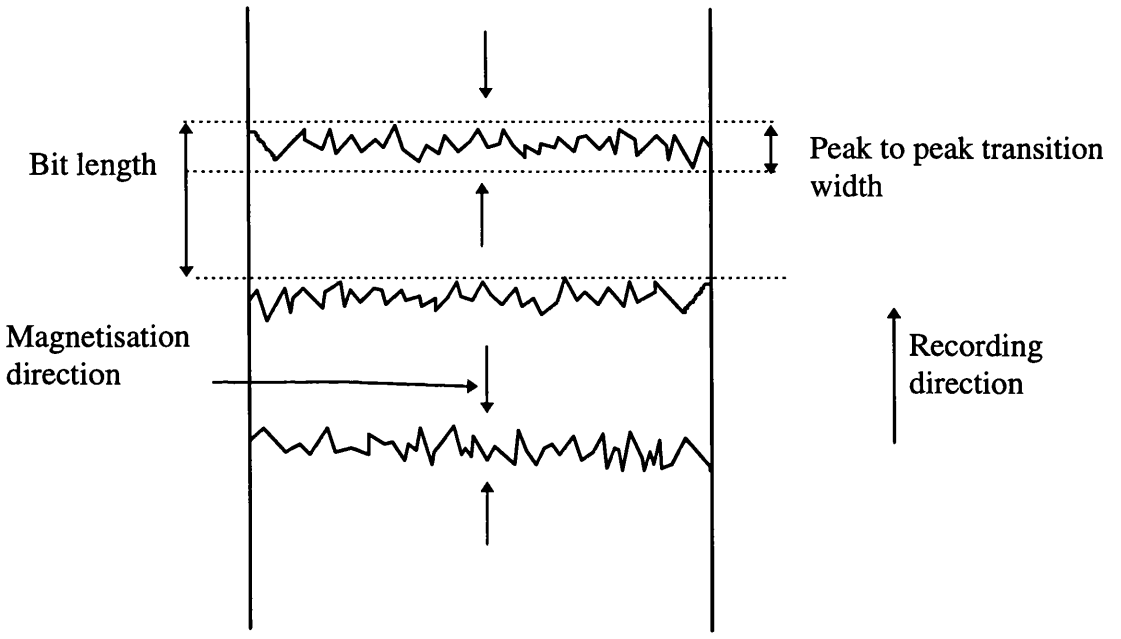

Figure 6.21: A schematic of the magnetisation direction in recorded bits showing the transition width.

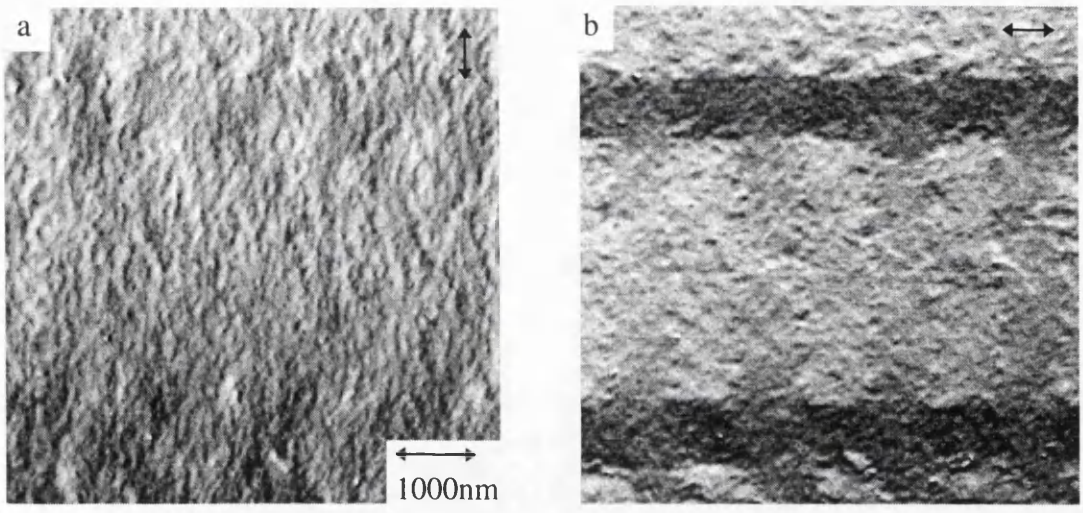

Figure 6.22a,b: DPC images of tracks written at 15mbits/In^2, mapping in directions shown.

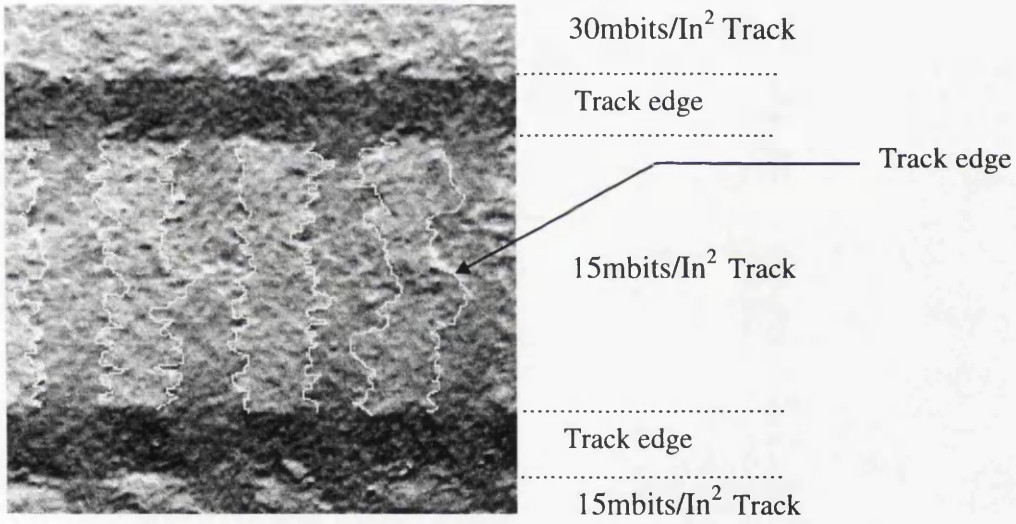

Figure 6.22c: A DPC image with the track edges highlighted. The recording direction is horizontal.

approximately 0.25μm (this can be seen more clearly in figure 6.22c where the bit boundaries have been highlighted). The total bit length was 2μm and track width is 10μm. The bits recorded at 30Mbits/in^2 could not be imaged clearly.

To act as a direct comparison, a magnetisation sequence was recorded for sample C (figure 6.23). This showed a reversal mechanism which was again similar to that for sample G, with the domains which were formed during reversal being ≈250nm in diameter.

6.6 Discussion

In this chapter I have been able to describe the micromagnetic properties of a range of CoPt alloy thin film samples. The structural information has been recorded to a resolution of better than 2nm, and the magnetic information to a resolution of better than 50nm in the presence of an applied field up to 2500Oe. The micromagnetic reversal mechanisms of certain samples has been recorded to the same resolution. I have also demonstrated that by using suitably designed experiments on the TEM I can determine the differences in micromagnetic behaviour of thin film CoPt alloys with changing structural properties.

The results from section 6.2 and 6.3 suggest strongly that while the composition may be a factor in the magnetic properties of the sample, the microstructure is much more important and is dependent primarily on the deposition parameters and substrate. This is especially evident from sample A, where two regions of the same sample, with the

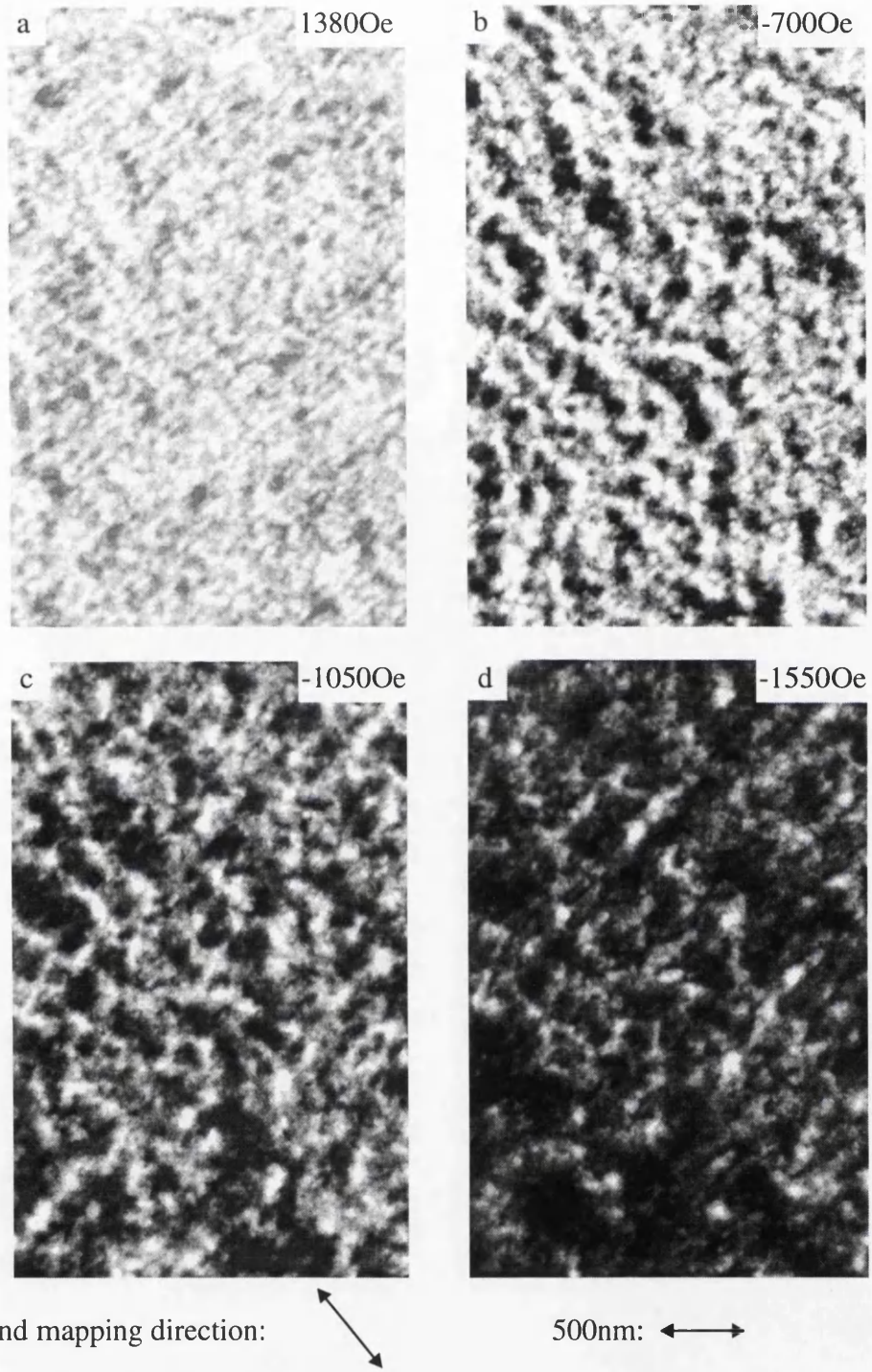

Figure 6.23: Foucault images of magnetisation processes in sample C

same thickness and composition can support in-plane or perpendicular magnetisation, the magnetisation supported being dependent on the crystal structure of the region. However more information is needed on the deposition parameters for the samples in order to draw coherent conclusions from these results.

The results from section 6.4 show that the micromagnetic structure of the samples changes as the sample thickness changes. Previously this had been put down to a changing microstructure, however my results show that the crystal structure remains constant under the growth conditions for these films. This suggests that the changing properties are caused by the changing thickness alone. As the sample thickness is increased, the in plane anisotropy will decrease. This is a similar reduction to the in plane anisotropy that will be caused by the texturing of the "c" axis perpendicular to the plane as seen in sample C.

The transition width measured for the bits recorded onto sample C is of the same order of magnitude as the average domain size apparent from the magnetisation sequence (0.25μm). This is slightly larger than the estimated transition width measured from MFM images (0.1μm) [12]. Since the MFM images the stray field around the bit patterns, this will look smoother than the actual bit transition width, so this result is not surprising.

References

[1] J.G.Zhu and H.N.Bertram, IEEE Trans. Magn. **MAG-26** (1988) 2706.

[2] J.G.Zhu, IEEE Trans. Magn. **MAG-27** (1992) 5040.

[3] J.J.Miles and B.K.Middleton, J Magn. Magn. Mat. **95** (1991) 99.

[4] V.Tutovanet and V.Georgescu, Thin Film Solids **61** (1979) 133.

[5] T.Yogi, C.Tsang, T.A.Nguyen, K.Ju, G.L.Gorman and G.Castillo, IEEE Trans. Mag. **26** (1990) 2271.

[6] J.A.Abouf, S.R.Herd and E.Klokholm, IEEE Trans. Mag. **19** (1983) 1514.

[7] M.Kitada and N.Shimizu, J.Appl. Phys. **54** (1983) 7089.

[8] S.Casey, E.W.Hill, J.J.Miles, P.Sivasamy, K.Birtwistle, B.K.Middleton, J.N.Chapman, J.Rose, IEEE Trans. Mag. **32** (1996) 3831.

[9] J.D.Livingston, J. Appl. Phys. **52** (1981) 2544.

[10] J.J.Miles, M.Wdowin, J.Oakley and B.K.Middleton, IEEE Trans. Mag. **31** (1995) 1013.

[11] S.Casey, E.W.Hill, J.J.Miles, P.Sivasamy, K.Birtwistle, B.K.Middleton, J.N.Chapman, J.Rose, J.Magn. Magn. Mat. **155** (1996) 348.

[12] S.Casey, E.W.Hill, J.J.Miles, P.Sivasamy, K.Birtwistle, B.K.Middleton, J.N.Chapman, J.Rose, in press.

Chapter 7

Discussions and future work

7.0 Introduction

The aim of this thesis has been to investigate the physical and magnetic nanostructure of thin film magnetic systems. In particular the change in the magnetic nanostructure as an external magnetic field is being applied was to be investigated. This investigation primarily involved developing techniques for applying a magnetic field to a sample, which will be large enough to reverse the magnetisation of the sample and which can be applied while the sample was being imaged in a TEM. These techniques were then to be used to examine the magnetic behaviour of three classes of magnetic thin films: GMR sensing media, MO recording media and magnetic longitudinal recording media. The results of these studies were then to be analysed to determine the nanomagnetic and nanostructural properties appropriate to the suggested application.

7.1 Discussion

In chapters two and three I outlined the techniques that were used in this thesis. The success of these techniques has been discussed with reference to the results obtained in chapters four to six.

7.1.1 GMR sensing media

In chapter four I investigated GMR sensing media. These media were Co/Cu and CoCu/Cu multilayers with different layer thicknesses. Structurally it was found that the samples were indistinguishable on the basis of their crystal size distributions, however, the crystal structures of their magnetic layers varied. If the Co layers were thicker than 2.0nm, both FCC and HCP stacking were found to be present but in the thinner Co layers only FCC crystallite structures are present in the Co layer. The CoCu alloy was found to be entirely FCC. These results are entirely consistent with previous NMR studies [1].

Magnetically the systems showed three different types of behaviour when a reversing field was applied:

(i) The samples with Cu spacer layers of 0.9nm, corresponding to the first AFM maximum, reversed by means of magnetisation rotation. The exact mechanism of the reversal changed as the thickness of the Co layers changed but the two mechanisms could be explained by the presence of an anisotropy field. The reason for this field could not, however, be explained.

(ii) The sample with a CoCu alloy in the magnetic layers and Cu layers corresponding to the second AFM maximum reversed by means of magnetisation rotation in some layers and domain wall motion in other layers. The reason for different mechanisms in the different layers could not be confirmed, although it was suggested that it was caused by changing coupling strengths at different depths within the multilayer system.

The presence of an anisotropy field for this sample was also detected and once again the reason for this field was not found.

(iii) The third type of behaviour occurred in the samples deposited with 2.0nm thick Cu spacer layers, corresponding to the second AFM maximum and Co in the magnetic layer. These samples behaved in a similar manner to Co/Cu multilayers investigated elsewhere [2] and the reversal mechanism involved a loss of directionality in the magnetic structure as the field was reduced followed by an increase in the directionality as reverse saturation was approached. There was no apparent anisotropy for these samples.

There is no immediately apparent reason why there should be an anisotropy present in some of the multilayers but not others. They were all deposited under the same conditions and the antiferromagnetic coupling between the layers should if anything make anisotropy more apparent, in the films which do not show the anisotropy, due to the weaker coupling at the second AFM maximum.

More work will have to be done to understand the reversal mechanisms of all these samples. More use could be made of the DPC mode of Lorentz microscopy in order to facilitate this, since this mode gives a more quantitative measure of the magnetic state than Fresnel or Foucault modes [3], and can be implemented at the small applied fields that are required to reverse this sample. The reason for the anisotropy in only some of the samples will also have to be investigated, along with how the anisotropy affects the GMR response of the multilayer. Extra MR loops could be easily measured, and would

determine whether the anisotropy can be used to advantage, or whether it is undesirable.

Once the properties of an extended thin film are understood, the properties of patterned elements will have to be examined, since these multilayers will almost certainly be used in this form. Changing the dimensions of the film will change the magnetostatic energy term in the energy equation, and may change the magnetic behaviour of the multilayer significantly.

7.1.2 MO media

The MO media characterised in chapter five could be divided into two categories based on their bulk magnetic properties: (i) two samples which when undergoing a reversing field sequence nucleated reverse domains at fields lower than that required for reverse saturation and (ii) three samples which nucleated reverse domains at fields higher than that required to attain reverse saturation. These two cases were characterised by hysteresis loops which had a kink in case (i) and were essentially square in case (ii).

Micromagnetic studies of these two cases were carried out in conjunction with bulk magnetic characterisation using an AGFM. The use of several investigation techniques aided the understanding of the results.

In case (i) the domains which were nucleated were maze like in structure, with each branch of the domain structure having a narrow range of widths. Once formed the

domains appeared also to be fixed in position with little or no domain wall motion apparent in the initial stages of reversal. The difference between the two samples of this type was simply that the sample which had been annealed had an increased domain nucleation field, and there was no evidence for any other effect on the micromagnetic behaviour. Previous studies of similar samples have suggested that the effect of annealing is to cause silicon or oxygen diffusion into the edges of the crystallite [4], although the reason why this would increase the domain nucleation field is not immediately apparent. Magnetic simulations have suggested that a defect is required for domain nucleation [5]. It is perfectly reasonable to suggest that annealing will remove some of these defects and thus reduce the number of possible nucleation sites. This could be the mechanism by which the domain nucleation field is increased.

The micromagnetic behaviour of these samples was simulated using a Monte-Carlo model in an attempt to estimate various parameters which are difficult to measure. By matching calculated domain patterns with recorded domain patterns, an estimate for the value of the wall energy ($\sigma_w \approx 1.8 \times 10^{-3} Jm^{-2}$) and the activation volume ($V_{act} \approx 0.015$ of the crystallite volume ($\approx 3 \times 10^{-23} m^3$)) was obtained. The value for σ_w was compared to previously measured values for Co/Pt multilayers, and was found to be consistent with the change in the M_s value. The value for V_{act} represents a column, $5nm^2$ running through the height of the multilayer, or approximately ¼ of a crystallite on a single layer. Both these scenarios appear reasonable, although there are no measures for direct comparison.

In case (ii) the domains which are formed during the initial stages of the reversal process are much more variable in width than for case (i) and there is evidence for

substantial domain wall motion during all stages of the domain wall process. The differences between the samples are in the scale of the domains and the shape. The domains nucleated in the RE-TM samples were more elongated, and had a larger average width than those nucleated in the $Co_{40}Ni_{60}$/Pt multilayer.

The next stage of the simulation process will be to match the time dependence of the magnetisation reversal more closely. In order to achieve this, one possible solution involves the addition of pinning sites to the simulation. This method has shown some promising initial results, but is still ongoing. In future the parameters for the other multilayer sample (with $Co_{40}Ni_{60}$ in the magnetic layer) could be incorporated into the equation, and simulated. This would give an idea of how the unknown parameters change as the shape of the hysteresis loop changes. This will indicate whether the changes in the reversal mechanism are due purely to the fundamental energy considerations described in chapter one or whether they are due, for example, to changes in the wall energy due to a different wall structure.

The proposed application for these media will be the recording of MO marks, so written MO marks will have to be examined in the TEM. Some marks have been recorded onto the sample with $Co_{40}Ni_{60}$ in the magnetic layer (figure 7.1). The investigation of these marks will involve recording them with different laser powers and using different field values. The marks can then be examined using DPC imaging to determine whether, for example, there have been any changes to the physical microstructure, or to determine the bit roughness. The bit roughness is a measure of how well defined the written mark is and will be a determining feature in the signal to noise ratio.

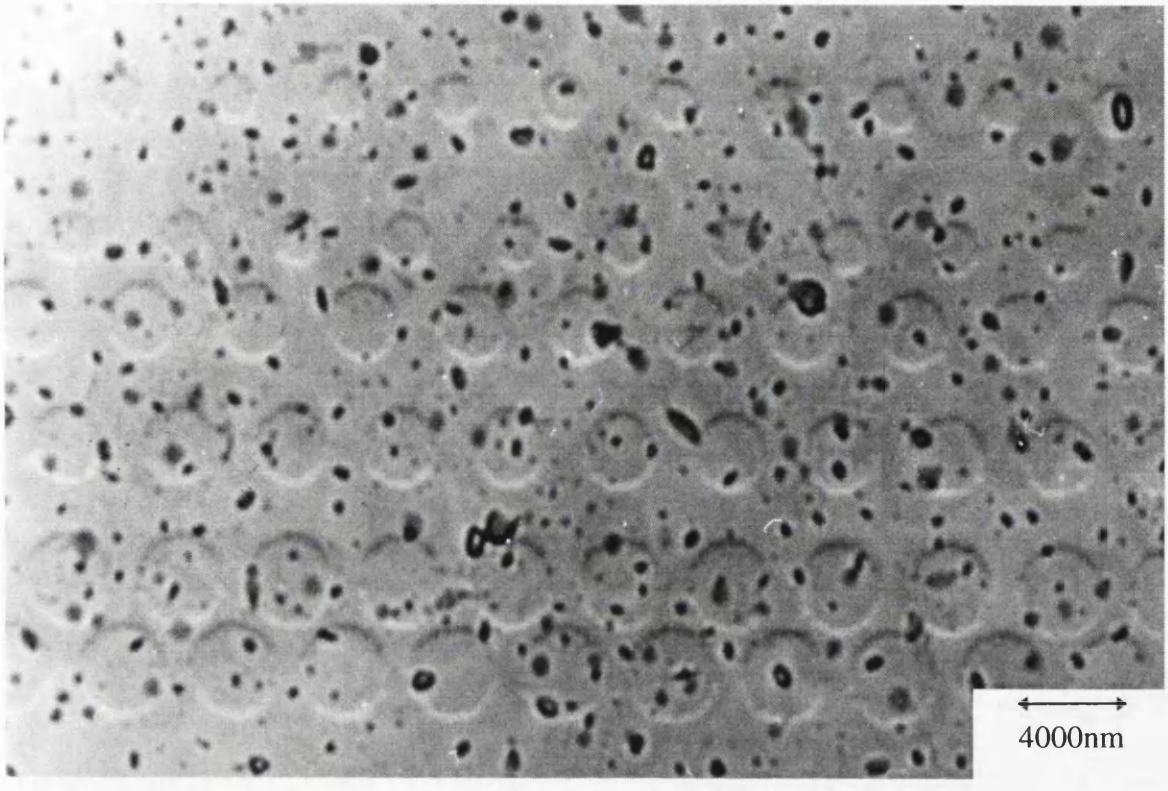

Figure 7.1: Fresnel image of marks recorded at different laser powers on sample with $Co_{40}Ni_{60}$ in the magnetic layer. (courtesy D.M.Donnet)

7.1.3 Magnetic recording media

In chapter six the nanomagnetic properties of CoPt alloys were investigated with the aim of referencing them to the physical nanostructure. The physical nanostructure itself was found to be completely independent of the sample thickness in the ranges measured. No correlation was found with the sample composition and the crystallite structure, which was found to be heavily dependent on the substrate condition and the deposition conditions (which were known to change but the exact details of which were unknown). Indeed it was found that all the samples investigated in this chapter were HCP in structure whereas on the basis of previous investigations on CoPt alloys samples some of them would be expected to be FCC in structure [6]. This anomaly can only be put down to either the different deposition conditions or the fact that the samples in the other studies were deposited onto glass substrates [6]. More would have to be known about the changes in the deposition conditions before more conclusions could be drawn. This forms the part of a different investigation.

The micromagnetic response of some of the alloys to an applied magnetic field was measured. This showed two different types of behaviour which resulted from changing degrees of coupling between the crystallites. If the crystallites were magnetically coupled, domain walls moved through the sample as a reversing field was applied, whereas if the crystallites were essentially magnetically decoupled, reversal proceeded by the nucleation of many unconnected domains which were of the order of 200nm in diameter. This second type of behaviour was found to be present in the samples which were deemed most suitable for magnetic recording. As part of

recording the micromagnetic response of these samples to a magnetic field, the saturation magnetisation of two of the samples was measured in the TEM, and found to be consistent with the change in composition.

The samples which displayed the domain sizes most suitable for magnetic recording were found to have texturing, with the "c" axis pointing out of the plane of the film. This would have the effect of reducing the in plane anisotropy, which in turn acts to decrease the average domain sizes. This effect was also witnessed as samples were grown to different thicknesses, where the samples maintained the same nanostructure, but the average domain size decreased as the sample thickness increased. This could only be explained by the decrease in the in-plane anisotropy caused by changes in the demagnetising field. It is not clear by how much more the average size of the domains can be decreased by thickening the film before the shape anisotropy becomes too small to overcome perpendicular anisotropy from the "c" axis texturing and the preferred magnetisation direction becomes perpendicular to the surface of the film. This will be a source of future experiments once the deposition conditions have been proven to provide reproducible samples.

The written domains themselves were written to a density of 15 and 30Mbits/inch^2 onto the sample which was judged to have the most suitable domain configuration, although only the bit patterns written to a density of 15Mbits/inch^2 could be successfully imaged. The peak to peak transition width for these bits was measured to be ≈0.25μm. This length was comparable with the transition width simulations would predict for this sample (≈150nm) [7]. The recording density demonstrated in this regime is not of the highest attainable. This is an obvious source of future work, with

both the sample and the writing conditions being optimised to produce the highest bit densities possible on this type of sample.

Much of the proposed work with the aim of increasing the density of hard disk recording has focused on etching tracks or other features in the media. Since the nanomagnetic behaviour of the various samples has been well established by the TEM experiments the properties of the most promising alloys can be determined once they are patterned into elements. Indeed this is already underway as part of a different project.

7.2 Conclusions

In the course of these investigations I have demonstrated the ability of the TEM to determine the nanomagnetic and nanostructural properties of a wide variety of thin film systems. In particular I have been able to image and understand the evolution of the nanomagnetic properties of these thin film systems in a changing magnetic field. Investigations such as these will be invaluable in the search for higher capacity recording systems as they are used to characterise both the recording media and the materials for use in the read heads. A final note on the success of these techniques is that they are already being made use of in the study of other thin film systems with great success.

References

[1] E.Jedryka, M.Wojcik, S.Nadolski, D.J.Kubinski, H.Holloway and P.Panissod, accepted for publication 1997.

[2] P.R.Aitchison, J.N.Chapman, D.B.Jardine and J.E.Evetts, J. Appl. Phys. **81** (1997) 3775.

[3] J.N.Chapman, I.R.McFadyen and S.McVitie, IEEE Trans. Mag. (1990) 1506.

[4] Q.Meng, Ph.D. Thesis, University of Twente, (1996).

[5] R.Giles and M.Mansuripur, Computers in Physics (1991) 204.

[6] M.Kitada and N.Shimizu, J.Appl. Phys. **54** (1983) 7089.

[7] J.J.Miles, M.Wdowin, J.Oakley and B.K.Middleton, IEEE Trans. Mag. **31** (1995) 1013.

Have fun.